Electron Diffraction Studies of Unsupported Bismuth Clusters

A thesis
submitted in partial fulfilment
of the requirements for the Degree
of Doctor of Philosophy in Physics
in the University of Canterbury

by

Andreas Wurl

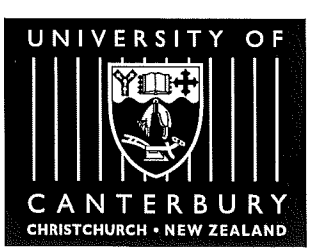

Department of Physics and Astronomy
University of Canterbury

2003

SCIENCES
LIBRARY
QC
173.4
.M48
.W967
2003

Abstract

This study uses electron diffraction to investigate the structure of clusters, which are small particles containing between 3 and 10^5 atoms. Because of their size clusters represent the link between molecules and bulk material. Of particular interest is the appearance of structures that are forbidden in the bulk as the particle size decreases. One of the main reasons why structural changes occur is the increased proportion of surface atoms in small clusters which may lead to a rearrangement of the atoms in a cluster due to the need to minimise surface as well as bulk energies.

Electron diffraction applied to cluster beams allows the study of the structure of small particles, free of contamination and without interaction with a substrate. The exposure time of the clusters in the beam is very short limiting the possibility of altering the clusters by the electron beam. The high intensity cluster beam necessary for this diffraction experiment is generated by an inert-gas aggregation source.

The two main parts of this thesis work are the development of a new detector system to record electron diffraction patterns and the study of the structure of unsupported Bi clusters. Furthermore, two new analysis tools based on existing techniques have been developed and implemented.

The new detector system uses a pair of linear diode arrays to measure the radial intensity profile of the Debye–Scherrer ring diffraction pattern. The scattered electrons are detected through secondary charge created on impact in the semiconductor material of the sensor pixels. The detector operates differently compared to its predecessor enhancing the quality of the diffraction patterns.

The diffraction patterns from Bi particles can be categorised into patterns from crystalline clusters and patterns with liquid/amorphous features. In the case of the crystalline particles, the diffraction patterns indicate a rhombohedral structure. It has been found that the size estimates determined from the diffraction patterns are smaller than the estimates calculated from TEM images of deposited clusters. This suggests that the particles consist of domains that are separated by lattice defects. The mean sizes of the crystalline particles range from 109 to 231 Å. In the case of liquid/amorphous particles, the patterns have been compared to patterns of liquid drops calculated from structure data of liquid Bi. Although the features in the patterns are similar, the peak positions and relative intensities are different suggesting a new, probably amorphous structure.

Contents

Chapter 1

Introduction

Small particles consisting of between 3 and about 10^5 atoms, also called clusters, occupy a central position in the search for materials with new properties. This is because there is, apart from the type of element which the cluster is composed of, an additional parameter that influences the properties: the cluster size or, more accurately, the number of atoms in the cluster.

The size of the clusters has a direct influence on the electronic structure (and therefore on the cluster properties) as can be illustrated by the following two extremes: particles consisting of only a few atoms have discrete electron energy levels, whereas the energy levels of larger microcrystalline particles are quasi continuous. As a cluster grows the electronic structure changes with every atom added and only at large sizes approaches the limit of the bulk material where it can be described by band theory. Another characteristic of clusters is that a large proportion of their atoms is on the surface. While, for example, a large cluster with 10,000 atoms has already nearly 20% of its atoms on the surface, this proportion increases to more than 80% for a particle with only 100 atoms [1]. The size dependence of the electronic structure and the large number of surface atoms gives clusters an important role as catalysts in certain chemical reactions as their reactivity and selectivity is strongly enhanced compared to bulk surfaces [2]. Furthermore, a small cluster can also adopt a crystal structure that does not correspond to the structure of the bulk solid. Examples are the clusters with five-fold symmetry discovered by Ino, Allpress and Sanders [3, 4] or the soccer ball shaped C_{60} clusters [5].

However, there is no reason to assume that properties will scale smoothly with cluster size (number of atoms). On the contrary, small clusters are likely to show oscillations in their properties as the electronic level structure varies strongly if only a single atom is added or removed and as structural changes can occur. Depending on the number of atoms small clusters have their own individual properties. Only for larger clusters will many properties, such as melting temperature or ionisation energy, show a regular variation with cluster size and scaling laws can be applied. Cluster properties

are the subject of intense research and more information can be found in general review articles, e.g. [2, 6, 7].

The subject of this thesis work is the study of the structure of small metal clusters and how the structure is influenced by the particle size. For this purpose a high energy electron diffractograph is used in combination with a cluster beam source. The clusters are produced in an inert-gas aggregation (IGA) source and are extracted through a series of pumping stages whereby they form a cluster beam. In the diffraction chamber the particles are probed in flight by a high energy electron beam and give rise to a Debye–Scherrer type diffraction pattern.

The technique of electron diffraction on a beam of clusters offers several advantages compared to other methods used for structural investigations, such as high-resolution transmission electron microscopy (HRTEM) or X-ray and neutron diffraction techniques. Firstly, the particles in the beam (unsupported) are probed in a high vacuum environment and are therefore free of contamination and any perturbing effects due to a substrate. Secondly, as the particles pass through the electron beam they are only exposed for a very short time, thereby minimising the risk of structural changes due to the influence of the electron beam. These advantages, however, come also at a cost: while in HRTEM studies individual particles can be investigated, the information from diffraction experiments is averaged over randomly orientated particles with possibly different sizes and structures. This fact necessitates a complicated analysis of the diffraction patterns.

General ideas and concepts concerning the structure of clusters are presented in the next section. This is followed by an overview of theoretical methods to predict the cluster structure. Then a review of other diffraction experiments on unsupported clusters is combined with the history of the equipment used for this thesis work. The final section of this chapter describes the outline of the following thesis chapters.

1.1 The Structure of Clusters

Although the structure of a small particle is strongly influenced by the thermodynamics during the growth process, kinetic factors (e.g. growth and diffusion rates) can also be important. If the cluster is in thermal equilibrium with its vapour it adopts a structure that minimises its total energy. On the other hand, if there is strong kinetic control of the growth the particle will have a non-equilibrium structure with higher total energy.

As mentioned above, a high proportion of atoms in a cluster are on the surface. Under the assumption that thermodynamics plays a major role, a larger particle with the structure of the bulk material will adopt a shape that minimises its surface energy. This leads to the so-called Wulff shape of a cluster which will be treated in more detail in the following section. For smaller clusters with a naturally larger proportion of surface atoms, it may even be energetically favourable to rearrange the interior of the cluster, thereby accepting a strained structure, and adjust the shape of the particle to further reduce the surface energy. Such particles are, for example, the so-called Multiply Twinned Particles (MTPs), which are frequently found for materials with a face centred cubic (FCC) or a diamond cubic (DC) structure in the bulk.

MTPs are non-crystalline structures with five-fold axes of symmetry which means that their symmetry is incompatible with the three-dimensional periodicity required to form a bulk crystal. The two characteristic types of MTPs, the decahedron and the icosahedron, can be constructed from tetrahedral subunits of the regular bulk lattice [3]. The decahedron consists of five tetrahedra sharing a common edge while the icosahedron is composed of twenty tetrahedra sharing a common point in the centre. In order to fit the tetrahedra into the volume of the polyhedra the subunits must be distorted which results in the strain mentioned above. The name for these structures is derived from the twin planes found between the tetrahedra (see [8–10] and references therein).

A perfectly polyhedral shaped particle can only be achieved with certain numbers of atoms. Therefore, for every particular shape there is a sequence of numbers which is referred to as geometric magic numbers[1] (see e.g. [9]). Although a different shape usually leads to a different set of magic numbers there are cases where the sequences are identical as, for example, for the icosahedra and the cuboctahedra with triangular facets [9]. Clusters with completed outer layers or even completely covered individual faces are visible as peaks or dips (depending on the type of experiment) in mass spectra. By analysing the mass spectra, it is then sometimes possible to distinguish between different particle structures.

Marks *et al.* pointed out [8] that it is rather common to find more than one structure in a population of small particles. It is also emphasised that the spectrum of particle structures is not restricted to perfect structures or structures that can be described by simple models (e.g. MTPs), but also contains a large proportion of particles with

[1] A completely different type of magic numbers are the electronic magic numbers which are due to a electronic shell structure in small particles [6, 11].

defects or with more complicated structures. These findings are based on HRTEM investigations. Despite the fact that the structure may be affected by the substrate and the intense electron beam, these studies provide very useful information about possible model structures for the interpretation of the diffraction patterns. Therefore, in the most general case the beam of particles may contain the following type of particles:

- Single crystals
- Single crystals with lattice defects (twins, stacking faults, etc.)
- Multiply twinned particles
- Polyparticles:
  Particles with a much more complicated structure than MTPs which are present whenever MTPs are observed. The structure may be described as MTP-like with additional defects. For details and references see [8, 12, 13].
- Other morphologies:
  This includes structures that are strongly influenced by kinetic factors, structures that could not be readily identified by HRTEM because the contrast pattern was too complex, as well as possible new structures [8].

The diversity of small particle structures and the influence of growth conditions can be visualised with the concept of a potential energy surface as, for example, discussed by Marks *et al.* [8, 14, 15]. In this model, the different structures are represented by global and local minima in the potential energy surface. Particles do not automatically adopt the structure associated with the global minimum but rather than this, occupy minima on a statistical (Boltzmann-like) basis depending on the temperature of the particles and the energy barrier between minima. As a consequence, even without kinetic effects the (configurational) distribution of particles may contain different structures if the energy barriers between minima are small compared to thermal fluctuations. Since the energy difference between different morphologies and structures decreases with particle size [14] structural transitions due to thermal fluctuations are much more likely for small clusters and may lead to several (isomeric) structures in a particle distribution.

During the *growth of a particle* the potential energy surface changes with every atom added. If particles have sufficient time and thermal energy to overcome the barriers they can adjust to the changing surface and maintain a Boltzmann-like occupation of the minima. The larger the particles get the larger will be the difference between the

relative energies of the minima, resulting in most of the particles occupying the global minima. On the other hand, particles with insufficient time or thermal energy may become trapped in the minima during growth causing kinetic structures[2] to develop. Thus, it is expected that at higher temperatures the growth is more thermodynamic, whereas at lower temperatures kinetic effects become more important. The growth rate determines how much time the system has to adjust to the changes of the potential energy surface. Rapid growth hinders structural transformations, trapping particles in local minima from where they evolve further to other (kinetic) structures.

1.2 Theoretical Predictions

The analysis of measured diffraction patterns from clusters strongly relies on those patterns being compared to calculated patterns from model structures. This is especially true for non-crystalline clusters (e.g MTPs, amorphous particles). Together with model structures based on information gained from other observations (e.g. HRTEM), theoretical predictions are therefore most useful. Four general approaches are listed here. For further details review articles or the standard text books should be consulted, e.g. [19–22].

- Ab initio or first principles methods use the laws of quantum mechanics to compute the geometry and electronic structure of a particle. Their particular strength is that the only parameters used are the type of elements that make up the particle and, preferably, the approximate positions of the atoms within the particle. These methods are extremely computationally expensive. There are two main approaches: The calculations based on the Hartree–Fock theory [23] compute the electronic many body wave function by directly solving the Schrödinger equation. The wave function describes the electrons and depends on the positions of all electrons. Therefore, the method scales extremely badly with size and is limited to typically 10–20 atoms. In density functional theory (DFT) [24] the basic quantity is the electron density. In contrast to the wave function the electron density depends only on the three position variables and not on the positions of all electrons. This enormous simplification allows the treatment of larger systems (typically 10–100 atoms).

- The Molecular Dynamics (MD) technique [21] calculates the trajectories of all

[2]The influence of kinetic effects on the cluster structure and morphology can, for example, be studied by means of computer simulations. For details see [16–18].

atoms in a cluster as they interact with each other. The atoms move according to Newtonian mechanics (deterministic approach) whereby the forces on the atoms are computed from an empirical potential energy function. Starting from a set of initial conditions the positions and velocities of the particles are calculated in a series of time steps (usually 1 fs). Because of the short time intervals and the computational complexity, the total simulation time span is usually restricted to a few nanoseconds. However, compared to ab initio calculations MD simulations are far less computationally demanding and therefore permit several ten thousands of atoms to be followed. This technique strongly depends on the quality of the energy potential that describes the interaction between atoms.

- The Monte Carlo (MC) technique [21] follows a stochastic approach and tries to find an atomic configuration with a lower energy by randomly probing the geometry of the particle. In the standard Metropolis MC method, a randomly selected atom is moved through a random displacement and the energy change (based on an empirical potential energy function) for the entire cluster, ΔE, associated with this trial movement is calculated. If the energy is lowered, the trial is accepted. Otherwise, the trial is accepted with a probability given by a Boltzmann factor $p = \exp(-\Delta E/k_B T)$. After many trials the system reaches an equilibrium state. As for the MD technique MC calculations require an accurate model of the energy potential that describes the interaction between atoms. The computational requirements for MC simulations are comparable to those of MD simulations allowing similar sized systems to be treated.

- In the case of larger clusters with the structure of the bulk material, it is the shape of the particle which is of particular interest. It can be assumed that in thermodynamic equilibrium, the particle takes a shape that minimises its total surface energy F,

$$F = \int \gamma \, dA, \tag{1.1}$$

where γ is the surface free energy and dA the surface area. For a faceted particle (1.1) is equivalent to:

$$F = \sum_i \gamma_i A_i \tag{1.2}$$

where the subscript i describes a particular surface facet with an area A_i. As a

result, the particles will adopt a compact shape which reduces the surface area and will have facets with low surface energy. A simple geometric method to solve (1.2) was given by Wulff [25]. According to Wulff the shape of the particle can be constructed in the following way: crystallographic planes are drawn with a normal distance to an origin that is proportional to the planes' surface energies. Then, these planes will shape a polyhedron around the origin which represents the equilibrium shape of the crystal. This polyhedron is called the Wulff shape for the cluster.

In summary, ab initio methods promise the most accurate results but are restricted to very small particles. With the advancements in computer technology MD and MC simulations are increasingly becoming the standard tools for the prediction of the particle structure. However, they require well tested potential energy functions which are not available for all materials. This is in particular the case for bismuth which is the subject of this thesis work.

1.3 Electron Diffraction Studies of Unsupported (Metal) Clusters

This section provides a brief history of the technique used in this study as well as an overview of the ongoing experiments. A more extensive review of previous experiments and results can be found in the book chapter that is included in this thesis as Appendix A.

The technique of electron diffraction to investigate the structure of clusters was first used by P. Audit in 1969, at the Université Paris-Sud, France [26]. The clusters studied were produced in supersonic beam expansions and included rare-gases and CO_2 clusters. Following these experiments an improved apparatus was developed by B. Raoult and F. Farges [27] and has been used to study e.g. Ar, CH_4 and N_2 clusters (see [28] and references therein).

The group of G. Stein at Northwestern University, USA, was the first to perform diffraction experiments on unsupported metal particles [29–31]. Since supersonic expansions are not suitable for the production of a high intensity cluster beam of larger metal clusters [32], a new source based on the inert-gas-aggregation technique was constructed. This so-called Northwestern source was successfully used for the study of Ag, Bi, In and Pb clusters.

The equipment used in this study originated from a collaboration between G. Stein and the laboratory of J. P. Borel and R. Monot at EPFL, Switzerland. The new apparatus combined an improved version of Stein's cluster source [33] with an existing electron diffractograph [34]. Also involved in the construction of the equipment was B. D. Hall who used this equipment for studies on Ag clusters [35, 36]. After these experiments the equipment underwent substantial modifications. With the source performing well, B. D. Hall focused on improving the diffractograph. The single channel detector was replaced by a much faster multi-channel system based on a pair of linear CCDs. In addition, a new electron illumination system was installed which was capable of operating at higher electron energies (up to 100 kV) and provided better electron optics [37]. This second generation apparatus was subsequently used by D. Reinhard to perform further experiments on Ag clusters [38, 39] and new studies on Cu [39, 40] and Ge particles [39]. While diffraction patterns from Ag and Cu cluster could be obtained easily, the production of a high intensity beam of Ge clusters turned out to be more difficult. The experiments on Ge clusters only resulted in patterns with very weak features which were not suitable for a detailed analysis [39].

After these experiments the EPFL apparatus was first relocated to Massey University, New Zealand, by B. D. Hall and after a brief period was shifted a second time to the laboratory of S. A. Brown at the University of Canterbury, New Zealand. Following the reconstruction of the equipment, experiments resumed in 1999 with studies on Zn, Pb and Bi clusters. While diffraction patterns from Pb clusters could be easily obtained in the experiments by M. Hyslop [41, 42] it was not possible to produce sufficient quantities of Zn clusters to measure diffraction patterns. Experiments on Bi clusters and additional improvement to the equipment are the subject of this thesis. Further experiments on Sb clusters are underway and are being performed by M. Kaufmann.

A *different* technique for electron diffraction on unsupported clusters has been developed at the Rowland Institute in Boston, USA [43]. This Trapped Ion Electron Diffraction (TIED) technique allows storage and thermalisation of small size selected ionised clusters in a RF Paul trap which then can be probed by an electron beam (40 kV). So far, diffraction experiments have been performed on C_{60} [43] and $(CsI)_nCs^+$ clusters [44]. Similar experiments on metal clusters are planned with a new TIED system at the research centre (FZK) in Karlsruhe, Germany [45].

1.4 Outline of the Following Chapters

This thesis is organised as follows: Chapter 2 describes the design and operation of the experimental equipment which consists of an electron diffractograph, a cluster beam source and beam sampling devices. The theory of cluster nucleation and growth in an inert gas aggregation source is outlined as well as some general trends for the cluster production with this type of source. Several processing steps are necessary to convert the raw data into diffraction patterns that can be analysed. These steps are described in detail. The chapter closes with a brief outline of the procedure used for the analysis of the TEM images obtained from deposited clusters.

Chapter 3 focuses on the new detector developed to measure the intensity of the Debye–Scherrer diffraction pattern. Similar to its predecessor it uses a pair of linear pixel sensors that are directly exposed to the scattered high-energy electrons. Since the new and the old detector operate differently, the two modes of operation are explained and compared with the help of experimental data and data from simulations. This is followed by a detailed description of the design of the new detector system and the presentation of test results.

Chapter 4 describes the calculation of diffraction patterns from model structures and the different methods used to extract information from an experimental diffraction pattern. In addition to the existing techniques two new methods are presented: the constraint inversion and an analysis tool based on the Reverse Monte Carlo (RMC) method. Since the analysis strongly relies on the comparison of the experimental patterns to patterns calculated from model structures, example diffraction patterns from Bi clusters are shown. For crystalline Bi clusters with the bulk structure, several series of patterns are calculated for a range of sizes and shapes. Patterns from liquid clusters are given for different sizes and different droplet temperatures.

Chapter 5 presents the results from the diffraction experiments on Bi clusters. It begins with a review of previous studies on Bi clusters to provide background information. The measured diffraction patterns are displayed in three groups depending on the carrier gas used (Ar, He, Ar/He mixture). In most cases a sequence of diffraction patterns are obtained by varying only one source parameter. In the analysis section, patterns from crystalline particles and patterns with liquid/amorphous features are investigated separately. The chapter closes with the discussion of the results.

In chapter 6 the findings from the previous chapters are reviewed and are combined with an outlook for electron diffraction studies on clusters and future work.

References

[1] R. L. Johnston, *Atomic and Molecular Clusters*, Taylor & Francis, 2002.

[2] W. Eberhardt, Surf. Sci. **500**, 242 (2002).

[3] S. Ino, Soc. Jpn. **21**, 364 (1966).

[4] J. G. Allpress and J. V. Sanders, Surf. Sci. **7**, 1 (1967).

[5] H. W. Kroto, J. R. Hearth, S. C. O'Brien, R. F. Curl, and R. E. Smalley, Nature **318**, 162 (1985).

[6] R. L. Johnston, Phil. Trans. R. Soc. Lond. A **356** (1998).

[7] W. A. de Heer, Rev. Mod. Phys. **65**, 611 (1993).

[8] L. D. Marks, Rep. Prog. Phys. **57**, 603 (1994).

[9] T. P. Martin, Phys. Rep. **273**, 199 (1996).

[10] H. Hofmeister, Cryst. Res. Technol. **1**, 3 (1998).

[11] W. D. Knight, K. Clemenger, W. A. Saunders, M. Y. Chou, and M. L. Cohen, Phys. Rev. Lett. **52**, 2141 (1994).

[12] L. D. Marks and D. J. Smith, J. Micros. **130**, 249 (1983).

[13] D. J. Smith and L. D. Marks, Phil. Mag. A **44**, 735 (1981).

[14] P. M. Ajayan and L. D. Marks, Phase Transitions **24**, 229 (1990).

[15] N. Doraiswamy and L. D. Marks, Phil. Mag. **71**, 291 (1995).

[16] S. Valkealahti, Phys. Rev. B **57**, 15533 (1993).

[17] F. Baletto, C. Mottet, and R. Ferrando, Phys. Rev. B **63**, 155408 (2001).

[18] F. Baletto, C. Mottet, and R. Ferrando, Phys. Rev. Lett. **84**, 5544 (2000).

[19] A. Gross, Surf. Sci. **500**, 347 (2002).

[20] F. Starrost and E. Carter, Surf. Sci. **500**, 323 (2002).

[21] D. W. Heermann, *Computer Simulation Methods in Theoretical Physics*, Springer Verlag, 2nd edition, 1990.

[22] M. P. Allen and D. J. Tildesley, *Computer simulation of liquids*, Oxford University Press, 1989.

[23] A. Szabo and N. S. Ostlund, *Modern Quantum Chemistry: Introduction to the Advanced Electronic Structure Theory*, Dover Publications, 1996.

[24] P. Hohenberg and W. Kohn, Phys. Rev. B **136**, 864 (1964).

[25] G. Wulff, Z. Kristallog. **34**, 449 (1901).

[26] P. Audit, J. Phys. **30**, 192 (1969).

[27] B. Raoult and J. Farges, Rev. Sci. Instr. **44**, 430 (1973).

[28] F. Calvo, G. Torchet, and M. F. de Feraudy, J. Chem. Phys. **111**, 4650 (1999).

[29] A. Yokozeki, J. Chem. Phys. **68**, 3766 (1978).

[30] A. Yokozeki and G. D. Stein, J. Appl. Phys. **49**, 2224 (1978).

[31] B. G. D. Boer and G. D. Stein, Surf. Sci. **106**, 84 (1981).

[32] G. D. Stein, Surface Science **156**, 44 (1985).

[33] M. Flüeli, *Observation des Structures Anormales de Petites Particules d'Or et d'Argent par Microscopie Electronique à Haute-Résolution et Diffraction d'Electrons par un Jet d'Agrégats d'Argent*, PhD thesis, EPFL, 1989.

[34] C. Solliard, *Etude par Diffraction et Microscopie Electroniques, de la Structure et Propriétés Thermodynamiques de Petits Grains d'Or et de Platine: Effets de Taille*, PhD thesis, EPFL, 1983.

[35] B. D. Hall, M. Flüeli, R. Monot, and J.-P. Borel, Phys. Rev. B **43**, 3906 (1991).

[36] B. D. Hall, *An Installation for the Study of Unsupported Ultrafine Particles by Electron Diffraction with Application to Silver: Observation of Multiply Twinned Particle Structures*, PhD thesis, EPFL, 1991.

[37] B. D. Hall, M. Flüeli, D. Reinhard, J.-P. Borel, and R. Monot, Rev. Sci. Instrum. **62**, 1481 (1991).

[38] D. Reinhard, B. D. Hall, D. Ugarte, and R. Monot, Phys. Rev. B **55**, 7868 (1997).

[39] D. Reinhard, *Croissance et Stabilité d'Agrégats d'Argent et de Cuivre, Etudiés en Jets Moléculaires par Diffraction d'Electrons à Haute Energie*, PhD thesis, EPFL, 1996.

[40] D. Reinhard, B. D. Hall, P. Berthoud, S. Valkealahti, and R. Monot, Phys. Rev. B **58**, 4917 (1997).

[41] M. Hyslop, A. Wurl, S. A. Brown, B. D. Hall, and R. Monot, Eur. Phys. J. D **16**, 233 (2001).

[42] M. Hyslop, *Electron Diffraction Studies of Unsupported Clusters*, PhD thesis, University of Canterbury, 2002.

[43] M. Maier-Borst, D. B. Cameron, M. Rokni, and J. H. Parks, Phys. Rev. A **59**, 3162 (1999).

[44] S. Krückeberg, D. Schooss, M. Maier-Borst, and J. H. Parks, Phys. Rev. Lett. **85**, 4494 (2000).

[45] D. Schooß, Personal communication, 2002.

Chapter 2

The Experimental Apparatus

The experimental apparatus used during this study is a high energy electron spectrograph specifically designed to study the structure of unsupported clusters. The instrument was originally designed and built at the EPF in Lausanne and is described in detail in [1–3]. After the relocation of the equipment to the University of Canterbury, the old detector system was replaced by a newly developed system which will be described in chapter 3.

A schematic of the experimental equipment is shown in Fig. 2.1. Clusters are produced with an inert-gas aggregation source. A beam of clusters and inert-gas emerges from the source and passes through two differential pumping stages, in which a large proportion of the carrier gas is removed. In the diffraction chamber the beam is probed by a 80 keV electron beam. The particles in the beam are randomly orientated and give rise to a Debye-Scherrer type ring diffraction pattern. The intensity of the scattered electrons is measured with a pair of linear diode arrays aligned along a diameter of the pattern. Further downstream of the cluster beam the particles can be sampled by a quartz deposition rate monitor and a transmission electron microscope (TEM) grid holder.

The cluster source, the electron diffractograph and the sampling devices are described in more detail in the following sections.

2.1 The Cluster Beam Source and Pumping System

Clusters are produced with the inert-gas aggregation (IGA) technique. In the inner chamber of the source, bulk material is resistively heated in a crucible. The hot metal vapour mixes with a flow of inert gas which cools down the vapour and leads to regions with highly supersaturated metal vapour. In these regions clusters can form by homogeneous nucleation and grow by adsorption from the vapour and coalescence with other particles. The stream of inert gas carries the particles away from the growth region and finally out of the inner source chamber. The mixture of gas and particles then

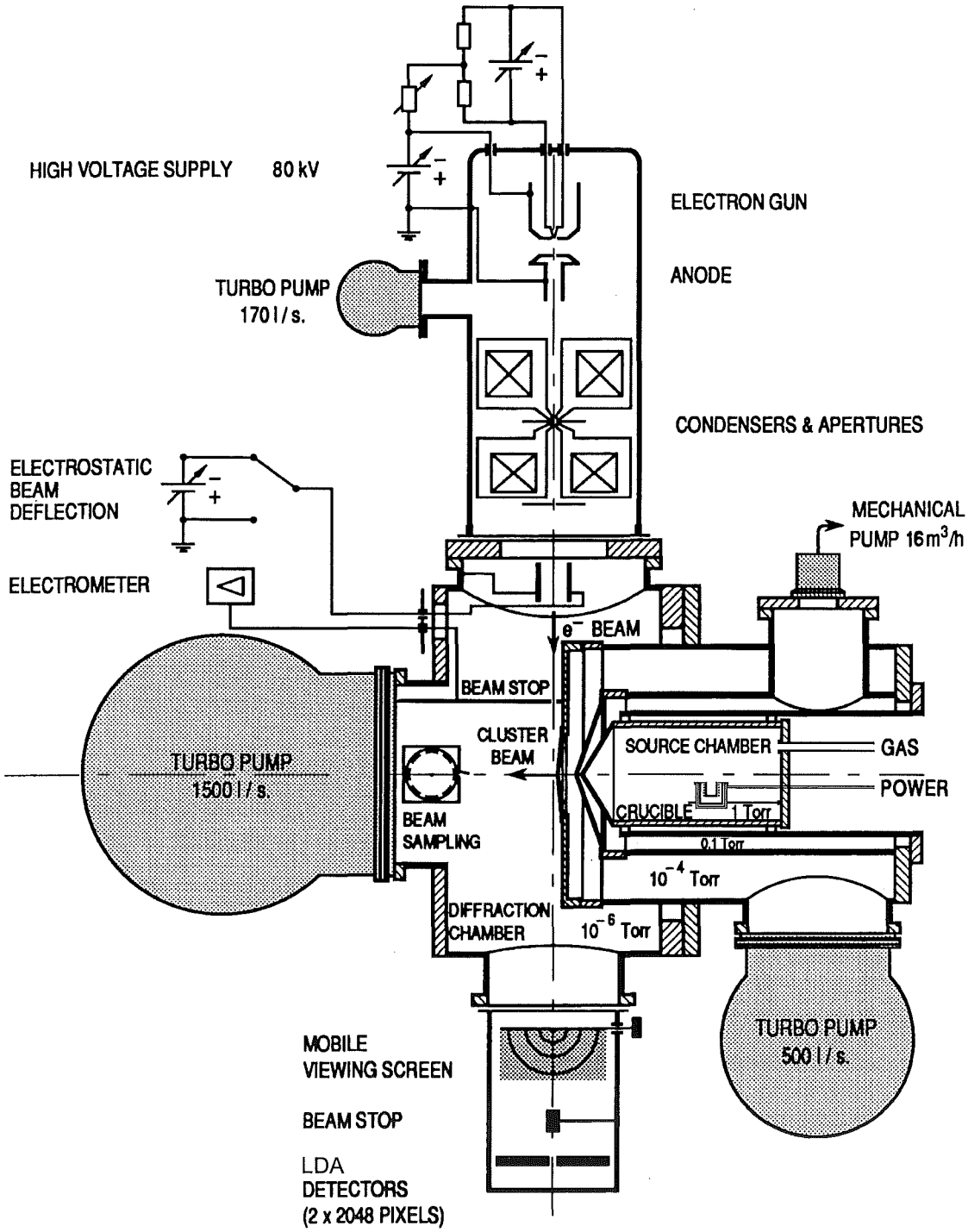

Figure 2.1: Schematic of the experimental equipment. The apparatus combines a high energy electron diffractograph with a cluster beam source. After Hall [3].

passes through two pumping stages separated by a series of nozzles before it enters the diffraction chamber. In this process, a large proportion of the carrier gas is removed and a beam of particles is formed by the series of collimating nozzles.

Figure 2.2 shows a diagram of the source chamber and the differential pumping stages. The crucible is made of boron nitride (BN) and rests on a thin BN disk that has a small hole for the thermocouple. The crucible is heated by a tungsten filament. Since magnetic fields can affect the diffraction pattern the shape of the filament is optimised to reduce the magnetic field created. This arrangement is enclosed by a cup shaped alumina insulator that itself is surrounded by two layers of tungsten heat shields. The opening at the top is covered with a tantalum cap with a hole for the crucible. Another horizontal heat shield divides the source chamber into two separate halves. The whole crucible arrangement sits on supports which are connected to the flange shown in Fig. 2.2. The flange has feedthroughs for the gas inlet, the thermocouple, the filament power and the source pressure gauge. The walls of the inner chamber and the flange are water-cooled to maintain a constant temperature of the source chamber walls.

The inert gas flow is regulated by a newly built flow control system. It consists of two MKS Instruments flow controllers[1] and separate electronics and allows a well defined mixing of different gases (Ar and He) with a high accuracy in the gas flow rates. For a given set of nozzles the pressure in the source chamber is proportional to the total gas flow and the desired pressure can be set by changing the total flow rate.

In the inner chamber the pressure of the inert gas is typically between 1 and 50 Torr. The first pumping stage is connected to a rotary pump (16 m^3/h) maintaining a pressure of approximately 0.1 Torr. The second stage is pumped by a 500 l/s turbo molecular pump resulting in a pressure of approximately 10^{-4} Torr. The diffraction chamber is connected to a 1500 l/s turbo pump and without gas flow, a pressure of as low as $2.5 \cdot 10^{-7}$ Torr can be achieved. During a diffraction experiment, the pressure in the diffraction chamber typically ranges from 0.8 to $3 \cdot 10^{-6}$ Torr.

The dimensions and geometry of the nozzles shown in Fig. 2.2 are given in Table 2.1. The separation of the nozzles can be adjusted during the assembly of the source chamber.

[1]MKS 1179A general purpose mass flow controller

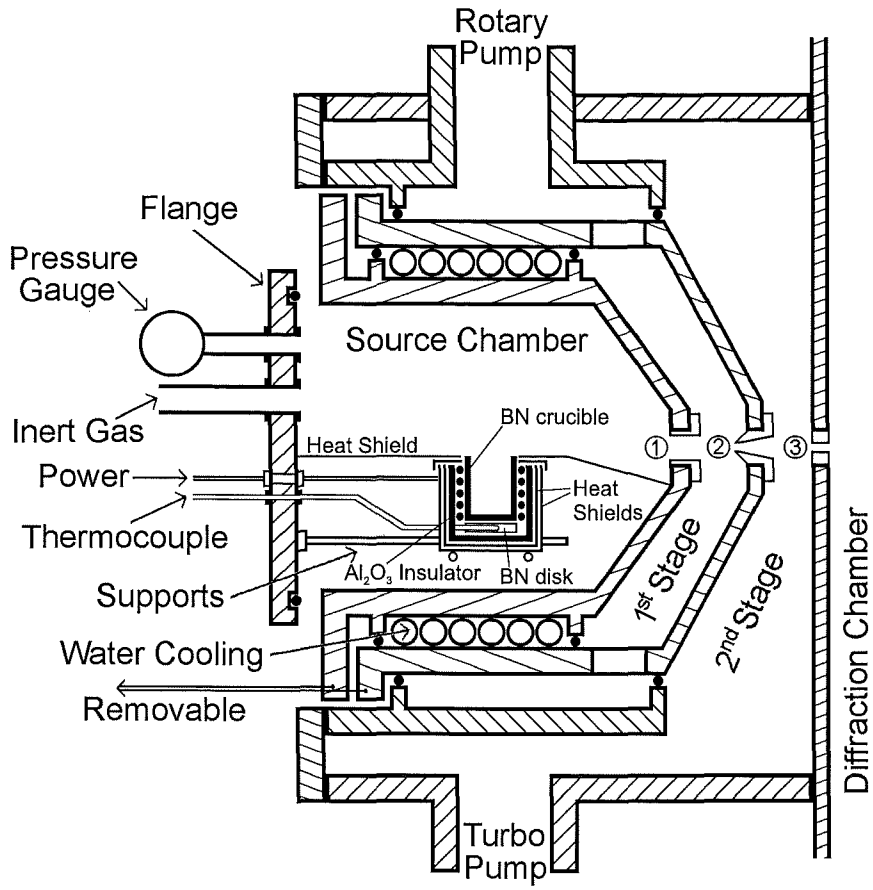

Figure 2.2: Diagram of the source chamber and the differential pumping stages, after [4] (modified). The inner chamber has a diameter of 87 mm and a length of 110 mm. The encircled numbers refer to the nozzles described in Table 2.1.

Table 2.1: Properties of the nozzles as shown in Fig. 2.2 and as used in the experiments with Bi. The nozzle material is graphite.

Nozzle	Geometry	Diameter [mm]
1	cylindrical, length: 15–30 mm	0.8–4
2	Skimmer, length: 4 mm	1.5
3	cylindrical, length: 2 mm	1.5

Cluster Nucleation and Growth

The formation of clusters within the condensation chamber depends on several complex processes and so far it has not been possible to create a complete quantitative model of an IGA source. The difficulties arise from the complicated flow pattern of the gas in the chamber and the many parameters influencing the nucleation, such as the dimensions of the various components, gas flow rate and metal vapour density. Therefore, every IGA

source performs differently and has to be characterised by experiment. However, some insight about the nucleation process can be gained with the help of the homogeneous nucleation theory.

Homogeneous Nucleation Theory

A detailed introduction to this theory can be found in [5]. The homogeneous nucleation theory describes the formation of a liquid phase by condensation from the vapour. The phase transition is blocked by a free-energy barrier ΔF which is due to the creation of a new surface when a droplet with a radius r, density ρ and temperature T forms [5]:

$$\Delta F = 4\pi r^2\gamma - \frac{4}{3}\pi r^3 \rho\, RT \ln S, \tag{2.1}$$

where γ is the surface tension and R the molar gas constant. The supersaturation S equals the ratio of the vapour pressures at evaporation temperature T_0 and the pressure of the cooled vapour at the temperature T. The first term in (2.1) represents the cost in free-energy of creating the surface, while the second term represents the gain (for $S > 1$) in the bulk free-energy. For $S > 1$, ΔF passes through a maximum at $(r^*, \Delta F^*)$. The maximum positions are given by:

$$r^* = \frac{2\gamma}{\rho\, RT \ln S} \tag{2.2}$$

$$\Delta F^* = \frac{16\pi\gamma^3}{3(\rho\, RT \ln S)^2} = \frac{4}{3}\pi (r^*)^2\gamma\,. \tag{2.3}$$

Figure 2.3 visualises that the phase transition is blocked by an activation energy barrier ΔF. Droplets with a radius smaller than the so-called critical radius r^* can only reduce their free energy by reducing their size which means that they evaporate. On the other hand, growth for droplets with sizes greater than r^* is a spontaneous process due to the lowering of ΔF. This leads to an irreversible growth at the expense of the supersaturated vapour. The height of the energy barrier depends on the supersaturation of the metal vapour and can be lowered by increasing the supersaturation S.

Furthermore, in a sub-saturated or just saturated vapour ($S \leq 1$) there will be, at steady state, a statistical distribution of droplets satisfying a Boltzmann-type rela-

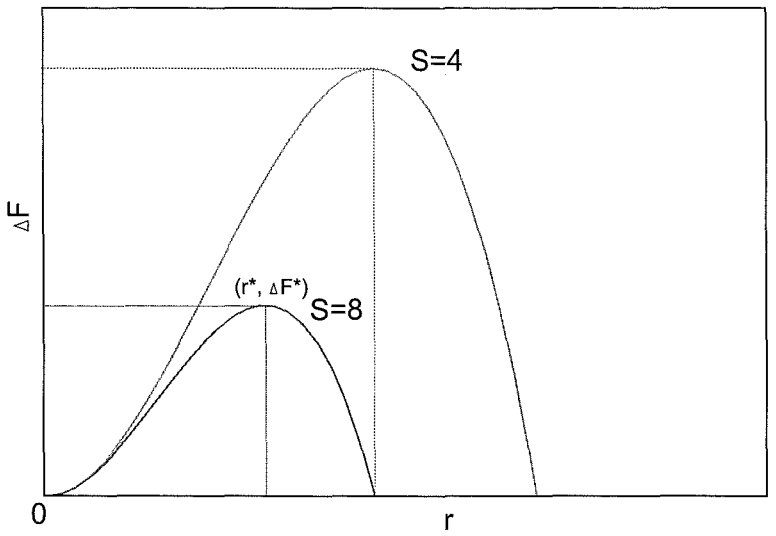

Figure 2.3: Difference in free energy as a function of the supersaturation S and the droplet size. Droplets with a radius smaller than the critical radius r^* reduce their free energy by evaporating while droplets larger than r^* grow exponentially.

tion [5]:

$$n_g = n \cdot e^{-\Delta F_g/kT}, \tag{2.4}$$

n_g: number of clusters of g molecules per unit volume

n : number of monomers per unit volume

This means that sub-saturated vapour is not completely free of embryos of the liquid phase. Even though (2.4) is not valid for super-saturated vapour it suggests that at $S > 1$ there will be a general increase in the population of droplets. Hence, for some large S those fluctuations can cause droplets with radii greater than the critical radius. These droplets can grow without limits until the vapour pressure in their surroundings is reduced from $p(T_0)$ to $p(T)$ (diffusional growth).

The nucleation rate I, at which droplets of size r^* are formed can be calculated using the physical model of the unbalanced steady state nucleation [5]:

$$I = q\left(\frac{n^2}{\rho}\right)\left(\frac{2\gamma m}{\pi}\right)^{\frac{1}{2}} e^{-\Delta F^*/kT} \tag{2.5}$$

Using (2.4) and the kinetic gas theory relation $p = nkT$, (2.5) can also be written as:

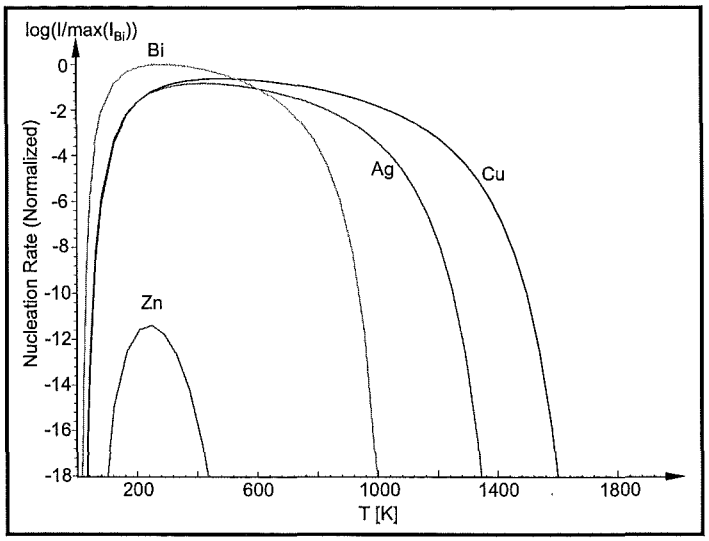

Figure 2.4: Nucleation rate for different elements as a function of the vapour temperature T after cooling. The evaporation temperatures T_0 of the various elements were chosen to achieve a vapour pressure of 1 *mbar*. The corresponding evaporation rates were in the order of $10^{-2}\frac{g}{cm^2 s}$ [6]. Note that the rate is plotted with a logarithmic scale.

$$I = q\left(\frac{p}{\rho kT}\right)\left(\frac{2\gamma m}{\pi}\right)^{\frac{1}{2}} n^* . \tag{2.6}$$

This equation visualises two important aspects of the problem. Firstly, the nucleation rate depends on the super-saturated vapour pressure p. The pressure p is approximately equal to the vapour pressure of the metal at the temperature of the evaporation source. Therefore, high evaporation temperatures will be necessary to achieve a sufficiently high cluster concentration in the source. Secondly, the rate is proportional to the number n^* of critical size droplets at a temperature T. The temperature dependence of n^* results in a maximum in the nucleation rate as shown in Fig. 2.4. Given a specific amount of metal vapour in a certain volume, the critical size clusters start to grow exponentially until all metal atoms are used up. Therefore, at a high nucleation rate, many critical size clusters will be produced and subsequently share the remaining available metal atoms. Because of the high initial number they cannot grow as big as in the case of a lower nucleation rate of clusters. In this context, Fig. 2.4 provides some interesting insights. It shows clearly that the nucleation rates differ dramatically from element to element. In particular, the low rate for Zn may explain the difficulties encountered for the production of Zn clusters [4] using the source described here. The temperature range for the nucleation rate for Zn is very narrow and has a maximum at approximately 240

K. The lowest cooling temperature that can theoretically be achieved with the source is 290 K. This suggests the cooling of the carrier gas and the walls of the source down to liquid nitrogen temperature. According to Fig. 2.4, an improved cooling of the metal vapour may not only make it possible to produce Zn clusters in sufficient quantities but it would also increase the nucleation rate for Bi. A higher rate, in turn, promotes the growth of smaller particles. Homogeneous nucleation theory is a very simplified theory that does not consider the diffusion of the metal vapour, the source geometry, flow conditions and other details. Despite this, the general principles outlined above can be used to help understand the behaviour of an IGA source when the source conditions are varied.

Guidelines for Cluster Production

The guidelines listed below attempt to explain the effect of the source parameters on the average cluster size and are mostly based on the reviews in [2, 4, 7]. For every listed parameter variation the results of experimental observations are given first.

- *Increasing the crucible temperature produces larger mean particle sizes [4, 8]*

  An increase in evaporation temperature produces more metal vapour and therefore the mass output of the source is greater. The larger amount of vapour combined with a higher vapour density, especially near the source, leads to a larger number of clusters (homogeneous nucleation theory). The increased number and also the higher cluster density results in the growth of larger clusters through coalescence.

  The higher crucible temperature may also reduce the cooling efficiency of the inert gas, lowering the supersaturation ratio and nucleation rate. As a result, fewer clusters grow to larger sizes.

  In both scenarios the mean diameter of the clusters increases with increasing crucible temperature.

- *Increasing the inert gas pressure produces larger mean particle sizes [4, 8, 9]*

  An increase in the inert gas pressure provides better cooling and limits the diffusion of the metal vapour. The improved cooling increases the supersaturation and leads to a larger number of smaller clusters (homogeneous nucleation theory). As the vapour is also restricted to a smaller volume coalescence of clusters will be more frequently resulting in larger clusters.

In the end, growth of the clusters due to coalescence seems to dominate.

- *Increasing the inert gas molecular weight produces clusters with a larger mean diameter [8]*

  An increase in the molecular weight is expected to reduce the diffusion of the vapour [10, 11] and so the density of the vapour is increased around the crucible. The collisions with heavier gas molecules also lead to a better cooling of the vapour [10]. As in the previous case the growth occurs in a cooler and denser vapour, resulting in more coalescence and larger clusters.

- *Changing the coolant of the condensation cell from water to liquid nitrogen results in smaller particles [12]*

  An improved cooling of the metal vapour due to the lower temperature of the inert gas increases the supersaturation of the vapour. As a result, a larger number of critical size clusters compete for the metal vapour, leading to the formation of smaller clusters (see also [13]).

- *Increasing the inert gas flow rate produces larger mean particle sizes [9]*

  An increase in the inert gas flow rate shortens the time clusters spend in the growth region. In addition, an increased flow rate disperses the clusters and limits the growth due to coalescence. As a result, smaller particles will form.

- *An increase in the growth distance increases the mean particle diameter [9, 14]*

  The growth distance is the distance between the crucible and the first nozzle. A larger distance will promote the growth of larger clusters. However, the particle size will not increase further if the distance exceeds the dimension of the growth region.

Suggested Improvements to the Source

The source described above has been successfully used to produce beams of Ag, Cu, Pb and Bi clusters. However, during the operation of the source several shortcomings have been noticed and improvements should be considered for future experiments and source designs. The suggested modifications cannot be easily applied to the present source and would require the building of a new source. Firstly, particles and metal vapour condense on the nozzles and lead to deposits that reduce the effective diameters of the nozzles. As a result, the characteristics of the particle beam change over time and the experiment

eventually has to be stopped when the nozzles are completely clogged. For low melting point materials, this problem could be avoided by heating of the nozzles. On the other hand, the heating of the nozzles may lead to an undesired heating of the clusters and therefore should be tested thoroughly. Secondly, important parameters for the cluster production are fixed (distance between crucible and first nozzle) or can only be changed between experiments (diameter of the first nozzle). It would be very desirable to be able to change these parameters during an experiment to tune the growth conditions and optimise the source performance. A nozzle with a variable diameter could be built, for example, by using an adjustable iris. Furthermore, it has been observed that a large proportion of the evaporated material is deposited on the inner wall above the crucible and is therefore lost. A more efficient use of the material and possibly a higher intensity of the cluster beam could be achieved with a crucible tilted towards the nozzle to help direct the vapour out of the condensation chamber [14]. Finally, the supersaturation of the vapour is influenced by the temperature of the carrier gas and the temperature of the walls of the inner chamber. Changing the water cooling to a liquid nitrogen cooling system would allow more efficient cooling of the gas and therefore increase the flexibility of the source by promoting the growth of smaller clusters [12, 13].

2.2 The Electron Diffractograph

Figure 2.5 provides an overview of the electron diffractograph. The electron gun, electron optics and associated electronics are original parts from a Philips EM300 transmission electron microscope. Only the upper part of the microscope column (above the second condenser lens) is used and has been mounted on top of the diffraction chamber. The acceleration voltage can be varied in 20 kV steps from 20 kV to 100 kV. In general the 100 kV setting is preferable. Higher beam energies mean a higher diffraction signal from clusters relative to the signal from the gas background [2] and also lead to reduced dynamic diffraction effects (see chapter 4). On the other hand, a high accelerating voltage reduces the diameter of the diffraction rings in the detector plane and make it difficult to observe peaks at low scattering angles. In the experiments with Bi the electron gun was operated at 80 kV with typical beam currents of ~ 2 μA. In the present setup and at 80 kV diffraction patterns can be detected for a scattering parameter[2] s ranging from 0.25 Å^{-1} to 1.4 Å^{-1}.

Below the electron gun and optics there is a beam blanking device that is operated

[2]The scattering parameter, s, is defined as $s = 2\sin(\theta)/\lambda$, where θ is half of the scattering angle and λ is the electron wavelength [15]. See also section 4.1.

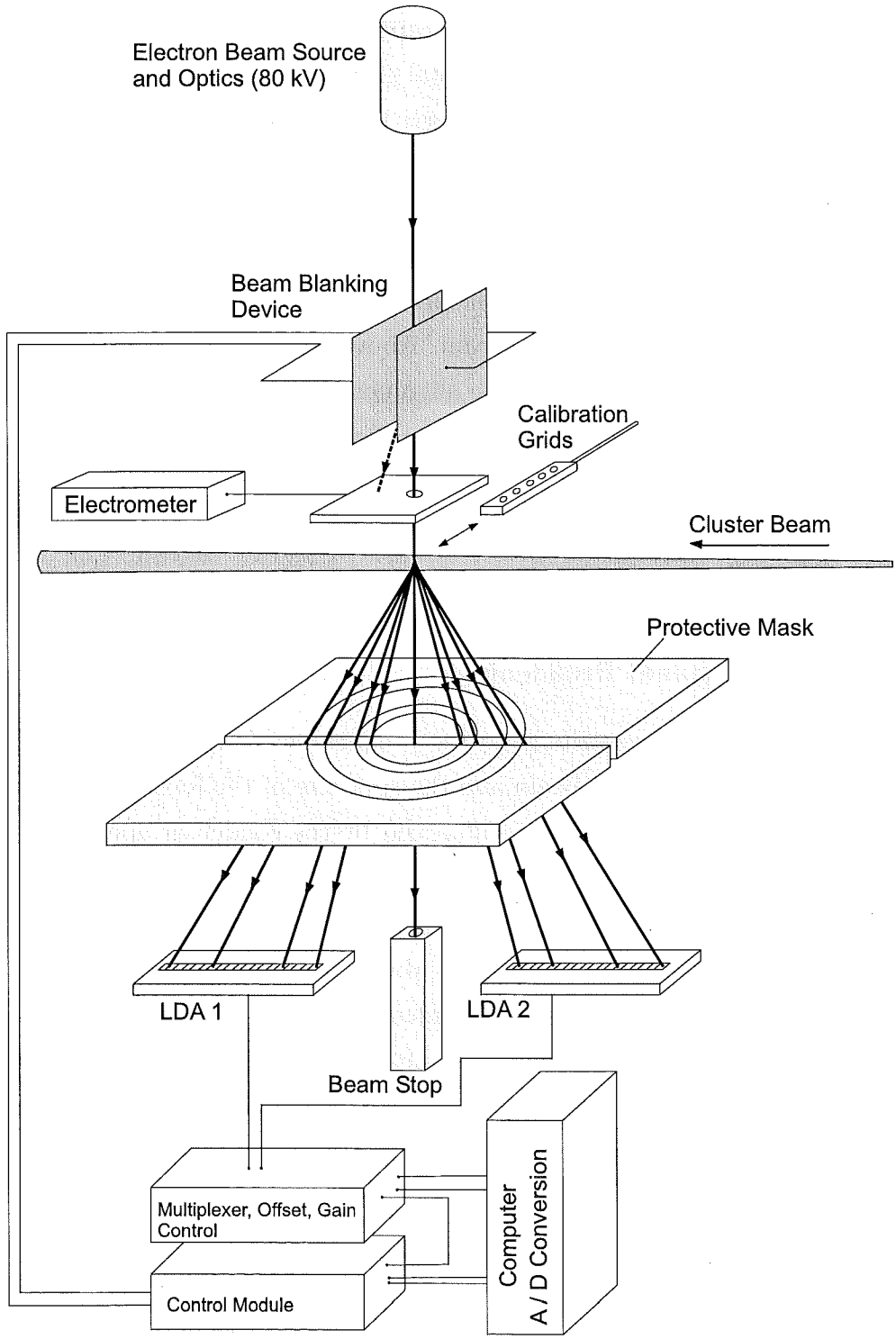

Figure 2.5: Schematic of the electron diffractograph. The electron gun and optics is derived from a Philips EM 300 electron microscope. The new detector is based on two linear diode arrays (LDA) and is described in chapter 3.

by the detector electronics and controls the exposure of the detector. It consists of a parallel plate deflection system and a horizontal graphite plate with a small hole. When the plates are grounded the electron beam passes through the hole in the graphite plate. The beam is deflected when a high voltage (400 V) is supplied to the parallel plates. The horizontal graphite plate is connected to ground via an electrometer allowing the electron beam current to be measured. For alignment or calibration purposes a needle or calibration grids on a retractable arm can be moved into the crossing point of the electron beam and the cluster beam. Above the detector there is a movable phosphorescent screen that is used for the alignment of the electron beam.

The new detector is based on a pair of linear diode arrays (LDA) and measures the intensity of the diffraction pattern by measuring the secondary charge created when the scattered electrons impact into the pixels of the sensor. The detector is described in detail in chapter 3.

Instrumental Peak (Line) Broadening

The two main factors that contribute to the broadening of the diffraction peaks are the vertical extent of the cluster beam and the spot size of the focused electron beam in the detector plane. The spot size is influenced by the condenser apertures and the quality of the electron optics.

The usual approach for determining the instrumental line broadening is to use a polycrystalline test sample with a grain size above 300 nm [16]. The large grain size insures that the (grain) size related peak broadening is negligible. In our case, however, this procedure has several shortcomings. Firstly, the test sample is usually very thin and therefore the broadening due to the vertical extent of the cluster beam is not accounted for. Secondly, the diffraction pattern of the test sample is very intensive and a smaller aperture has to be used to protect the detector. A smaller aperture reduces the diameter of the electron beam and may lead to a smaller spot size of the focused electron beam and therefore to a smaller peak broadening.

On the other hand, it is possible to estimate the instrumental broadening. It is typically defined as the increase of the full width of a diffraction peak at half-maximum intensity (FWHM). The zone of interaction (electron beam–cluster beam) is a narrow truncated cone. The electron beam has a diameter of 300 µm at the condenser aperture and is focused on the detector plane. Since the beam is focused the important quantity is not the diameter of the electron beam (250 µm) at the position of the cluster beam but the spot size of 90 µm [17] at the detector. This spot size directly translates to a

peak broadening of 3.8×10^{-3} Å^{-1} at 80 kV. The vertical extension of the cluster beam h (1.5 mm) gives rise to a broadening b that depends on the scattering angle 2θ:

$$b = h \cdot \tan(2\theta) \ . \tag{2.7}$$

For scattering parameters s = (0.25, 0.3, 1.4 Å^{-1}) and at 80 kV this relation leads to a peak broadening of (0.68, 0.76, 3.75 $\times 10^{-3}$ Å^{-1}). These s values correspond to the two extremes of the measurement range and the position of the first peak in a bulk Bi diffraction pattern.

The net broadening in the vicinity of the first Bi peak is therefore about 4.5×10^{-3} Å^{-1} and has to be considered[3] for size estimates obtained with the Scherrer Equation (as described in section 4.2.2). The broadening should also be included in the calculation of diffraction patterns from model structures, especially when calculated patterns are fitted to experimental data.

2.3 The Sampling Devices

Downstream from the electron beam–cluster beam crossing, the particle beam can be sampled by a quartz deposition rate monitor (DRM) and a TEM grid holder. The DRM has a fixed position while the grid holder can be moved in and out of the cluster beam in front of the DRM. The exposure time is controlled by a shutter which is used for both devices.

Figure 2.6 shows the shutter arrangement and the grid holder. The TEM grids consist of a standard microscopy copper mesh covered by a very thin ($\sim$ 50 Å) amorphous carbon film.[4] Up to 8 grids can be mounted on the wheel of the TEM grid holder. The exposure time is controlled by the speed of the shutter movement as clusters reach the grids only when the rectangular hole in the shutter passes across the path of the particle beam. After the experiment the exposed grids are removed from the diffraction chamber and transferred to a transmission electron microscope for observation. During the transfer the clusters are inevitably exposed to air. The TEM photographic images are scanned and analysed numerically. In the bright-field images the clusters on the carbon support appear as dark objects on a gray background and their occupied area is used to obtain the distribution of particle sizes. The image analysis is described further

[3]For comparison: the size related peak broadening for spherical particles with a diameter of 30, 50 and 80 Å is approximately 30, 18 and 11 $\times 10^{-3}$ Å^{-1} (FWHM). Thus, the instrumental peak broadening is most noticeable for large particles with narrow diffraction peaks.

[4]The grids were produced at EPFL and provided by Prof. R. Monot.

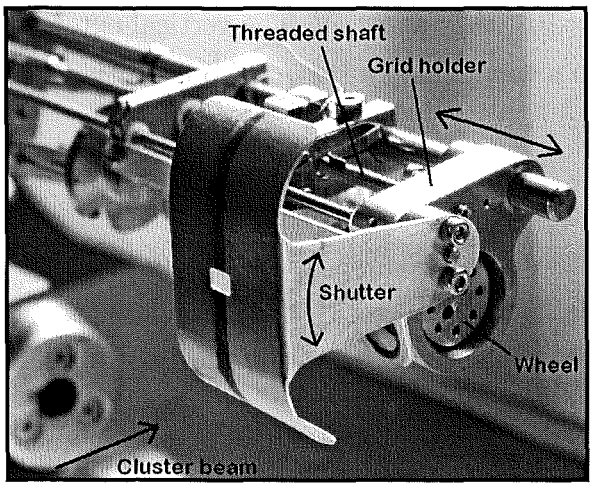

Figure 2.6: The TEM grid holder and the shutter arrangement. It is located downstream of the electron beam–cluster beam crossing and allows a sample of particles to be taken from the cluster beam. Further downstream is a deposition rate monitor (not shown). After [4].

below.

Further downstream from the shutter and grid holder is a Sycon Instruments STEM 100/MF deposition rate monitor. The rate is determined from the change of the oscillation frequency of the quartz crystal when additional material is deposited.The rates can be measured to 0.1 Å/s. The DRM has been found very useful as a tool to find the source parameters that produce clusters. The parameter space can be scanned in a reasonable amount of time without the need to perform time consuming diffraction measurements. The deposition rate also provides a good indication of the signal to noise ratio of the expected diffraction pattern. In addition, the DRM readings are used to estimate the exposure time for the TEM grids.

2.4 Experimental Procedure

This section provides a summary of how the experiments were performed. The main steps for a typical experiment are the following:

- The source and the nozzles are cleaned, the crucible loaded and the source is inserted into the system. The system is left to evacuate overnight.
- The experiment starts with the heating of the crucible while a low inert gas flow is present.
- The electron beam is brought to operating conditions (80 kV, beam current of approx. 2 µA or higher) and is left for about 1 hour to stabilise.

- Alignment of the electron beam and the detector. A needle on a movable arm is positioned in front of the third nozzle so that it marks the location of the cluster beam. The needle can be seen as a shadow on the phosphorescent screen and is used to align the electron beam. Then a calibration grid (a thin polycrystalline ThCl or Au film) is moved into the electron beam–cluster beam crossing point. In order to align the LDA sensors the ring diffraction pattern from the calibration sample is observed in both LDAs. To position the LDA sensors across the diameter of the diffraction rings the detector plate is moved until the peaks in the two LDAs are at the same pixel positions and at the same time are furthest away from the centre of the electron beam. If an increased detection range (scattering angle) is desired the detector plate can be shifted along the diameter of the diffraction rings to obtain an asymmetric coverage.

- Diffraction patterns from the two calibration samples (Au, ThCl) are taken. They are later used to assign a scattering parameter s (see chapter 4 for a definition of s) to every pixel.

- The source parameters are adjusted to provide a high intensity cluster beam and diffraction patterns are obtained. During an experiment the crucible temperature, the gas flow (which also controls the pressure) and the gas composition (e.g. Ar/He ratio) can be varied. A measurement of a diffraction pattern typically involves 4000 exposure and read out cycles (see chapter 3) and takes about 50 seconds. The exposure time per cycle is chosen so that the diffraction pattern (gas background plus cluster pattern) has a high signal to noise ratio. If the cluster contribution in the diffraction pattern is weak then more patterns are obtained under the same conditions and are later combined to improve the signal to noise ratio. TEM grids are exposed after the diffraction measurement, however, due to the limited number of grids available a grid cannot be exposed for every pattern.

- In order to be able to remove the gas background additional diffraction patterns are measured with the cluster beam turned off. For this purpose the crucible temperature is lowered until the cluster beam intensity is sufficiently reduced. A gas background pattern is obtained for every cluster diffraction pattern with the same gas background pressure in the diffraction chamber and the same gas composition.

- A second set of calibration patterns is obtained.

2.5 Data Preparation

Three more steps are necessary to obtain the final diffraction pattern. First, the number of pixels is effectively halved by adding together the intensity of adjacent odd and even pixels. This step minimises the errors in the intensity due to a possible misalignment of the protective mask located above the LDA sensor (see chapter 3). The remaining two steps are the calibration of the scattering angle and the subtraction of the gas background.

The raw diffraction pattern displays the diffraction intensity as a function of the LDA pixel number. In order to be able to compare the measured pattern to calculated patterns from model structures or patterns from the literature, the pixel number has to be related to the scattering parameter s. This can be achieved by using the patterns from the calibration samples (Au, ThCl) that show distinct peaks with known scattering parameters. In the general case it is not possible to perfectly align the LDAs along a diameter of the diffraction rings. Using the definitions provided by Fig. 2.7 the following equation for a calibration curve can be obtained:

$$\left(\frac{s}{c}\right)^2 = w^2n^2 + 2bwn + (d^2 + b^2). \tag{2.8}$$

Since we are only interested in the conversion from pixel number[5] to s, it is sufficient to determine the three parameters of (2.9):

$$s^2 = Am^2 + Bm + C\,, \tag{2.9}$$

where m is the pixel number and s the scattering parameter. The three parameters can be calculated with a least-squares fitting procedure from the peak positions of the calibration patterns (see Fig. 2.8c). The Au and the ThCl sample together provide 20 peaks. The peak positions are determined by fitting a parabola over the data points that contribute to the peak and can be estimated to about ± 0.3 effective pixel widths.

When comparing the peak positions in calibration patterns taken before and after the experiment, often an offset of up to 1.5 effective pixels can be noticed, indicating a shift of the electron beam during the experiment. Among the two available calibration curves, the one is chosen that results in the smaller deviation of the peak positions when comparing the patterns of the left and the right LDA. In the last step, the gas background pattern is subtracted from the cluster diffraction pattern (see Fig. 2.8).

[5]The relationship between the pixel number m and the number of pixel widths n depends upon the adopted numbering scheme for m, e.g. for $m = 1 \ldots 2048$: $m = n + 1$.

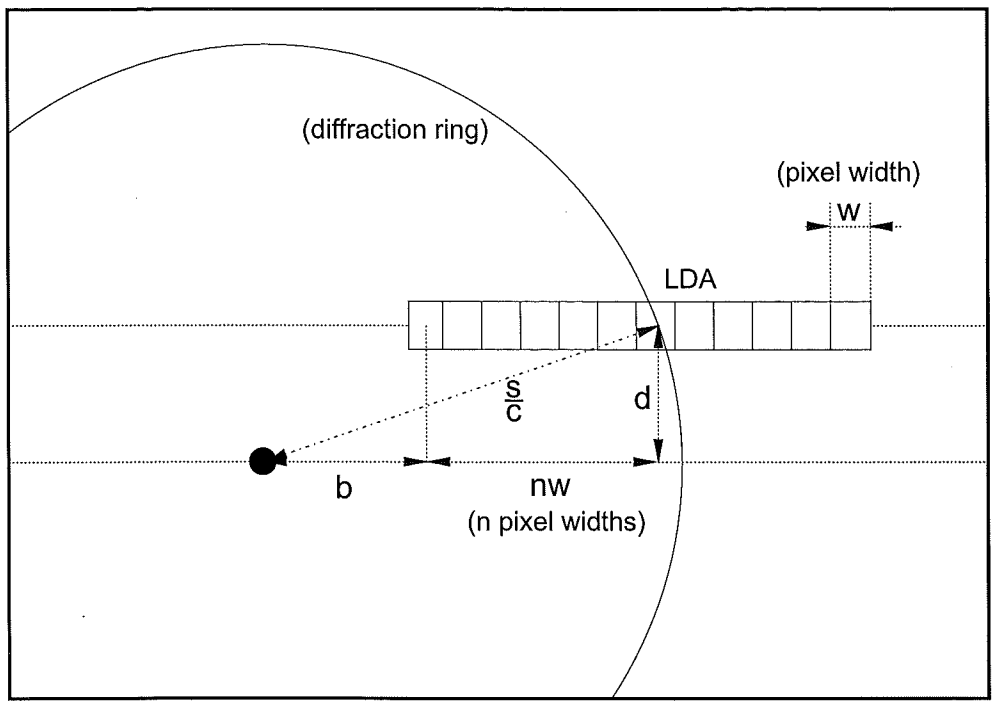

Figure 2.7: Calibration of the LDA sensors. The diffraction peak seen with the linear array of pixels corresponds to the scattering parameter s. The offsets b and d, the pixel width w and the number of pixel widths define the equation of the calibration curve (2.8). The factor $1/c$ converts the scattering parameter to a physical length.

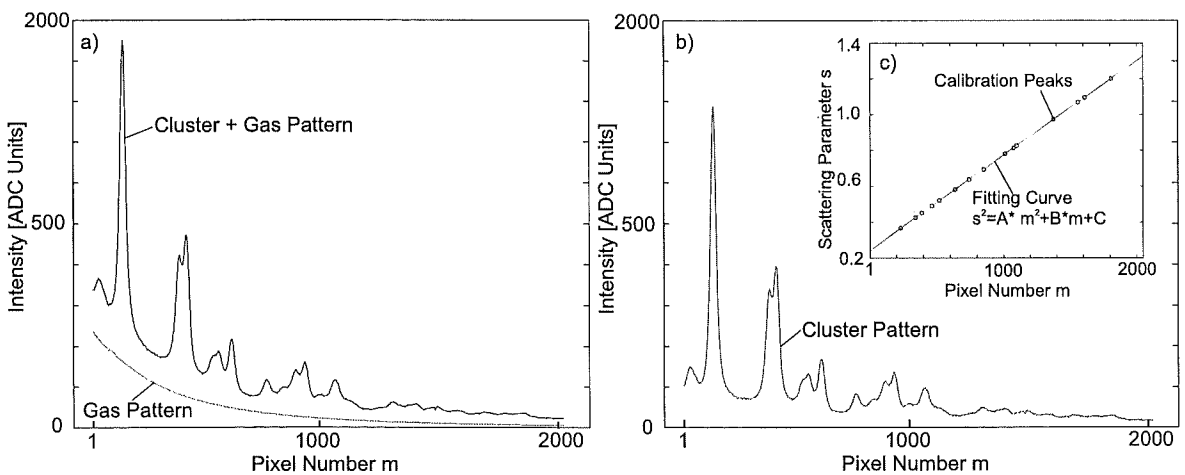

Figure 2.8: Subtraction of the gas background and calibration. (a) Raw diffraction patterns from a beam of clusters and the corresponding gas background. (b) The gas background is subtracted to obtain the cluster diffraction pattern. (c) The two calibration grids provide up to 20 peak positions on the pixel sensor with known scattering parameters s. Equation (2.9) is fitted to the data points to obtain scattering parameters for the pixels.

2.6 Analysis of the TEM Images

The TEM grids were observed with a JOEL 1200 EX TEM at a magnification of 100,000× and several images were exposed for each sample. The magnification of the TEM was calibrated using a line grating replica with latex spheres from EMS[6]. An Epson Perfection 1650 scanner was employed to digitise the TEM negatives in 10-bit grayscale at a resolution of 1200 dpi.

The TEM images are bright-field images and the clusters appear as dark spots on a gray background (see Fig. 2.9). In the image analysis, the area of the clusters is measured and used to calculate the size distribution of the particles based on a spherical approximation of the particle shape. The method has been developed by Hall [2] and the software employed in the present study is based on a recent implementation by Hyslop [4]. The software consists of several Matlab scripts and libraries.

In the following, the main steps in the image analysis are explained. Detailed information about the method and implementation can be found in [2, 4]. The processing steps are:

- The 10 bit grayscale image is processed with a mean and a median filter to remove noise in the image. Then an image background is calculated from the grayscale histogram and is afterwards subtracted from the filtered image. This step significantly reduces the variation of the image background.

- A threshold is used to distinguish between background and cluster regions. The threshold value can be determined by the software but for low contrast images a visual inspection is recommended to optimise the results. When a good threshold value is found the image is converted to a black and white image.

- A software routine scans the image for clusters. When a cluster is found, the perimeter P and the area A is calculated. These two parameters define the compactness of a cluster region:

$$C = \frac{4 \cdot \pi \cdot A}{P^2} . \tag{2.10}$$

The compactness is a measure of the roundness of a shape (circle: C=1) and can be used to distinguish between single particles and regions that represent joined particles. The idea is that when clusters join together the region in the image will

[6]Electron Microscopy Sciences, http://www.emsdiasum.com

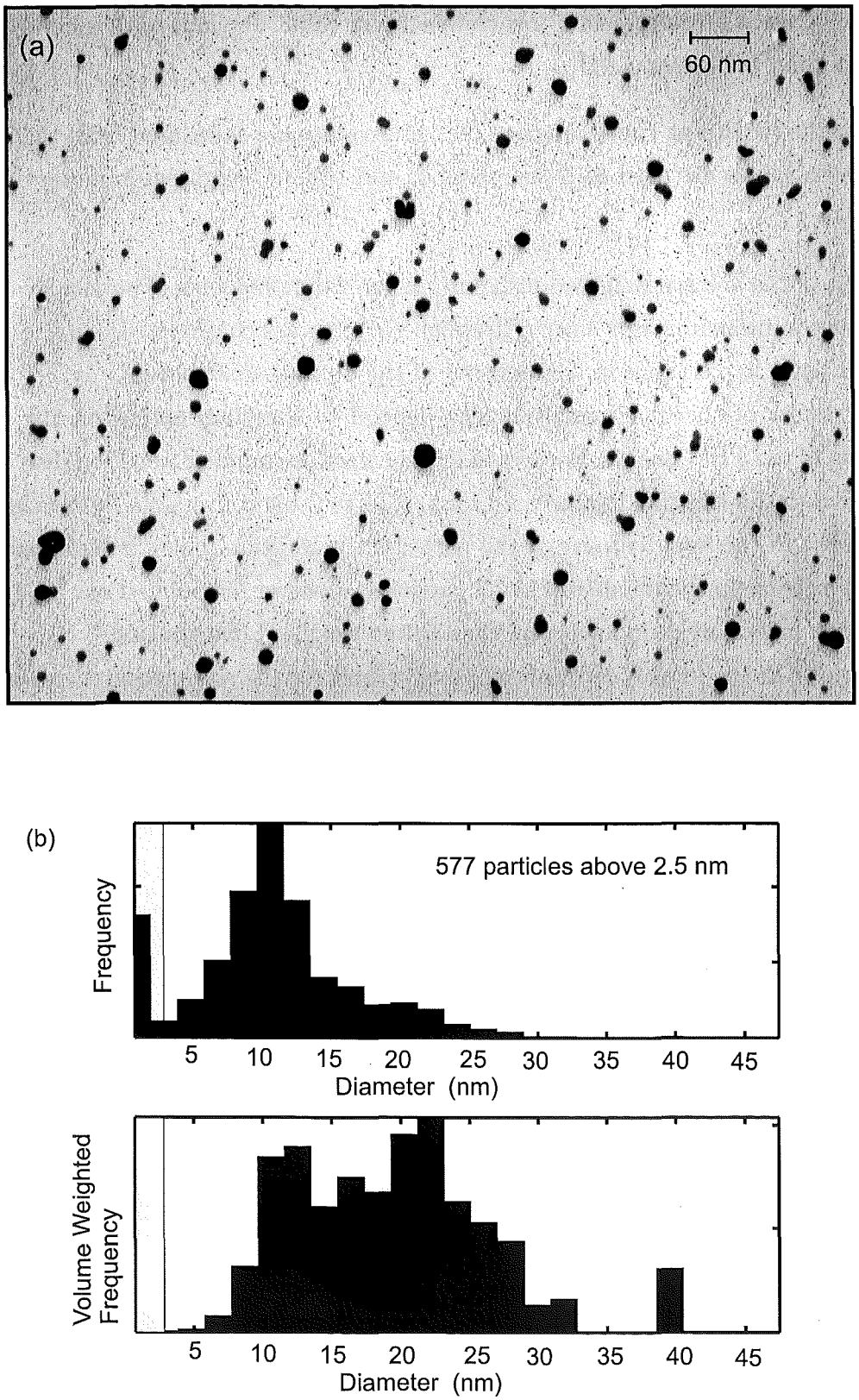

Figure 2.9: Sample TEM image before processing (a). The number (top) and volume (bottom) weighted diameter distribution (3rd moment) for the image above and other images from the same sample (b).

be elongated resulting in a low compactness value. Regions with a compactness less than 0.7 are rejected.

- For the remaining cluster regions diameter values are calculated from their areas. These values are used to create number and volume weighted diameter distributions.

The mean of the volume weighted distribution (or 3rd moment) is of particular interest for diffraction measurements since diffraction patterns are characteristic of the volume weighted particle distribution [18] and not of the number distribution.

The results of the image analysis also depend to a certain extent on the quality (contrast) of the TEM images. In cases of low contrast the number weighted distribution is sensitive to the threshold value used for the 10 to 2-bit conversion. A low threshold value increases the apparent size of the particles. In addition, noisy images lead to an artificial increase in the number of small particles. However, as pointed out in [4], these effects only have a weak influence on the volume weighted distribution.

The noise in the images certainly imposes a limit for the size measurement of small clusters. In this study, the noise in the images has been found to restrict the analysis to particles larger than 2.5 nm. A similar study on Ag particles [19] estimated the limit to be 1.4 nm.

References

[1] M. Flüeli, *Observation des Structures Anormales de Petites Particules d'Or et d'Argent par Microscopie Electronique à Haute-Résolution et Diffraction d'Electrons par un Jet d'Agrégats d'Argent*, PhD thesis, EPFL, 1989.

[2] B. D. Hall, *An Installation for the Study of Unsupported Ultrafine Particles by Electron Diffraction with Application to Silver: Observation of Multiply Twinned Particle Structures*, PhD thesis, EPFL, 1991.

[3] B. D. Hall, M. Flüeli, D. Reinhard, J.-P. Borel, and R. Monot, Rev. Sci. Instrum. **62**, 1481 (1991).

[4] M. Hyslop, *Electron Diffraction Studies of Unsupported Clusters*, PhD thesis, University of Canterbury, 2002.

[5] J. E. McDonald, Homogeneous nucleation of vapor condensation, in *Homogeneous Nucleation Theory*, pages 225–256, F. F. Abraham, New York, 1974.

[6] A. Roth, *Vacuum Technology*, Elsevier Science Publishers B. V., 1990.

[7] I. M. Goldby, *Dynamics of Molecules and Clusters at Surfaces*, PhD thesis, Clare College Cambridge, 1996.

[8] A. Yokozeki and G. D. Stein, J. Appl. Phys. **49**, 2224 (1978).

[9] F. Frank, W. Schulze, B. Tesche, J. Urban, and B. Winter, Surf. Sci. **156**, 90 (1985).

[10] N. Wada, Jpn. J. Appl. Phys. **7**, 1287 (1968).

[11] C. Granqvist and R. Buhrman, Appl. Phys. Lett. **27**, 693 (1975).

[12] W. Schulze, F. Frank, K. P. Charle, and B. Tesche, Ber. Bunsenges. Phys. Chem. **88**, 263 (1984).

[13] H. Haberland, editor, *Clusters of Atoms and Molecules*, Springer-Verlag, 1994.

[14] H. Schaber and T. P. Martin, Surf. Sci. **156**, 64 (1985).

[15] A. Guinier, *X-Ray Diffraction in Crystals, Imperfect Crystals, and Amorphous Bodies*, W. H. Freeman and Company, 1963.

[16] H. P. Klug and L. E. Alexander, *X-Ray Diffraction Procedures*, John Wiley & Sons, Inc., 1954.

[17] D. Reinhard, *Croissance et Stabilité d'Agrégats d'Argent et de Cuivre, Etudiés en Jets Moléculaires par Diffraction d'Electrons à Haute Energie*, PhD thesis, EPFL, 1996.

[18] B. D. Hall, J. Appl. Phys. **87**, 1666 (2000).

[19] D. Reinhard, B. D. Hall, D. Ugarte, and R. Monot, Phys. Rev. B **55**, 7868 (1997).

Chapter 3

The New Detector for Electron Diffraction

The measurement of electron diffraction patterns from a beam of small particles requires an especially sensitive and precise detector. First of all, a beam of small particles probed with a high-energy electron beam, gives rise to only a very weak diffraction signal. This is mainly due to the low number and small size of the clusters in the beam. Another performance constraint arises from the use of an inert gas aggregation source. In this type of source the characteristics of the beam evolve during an experiment and therefore limit the time for a single measurement to less than 10 minutes.

When the diffraction apparatus was transferred to the University of Canterbury in 1998 it came with a detector developed by B. D. Hall [1–3]. That detector had been used in diffraction experiments on silver and copper clusters by B. D. Hall [1] and D. Reinhard [4]. During operation the chips are damaged by the scattered high energy electrons which results in a lifetime of about six months. As nearly a decade had passed since the development of the detector it turned out to be impossible to source the original CCD[1] detector chips. With only a few chips left it became apparent that sooner or later the old detector had to be replaced. In addition, a series of tests revealed problems with the linearity of the detector response to the diffraction intensity. The tests diagnosed that the non-linearity was caused by the way the detector was operated and was possibly enhanced by the degradation of the electronics and the detector chips. The old detector was based on an electron counting scheme [3] which required the use of a threshold to distinguish between electron impacts and thermal noise. The threshold, in turn, introduces a systematic error. As a consequence of that, work started on the design of a new detector. Computer simulations suggested that systematic errors could be avoided by a different, even simpler detection scheme. These promising results and the availability of new detector chips that were suitable for electron diffraction experiments encouraged the development of a new detector.

This chapter begins with an overview over the experimental setup, requirements for the detector and information about the detection process. After which, the two

[1]Charge coupled device

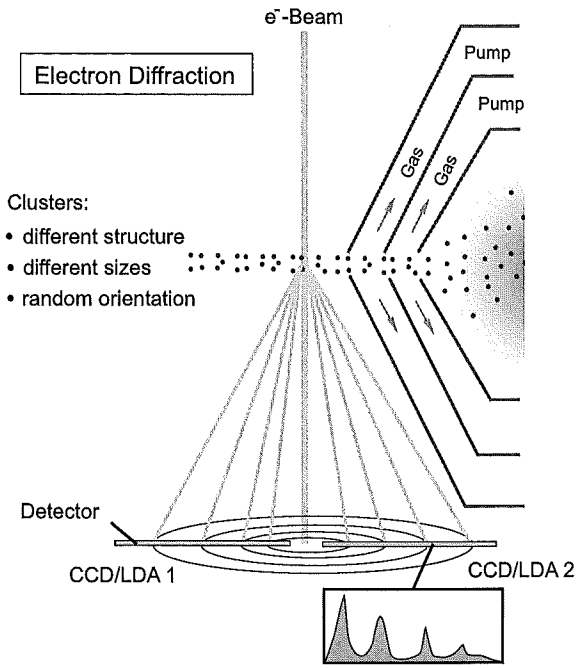

Figure 3.1: The randomly oriented particles give rise to a Debye–Scherrer (powder) type diffraction pattern. The diffraction pattern is detected by a pair of linear pixel sensors aligned along a diameter of the pattern.

different detection schemes are explained and computer simulations of the detection process are presented and discussed. This is followed by a detailed description and explanation of the new linear diode array (LDA) based detector.

3.1 General Concepts

When a cluster beam consisting of randomly oriented particles is probed by the electron beam it gives rise to a Debye–Scherrer type diffraction pattern (see Fig. 3.1). We use two linear pixel sensors to measure a profile of the diffraction pattern along a diameter. Two detector chips are necessary to align the detector in reference to the electron beam and to verify the detector performance.

Both detectors, the old CCD and the new LDA based detector, detect high-energy electrons directly. When an electron enters the silicon of the pixel one electron-hole pair is created on average for every 3.6 eV of energy deposited in the substrate [5]. The incident high-energy electrons give rise to a roughly pear-shaped distribution of secondary charges over a volume which is determined by the electron energy.

The interaction of an electron beam with a solid can be made visible by using Monte Carlo simulations [6]. Figure 3.2 shows the results of Monte Carlo simulations

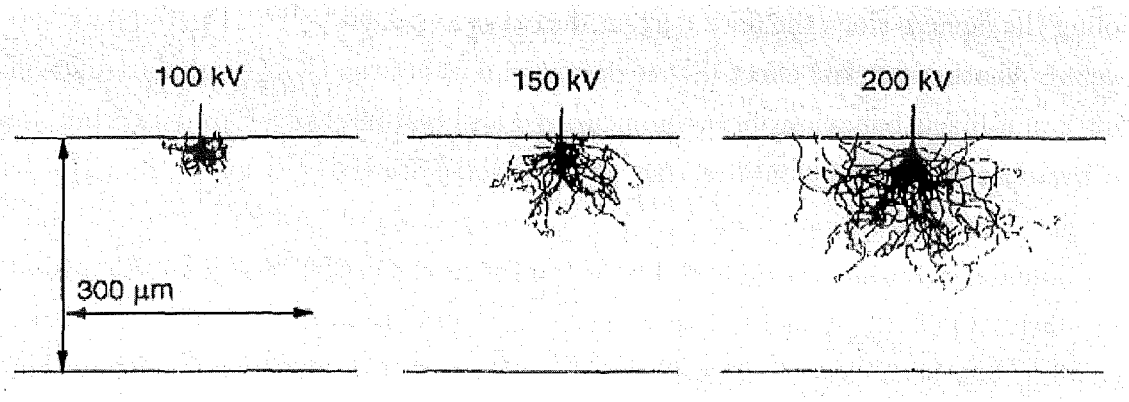

Figure 3.2: Monte Carlo simulations of electron scattering in a 300 µm Si layer for 100, 150 and 200 kV electrons. From G. Y. Fan et al. [6].

of electron scattering in a layer of Si. At 100 kV the diameter of the cloud of secondary charges is about 50 µm. The extension of the charge cloud decreases with decreasing electron energies. For 40 kV (80 kV) electrons the penetration depth in Si is approx. 12.5 µm (42 µm) [7]. With pixels of a size of 13×13 µm^2 the charge cloud may cover several pixels at high voltages.

Depending on the location of the impact on the detector, charge will be collected by one or more pixels. For example, an impact away from the line of pixels might deposit only a small fraction of the charge in one pixel. On the other hand, an impact in the centre of a pixel will deposit a maximum amount of charge in this pixel. An electron falling near the boundary between two pixels will share its charge between them. During exposure of the detector to the scattered electrons it is very likely that pixels collect charges from several impacts: charges from multiple impacts in the pixel and from impacts into neighbouring pixels. In order to resolve the question how multiple counting effects intensity measurements by the detector, the charge collection process has been simulated (see section 3.3).

Damage due to High-Energy Electrons

The exposure of the detector chips (CCDs or LDAs) to high-energy electrons results in damage to the semiconductor material. The effects on the detector performance that will be discussed below mostly refer to damage in the CCD sensors. There are noticeable changes in the characteristics of the CCDs as the cumulative electron dose on the devices increases. One effect is that the dark current increases. An increased dark current will limit the amount of charge that can be deposited in a pixel and eventually will make the device unusable. However, this effect can be suppressed by

cooling the devices since the dark current decreases exponentially as the temperature is lowered. Another marked effect is that damaged parts of the CCD (high dark currents) show a non-linear behaviour between measured and real intensity. Up to a certain level the response is linear but above that the measured intensity is lower than the true intensity. These radiation effects are due to the creation of interface states at the Si-SiO_2 boundary (dark current) and due to the fixing of positive charge in the insulator (non-linearity) [8, 9]. A method to reverse the degradation of the CCDs by thermal annealing has been described in [8, 9]. The devices were annealed for a few hours at temperatures between 200 and 372°C. Further experiments [9] show that damaged devices can be annealed, used and then be annealed again to extend the lifetime of these devices to a large extent.

The LDA sensors used in the new detector also show an increase in dark current after long exposure. A non-linear behaviour, however, has not been observed.

3.2 Converting Measured Charge into Intensity

During exposure of the detector high-energy electrons impinge on the detector and create pear-shaped clouds of secondary charge. Events that occur in or close to the pixels of the sensors deposit charge in them. After exposure, the pixels are read out and the amount of charge is determined.

In order to understand how the detector works in general it is helpful to investigate the special case where the volume occupied by the secondary charge is very small compared to the pixel size. In this limit it is very unlikely that an event generates charge in more than one pixel. The only likely events are single and multiple impacts in a pixel. It is therefore expected that a histogram of the accumulated charge in a pixel shows only measurements at multiples of the maximum charge deposited by a single impact Q_{max}. This situation is shown in Fig. 3.3. The two histograms in Fig. 3.3 are different in the average charge deposited per exposure which is proportional to the average number of electron impacts. If normalised by the total number of counts in a histogram the values in a histogram represent estimates of the probability of measuring the corresponding charge in a pixel. Since the detector registers independent random events (impacts of electrons) the distribution of the counts in the histogram follows Poisson statistics. The probability of observing x impact events (equivalent to a charge

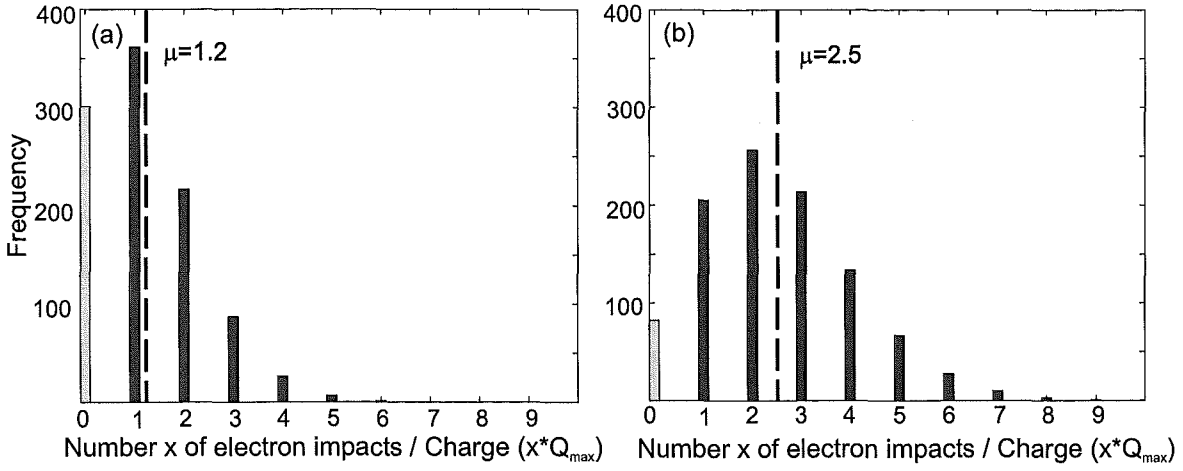

Figure 3.3: Calculated histograms of the accumulated charge in a pixel for 1000 exposures and for the special case where the charge cloud is very small compared to the pixel size. In this case the deposited charge is a multiple of the charge generated by a single electron impact Q_{max}. The two histograms differ in their mean $\mu \cdot Q_{max}$ and in terms of detecting electrons they differ in the average number of electrons impinging on the detector.

of $x \cdot Q_{max}$) during the exposure time t therefore is:

$$P(x;\mu) = P(x;t,\rho) = \frac{e^{-\rho t}}{x!}(\rho t)^x \,, \tag{3.1a}$$

$$P(x;\mu) = \frac{\mu^x}{x!}e^{-\mu} \,, \tag{3.1b}$$

where $\mu = \rho t$ is the average number of events observed in the time interval t and ρ is the rate at which these events are occurring. Since the exposure time t is known the rate ρ can be calculated from μ.

The quantity that we are interested in is the average number μ of electrons per exposure hitting each pixel. This number in turn is proportional to the average charge per exposure deposited in a pixel. There are basically two ways of determining μ. The first way is to calculate the mean of the distribution. The mean of the Poisson distribution equals the parameter μ that appears in the probability function $P(x;\mu)$. Another approach that has been used by B. D. Hall [3] is to determine μ from the number of zero events (no electron impact registered during exposure, $x = 0$ in Fig. 3.3). Using (3.1b) with $x = 0$ the average number of events observed is:

$$\mu = -\ln(P(0)) \,. \tag{3.2}$$

In the following sections the term *integration mode* refers to the method of determining the electron intensity from the mean of the histogram and the term *counting*

mode refers to determining the intensity from the number of zero events. The fact that the intensity is related to the mean μ of Poisson distributed data implies that we have to expect a standard deviation of the mean (uncertainty) that equals $\sqrt{\mu}$.

To get a complete picture of the detector two more effects have to be considered. While the detector is exposed to scattered electrons thermally generated charge builds up in the pixel. For multiple readings this charge shows a Gaussian-like distribution centred on the average dark level for the pixel ([1], see also Fig. 3.8h). Secondly, the cloud of the secondary charge is comparable to or larger than the pixels size. Therefore, the amount of charge deposited in a pixel depends on the location of the impact and it is also possible that one impact is registered in several pixels.

Implementation of the Integration Mode

In the integration mode the electron intensity is determined from the average charge collected in a pixel from a number of exposure and readout cycles. In order to relate the charge readout to the electron intensity the dark current in the individual pixels has to be considered. Therefore, the average dark level in every pixel is determined from a sufficient number of measurement cycles without exposure to the electron beam. Then the intensity for the nth pixel $I_r(n)$ is:

$$I_r(n) = \overline{C}(n) - \overline{R}(n), \tag{3.3}$$

where $\overline{C}(n)$ represents the average charge of the nth pixel and $\overline{R}(n)$ the average dark level.

Implementation of the Counting Mode

In the counting mode [3] the rate of electron impacts is calculated from the number of exposures in which no impacts could be detected (zero counts). In order to do so it is necessary to discriminate against the thermal noise charge generated in the pixels. The detector system returns a value of 0 if the readout charge is below a threshold value and a value of 1 if it is above. In the implementation of the counting mode described in [3] the threshold value of a pixel is the sum of the pixel's average dark level and a constant. The choice of a constant as the second term in the sum is based on the assumption that the width of the distribution of the dark level noise is the same for all pixels.

According to (3.1b) the probabilities to register a zero $P(0)$ and to register a one

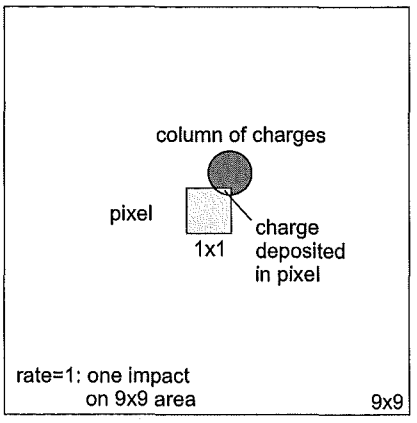

Figure 3.4: Geometry used in the detector simulations. In the simulations, a rate of x corresponds to x electron impacts on the 9×9 area during one exposure.

$P(1)$ during an interval t are:

$$P(0) = e^{-\mu}, \tag{3.4a}$$

$$P(1) = 1 - P(0) = 1 - e^{-\mu}, \tag{3.4b}$$

where $\mu = \rho t$ corresponds to the average number of events per interval for an event rate ρ. Therefore, the event rate can be determined from either $P(0)$ or $P(1)$ as $P(1)$ can be easily converted to $P(0)$. In the implementation of the counting mode used for the old detector, the probability $P(1)$ is estimated from the number of 1's, C, recorded in N exposures, resulting in $P(1) \simeq C/N$ and consequently $P(0) \simeq 1 - C/N$. This allows estimation of μ with (3.4a), giving:

$$\mu_{estimate} = -\ln(1 - \frac{C}{N}). \tag{3.5}$$

3.3 Modelling the Detector

The charge collection process has been simulated in order to understand the capabilities and limitations of this type of detector. The simulations include the thermally generated charge in the pixels and the effect of charge spreading.

In this model, it is assumed that secondary charge generated by the electron impact is distributed uniformly in a cylindrical volume. The geometry used in the detector simulation is shown in Fig. 3.4. During one exposure of a pre-determined time t a number of electrons, specified by the rate ρ, impact into the detector and generate columns of charge. Events that occur close enough to the pixel deposit charge in the pixel. At

the end of the exposure the total amount of charge is determined and saved. The detector is exposed and read out a larger number of times (N=5000, 10000, 20000 and 40000 cycles). The intermediate results, used for further analysis, are four histograms of the charge read out in N cycles. The diameter of the column occupied by the secondary charge was chosen to be comparable to the pixel dimensions (see Fig. 3.4) which corresponds to a simulation of impacts of 40 kV electrons in Si [7].

As mentioned above, thermally generated charge builds up in the pixel during exposure. Any charge collected from electrons impinging on the detector add to the Gaussian distributed dark current. Figure 3.5 shows two examples of histograms obtained with the simulations. They show the number of times each amount of accumulated charge is observed in 40000 cycles of exposure and read out. For these two examples the standard deviation σ_n of the thermal noise distribution was chosen (for display purposes) to be 1/20 of the maximum charge a created by one impact in a pixel. The relation between σ_n and a depends mostly on the actual detector design (geometry, material), the energy of the electrons and the conditions the detector is operated in (temperature). In the case of there being no charge from impinging electrons during an exposure the readout value will only be determined by the thermal charge. The number of cycles in which no external charge is collected is described by the number of zero counts and corresponds to the area of the Gaussian peaks[2] in Figs. 3.5a,b. Depending on the rate the number of zero counts can be substantial as shown in Fig. 3.5a.

All the results that are presented in the following section were calculated from configurations in which the dark-level noise distribution was characterised either by $\sigma_n = a/5$ or $\sigma_n = a/10$ (see Fig. 3.5). These values were chosen since σ_n has been estimated from measured histograms to be between $a/5$ and $a/8$ for the new detector and between $a/7$ and $a/12$ for the old detector system.

Results of the Simulations and Discussion

The simulations have been used to compare the different modes of operation of the detector: integration mode and counting mode. For both modes, the primary result of a simulation is the plot of true rate vs. estimated rate. In an ideal case the curve would be a straight line going through the origin. In order to determine the systematic error all curves were fitted with a straight line through the origin and the systematic error was calculated as the deviation from the fitted line. The uncertainties in the estimates of the

[2]calculated from an analytical expression using the number of zero counts and σ_n to obtain a smoothed curve.

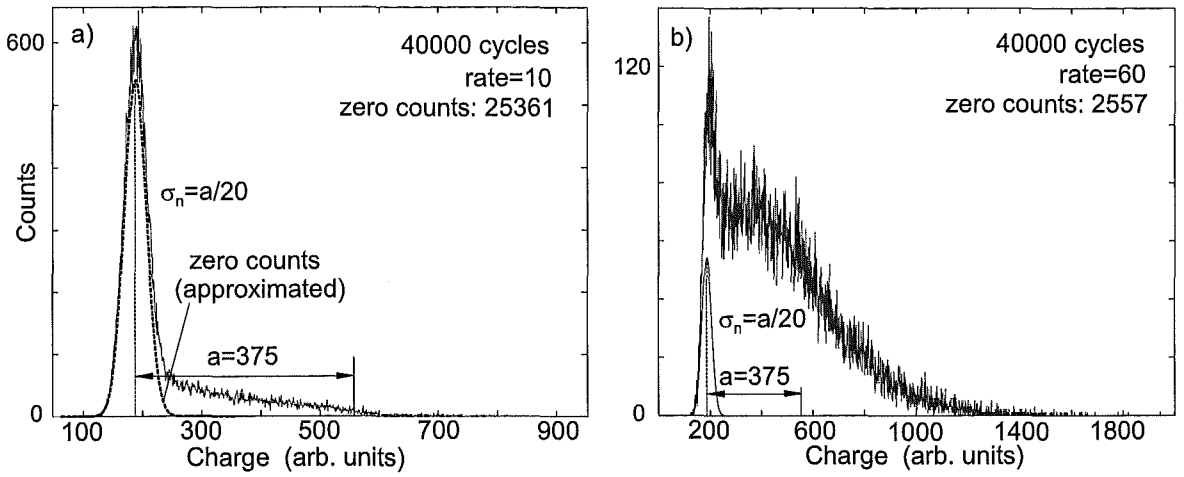

Figure 3.5: Examples of the simulated histograms of the charge in a pixel determined in 40000 cycles of exposure and read out. The two histograms are different in the rate of electrons impinging on the detector (see Fig. 3.4). The charge that is created by electron impacts and collected in the pixel adds to thermally generated charge. The standard deviation σ_n of the thermal noise distribution was chosen to be 1/20 of the maximum charge a created by one impact in one pixel. The number of zero counts is the number of cycles in which no extra charge from electron impacts was detected. This number is important for the counting mode.

rate are characterised by the standard deviation σ of the distribution of the estimated rate determined from 500 repeated simulations for which the conditions were identical. The relative uncertainties in the estimate of the rate are calculated as the ratio of σ and the mean of the 500 estimated rates. Note that σ and σ_n describe different quantities.

Figure 3.6 displays the systematic errors for the two modes and for different parameters. Compared to the integration mode the counting mode shows very large systematic errors. In the counting mode the error depends strongly on the chosen threshold. For a threshold smaller than approx. $1 \cdot \sigma_n$ too many events are counted at low event rate due to the presence of the thermally generated charge. With a high threshold the missing of actual impact events becomes very noticeable. The error is less extreme for a threshold of about $2 \cdot \sigma_n$, however, the error is still large. Another important point is that the sign of the systematic error depends on the event rate, therefore changing the shape of the diffraction pattern. For the counting mode, the systematic error decreases with decreasing σ_n, assuming that all other parameters remain unchanged.

The relative uncertainties in the estimates of the rate for the different modes and parameters are displayed in Fig. 3.7. The relative uncertainty for the integration mode (Fig. 3.7a) decreases with increasing rate and follows the behaviour expected from Poisson distributed data. For a fixed exposure time the standard deviation of the mean of the rate ρ equals $\sqrt{\rho}$ which leads to a relative uncertainty $\sqrt{\rho}/\rho$. The relative

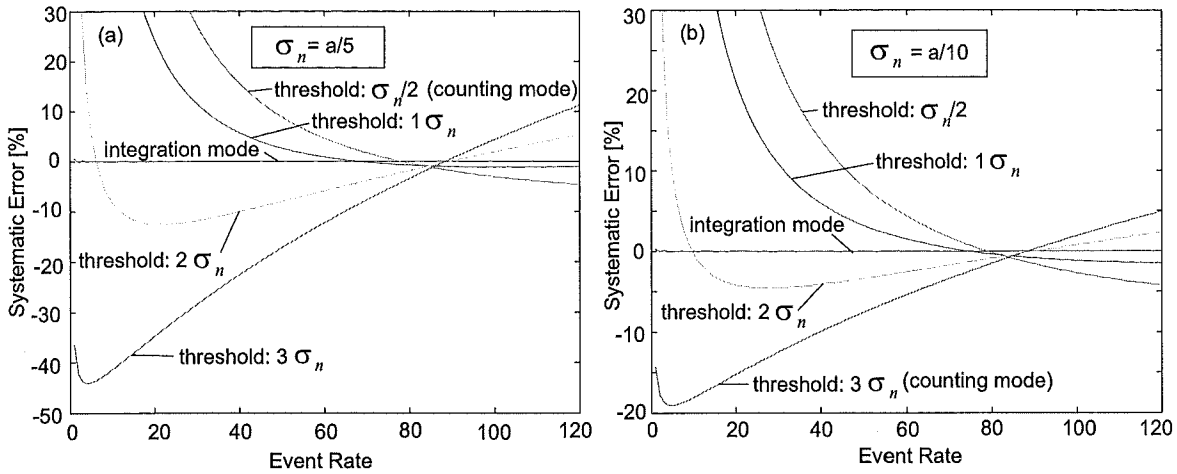

Figure 3.6: Systematic error in the estimate of the event rate. The standard deviation of the noise distribution σ_n was chosen to be 1/5 of the maximum charge deposited by a single impact in (a) and $\sigma_n = a/10$ in (b). Note that the discrimination value for the counting mode is the sum of the threshold value and the mean of the thermal noise distribution.

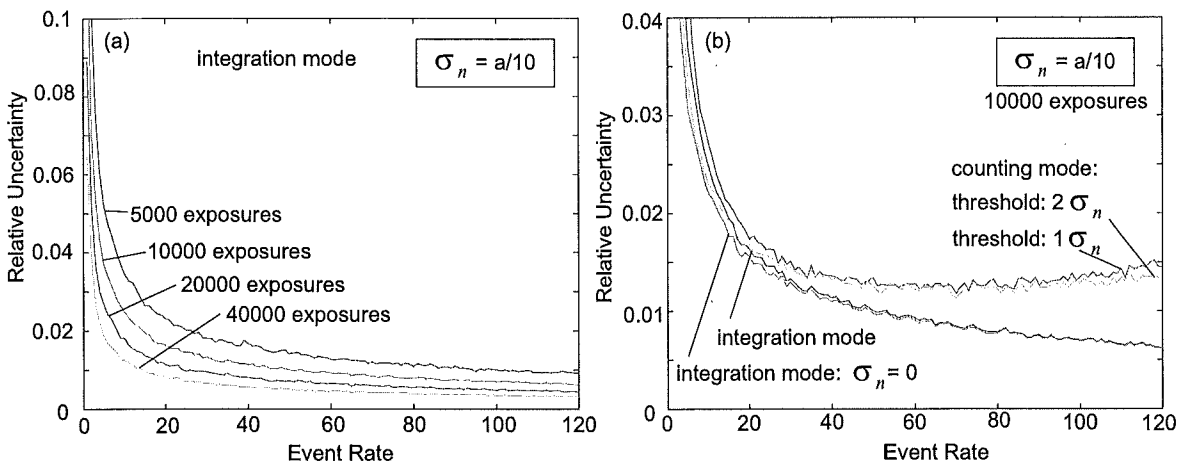

Figure 3.7: Relative uncertainties in the estimated rate for different modes of operation of the detector. This set of figures was calculated from simulations using the parameter $\sigma_n = a/10$.

uncertainty for the counting mode follows the trend observed with the integration mode at low ρ. At higher rates a different effect becomes dominant [3]: In the counting mode the probability of detecting an electron impact during an exposure is used to estimate the rate. For high rates this probability is very close to 1 and uncertainties are introduced since the probability is approximated by the ratio of the two integer quantities C and N (see section 3.2). The uncertainty in C/N is then magnified due to the logarithm in the conversion from C/N to $\rho(C/N)$ in (3.5) and results in an estimated rate that becomes increasingly coarse with increasing C.

Conclusion Concerning the Detection Modes

Based on the results of the simulations it is clear that the integration mode is a far better choice. The counting mode shows large systematic errors due to the need to distinguish between thermal noise and electron impact events. In addition, the relative uncertainties of the counting mode are larger than with the integration mode.

The counting mode approaches the performance of the integration mode when $\sigma_n \ll a$, i.e. when the width of the dark level noise distribution is very small compared to the maximum charge generated from a single impact. In this case, a small threshold can be used and therefore the systematic error becomes small. This condition could be achieved by cooling the detector to reduce σ_n or by using a detector that shows a higher response or gain to impinging electrons. The other difficulty connected to the counting mode is that σ_n increases with the electron dose received by the individual pixels. Since the radiation damage will vary between the pixels (the regions closer to the origin of the diffraction pattern receive a higher average dose) the systematic error will also depend on the history of the individual pixels.

The counting mode introduces systematic errors that can be simply avoided by implementing the integration mode instead.

3.4 Comparison: Simulation – Experiment

In this section the counting mode is compared to the integration mode using experimental data from the new and the old detector system. Although the detectors are only described in the next sections (3.5, 3.6) the results from the different modes are presented here to allow an easy comparison to the simulations.

In the case of the new detector system, the primary result of a measurement is a histogram for every pixel of the charge obtained from N exposure and read-out cycles. The dark level noise distribution of the new detector is characterised by σ_n estimated to be between $a/5$ and $a/8$ (see Fig. 3.5). The histograms were then processed to obtain diffraction patterns for the integration and counting mode. Figure 3.8 shows diffraction patterns from a thin gold film. The data for 1000 exposures was recorded and processed. The sub-figures (a–f) in Fig. 3.8 display the pattern obtained with the integration mode and a counting mode pattern for the corresponding threshold value. The threshold values and their units refer to the histogram of dark current readings shown in Fig. 3.8h. As predicted in the simulations, in the case of a small threshold extra counts due to the thermal noise lead to an over-estimate of the diffraction intensity for

small signal intensities (see right marked region in Fig. 3.8b). At the same time, the intensity in other areas of the diffraction pattern is underestimated (see left marked region in Fig. 3.8b). On the other hand, a large threshold misses a large number of electron impact events and underestimates the diffraction intensity (e.g. Fig. 3.8e). Since the systematic error is also a function of the signal intensity the shape and the peak ratios in the diffraction patterns are affected.

In the case of the old detector, it is possible to obtain the histograms of the charge measured in N exposures which is necessary to compare the two modes[3]. However, the old detector was designed and optimised to operate in counting mode and running the integration mode inflicts a big performance (time) penalty and therefore is only possible for testing purposes.

The dark-level noise of the old detector σ_n is estimated to be between $a/7$ and $a/12$ (see Fig. 3.5). The diffraction patterns in Fig. 3.9 were calculated from the diffraction data of a thin Au film recorded from 1000 exposure and readout cycles. Figure 3.9 visualises the strong influence of the threshold on the diffraction pattern. A small threshold leads to an over-estimate of the diffraction intensity (Figs. 3.9a,b) while a large threshold causes the opposite effect (Figs. 3.9d–e). Figure 3.9c shows an example where the threshold results in an under-estimate of the intensity at intermediate intensities and much smaller systematic errors at low and high intensities. Another important point is that the systematic error is very sensitive to the actual threshold value as can be seen by comparing Figs. 3.9a–c. The systematic error is a function of threshold and intensity and therefore changes the shape of the diffraction pattern. The effect of the systematic error on the performance of the old detector is discussed in the following section.

3.5 The Old CCD Detector System

The old CCD detector was developed by B. D. Hall in 1990/91 at EPFL in Switzerland and is described in detail in [1–3]. The detector system provides a wealth of features for alignment and operation. Its design is based on the counting mode which was implemented in the following way:

- An averaged quantity for the dark current in every pixel is calculated from 200 readings of the unexposed CCDs.

[3]This can be achieved by operating the detector in the 12-bit accumulator mode usually used to read out the dark current in the pixels, see [1].

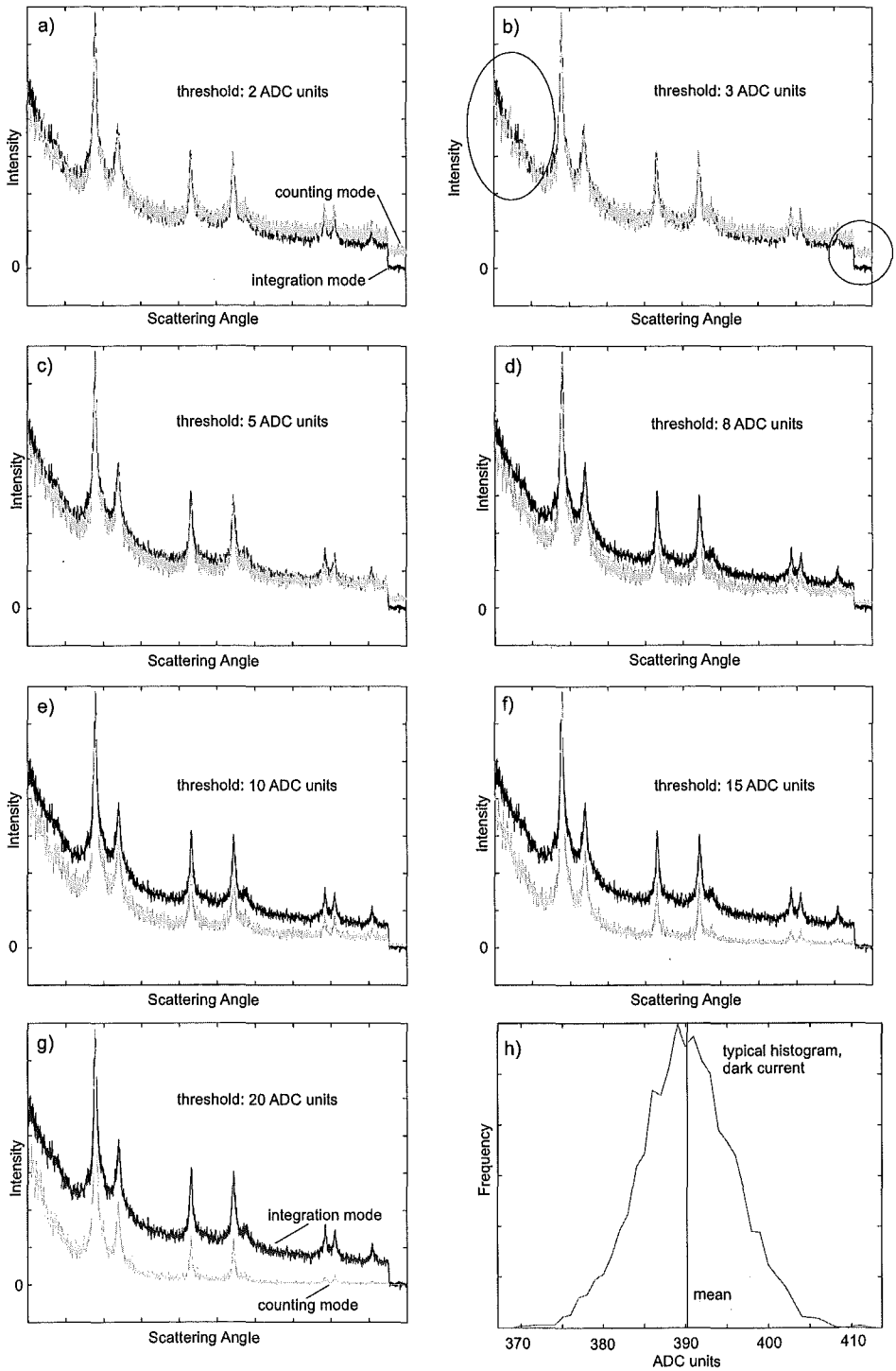

Figure 3.8: Comparison of integration and counting mode for the *new* detector system. (a–f) Diffraction data from a thin Au film processed according to the integration mode and the counting mode using different threshold parameters. The diffraction patterns were scaled so that the intensity for the highest peak in each diffraction pattern is equal. (h) Histogram of dark current readings. The threshold values refer to this histogram. The ADC units are equivalent to measured charge.

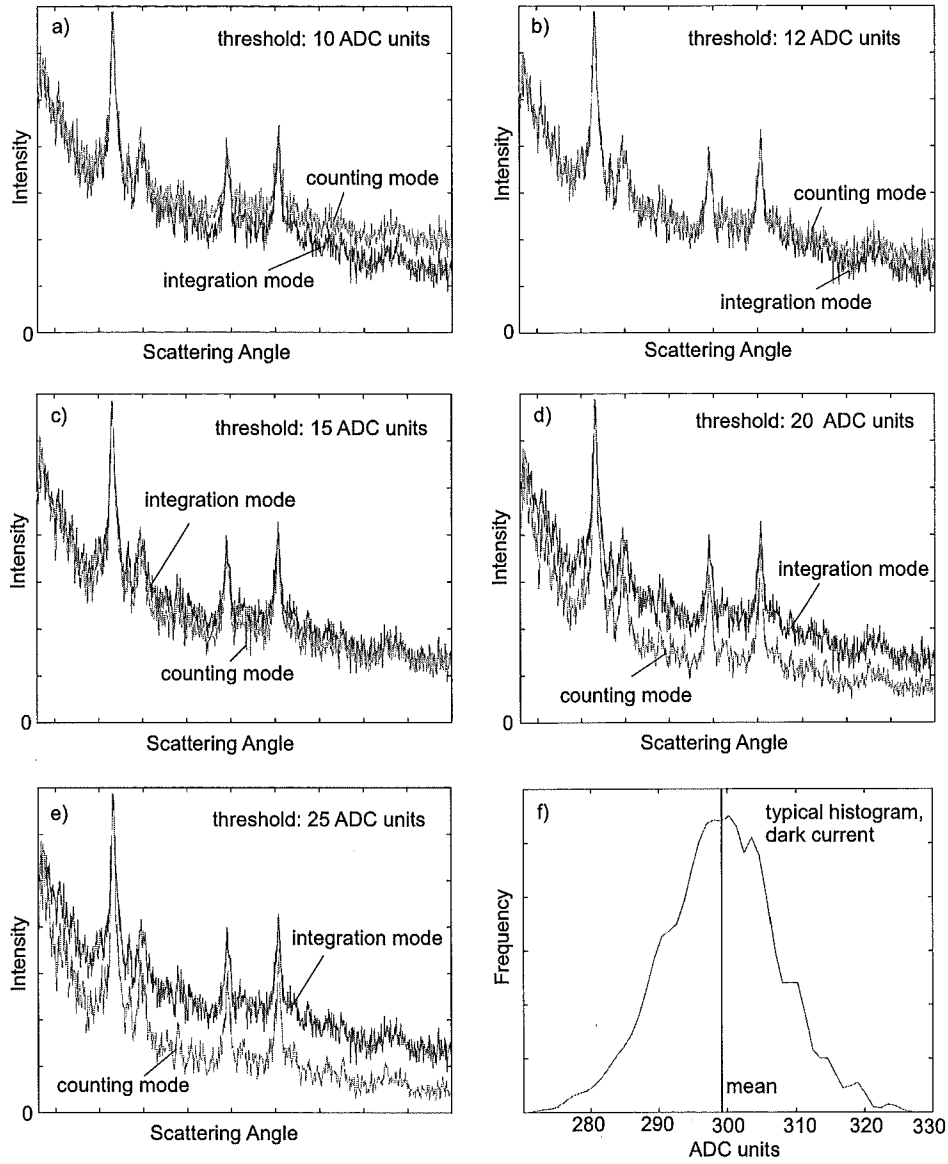

Figure 3.9: Comparison of the integration and counting mode for the *old* detector system. (a–e) Diffraction data from a thin Au film processed according to the integration mode and the counting mode using different threshold parameters. The diffraction patterns were scaled so that the intensity for the highest peak in each diffraction pattern is equal. (f) Histogram of dark current readings. The threshold values refer to this histogram. The ADC units are equivalent to measured charge.

- A constant threshold is added to the dark current value for every pixel. The result is a discrimination value to distinguish between thermal noise and electron impact events.

- Every pixel is assigned a new variable, C_n, that is increased by one if the pixel reading (exposed CCD) is greater than the discrimination value. The CCD is exposed and read out a large number of times (typically 2000 times) to reduce

the relative uncertainty in the measurement.

- The value of C_n divided by the number of measurements represent an estimate of the probability to register an electron impact event in the nth pixel. The actual event rate or intensity is then determined using (3.5).

As shown above, the use of a threshold introduces a systematic error into the measurement which depends on the diffraction intensity and also on the threshold parameter. The evaluation of the systematic error, however, is more complicated as a cluster diffraction pattern consists of a cluster and a gas background contribution. The gas background is measured separately and is then subtracted from the cluster pattern (see section 2.5). Since the systematic error depends on the intensity and can be negative (under-estimate) as well as positive (over-estimate), there is no general reduction of the error over the full pattern due to the subtraction of the gas pattern. The influence of the removal of the gas background on the systematic error is illustrated by the following example:

For this example it is assumed that the detector works with a threshold of 1σ. According to the simulations (Fig. 3.6) this is a good choice as it shows an over-estimate of the intensity only at low intensities and restricts the error to less than 2% for higher intensities. Thus, the cluster pattern shows a small error in the intensity of the peaks while the low intensity regions between the peaks have a larger systematic error (over-estimate). The gas pattern, however, is largely affected (over-estimate) due to its low intensity especially at large s (see Fig. 2.8a). Therefore, the removal of the gas background most likely reduces the error at low intensities but also introduces an additional error in the peak regions. One could argue that the gas patterns should be measured with a longer exposure time to avoid low intensities and therefore avoid large errors. In this way, the error can certainly be reduced but this is only true for a limited range of exposure times which depend on the individual diffraction pattern. If the exposure time is too long the error in the gas pattern is small and the subtraction does not reduce the error in the low intensity parts of the cluster pattern.

Another important aspect is that the error is very sensitive to the choice of the threshold parameter as can be seen in Fig. 3.9 and can be very large if an unfavourable threshold is chosen. There are several problems associated with the choice of the threshold. Firstly, the implementation of the counting mode assumes that the dark-level noise distribution is the same for all pixels. However, with increasing electron dose received by CCDs the width of the noise distribution increases and varies between different areas of the sensor. In this case, the systematic error can be minimised for a range of

pixels but not for the whole CCD. Secondly, a change in operation temperature of the CCDs changes the dark-level noise distribution and also influences the result.

The old detector was designed with the assumption that $\sigma_n \ll a$ which was supported by test results during the development stage of the detector in 1990/91. Therefore, the only plausible explanation for the change in the detector characteristics is the degradation of the electronics and the CCDs as a result of ageing.

3.6 The New LDA Detector System

In order to avoid the problems connected to the counting mode, a new detector system has been developed that operates in integration mode. Like the old detector it uses linear pixel array imagers to detect scattered high energy electrons. The detector electronics and software have been designed from scratch. Clearly, without the experience with the old system and the helpful discussions with B. D. Hall the development process would have been more difficult and much longer. The main design objectives for the new detector were:

- Implementation of the integration mode. However, the system should be as flexible as possible to be able to incorporate new ideas.
- Keep or improve the speed of the data acquisition.
- Improvement of signal quality.
- Cooling of the sensor chips.

The following sections describe the design concepts and implementations for the different components of the detector.

3.6.1 The Sensor Chip

The detection system is based on commercially available linear pixel array imagers. The particular sensor we use is a linear charge-coupled photodiode array (CCPD) from EG&G Reticon (RL2048DAU-111, equivalent to RL2048DAG-111 with the protective window removed, Figs. 3.10a,d). It has 2048 13 µm x 13 µm pixels and operates at data rates up to 20 MHz. The sensing elements are a row of diffused p-n junction photodiodes. When operated with light, light incident on the pixels generates a photocurrent which is integrated and stored as a charge on the capacitance of each of the photodiodes. At the end of each integration period, the charges on all the diodes are

simultaneously switched (transfer clock, Fig. 3.10c) through transfer gates into one of the two CCD analog shift registers for readout. The odd and even numbered diodes are switched into two different registers. Readout is accomplished by clocking the CCD shift registers (video clocks, Fig. 3.10c) so that the charge packets are delivered sequentially into two on-chip charge-detection circuits. The registers deliver the charge packets to their outputs on alternate clock phases, allowing the inactive charge detector to be reset to a fixed level, while the opposite detector is active. A noteworthy aspect is that the video levels for the 2048 pixels are preceded and followed by levels that refer to dark reference pixels (see Fig. 3.10c). The dimensions of the transfer gates and of the horizontal CCD shift registers are important for the operation in an electron beam and are shown in Fig. 3.10b. The transfer gates, the shift registers and other parts of the chip are covered by a metal layer to stop light entering the device and producing charge. This thin coating is virtually transparent to high energy electrons and therefore extra protection is required. This is achieved by a pair of metal slits (see Figs. 3.14c,d) that are positioned above each sensor and are aligned along the pixels. The width of these slits can be adjusted but because of the small pixel size they only partially cover the transfer gates. Therefore, secondary charge from electron impacts are not only collected in the actual pixels but also in the unprotected part of the transfer gates. As a result, the effective sensor area is increased and is sensitive to the quality of the slit alignment. Because of the fact that odd and even pixels are read out to different sides, a misalignment of the slits becomes visible as a non-constant odd/even pixel readout ratio over the length of the pixel array.

3.6.2 The Electronics

The electronics associated with the LDA based detector is shown schematically in Fig. 3.11. The main part is a controller module that manages the LDA clock signals, the beam blanking and therefore the exposure of the sensors and the various signals sent to the computer. It contains a programmable microprocessor that responds to signals from the computer. The four video signals from the two LDAs are inputs to the multiplexer module. The signals enter a track-and-hold system that shifts pairs of adjacent reset and video levels so that all reset levels are at the same specified voltage. This procedure eliminates all shifts in the reset levels which otherwise may change, for example, because of temperature effects. Then the video signal is amplified and shifted in offset. The module provides six different gain settings to select a total gain between 15 and 65. The amplification of the video signal is done in two stages, the

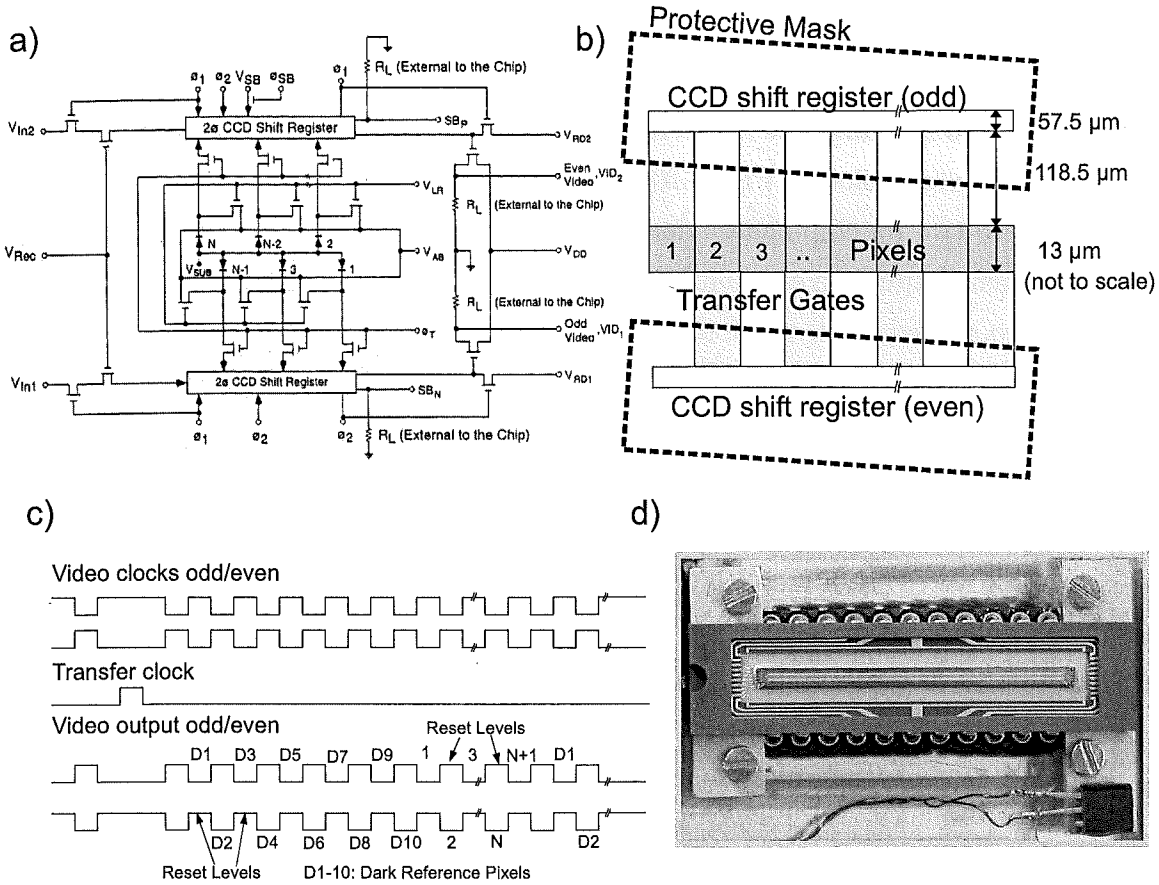

Figure 3.10: The sensor chip used in the new detector system [10]. (a) Simplified schematic circuit diagram. (b) Simplified sensor geometry including (unaligned) protective masks. (c) Timing relationship of the clock and output signals. (d) The sensor chip mounted on the detector base plate.

first being on the LDA circuit board, while the signal is amplified a second time in the multiplexer module. It is also possible to adjust the offset of the signals in order to bring odd and even reading together and to shift the voltage levels (dark current plus possible diffraction signal) of all pixels into a ±5 V voltage range. A difference in dark current levels between pixels is expected as the dark current increases with radiation damage combined with the fact that the average radiation dose is higher at low diffraction angles. Finally, odd and even video signals are multiplexed to create single continuous video outputs for LDA1 and LDA2.

The digitisation of the analog signals is done with a PCI-DAS4020/12 analog to digital multi-function I/O board from Measurement Computing®. It offers four 12-bit analog inputs for simultaneous sampling at a rate of up to 20 MHz. The use of a computer ADC card has the advantage of high sampling rates combined with a fast data transfer to the computer memory. The fact that all the data is analysed and

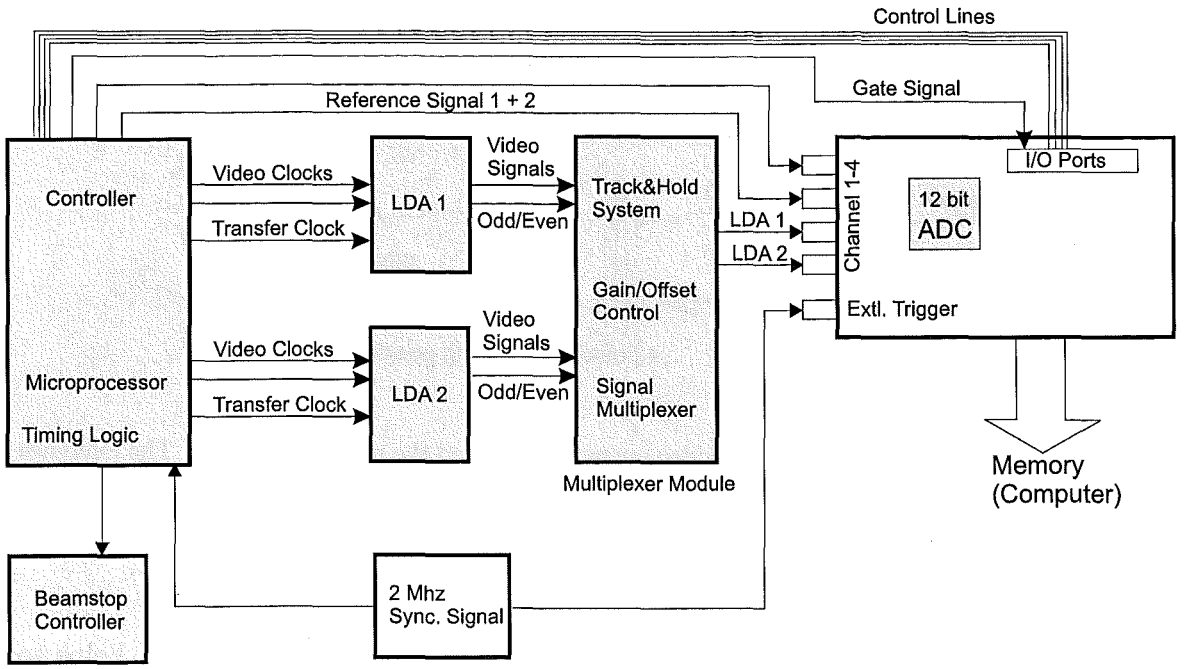

Figure 3.11: Schematic diagram of the electronics. The detector system consists of several modules which are all synchronised by an external 2 MHz clock. The video signals are digitised with a 12-bit computer ADC card.

processed with the computer provides a high degree of flexibility. Although the card now performs very well we cannot recommend it as we lost a great deal of time because of poor documentation and a series of problems that required extensive support from the manufacturer. In the current setup the card samples the video signal at a rate of 500kHz. The sampling is triggered by an external clock that synchronises the timing of the sampling with the timing of the LDA clock signals. A limitation of the ADC card turned out to be the requirement that the external clock had to be four times faster than the sample rate when used with four input channels. This means that sampling can take place at four different positions within a video level. The choice of the sampling position depends on the outcome of the internal synchronisation of the card when the sampling starts and was therefore completely random. Since the shape of the signal waveform is affected by the high amplification it is desirable to have a defined sampling position. As shown in Fig. 3.12 this problem was overcome by feeding a saw-tooth shaped reference signal into a spare input channel. When the sampling is started the value on this channel is checked and if necessary the sampling is restarted until the correct value (see Fig. 3.12) of the reference signal is obtained and therefore the correct sampling position is selected. This solution is not very elegant but achieves the goal with only a small delay (< 1 s) which is irrelevant for the measurement.

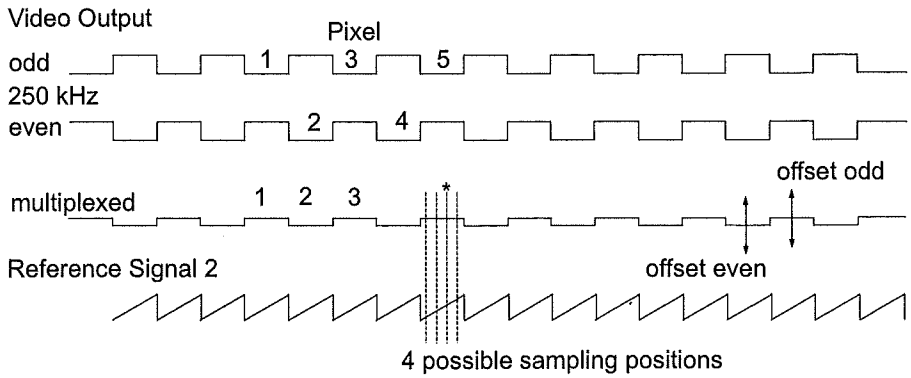

Figure 3.12: Timing relationship of the video output signals and the reference signal 2. The reference signal is used to determine the sampling position of the ADC. The sampling is stopped and restarted until the sampling takes place at the position marked with an asterisk (*).

The remaining fourth input channel is used for an extra reference signal that helps to determine the position of the first video level (D1) (see Fig. 3.10c). This is necessary since the sampling starts some time before and finishes some time after the actual readout values of the pixels are transferred to the ADC.

The data acquisition process begins with the starting and restarting of the data gathering function until the correct sampling position is found. At this point the gate line is set to low to pause the sampling while the synchronisation is maintained. This is then followed by n (n = number of exposures) sequences of exposure and readout of the sensors. The sequence is shown in Fig. 3.13. Only during the time interval T1 the sensors are exposed to electrons (explained below). Interval T2 ($\approx$ 2 ms) is used to clear the charges in the shift registers by clocking them out. In T3 ($\approx$ 4 ms) a transfer signal pulse shifts the charges from the pixels via the transfer gates into the shift registers. Then the gate line is set to high to continue sampling while the charges are read out. When the readout is finished the sampling is paused by changing the status of the gate line.

The exposure of the sensors requires a means of blanking out the electron beam during the process of clearing the shift registers and readout of the pixels (intervals T2 and T3). This is achieved with a beam stop [1, 2] that consists of a parallel plate deflection system and a horizontal graphite plate with a small hole ($\approx$ 0.5 mm). This hole is aligned on the vertical axis of the electron beam. The beam is deflected when a high voltage (400 V) is supplied to the deflection system and will only pass through the hole when the plates are grounded.

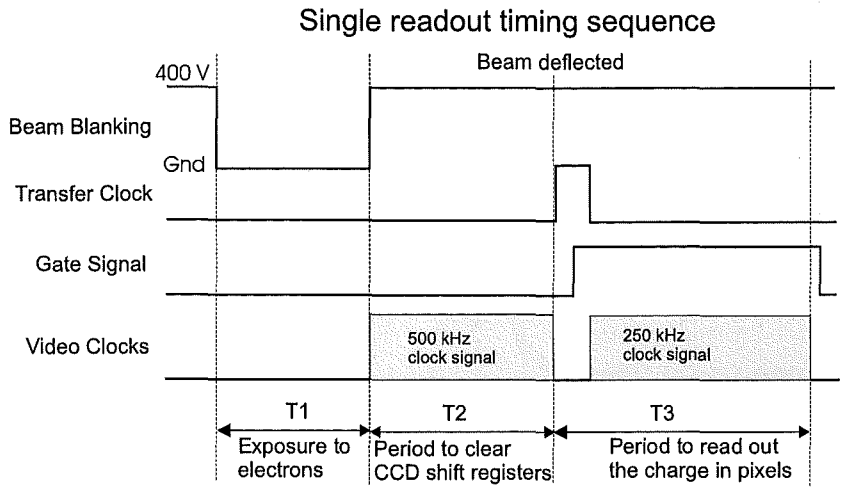

Figure 3.13: Exposure and readout cycle. Note that sampling of the multiplexed video signal only occurs when the gate line is high. This helps to reduce the amount of raw data stored in the RAM of the computer

3.6.3 Software

A software package for the measurement and display of diffraction patterns, alignment of the diffraction apparatus and for testing of the electronics has been developed. It uses the high level functions provided by the C/C++ library and drivers of the ADC card to acquire data and to communicate with the electronics control module.

The diffraction patterns are expected to be of very low intensity. In order to reduce noise on the patterns the sensors are exposed and read out a large number of times (typically: 4000 times). One measurement run consists of consecutive exposures and readouts of the sensors and all the results of the A/D conversions are stored as raw data in memory. The raw data is processed in several steps. First, the reference signal is used to identify the clock pulses in the video signal that belong to actual pixels. Both sensors have a number of pixels that are mechanically masked (Fig. 3.14c) to avoid exposure to the electron beam. The readout values of these pixels are used as reference values to correct for changes in the video levels during exposures. Tests have shown that the video levels of the unexposed sensors change during continuing exposure and readout cycles. These changes are probably due to temperature changes during operation and if uncorrected lead to a systematic error in the measurements. The correction procedure shifts the video levels of all pixels by the same amount so that the average of the video levels of the masked pixels has the same value for every exposure. In the final step, the results of all exposures are averaged to obtain an intensity pattern. A single measurement run with the electron beam on shows an intensity pattern that consists

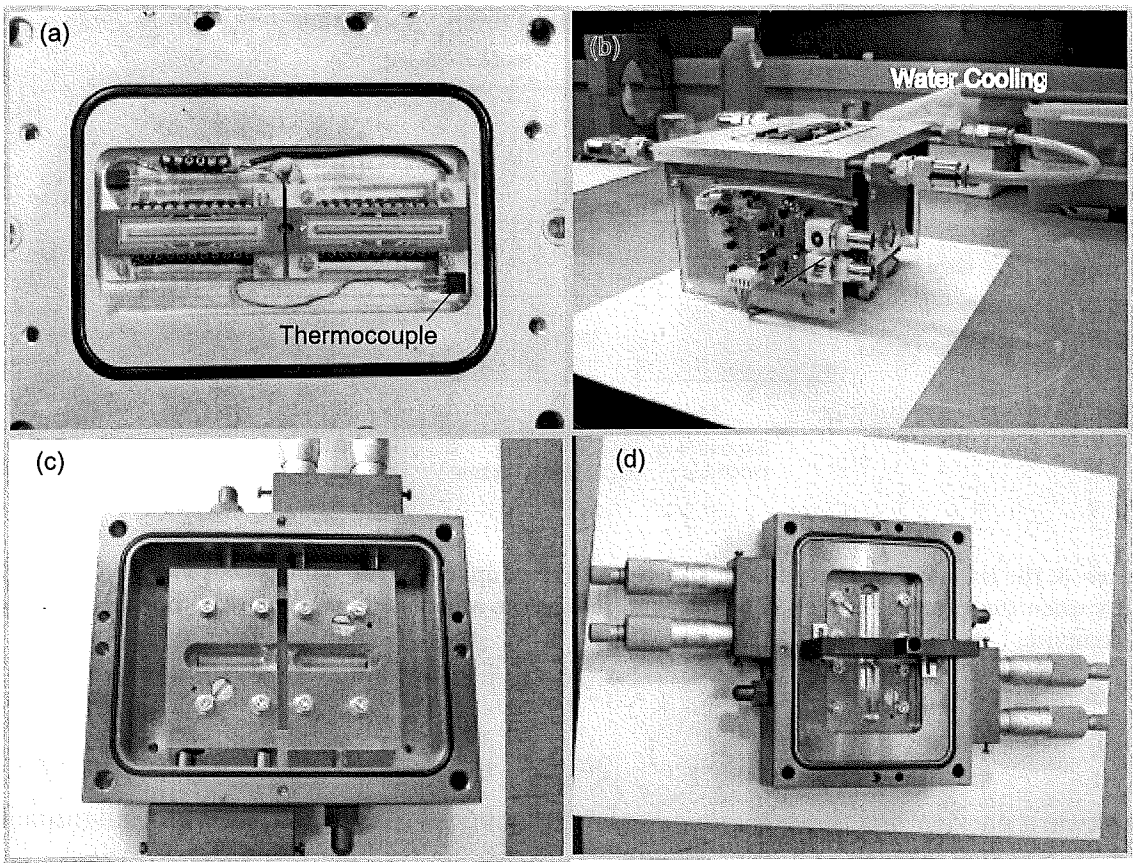

Figure 3.14: The Peltier coolers (not visible) are mounted between the LDA chips and the base plate of the vacuum chamber. To remove the heat from the Peltier elements the base plate is water cooled (a,b). The protective masks (c) stop electrons from reaching sensitive parts in the sensor chips. The electron beam stop (d) absorbs the central electron beam. The beam stop and the protective masks are original parts from the EPFL equipment [2].

of two contributions: the dark current signal and the actual charge due to electron impacts. The dark current contribution can be removed by subtracting an intensity pattern obtained shortly after the first run (same conditions and parameters) but with the electron beam off during the exposure period T1 (see Fig. 3.13). The subtraction of the dark current signal leads to the actual diffraction pattern. This implementation corresponds to the integration mode described in section 3.2.

3.6.4 Peltier Cooling

In order to reduce and stabilise the dark current in the pixels and also to reduce radiation damage the sensor chips are cooled by Peltier elements[4]. The Peltier elements have a size of 6 x 40 mm^2 and fit exactly between the pins of the sensor chips. The

[4]TEC-CCDL-40-6, obtained from Eureca Messtechnik GmbH, http://www.eureca.de.

heated side of the Peltier elements connects to the aluminium base plate of the vacuum chamber. In order to maintain sufficiently low temperatures of the base plate, it is connected to a water cooling system as shown in Fig. 3.14b. The installation allows cooling of the sensor chips down to −15°C. The temperature is measured with a thermocouple and a temperature controller is used to maintain a set temperature. We were not able to detect an influence of the magnetic field of the Peltier elements on the position or shape of the diffraction pattern.

3.6.5 Testing the Detector

For a given diffraction sample the intensity registered in a pixel depends on the number of scattered electrons which in turn depends on the exposure time and the intensity of the main electron beam. In order to test the linearity of the detector response to scattered electrons diffraction patterns have been measured with different exposure times. Two measurements of the same ring pattern with two different exposure times are expected to only differ by a scaling factor. In addition, the scaling factor should be equal to the ratio of the exposure times. The results of this test are shown in Fig. 3.15. The intensity ratio of two diffraction patterns from a polycrystalline ThCl film shown in Fig. 3.15a is independent of the features in the diffraction patterns and is only affected by the noise. Since the noise increases with decreasing intensity the intensity ratio is noisier at large scattering angles (large s). Moreover, the mean value of the intensity ratio equals the ratio of the exposure times of the two diffraction patterns. The same behaviour can be seen for the gas background in the diffraction chamber shown in Fig. 3.15b. In this case, the scattering signal is much weaker and larger exposure times are necessary (unchanged beam intensity) to obtain diffraction patterns that have a good signal to noise ratio. The exposure times for the patterns in Fig. 3.15 were chosen to cover the range of typical exposure times for cluster samples (approx. 1–6 ms).

As mentioned above, the characteristics of the sensors change due to the exposure to high energy electrons. A noticeable effect is an increase in dark current in the pixels. Even when the sensor chips are cooled down to −15°C it is easily possible to distinguish between a new and a used chip. Since the dark current contribution in the signal is subtracted the damage is only of concern if it leads to a non-linear response of the sensor to the scattered electrons. In order to compare the performance of two sensors with different degrees of damage the same diffraction ring pattern has been measured with two chips. The two diffraction patterns in Fig. 3.16 cover different ranges of scattering angles since the sensors are slightly offset relative to the centre

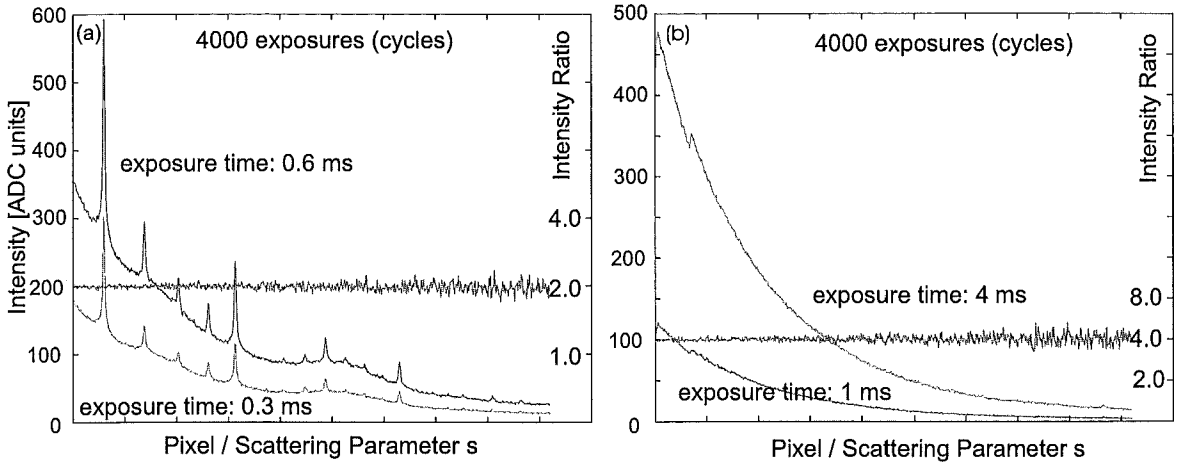

Figure 3.15: Linearity test on the detector. The ratio of the intensity of two diffraction patterns taken with different exposure times is expected to be independent of the intensity and to be a constant with a value equal to the ratio of the exposure times. (a) Polycrystalline ThCl film (b) Gas background in the diffraction chamber.

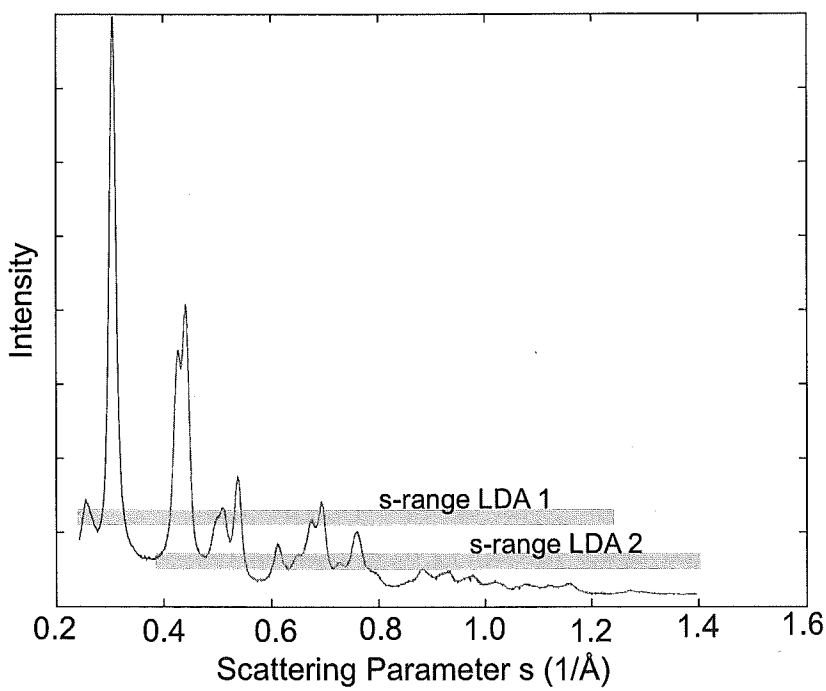

Figure 3.16: The same diffraction pattern measured with two LDAs with different amounts of damage (new chip, 6 month in use). The damage is visible through the increased dark current. The sensors are slightly offset relative to the centre of the diffraction ring pattern and therefore cover different ranges of scattering angles. For the s-range covered by both sensors the two diffraction patterns are only different in the noise.

of the diffraction ring pattern (standard configuration). For the s-range covered by both sensors the two diffraction patterns are only different in the noise. The results in Fig. 3.16 not only show that the level of the dark current has a negligible influence on the detector performance but also that the detector implementation is free of other systematic errors.

The speed of the data acquisition has been slightly improved compared to the old detector system as the minimum time between exposures (clearing of the transfer registers, readout) is only 6 ms compared to 10 ms [1]. A typical measurement with 4000 exposures and exposure periods of 4 ms takes about 50 s.

3.6.6 Conclusions

The new detector described in the previous sections uses a pair of linear diode arrays (LDA) to measure the diffraction patterns from a sample of unsupported clusters. It operates in the integration mode and thereby avoids all problems associated with the counting mode used for its predecessor.

The cooling of the LDAs has been found to be crucial to the operation of the detector. Thermally generated charges build up during exposure of the sensor and for long enough exposure times it can lead to saturation of the pixels. In addition, the amount of thermal charge created increases with the cumulative dose of high energy electrons received. Cooling the LDAs to $-15°C$ dramatically reduces the dark current in the pixels. Moreover, a stable temperature reduces shifts in the voltage levels of the LDAs during exposure and readout cycles that otherwise would cause measurement errors. The quality of the data is further enhanced by two correction schemes, one in hardware and one in software, to stabilise the voltage levels.

References

[1] B. D. Hall, *An Installation for the Study of Unsupported Ultrafine Particles by Electron Diffraction with Application to Silver: Observation of Multiply Twinned Particle Structures*, PhD thesis, EPFL, 1991.

[2] B. D. Hall, M. Flüeli, D. Reinhard, J.-P. Borel, and R. Monot, Rev. Sci. Instrum. **62**, 1481 (1991).

[3] B. D. Hall, Rev. Sci. Instrum. **66**, 2668 (1995).

[4] D. Reinhard, *Croissance et Stabilité d'Agrégats d'Argent et de Cuivre, Etudiés en Jets Moléculaires par Diffraction d'Electrons à Haute Energie*, PhD thesis, EPFL, 1996.

[5] S. M. Sze, *Physics of Semiconductor Devices*, John Wiley, London, 2nd edition, 1981.

[6] G. Y. Fan et al., Ultramicroscopy **70**, 107 (1998).

[7] J. Guldberg and D. K. Schroder, IEEE Transactions on Electron Devices **18**, 1029 (1971).

[8] P. T. E. Roberts, J. N. Chapman, and A. M. MacLeod, Ultramicroscopy **8**, 385 (1982).

[9] J. N. Chapman, F. Glas, and P. T. E. Roberts, Inst. Phys. Conf. Series **61**, 131 (1981).

[10] EG&R RETICON, *D Series Linear Family Charge-Coupled Photodiode Array*, 2001.

Chapter 4

Electron Diffraction and Analysis

The particles investigated in this study are produced in an inert-gas aggregation source. The mixture of gas and small particles is extracted through two pumping stages and then probed by a high energy electron beam. As a result the randomly oriented particles give rise to a Debye–Scherrer type diffraction pattern. It is important to note that the beam of particles may consist of particles with different sizes and also different structures. The scattering of electrons from atoms is based on the Coulomb interaction between electron and net charge of the atom. Since the atom is electrically neutral there is no interaction outside the atom and high energy electrons must penetrate the electron cloud of the atom for scattering to occur. Inside the atom, the electron senses a net positive charge because of the incomplete screening of the nuclear charge. As a consequence, detailed calculations of this scattering require accurate densities of the atomic electrons. Coulomb interactions are quite strong and therefore electrons are scattered much more strongly than X-rays in diffraction experiments. The scattered intensity from single atoms (vapour) is a monotonic decreasing function with increasing scattering angle. In the case of short range order (amorphous materials) and long range order (crystals) of atoms the intensity is concentrated at specific diffraction angles. For crystalline particles the features are more pronounced the bigger the particle is. Since we want to retrieve information about the structure and size of the particles probed by the electron beam we have to compare the measured diffraction pattern to calculated patterns from model structures. The next section deals with the methods to calculate diffraction patterns from model structures and their limitations. Thereafter a detailed overview is given of the different methods that can be used to extract information from experimental diffraction patterns.

4.1 Calculating Diffraction Patterns from Model Structures

We use the Debye Equation for electron diffraction to calculate diffraction patterns from model structures. The Debye Equation is part of the kinematic diffraction theory

and allows the calculation of diffraction patterns with modest computer resources. However, the kinematic approximation introduces systematic errors which may limit the analysis of the measured diffraction patterns. Therefore, it is necessary to compare kinematic diffraction patterns to patterns calculated with the more accurate dynamic theory. A detailed comparisons has been published in [1] and is discussed further below.

Kinematic Scattering: the Debye Equation

The Debye Equation is used to calculate diffraction patterns from a collection of identical objects with random orientation and position. In general, the Debye Equation can be used for polyatomic molecules and clusters but the equation given here is a simplified version for clusters that contain only one type of atoms [2]:

$$I_N(s) = I_0 N f^2(s) \left(1 + \frac{D}{N} \sum_{n \neq m} \frac{\sin(2\pi s r_{mn})}{2\pi s r_{mn}}\right) \tag{4.1}$$

I_0 : intensity of the incident beam
N : number of atoms in the cluster
r_{mn}: distance between atom m and atom n
D : Debye–Waller factor

The quantity $f(s)$ is referred to as the atomic scattering factor and is available in tabulated form. Its square, $f^2(s)$, is the elastic differential cross section of a single atom. In this thesis, the tabulated atomic scattering factors from [3] have been used. Electron scattering factors can be calculated from the published X-ray scattering factors using the Mott formula [3]. The scattering parameter, s, is defined as $s = 2\sin(\theta)/\lambda$, where θ is half of the scattering angle and λ is the electron wavelength [2](see Fig. 4.1). Note that in some publications a slightly different definition of s ($s = 4\pi\sin(\theta)/\lambda$) is used. The influence of the thermal vibrations in crystals on a diffraction pattern is considered by the Debye–Waller factor D. Thermal vibrations have two effects on the diffraction of electrons by a crystal: the Bragg peaks lose intensity and the intensity that is subtracted from the peaks reappears as thermal diffuse scattering in the background.

A simple correction for the thermal vibrations is made by assuming that the displacement of atoms is independent and isotropic [2]. In this case:

$$D = \exp\left(-\frac{4\pi^2 s^2}{3}(\Delta r)^2\right) \tag{4.2}$$

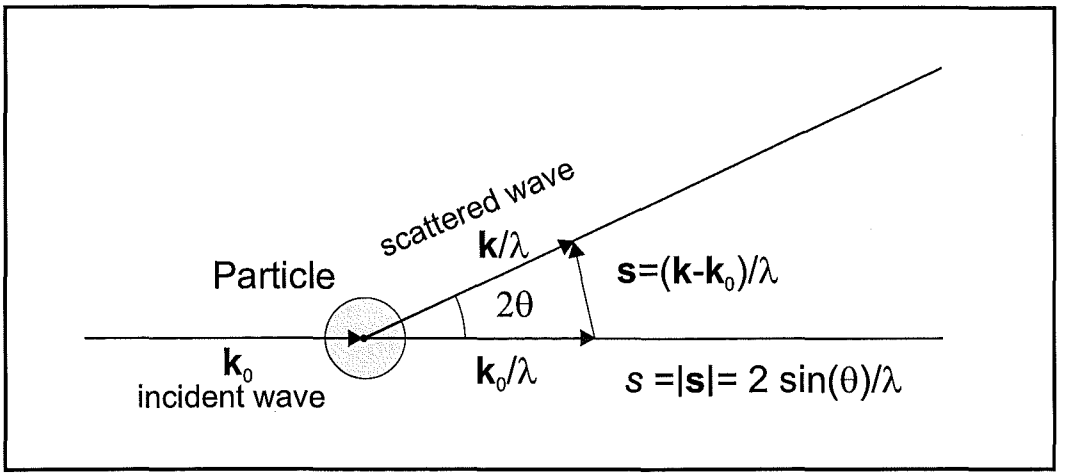

Figure 4.1: Definition of the scattering parameter s. The vectors $\mathbf{k}$ and $\mathbf{k}_0$ define the directions of the incident and the scattered waves respectively. For a wavelength λ and a scattering angle 2θ the scattering parameter is given by $s = 2\sin(\theta)/\lambda$.

where Δr is the root-mean-square (rms) atomic displacement from equilibrium at a temperature T. According to (4.2) the factor D increases with diffraction angle and the diffraction peaks at larger angles are therefore more affected than the others. The rms atomic displacement and therefore the Debye–Waller factor vary strongly from element to element. Elements like bismuth and lead show very strong attenuation effects while the diffraction patterns of other elements like copper are less affected. At modest temperatures, for certain elements (i.e. small $(\Delta r)^2$) and small s the exponential in (4.2) can be linearised to simplify the analysis.

In order to calculate diffraction patterns from model structures, (4.1) is modified to reduce computing time and to allow certain parameters to be determined from the experiment (i.e. these we do not know beforehand):

$$I_N(s) = \alpha f^2(s) \left(1 + \exp(-s^2\gamma^2) \cdot \frac{1}{N} \sum_r \frac{\sin(2\pi sr)}{2\pi sr} 2H(r) \right) . \tag{4.3}$$

We do not know the intensity of the incident electron beam and therefore need a parameter α that scales the calculated to the measured diffraction pattern. The second parameter to be determined is γ, a parameter which represents the unknown rms displacement of atoms. In order to speed up the calculations the interatomic distances are binned into a histogram $H(r)$ to reduce the number of evaluations of the sine function. The optimal bin size varies from problem to problem and has to be chosen carefully to avoid systematic errors in the calculated diffraction patterns.

It is often important to estimate the Debye–Waller factor for a material at a known temperature. In first approximation, $(\Delta r)^2$ and therefore γ^2 are directly proportional to the temperature T. Using the Debye model an expression for the Debye–Waller factor can be derived for temperatures comparable to the Debye temperature or above [2]. For Bismuth, the relation between γ^2 and the temperature in K can be approximated by:

$$\gamma^2 \simeq 0.00191 \cdot T \,. \tag{4.4}$$

Dynamic Calculations

The kinematical approximation assumes that the amplitude of the singly scattered electrons will be very small compared with the incident beam amplitude. The effect of multiply scattered electrons will then be negligible. The amplitude of the scattered beam depends to a great extent on the thickness of the material and on the material itself. Therefore, it is necessary to include dynamic effects for heavy elements and long path lengths through the material. A method to correct for dynamic effects has been developed by Bartell [4]. It provides additional terms which account for some multiple scattering and that are added to a kinematic calculation. Bartell's correction works well for small clusters and has been tested for gold clusters with up to 135 atoms [5]. It has the big advantage that it can be applied to arbitrary structures and that it calculates the Debye–Scherrer diffraction pattern directly. However, a more general approach is the multi-slice method, a numerical implementation of the "physical optics approach" to the diffraction problem (see [6] and references therein). It is a well established technique for the calculation of high resolution electron microscopy images (HRTEM) and is available through different software packages. However, one multi-slice calculation only calculates the diffraction patterns for one specific orientation. In order to determine a Debye–Scherrer ring pattern it is therefore necessary to calculate diffraction patterns for a large set of orientations. The multi-slice method is computationally intensive but can be used for larger particles (see [1]).

Errors due to the Use of the Kinematical Theory

The systematic errors introduced by the kinematic approximation for diffraction patterns of small gold and silver particles (147, 923 and 5083 atoms) have been investigated in [1]. In this study dynamic diffractions patterns were obtained with a multi-slice algorithm and the scattering cross-sections were compared to the corresponding kinematic

cross-sections. The results were presented as plots of the *absolute* values of the differential cross-sections obtained using the two methods. In order to estimate how much the systematic error affects, in particular, the analysis of diffraction patterns the original data from [1] has been replotted here in a different way (Fig. 4.2). The motivation for this procedure was the following: Analysing diffraction patterns always involves a matching of the calculated patterns to the measured patterns. If we assume, as an example, that the dynamic pattern represents the measured pattern then we have to determine the difference to the kinematic pattern after it is scaled to the dynamic pattern. An optimal scaling factor would be one that fulfils the following condition:

$$\text{Minimise} \sum_s (\alpha \cdot I_k(s) - I_d(s))^2 \,, \tag{4.5}$$

where α is the scaling factor and $I_k(s), I_d(s)$ are the kinematic and the dynamic diffraction patterns, respectively. If we then compare $I_d(s)$ with $\alpha \cdot I_k(s)$ we are able to obtain the relative systematic error introduced by the kinematic approximation. The series of plots in Fig. 4.2 visualises the systematic error due to the kinematic approximation for the clusters from [1] after the matching procedure (4.5). Several trends are visible in Fig. 4.2 (see [1] for a detailed discussion):

- The systematic error decreases with increasing electron energy (compare left and right column in Fig. 4.2),
- For the same material and structure the error increases with increasing cluster size (Figs. 4.2a,c).
- The systematic error for the Ag icosahedron is less than for the Au FCC cluster with the same number of atoms (Figs. 4.2c,e or d,f). The differences can be attributed to the different structure and the fact that dynamic corrections are smaller for silver than for gold [1].

After the fitting procedure (4.5) the absolute differences between dynamic and kinematic calculations are relatively small for $s > 0.45$ Å^{-1}. However, the different shape of the diffraction patterns becomes apparent in the mismatch of the largest peaks. The large negative relative differences are due to the subtraction of small closely valued numbers and are not significant for the analysis.

The different shape of dynamic and kinematic diffraction patterns clearly limits the amount of information that can be extracted from the measured diffractions patterns

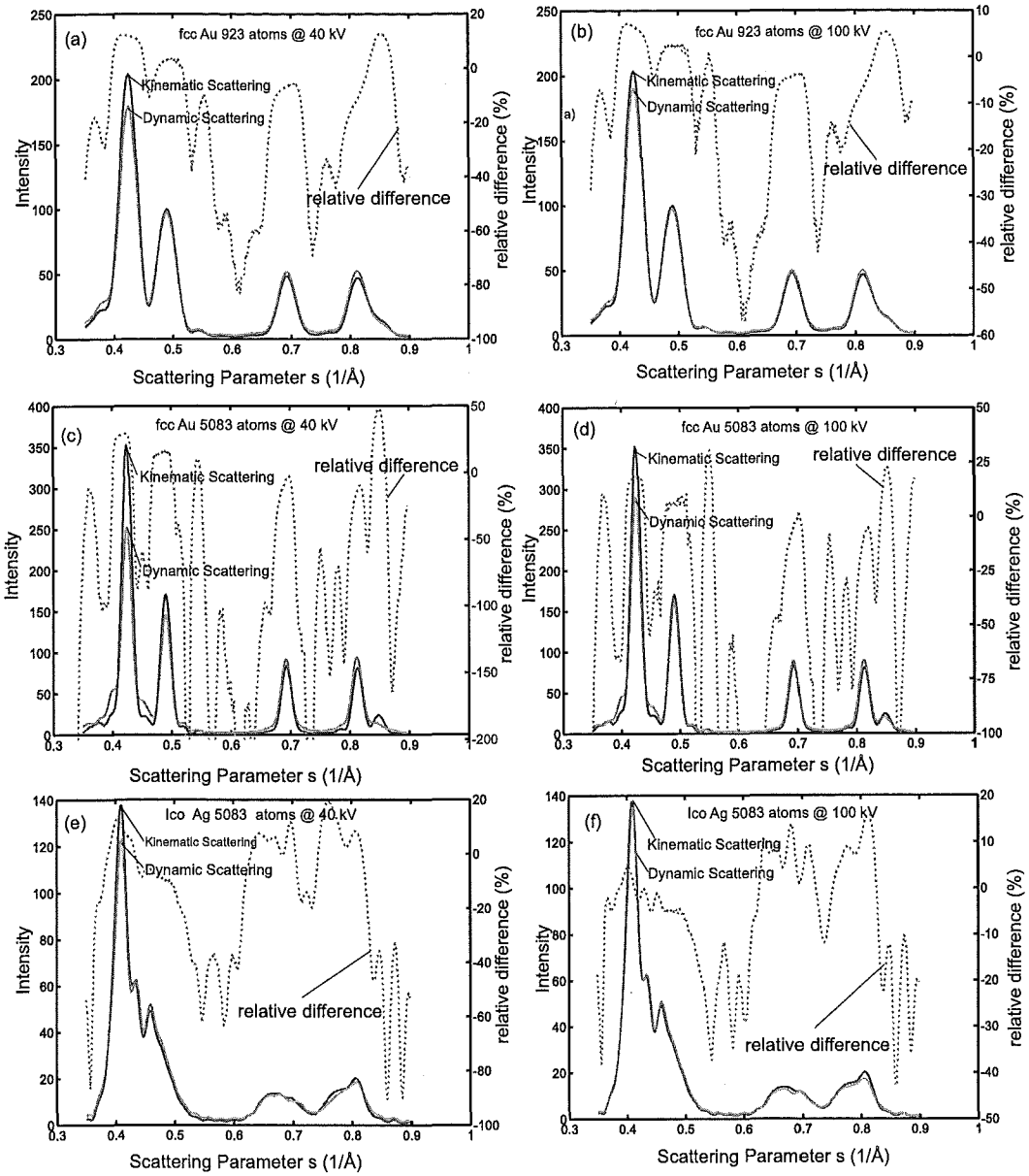

Figure 4.2: Systematic error due to the kinematic approximation for different cluster sizes, structures and energies of the incident electron beam. The data was provided by B. D. Hall and is identical to the data used in [1]. Each plot shows $I_d(s)$, $\alpha I_k(s)$ and the relative difference $(I_d(s) - \alpha I_k(s))/I_d(s)$. The scaling parameters fulfil condition (4.5).

(see section 4.2). In this study the clusters are probed with an 80 kV electron beam leading to slightly increased errors compared to the 100 kV examples. Bismuth is only slightly heavier than gold so that larger corrections are not expected from the different masses. Bismuth, however, crystallises in the rhombohedral structure and therefore these results represent only a rough estimate.

Table 4.1: Overview of the different methods to extract information from Debye–Scherrer diffraction patterns

Information about:	Method
Cluster size	Scherrer Equation, Inversion techniques, RMC[a] simulations , χ^2 fitting
Cluster structure	peak positions, χ^2 fitting
Lattice parameters	peak positions, χ^2 fitting
Cluster shape	RMC[a] simulations, χ^2 fitting

[a] Reverse Monte Carlo simulations, implemented only for large clusters with a known structure

In order to estimate the errors due to the kinematic approximation specifically for Bi clusters it would be necessary to develop an extensive software package. Considering the time and resources required and the fact that in this PhD project priority has been given to the development of a new detector system the calculation of dynamic diffraction patterns for Bi clusters has not been undertaken.

4.2 Retrieving Information from Diffraction Patterns

The analysis of a newly acquired set of diffraction patterns usually starts with a comparison of the measured pattern with the bulk diffraction patterns of the corresponding material. The characteristic peak positions for different materials and structures are easily obtainable. Larger clusters will most likely show the crystal structure of the bulk material. In this case, we are interested in the lattice parameters and the shape of the clusters. Diffraction patterns are not only sensitive to crystal structure and shape but also to the particle size. When clusters become small but maintain their structure the diffraction peaks become broader and some of the peaks eventually merge. Real changes in the lattice structure usually become visible by the appearance of new peaks at different positions. These peaks give a good indication of the structure but a more detailed analysis requires the comparison with calculated patterns from model structures. The tools that have been used to analyse diffraction patterns are summarised in Table 4.1 and are discussed in the next sections.

Most of these methods have been implemented as software tools and are available as C/C++ or Matlab packages.

4.2.1 χ^2 Fitting of Diffraction Patterns from Cluster Models

As mentioned above, the cluster beam may consist of particles of different structures and different sizes. One approach to extract as much information as possible is to fit a

combination of diffraction patterns of model structures to the experimental data [7, 8]. The first step in this approach is to generate model structures of clusters assumed to be in the beam. Then the diffraction patterns are calculated using the Debye Equation (4.1). The combination of the diffraction patterns with all the parameters to be determined can be expressed as:

$$I(s) = \alpha f^2(s) \left(1 + \exp(-s^2\gamma^2) \cdot \sum_n \beta_n L_n(s) \right) , \tag{4.6a}$$

$$L_n(s) = \frac{1}{N_n} \sum_r \frac{\sin(2\pi sr)}{2\pi sr} 2H_n(r) . \tag{4.6b}$$

The terms $L_n(s)$ are specific to the individual model clusters as they contain the histograms $H_n(r)$ of the interatomic distances of the clusters. These terms can be calculated in advance. The free parameters α, γ, β_n are then determined by a fitting procedure that minimises:

$$\chi^2 = \sum_s w(s) \frac{(I(s) - I_e(s))^2}{\sigma(s)^2}, \tag{4.7}$$

where the $\sigma(s)$ are the standard deviations of the measurement uncertainties of the diffraction pattern $I_e(s)$ and $w(s)$ is a weighting function. The χ^2 fitting corresponds to solving a non-linear minimisation problem with all its numerical difficulties. The method chosen in [7] was simulated annealing (see e.g. [9]). It has the advantage that additional fitting parameters, e.g. the lattice parameters of the model structures, can easily be included. In general, a change of the lattice parameters requires the computationally expensive re-evaluation of (4.6b). A shortcut is possible for the structures of the cubic crystal system for which a change of the single lattice parameter results in a rescaling of the r-axis of the histogram of interatomic distances. Therefore the re-evaluation of (4.6b) can be replaced by a new $L_n(s^*)$ with a rescaled s-axis ($s \longrightarrow s^*$).

Assuming that the minimisation algorithm is able to find the correct solution to the non-linear problem there are further difficulties related to this approach. Firstly, everything depends on the right choice of the model structures. If structure types or cluster sizes are missing or if diffraction patterns are not linearly independent and misleading results can easily be obtained. In order to avoid misinterpretations all fitting results that belong to a fitting curve that do not lie within the measurement uncertainties of the diffraction pattern should be very critically examined. Secondly, it should be emphasised that this fitting procedure (4.6a, 4.7) is based on the kinematic approxi-

mation and an application to diffraction patterns where this fails strongly limits the amount of information that can be extracted. On the other hand, this method will be very powerful if it is combined with the calculation of dynamic diffraction patterns.

The fitting procedure usually involves a large number of free parameters. Depending on the information content of the experimental pattern there may too many parameters which can lead to multiple solutions with very similar χ^2 values. If the χ^2 surface has several minima additional criteria (prior information about the clusters) are necessary to accept or reject solutions. Often problems become visible in the obtained size distributions. For larger particles the size distributions are expected to be smooth and without gaps or spikes. If the fitting procedure returns unreasonable distributions, it may be useful to constrain the size distribution by using an analytical size distribution (e.g. Gaussian, log-normal distribution), reducing the number of fitting parameters.

4.2.2 The Scherrer Equation

The Scherrer Equation originates from the kinematical theory of electron diffraction and relates the cluster size to the full-width-at-half-maximum (FWHM) of the diffraction peaks (for details see [10]):

$$L = \frac{K}{\sqrt{(\Delta s)^2 - (\Delta s_0)^2}} \tag{4.8}$$

where L is the size of the crystallite, Δs the FWHM of the diffraction peak measured in s, Δs_0 the instrumental peak broadening (section 2.2) and K the Scherrer constant that depends on the shape of the crystallite. For a flat crystallite with constant thickness K equals 0.89. The Scherrer constant depends in detail on the shape of the clusters and also on the distribution of particles sizes in the cluster beam. Often $K \simeq 0.9$ can be used, however, variations of K of the order of 20% are to be expected.

The Scherrer Equation assumes that particles are single crystalline. If clusters contain defects or disorder the diffraction peaks are additionally broadened [2, 11] which leads to an underestimate of the cluster size. The Scherrer Equation also underestimates the size of a particle if it consists of crystalline domains since diffraction is only sensitive to the domains within the cluster (see section 4.3.2).

4.2.3 Standard Inversion Methods

A different approach to extract information from experimental diffraction patterns is to retrieve an estimate of the radial distribution function (rdf) by inverting the diffraction

pattern. The rdf, $4\pi r^2\rho(r)$, is defined such that $4\pi r^2\rho(r)dr$ is the average number of atom centres with interatomic distances between r and $r+dr$ ([10]). For this definition the Debye Equation can be rewritten as [10]:

$$I_N(s) = I_0 N f^2(s)\left(1+\int_0^\infty 4\pi r^2\left[\rho(r)-\rho_a\right]\frac{\sin(2\pi sr)}{2\pi sr}dr\right) . \tag{4.9}$$

This more general form includes ρ_a the sample average atom density. Cluster samples are usually so dilute that ρ_a is negligible. It is not negligible, for example, for large (bulk) amorphous or liquid samples. For a single cluster the rdf is closely related to the histogram of interatomic distances broadened by the thermal vibrations of the atoms. In addition, the mixture of particles probed in an experimental situation results in an rdf averaged over the single particle contributions.

Equation (4.9) is further modified to adopt it to our experimental situation: The electron beam intensity I_0 and the number of atoms in the clusters are not known and therefore I_0N is replaced by a parameter α which has to be determined. Furthermore, $4\pi r^2\rho(r)$ is substituted by $P(r)$, giving:

$$I(s) = \alpha f^2(s)\left(1+\int_0^\infty P(r)\frac{\sin(2\pi sr)}{2\pi sr}dr\right) . \tag{4.10}$$

The inverse Fourier transform of (4.10) takes the form:

$$P(r) = 4\pi r\int_0^\infty 2sA(s)\sin(2\pi sr)ds , \tag{4.11a}$$

$$A(s) = \frac{I(s)}{\alpha f^2(s)} - 1 . \tag{4.11b}$$

The intensity $I(s)$ is only measured on a finite interval of $s : s \in [s_{min}, s_{max}]$ and therefore the Fourier transform results in $\hat{P}(r)$:

$$\hat{P}(r) = 4\pi r\int_{s_{min}}^{s_{max}} 2sA(s)\sin(2\pi sr)ds , \tag{4.12}$$

which can differ significantly from $P(r)$. $\hat{P}(r)$ and $P(r)$ are related to each other in the following way:

$$\frac{\hat{P}(r)}{r} = \int_0^\infty \frac{P(\bar{r})}{\bar{r}} 2\left[\frac{\sin\left(2\pi s(r-\bar{r})\right)}{2\pi(r-\bar{r})} - \frac{\sin\left(2\pi s(r+\bar{r})\right)}{2\pi(r+\bar{r})}\right]_{s_{min}}^{s_{max}} d\bar{r} . \tag{4.13}$$

The limited s-range causes a smoothing of $P(r)$. As a result, the peak positions in the rdf may be shifted due to the combination of peak broadening and the superposition of neighbouring peaks. In addition, $\hat{P}(r)$ is not anymore restricted to positive values.

Figure 4.3a shows the histogram of the interatomic distances for a spherical Bi cluster with 124 atoms and diameter of 20 Å. The diffraction pattern from this cluster has been inverted (Fig. 4.3b) using (4.12) with an s-range (0.25–1.2 $Å^{-1}$) typical for our measurements. Figure 4.3b displays the rdf of the noise-free diffraction pattern (dark line) and a grey band that shows the variation (two standard deviations from the noise free $\hat{P}(r)$) of the $\hat{P}(r)$ values calculated from 25 diffraction patterns with added Poisson noise[1]. Due to the limited s-range the peaks in the rdf are broadened and spurious oscillations are visible. In addition, the inversion result shows positive as well as negative values. It has been found useful to include a modification function $M(s)$ in (4.12) which reduces the effects of noise and dampens the oscillations introduced by the truncation of the diffraction pattern at s_{max}:

$$\hat{P}(r) = 4\pi r \int_{s_{min}}^{s_{max}} 2sA(s)M(s)\sin(2\pi sr)ds. \tag{4.14}$$

The most widely used modification function is $M(s) = \exp(-as^2)$ (pseudo-temperature function) [10]. It is a damping factor reducing the intensity of $I(s)$ at higher s-values thereby suppressing oscillations from noise and s-range truncation. Because of its similarities to the Debye–Waller factor it is often considered as a pseudo-temperature factor. The free parameter a is usually chosen so that the extension of the integral in (4.14) from s_{max} to ∞ becomes small [10]. The modification function specifically used for the size determination (see below) in [12] is $M(s) = \frac{sin(2\pi sb)}{(2\pi sb)}$ with $1/b = 2s_{max}$ (Lanczos function). The comparison of Figs. 4.3b–d shows that both modification functions reduce the oscillations visible in the direct inversion result. On the other hand, resolution is lost by the smoothing behaviour of the modification function as can be seen in Figs. 4.3b,c. In this comparison the loss in resolution is larger for the pseudo-temperature function (Figs. 4.3d,e: a=3 $Å^2$). With increasing s_{max} the resolution in the inversion result increases for the Lanczos results (compare Figs. 4.3d and 4.3f). The resolution remains nearly unchanged for the pseudo-temperature function (Figs. 4.3c,e) which is probably due to the strong damping at high s-values. Figures 4.3e,f also show that the Lanczos result is much more affected by noise if the s-range is increased.

[1]The noise-free diffraction pattern was scaled so that the highest peak was set to 4000 and 25 diffraction patterns were created using a Poisson random number generator [9], see also [12].

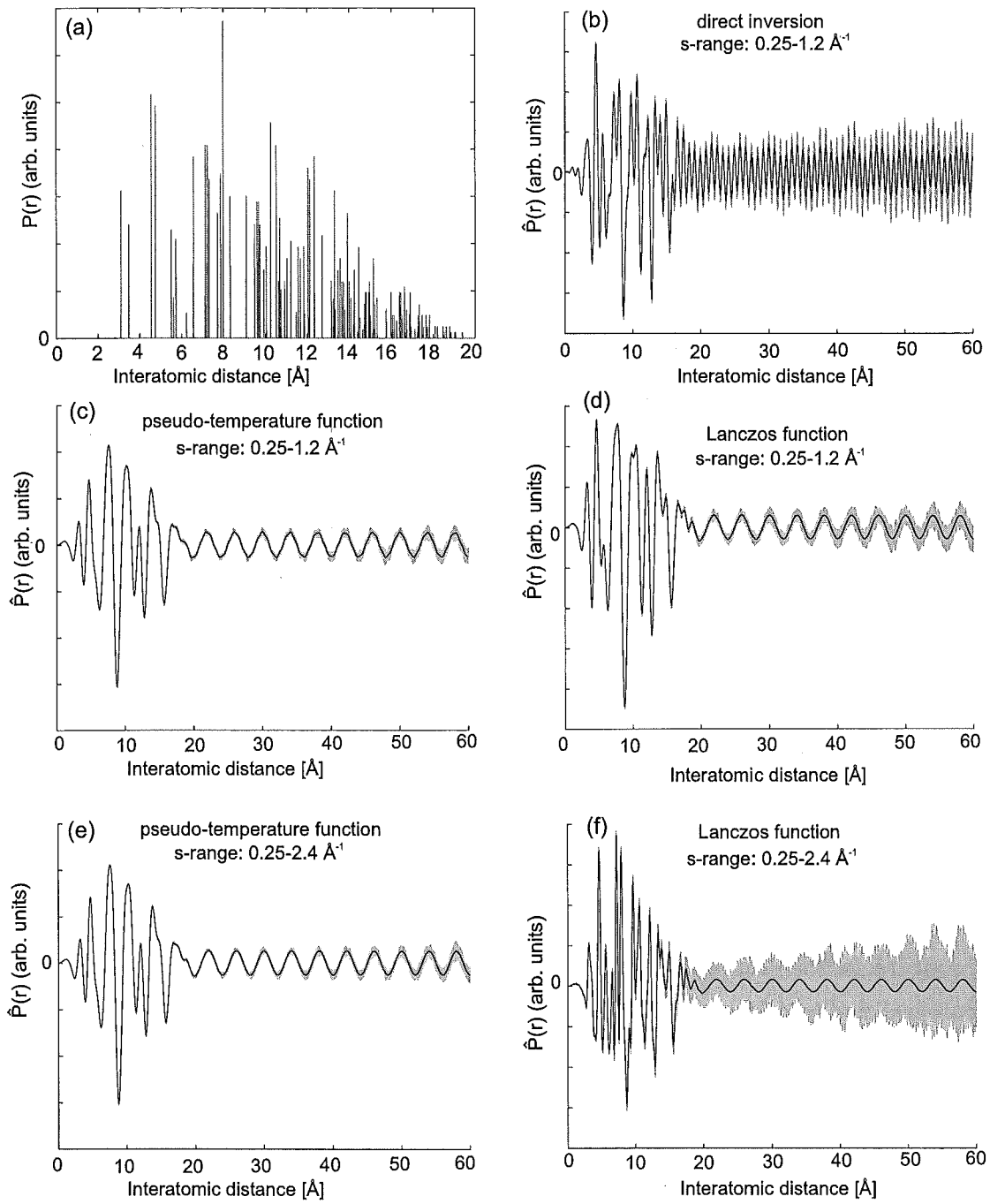

Figure 4.3: (a) Histogram of interatomic distances for a spherical bismuth cluster (124 atoms, diameter 20 Å). (b–f) Radial distribution function (rdf) for different inversion methods. Each figure consists of the rdf of the noise-free diffraction pattern (dark line) and a grey band that shows the variation (two standard deviations from the noise free $\hat{P}(r)$) of the $\hat{P}(r)$ values calculated from 25 diffraction patterns with added Poisson noise. The direct inversion result (a) shows oscillations which are introduced by the limited s-range of the diffraction pattern. The two modification functions (Lanczos, pseudo-temperature) reduce the effects of noise on the inversion results and dampen the oscillations. Figures (c–f) show the influence of the different modification functions and also of the s-range of the diffraction patterns.

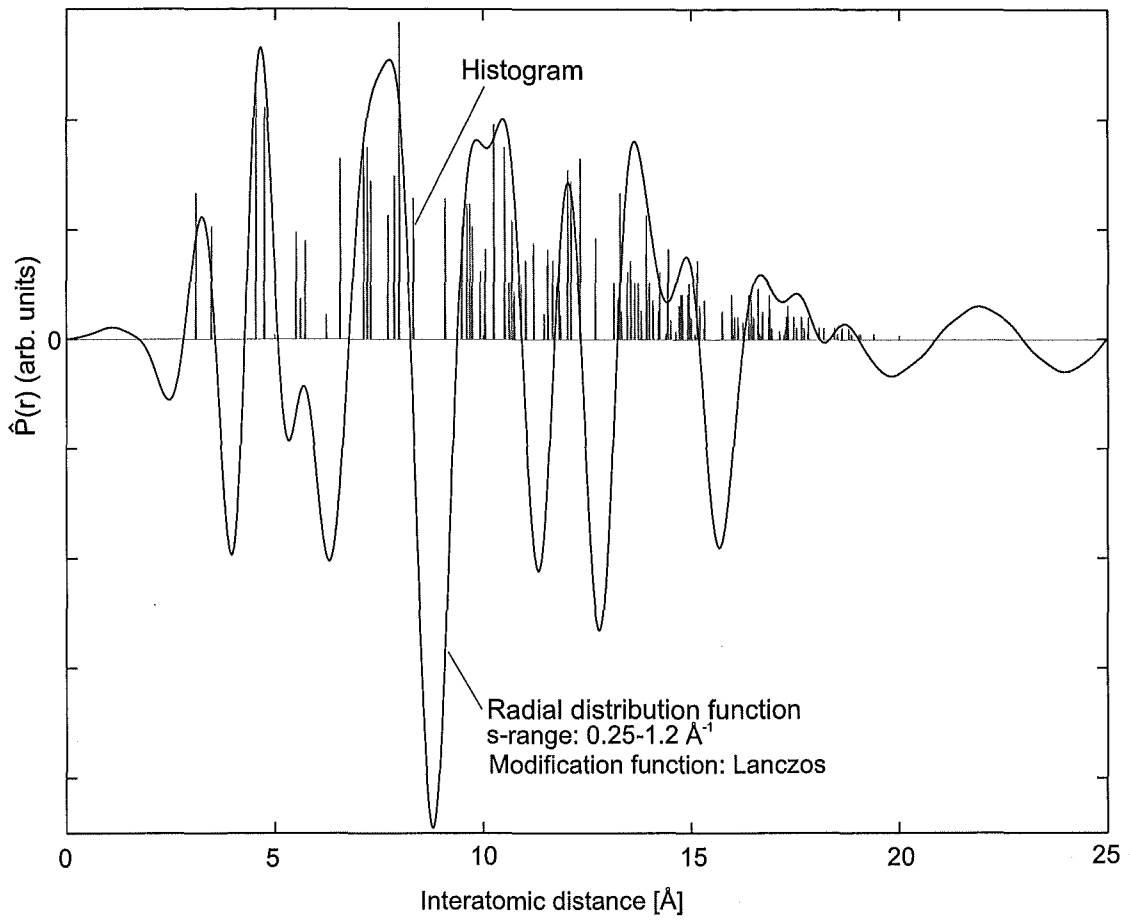

Figure 4.4: Radial distribution function (rdf) and histogram of interatomic distances from Fig. 4.3d,a. The peaks in the rdf are very broad due to the limited s-range of the diffraction pattern and it is not possible to resolve the first two peaks in the histogram.

Although $\hat{P}(r)$ differs significantly from $P(r)$ for small s-ranges (e.g. $s = 0.25$–2.4 Å^{-1}) it can be used to estimate the mean diameter of the nanoparticles [12]. The basic idea is that despite noise and the effects from the limited s-range the decrease in the amplitude of sharp features of $\hat{P}(r)$ can be related to the decrease in amplitude in $P(r)$, which therefore allows estimation of the particle size (see Fig. 4.3d). This method has been successfully applied to X-ray diffraction patterns of gold nanoparticles (diameters 2–5 nm) [12] and electron diffraction experiments on lead particles [13].

Inverted diffraction patterns can be used to determine the nearest-neighbour distance of the atoms in clusters if the first peak in $\hat{P}(r)$ can be clearly identified with the nearest-neighbour distance in the histogram of interatomic distances. This in turn depends on the particular diffraction pattern and the available s-range. In the example in Fig. 4.4 the rdf from Fig 4.3b is plotted together with the histogram of the interatomic distances of Fig. 4.3a. The first two smallest interatomic distances give rise to

one broad peak in $\hat{P}(r)$ and make it very difficult to determine the nearest-neighbour distance.

The remaining question concerning the inversion of diffraction patterns is how to determine the scaling factor α in $A(s)$ in (4.12). It has been shown in [14] that an error in the value of α becomes visible as sharp oscillations in the rdf at values of r close to zero. Therefore, an iterative procedure is used here to find the value of α that minimises these sharp oscillations.

4.2.4 Two New Analysis Tools

In order to see if it is possible to extract more information from the diffraction patterns two ideas have been investigated as part of this thesis and lead to new tools that complement the analysis of the diffraction patterns.

Constrained Inversion

The inversion problem as described by (4.10) has only a unique solution in the absence of noise and for a full range of s-values. When a diffraction pattern is measured only over a limited range of s-values an infinite number of solutions fulfil (4.10). This situation is illustrated by the example in Fig. 4.5. The diffraction pattern in Fig. 4.5a was used to calculated two rdfs (Figs. 4.5b,c) corresponding to a s-range of 0.25–1.2 Å^{-1} and 0.25–2.4 Å^{-1}, respectively. Although the rdfs are different they are both solutions to the inversion problem of diffraction pattern with the smaller s-range. Clearly, many other solutions exist. The details (information) in the rdfs are limited by the amount of information provided by the diffraction pattern. Consequently, the pattern with the larger range of s-values gives rise to a more detailed rdf.

This section describes a method that includes additional information to find a rdf which is closer to the rdfs produced by diffraction patterns with a larger s-range. To emphasise the difference between the solutions of the standard inversion methods and the constrained inversion, $\hat{P}(r)$ has been replaced with $\widetilde{P}(r)$. Equation (4.10) combined with (4.11b) then becomes:

$$2\pi s A(s) = \int_0^\infty \frac{\sin(2\pi s r)}{r} \widetilde{P}(r) dr \; . \tag{4.15}$$

Without making too many assumptions it is safe to state that the solution $\widetilde{P}(r)$ to the inversion problem (4.15) should be:

- positive for all r,

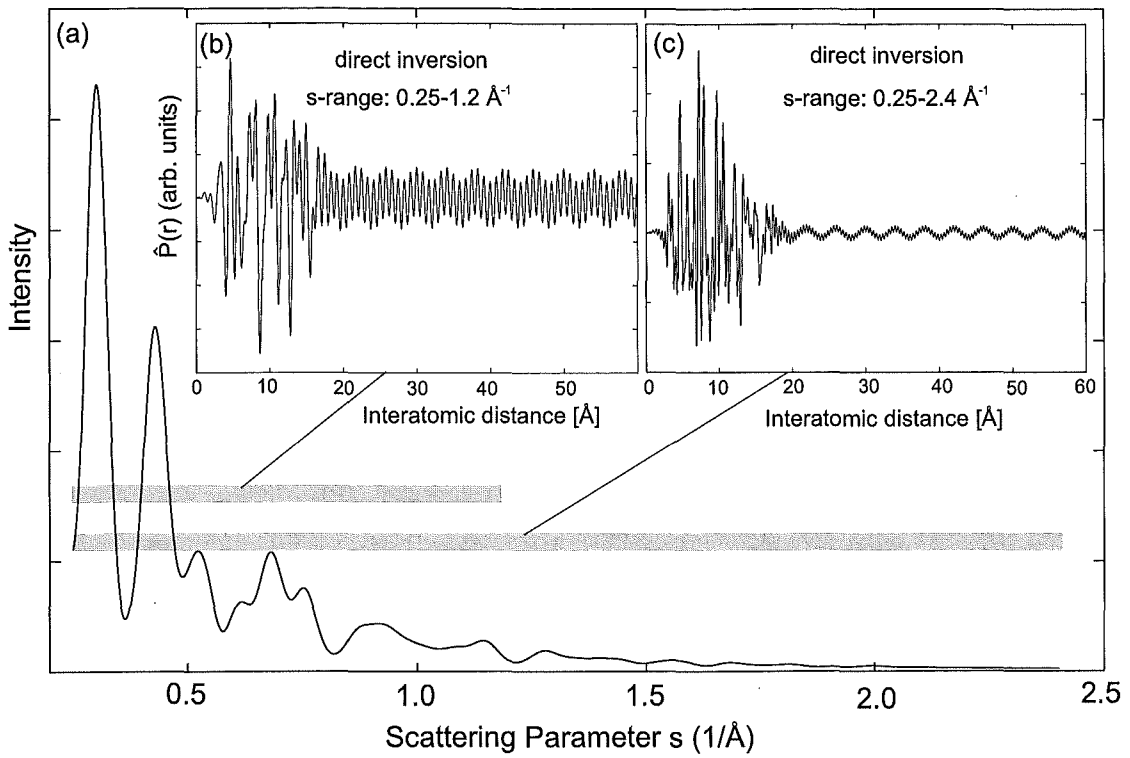

Figure 4.5: The inversion problem for a diffraction patterns measured over a finite s-range does not have a unique solution as shown by this example. The rdfs (b,c) were calculated for different s-ranges of the diffraction patterns shown in (a). Both rdfs are solutions to the inversion problem of the pattern with the smaller s-range. An infinite number of other solutions exist.

- zero for all r some distance below the first peak (nearest neighbour distance) in the rdf,
- zero for all r larger than the size of the largest cluster in the sample volume.

The inversion problem (4.15) involves an integral transform. In order to find a computational solution the problem has to be discretized, i.e. the calculation of $\widetilde{P}(r)$ must rely on the approximation of the integral by a sum. In this case the midpoint quadrature rule [15] has been used to transform (4.15) to a $m \times n$ linear matrix equation:

$$\vec{y} = \mathbf{K}\vec{x}\,, \tag{4.16a}$$

$$x_n = \widetilde{P}(r)\,, \tag{4.16b}$$

$$y_m = 2\pi s_m A(s_m)\,, \tag{4.16c}$$

$$K_{mn} = w_{mn}\sin(2\pi s_m r_n)/r_n\,, \tag{4.16d}$$

where w_{mn} are the quadrature coefficients. Assuming $n > m$ the problem is underdetermined.

Setting certain $\widetilde{P}(r)$ to zero can easily be achieved by not including the corresponding r-values in the equation. An algorithm that includes a positivity constraint and also finds a generalised solution is provided by the so-called projected Landweber method [16]. This is an iterative method for the approximation of positive least-squares solutions which can be used to solve (4.16a). Since the problem is underdetermined another criterion is necessary to select a single solution. A property of the projected Landweber method is that the solution that is obtained as the limit of the iteration depends on the initial guess. The solution with minimal Euclidean norm ($\|x\| = [\sum_{k=1}^{n} x_k]^{1/2}$) can be obtained using the smallest initial guess $x^{(0)} = 0$. The solution $\widetilde{P}(r)$ with minimal norm represents the smoothest of the possible least-squares solutions. The equation for the iteration is:

$$x^{(0)} = 0; \;\; x^{n+1} = P_+ \left[x^n + \kappa(\mathbf{K}^T \vec{y} - \mathbf{K}^T \mathbf{K} x^n) \right] \;, \tag{4.17}$$

were $\mathbf{K}^T$ is the transpose of the matrix $\mathbf{K}$. P_+ is the projection operator and is defined as follows:

$$(P_+ x_k) = x_k, \;\; if \; x_k > 0; \;\; (P_+ x_k) = 0, \; if \; x_k \leq 0. \tag{4.18}$$

The variable τ is the relaxation parameter, which can take any value satisfying the inequalities

$$0 < \tau < \frac{2}{\sigma^2} \;, \tag{4.19}$$

where σ is the largest singular value of $\mathbf{K}$. The results of the iteration x^n converge to the least-squares solution with minimal norm for $n \rightarrow \infty$. The relaxation parameter has a strong influence on the speed of the convergence. If τ is chosen too small the convergence can be very slow. In order to accelerate the convergence a relaxation parameter of $\tau \simeq 1.8\,\sigma^{-2}$ is recommended [16]. In the presence of noise the algorithm converges for ($n \rightarrow \infty$) to the mathematically correct solution which, however, can be strongly affected by noise propagation and numerical instabilities. An interesting feature of the algorithm is that the first iterations (noisy diffraction pattern) improve the approximation of the solution quite quickly and are only little affected by the noise. Therefore, after a certain number of iterations the result approaches the solution for the corresponding noise-free diffraction pattern. Further interactions improve the solution only slightly but lead to solutions that are more and more influenced by

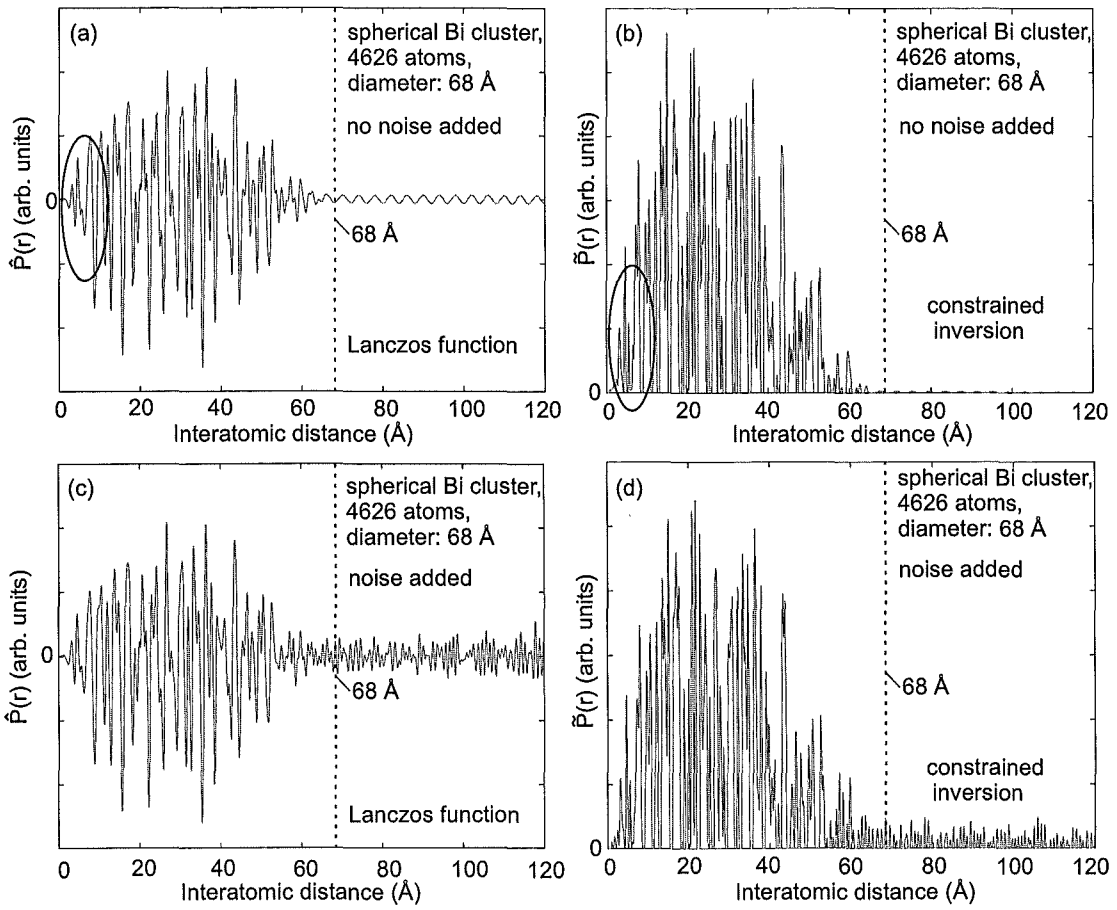

Figure 4.6: Results of the constrained inversion technique (b,d) in comparison to the standard inversion of diffraction patterns with the Lanczos modification function (a,c). For the constrained inversion only the non-negativity constraint was used. Profiles (a–d) show the results of inverting a calculated diffraction pattern from a spherical Bi cluster: (a,b) without noise, (c,d) with noise added.

the noise in the diffraction pattern. This suggests that there is an optimal number of iterations that provides a good approximation of the noise-free solution [17]. This inversion method based on the projected Landweber method has been implemented and is available as a Matlab package. Every 100 iterations the software provides plots of $\widetilde{P}(r)$ and the corresponding diffraction pattern $I_k(s)$ which then can be compared to the experimental pattern $I(s)$. The interaction is stopped when all diffraction features of $I(s)$ are visible in $I_k(s)$ and before the noise of the original pattern appears. The inversion of a typical diffraction pattern takes about 2 hours on a standard PC.

Figure 4.6 shows a comparison of the new constrained inversion technique with the standard inversion using the Lanczos modification function. The results in Figs. 4.6a–d are obtained by inverting a calculated diffraction pattern from a spherical Bi clusters consisting of 4626 atoms with a diameter of 68 Å. These inversion results show that

it is possible to estimate the cluster diameter with both techniques by determining the upper limit (interatomic distance) of the envelope of peaks. With this procedure estimates of between 62 and 70 Å are obtained for Figs. 4.6a–d. These figures also show that the size estimates are little affected by noise in the diffraction pattern. In addition, compared to the standard inversion techniques the constrained inversion provides rdfs with more details as can be seen in the marked areas in Figs. 4.6a,b. This can be attributed to the fact that the constrained inversion does not use a modification function with smoothing behaviour.

In Figs. 4.7e,f the inversion results of a measured diffraction pattern (shown in Fig. 5.6(4)) are displayed. The grey rectangular regions indicate conservative uncertainty intervals around diameter estimates. For this diffraction pattern the particle size has been estimated with 100 Å. A very interesting feature in the constrained inversion result are the low s peaks in the marked region which are not visible in the standard inversion results. Since the constrained inversion technique did not produce similar peaks for the Bi model structures (see Fig. 4.6) they are thought to be real features and not artifacts from the inversion algorithm. The presence of these low s peaks is very interesting since they are not expected for bulk Bi.

In summary, this technique can be used to estimate the size of the nanoparticles and offers an increased resolution of the inversion result compared to standard inversion techniques that use modification functions for noise suppression. The projected Landweber method used for this technique, on the other hand, reduces noise propagation by limiting the number of iterations. In addition, inversion results from measured diffraction patterns show details not found in the standard inversion results. The drawback of this technique is the longer computation time needed.

Shape Analysis for Clusters with a Known Structure

The diffraction patterns of a larger particle consist of a series of narrow peaks which can be used to determine the structure and the lattice parameter of the particle. Assuming that the cluster is single crystalline and knowing the structure and parameters the only remaining question is the question about the shape of the particle. If there is no prior information about the shape available, the fitting procedure is only of limited use as there are too many different shapes to consider. Therefore, it is desirable to find a technique that extracts additional information from the diffraction patterns, e.g. the number of facets, the lattice planes that make up the facets or in the best case the full shape of the particles.

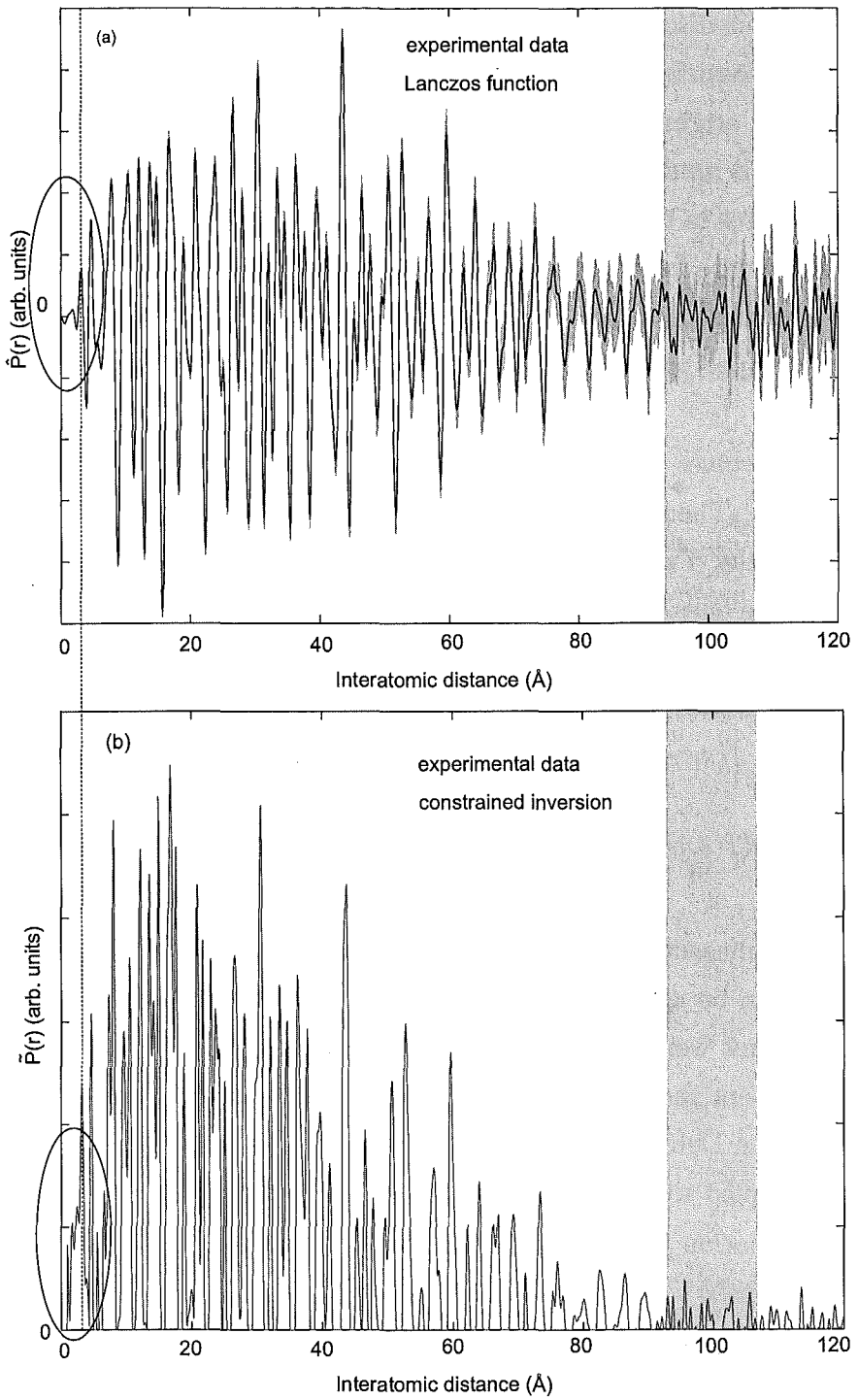

Figure 4.7: Inversion results of a measured diffraction pattern (shown in Fig. 5.6(4)). (a) Standard inversion with Lanczos modification function. The inversion result (black line) is shown together with a gray band representing the variation of the result (two standard deviations) when extra noise is added to the measured diffraction pattern (see Fig. 4.3). (b) Constrained inversion technique. Only the non-negativity constraint was used. (a,b) The estimate of the upper limit (interatomic distance) of the envelope of the peaks gives a cluster size of 100 Å±7 Å (gray rectangular regions). The rdf in (b) also shows extra peaks left of the dotted line which are not visible in (a).

The new technique discussed here was specifically developed to retrieve information about the shape of particles and is based on the so-called Reverse Monte Carlo (RMC) method [18]. In the original method, the difference between observed and calculated diffraction patterns is minimised as a function of the (variable) positions and occupancies of the atomic sites in the model crystal. In this implementation, it is assumed that the atomic positions are fixed within a large crystal lattice (known structure) and only the occupancies of these sites are subject to the minimisation procedure. The software that has been developed to solve this problem is based on the RMC algorithm described in [19] and [20].

The first step involves the setup of a large crystal lattice (larger than the expected cluster) in software. Then a list is generated which contains the coordinates of the calculated lattice sites. Two more lists are set up to keep track of the lattice sites that are occupied and the ones that are available for RMC operations. Starting with a small cluster of only a few atoms (occupied sites) the scattering intensity is calculated using the Debye Equation (4.3) assuming that it is valid for the clusters studied. Using the calculated intensity $I(s, \gamma, \alpha)$ a goodness-of-fit parameter χ^2 is computed:

$$\chi^2 = \sum_s w(s)(I(s, \gamma, \alpha) - I_e(s))^2 \,, \tag{4.20}$$

where $I_e(s)$ is the measured diffraction pattern and $w(s)$ is a weighting factor. The weighting factor can be used to emphasise specific features in the diffraction pattern. Otherwise, a constant weighting factor is used. In the next step the two parameters α and γ, which represent the scaling factor between the measured and calculated diffraction pattern and the Debye–Waller parameter in (4.3), are chosen to minimise χ^2 for a given list of occupied sites.

The RMC simulation then proceeds with a series of RMC processes which consists of the following steps:

- The model cluster is modified. There are three possible actions: addition/removal of an atom, one atom moves from a available site to another available site, or a series of consecutive moves of a selected atom. Only one action is performed per RMC process.

- Calculation of the histogram of interatomic distances for the new model cluster. The parameters α, γ are determined so that the goodness-of-fit parameter χ^2 is minimised.

- The change $\Delta\chi^2$ of χ^2 after the modification of the cluster is calculated. If the fit is improved $\Delta\chi^2 < 0$ the new cluster is accepted. Actions that worsen the agreement between observed and calculated intensities are accepted with a probability $P = \exp(-\Delta\chi^2/(2\sigma^2))$, with σ being a parameter to adjust the probability P.

The RMC process is repeated until χ^2 converges to its minimum or a specified maximum number of iterations is reached. The parameter σ controls the proportion of accepted modifications that worsen the fit. Usually χ^2 falls quickly after the start or when σ has been changed and then starts oscillating; at this point σ is further reduced.

It should be emphasised that in these simulations the positions of the lattice sites are fixed and that only their occupancies are varied. Furthermore, only lattice sites that are close to the surface of the model particle are available to the RMC process (list of available positions). The second constraint prohibits the development of vacant lattice sites within the cluster and the occupation of sites that are not attached to the particle. Another important point is that the RMC simulation creates a three dimensional model structure derived from one dimensional information (the diffraction pattern). The model structures are therefore not unique and other techniques may produce model structures that are just as valid as the results derived with the technique described above. The results are strongly tied to the assumptions made about the cluster and to the quality of the data.

During the implementation of this technique a series of tests was performed. In order to test the algorithm, RMC simulations were applied to noise-free diffraction patterns from model structures. In these cases the RMC results were identical to the original model structures. It could be observed that during the first ten thousand interactions (depending on the cluster size) the number of atoms in the model cluster increases quickly and approaches the number of atoms in the original cluster. At this stage of the simulation the cluster surface is not yet well defined. During the following iterations the number of atoms changes little and the cluster shape develops very slowly towards the original shape. In the case of the noise-free diffraction patterns the original model structures were obtained after $3 \cdot 10^5$ (or less) iterations.

The influence of noise in the diffraction patterns on the RMC results is shown in Figs. 4.8a,b. The two diffraction patterns in Figs. 4.8a,b are calculated from cluster (1) and differ only different within the noise. Although the noise affects the results shown in (2) and (3), valuable information about the cluster shape such as the number and type of facets can be obtained. The simulations also provide a good estimation of the number of atoms in the particle. In another example, diffraction patterns from three

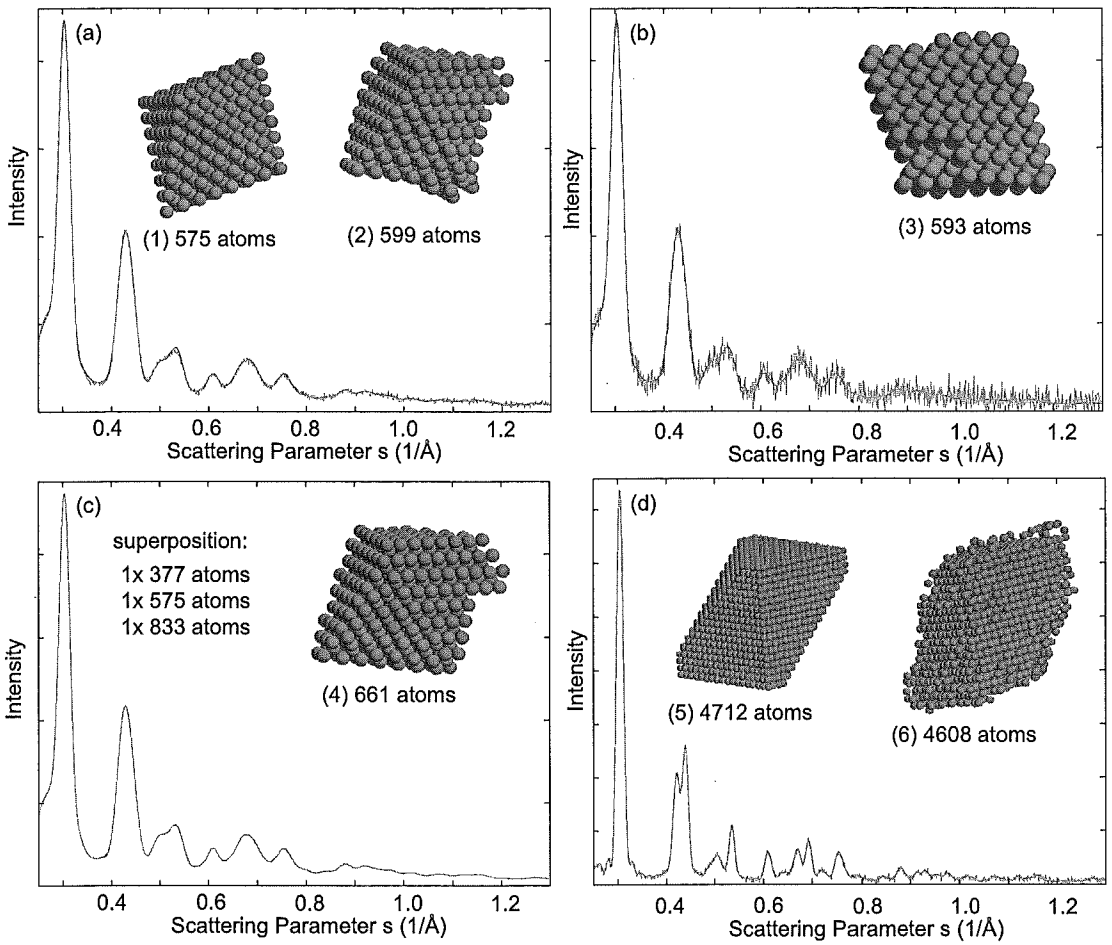

Figure 4.8: Results of RMC simulations applied to calculated diffraction patterns from model structures. The particles (2–4,6) in the insets are the RMC results from the corresponding diffraction patterns after $3 \cdot 10^5$ iterations. The plots (a–d) display the original diffraction patterns and the patterns calculated from the RMC results. (a,b) Diffraction patterns calculated from cluster (1) with different levels of noise. (c) Diffraction pattern from a superposition of three clusters with different sizes but the same shape as cluster (1). (d) Diffraction pattern from a large cluster (5) containing 4712 atoms and the corresponding RMC result (6).

model clusters with the same shape as (1) but different sizes (377, 575 and 833 atoms) were superimposed to study how much the RMC result is influenced by a distribution of cluster sizes. Again, the corresponding RMC result (Fig. 4.8c(4)) has a shape that is very similar to the shape of cluster (1) and can be used to extract the number, shape and type of the facets of the original clusters. The particle shown in Fig. 4.8d(5) is used to investigate the performance of the RMC technique when it is applied to diffraction patterns from larger clusters. Figure 4.8d displays the diffraction patterns from the cluster (5) with noise added and the pattern calculated from the corresponding RMC result (6). Note the good agreement between the two patterns. Although the result (6) shows some details about the cluster shape the facets are less resolved than the

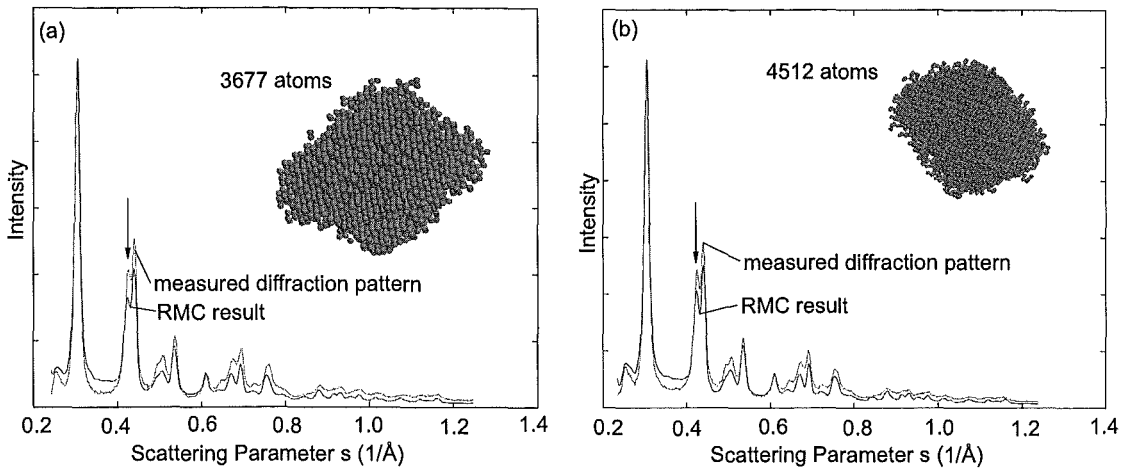

Figure 4.9: Examples of RMC simulations applied to two measured diffraction patterns. The insets show the clusters after $6 \cdot 10^5$ iterations. Only the main features in the diffraction patterns and not the full patterns could be reproduced. This is thought to be due to the deviation of the particle structure from the assumed Bi bulk structure as the peaks positions are slightly different. The difference in the peak positions is especially visible for the marked peaks. A detailed analysis is presented in section 5.7.5.

facets of the smaller clusters (2,3). This is probably due to the fact that a change of the position of an atom in a large cluster has only a very small effect on the diffraction pattern. If the diffraction pattern changes only slightly then the noise in the pattern makes it difficult to distinguish whether the shape of model cluster has improved or not. Therefore, RMC simulations applied to patterns from larger clusters require patterns with very little noise. Nevertheless, the number of facets, the approximate shape of the cluster and the type of the larger facets can be determined from cluster (6). In addition, the number of atoms in the clusters (6) is close to number of atoms of the original cluster (5).

Figure 4.9 shows two examples of RMC simulations applied to measured Bi diffraction patterns. The patterns calculated from the RMC model clusters reproduce the main features but do not completely agree with the measured diffraction patterns. The better agreement of the patterns obtained from RMC simulation applied to diffraction patterns from model structures (Fig. 4.8) suggests that the assumptions made for this technique are not valid for the measured diffraction patterns. A detailed analysis of the peak positions of the measured patterns has indeed revealed (see section 5.7.5) that the structure of the particle is different to the bulk structure of Bi which was assumed for these calculations. Therefore, RMC simulations can only be used to analyse the measured diffraction patters from Bi clusters when a more accurate description of the structure of the Bi particles is available.

This technique could easily be used for X-ray diffraction data, especially since there would not be any problems with dynamic diffraction effects. If diffraction patterns of mass-filtered clusters were available this method could be extended to retrieve the full structure (positions of the atoms) of the clusters.

4.3 Examples of Diffraction Patterns

The diffraction patterns displayed in this section are calculated patterns from Bi model clusters. The section starts with crystalline Bi clusters with the rhombohedral structure of the bulk material (see [21]). Several series of clusters of various shapes and sizes are shown. Then the effect of domains within the cluster on the diffraction pattern is examined. The section finishes with two series of diffraction patterns from liquid drops.

All patterns, except the ones from liquid drops, are calculated using the Debye Equation (4.3). The Debye–Waller factor (4.2) was calculated with a parameter γ^2 of 0.5 (i.e. $T = 260$ K).

In each series of diffraction patterns, the patterns are scaled so that the intensity of the highest peak is equal. The given values for the particle size refer to the largest distance between two atoms in a cluster (largest interatomic distance).

4.3.1 The Effect of Size and Shape

Large Bi clusters are expected to have the structure and lattice parameters of the bulk material. Having a fixed crystal lattice the diffraction patterns only depend on the size and the shape of the particles. Since it is relevant for the analysis of the experimental diffraction patterns (described in chapter 5), patterns from model clusters of various sizes and shapes have been calculated. The particle shapes are defined by up to five sets of surface planes ($\{111\}, \{011\}, \{100\}, \{112\}, \{1\bar{1}0\}$). Each set of planes is associated with a parameter specifying the distance of the planes to the centre of the particle. Therefore, the surface types and the their relative distances characterise the particle shape.

The presentation of the diffraction patterns starts with a pattern from a large spherical Bi cluster (Fig. 4.10) with Miller indices of the corresponding rhombohedral lattice assigned to the pattern. Figures 4.11 to 4.21 show the evolution of diffraction patterns of model clusters with different shapes as a function of cluster size and can be categorised into the following groups:

- Spherical clusters
  Figure 4.11 shows a series of spherical clusters with sizes ranging from 822 to 7562 atoms. The clusters were created by cutting a spherical section out of a large rhombohedral lattice.

- Clusters faceted by a single set of planes
  The shape of a cluster is dominated by only one set of crystallographic planes

if the surface energy of this set of planes is much lower than the energies of the other surfaces (Wulff's criterion [22]). Figures 4.12–4.14 display series of clusters faceted by either six {011}, six {100} or six {112} planes.

- Clusters faceted by six {112} and six $\{1\bar{1}0\}$ surfaces
  These two sets of planes are of particular interest since the ratio of their distances to the centre of the particles *directly* controls the intensity ratio of the corresponding peaks in the diffraction pattern. This intensity ratio is used in the analysis of the experimental diffraction patterns. Figs. 4.15 and 4.16 show two size series with different ratios.

- Clusters with hexagonal facets
  Bismuth clusters with a hexagonal shape have been observed in TEM investigations of supported clusters [23, 24]. A hexagonal shape can be achieved with six $\{1\bar{1}0\}$ and two {111} surfaces. The facets with a hexagonal shape are the {111} facets which are orthogonal to the $\{1\bar{1}0\}$ planes. From Figs. 4.17 to 4.19 the ratio $d_{111}/d_{1\bar{1}0}$ of the distances of the surfaces to the centre of the particle is increased from 0.5 via 0.65 to 1.0. A larger ratio leads to a more column-like shape.

- Clusters described in [25]
  The series in Figs. 4.20 and 4.21 are calculated from two different cluster models that were suggested in [25]. The first type of particles (Fig. 4.20) is faceted by two {111}, six {011}, six {100}, six {112} and six $\{1\bar{1}0\}$ surfaces. The relative distances of the surfaces to the centre of the particle were chosen according to Wulff's criterion [22] to agree with the order of surface energies suggested in [25]. The second type of clusters described in [25] has a complicated structure with lattice defects and is faceted by {110} and {111} surfaces. The particles that were used here to generate the size series in Fig. 4.21 have the same surfaces but are based on a defect free rhombohedral lattice with the parameters of the Bi bulk material.

In general, as the cluster size increases the diffraction intensity is more concentrated at the specific peak positions, the diffuse background reduces and the peak width decreases. With increasing size more features appear in the diffraction patterns. For a given size (number of atoms) the shape of a cluster influences the relative peak heights and the width of individual peaks in the diffraction pattern.

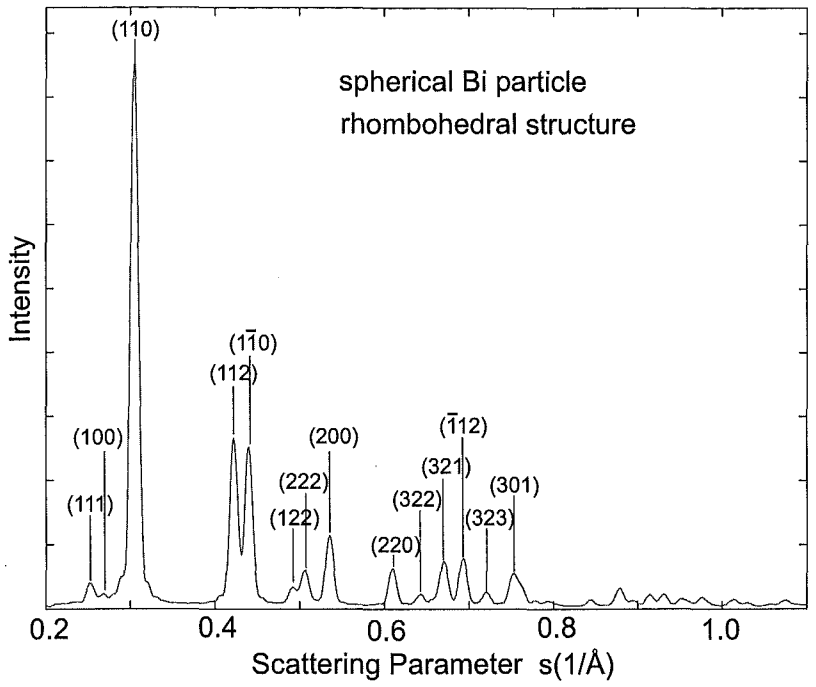

Figure 4.10: A calculated diffraction pattern from a spherical Bi cluster (Bi bulk structure) with a diameter of 100 Å (14710 atoms). The Miller indices corresponding to the rhombohedral cell are assigned to the larger peaks.

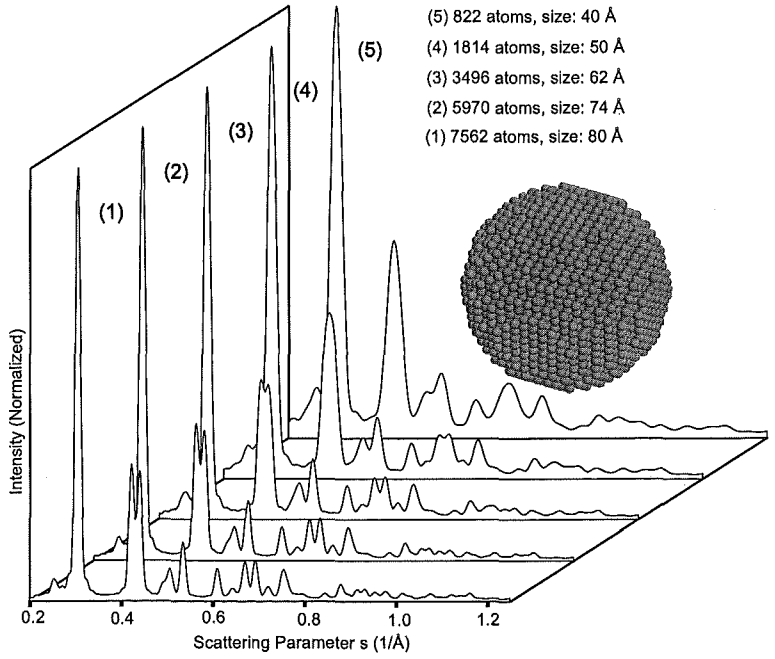

Figure 4.11: Calculated diffraction patterns from a series of spherical model clusters. The clusters are single crystalline and have the Bi bulk structure.

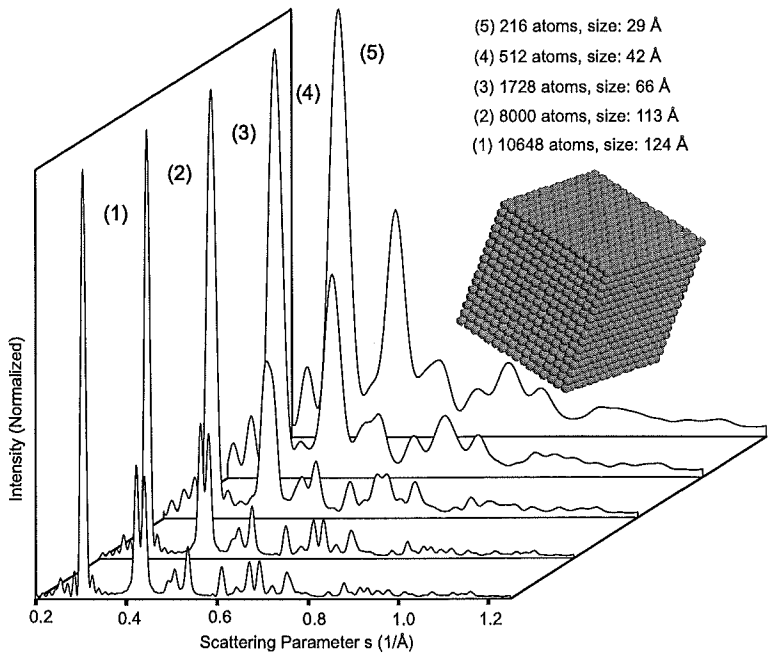

Figure 4.12: Calculated diffraction patterns from a series of model clusters. The clusters are single crystalline (Bi bulk structure) and are faceted by six {011} planes.

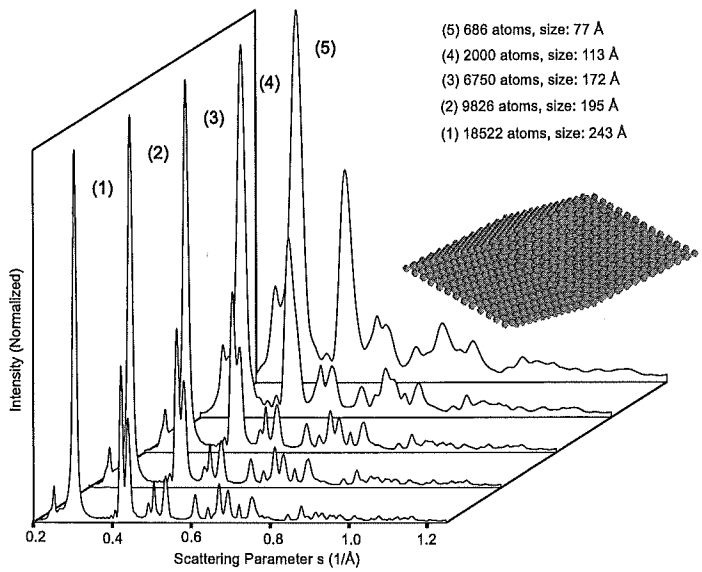

Figure 4.13: Calculated diffraction patterns from a series of model clusters. The clusters are single crystalline (Bi bulk structure) and are faceted by six {100} planes.

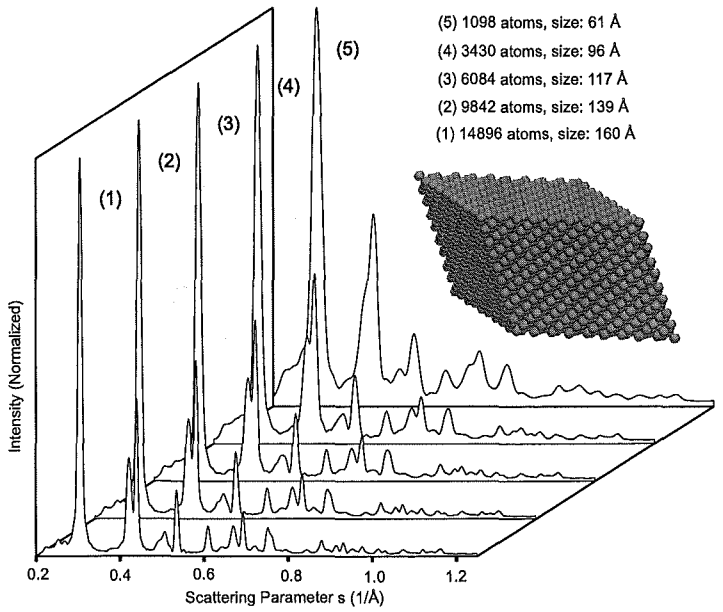

Figure 4.14: Calculated diffraction patterns from a series of model clusters. The clusters are single crystalline (Bi bulk structure) and are faceted by six {112} planes.

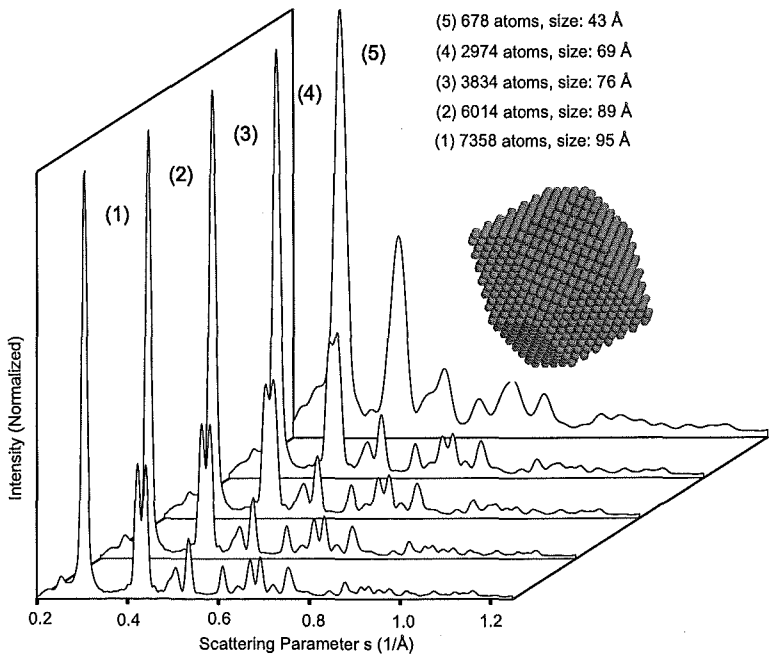

Figure 4.15: Calculated diffraction patterns from a series of model clusters. The clusters are single crystalline (Bi bulk structure) and are faceted by six {112} and six $\{1\bar{1}0\}$ planes. The relative distances of the surfaces to the centre of the particle are 1.0 and 1.2 in the order of the sets of planes given above.

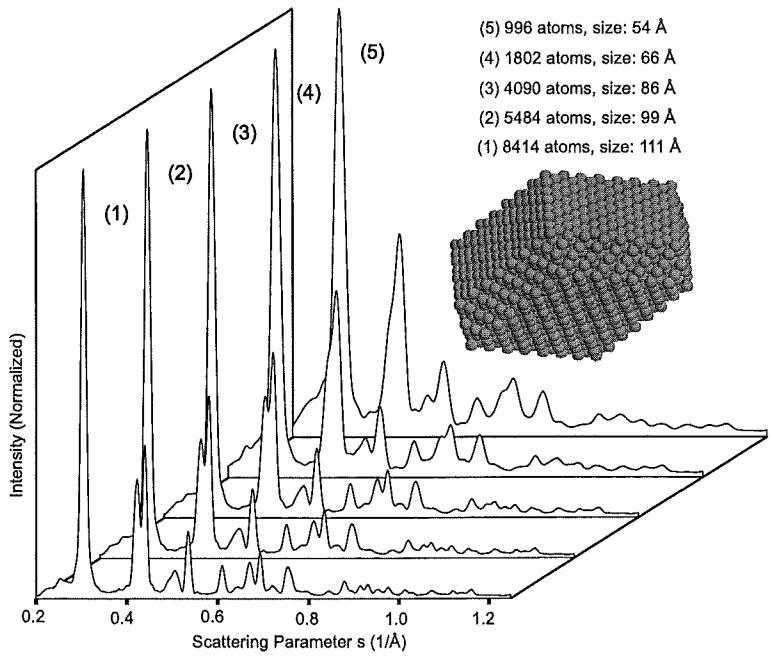

Figure 4.16: Calculated diffraction patterns from a series of model clusters. The clusters are single crystalline (Bi bulk structure) and are faceted by six $\{112\}$ and six $\{1\bar{1}0\}$ planes. The relative distances of the surfaces to the centre of the particle are 1.0 and 1.5 in the order of the sets of planes given above.

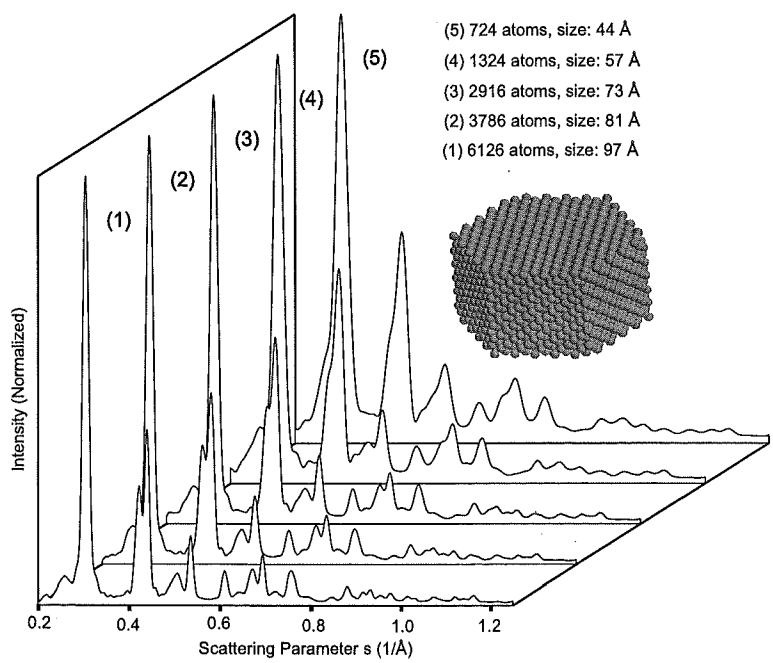

Figure 4.17: Calculated diffraction patterns from a series of model clusters. The clusters are single crystalline (Bi bulk structure) and are faceted by six $\{1\bar{1}0\}$ and two $\{111\}$ planes. The relative distances of the surfaces to the centre of the particle are 1.0 and 0.5 in the order of the sets of planes given above.

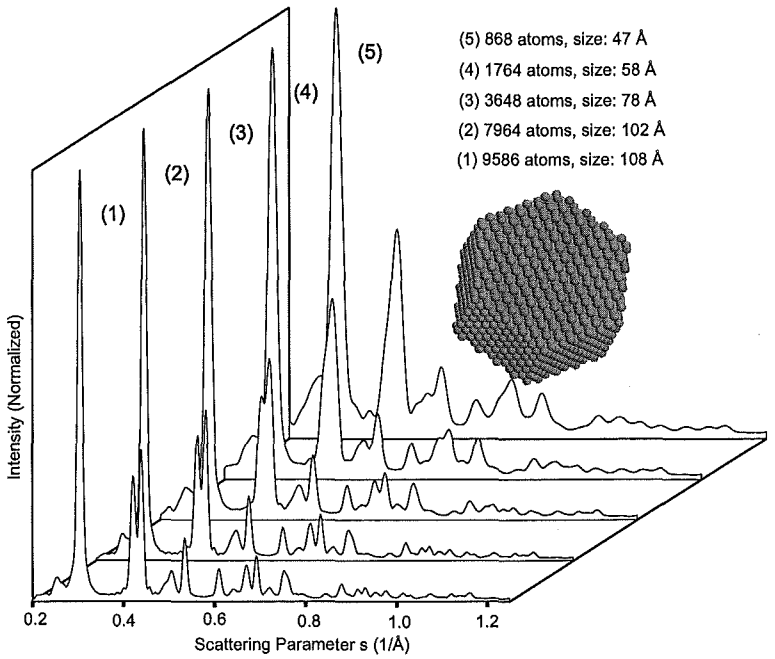

Figure 4.18: Calculated diffraction patterns from a series of model clusters. The clusters are single crystalline (Bi bulk structure) and are faceted by six $\{1\bar{1}0\}$ and two $\{111\}$ planes. The relative distances of the surfaces to the centre of the particle are 1.0 and 0.65 in the order of the sets of planes given above.

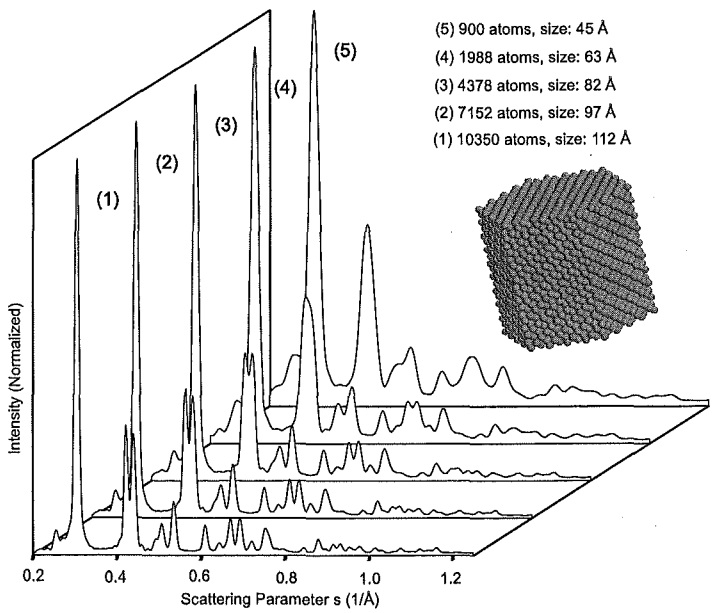

Figure 4.19: Calculated diffraction patterns from a series of model clusters. The clusters are single crystalline (Bi bulk structure) and are faceted by six $\{1\bar{1}0\}$ and two $\{111\}$ planes. The relative distances of the surfaces to the centre of the particle are 1.0 and 1.0 in the order of the sets of planes given above.

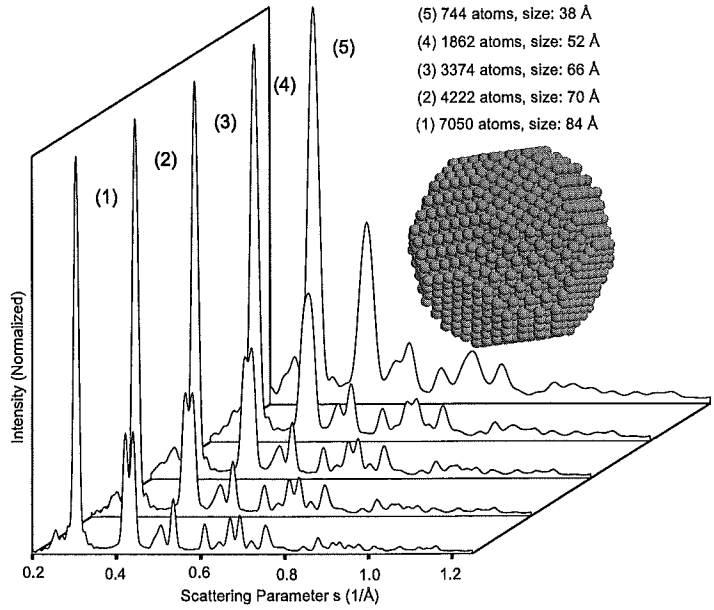

Figure 4.20: Calculated diffraction patterns from a size series of model clusters described in [25]. The clusters are single crystalline (Bi bulk structure) and are faceted by two {111}, six {011}, six {100}, six {112} and six $\{1\bar{1}0\}$ surfaces. The relative distances of the surfaces to the centre of the particle are 0.85, 0.9, 0.95, 1.0, 1.05 in the order of the sets of planes given above. The values of the parameters were chosen according to Wulff's criterion [22] to agree with the order of surface energies suggested in [25].

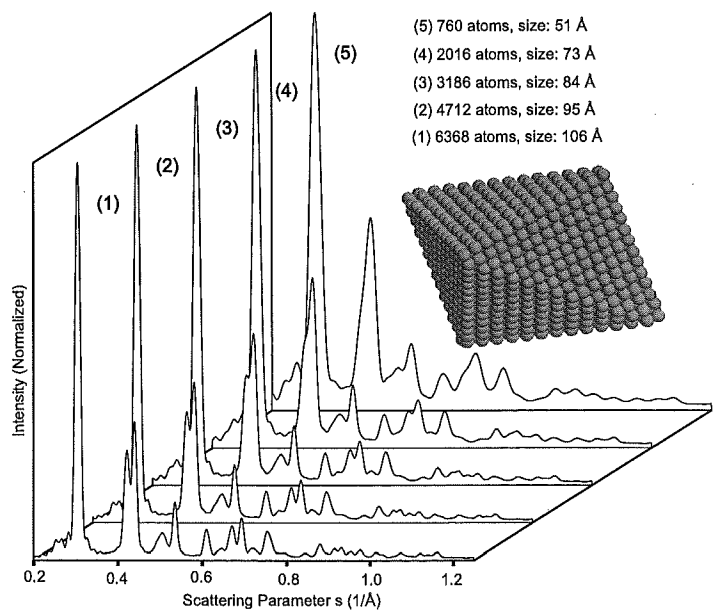

Figure 4.21: Calculated diffraction patterns from a series of model clusters. The clusters are single crystalline (Bi bulk structure) and are faceted by six {110} and two {111} planes. The relative distances of the surfaces the centre of the particle are 1.0 and 0.75 in the order of the sets of planes given above.

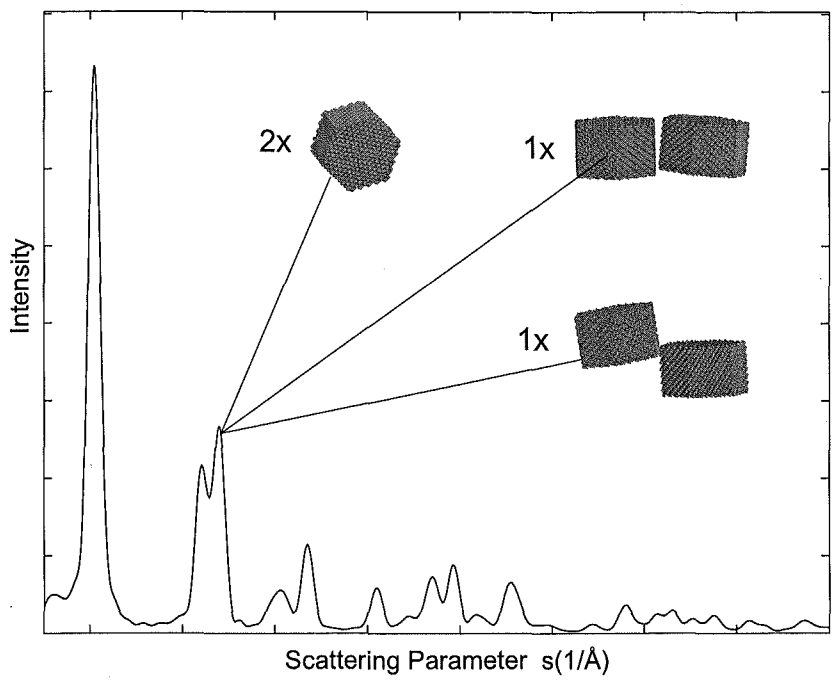

Figure 4.22: The diffraction patterns from three configurations of clusters to show the effect of domains. The differences are very small so that the three patterns appear as one diffraction pattern. The diffraction patterns were calculated from identical clusters in the configurations shown in the insets. In the case of the single cluster the intensity was scaled by a factor of two.

4.3.2 The Effect of Domains

The diffraction patterns in the previous section show size and shape related features that may allow extraction of the corresponding information from the measured diffraction patterns. This, however, assumes that the particles are single crystalline. If a cluster contains multiple domains due to the presence of lattice defects (e.g. dislocations, stacking faults) then the structure of the domains will dominate the diffraction pattern [8]. In this case, the size estimate from the diffraction pattern refers to the domain size. It also means that surface features of the particle cannot be estimated.

In order to show this effect, the diffraction pattern from two identical neighbouring but differently oriented Bi clusters has been compared to the diffraction pattern of one of the two clusters. In Fig. 4.22 the diffraction patterns from the three shown configurations are presented. The differences between the diffraction patterns are very small which means that the inter cluster interference is negligible. Consequently, diffraction patterns are sensitive to the domains within the cluster rather than to the entire particle.

4.3.3 Liquid Clusters

Since results from MD simulations for liquid Bi clusters were not available, diffraction patterns for liquid clusters could not be calculated from model structures. Instead, the diffraction data available for liquid Bi [26–28], obtained by neutron, electron and X-ray diffraction methods, have been used to estimate diffraction patterns for small liquid drops.

The structure factor for liquid Bi can be directly determined from diffraction measurements and is equivalent to the interference function $I(s)/(\alpha f^2(s))$, using the definitions from (4.3). In order to calculate diffraction patterns of nanometre sized drops using the structure factor of liquid Bi, the effect of the finite volume has to be dealt with. Note that only diffraction effects are considered and effects due to structural changes in the small particles are not taken into account. The scattering from a finite volume is obtained by convolving the structure factor with the Fourier-transform squared of the function delimiting the diffraction volume, $|Y(s)|^2$ [2, 29]:

$$I(s)_{drop} = \int_0^\infty I_{Bi}(t)|Y(s-t)|^2 dt \; . \tag{4.21}$$

For a spherical particle with a radius R:

$$Y(s) = \frac{4}{3}\pi R^3 \frac{3\,(sin(u) - u \cdot cos(u))}{u^3} \; , \tag{4.22}$$

with $u = 2\pi sR$ (see [2]). The structure factors used to calculate the diffraction patterns in Figs. 4.23 and 4.24 are available as an analytic expression for various temperatures of liquid Bi [30, 31]. These were obtained by fitting the structure factor based on the hard sphere cluster model to experimental data. The use of the analytic expression is justified by the good agreement with the experimental data [30, 31].

The influence of droplet size on the diffraction patterns is shown in Fig. 4.23. The patterns consist of a small number of very broad diffraction peaks. A characteristic feature of Bi is the shoulder peak at the high s side of the first peak. As the size of the particles decreases the width of the peaks and the background slope increases while the shoulder peak loses intensity. Figure 4.24 shows the evolution of the diffraction patterns as the temperature increases from 300°C, slightly above the bulk melting point (271°C), to 950°C. These patterns are based on measured structure factors available for different temperatures from [30, 31]. With increasing temperature the shoulder peak becomes smaller and is not visible in the two high temperature patterns. The increase

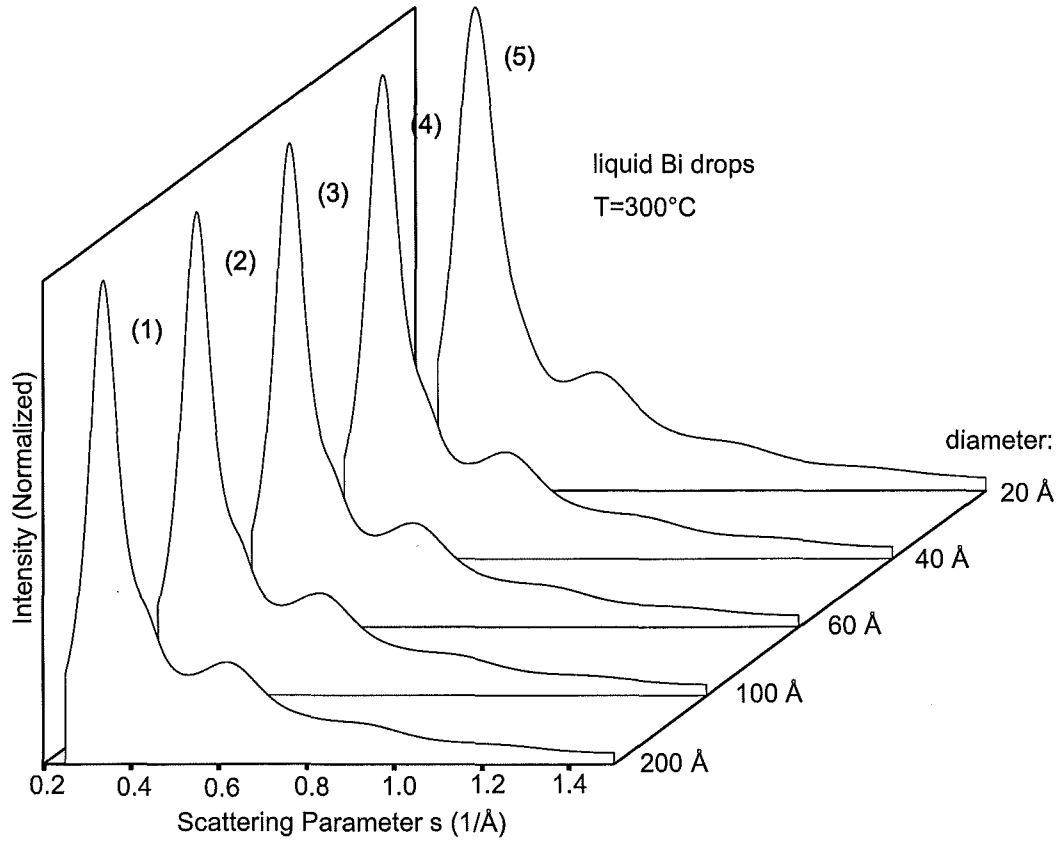

Figure 4.23: Diffraction patterns from liquid drops of Bi of various sizes and a temperature of 300°C. The patterns are calculated from structure factor data of liquid Bi [30, 31].

in temperature is also connected to an increase in background and a shift of the first peak from 0.337 $Å^{-1}$ (at 300°C) to 0.332 $Å^{-1}$ (at 950°C). The shift of the peak may be attributed to the thermal expansion with increasing temperature.

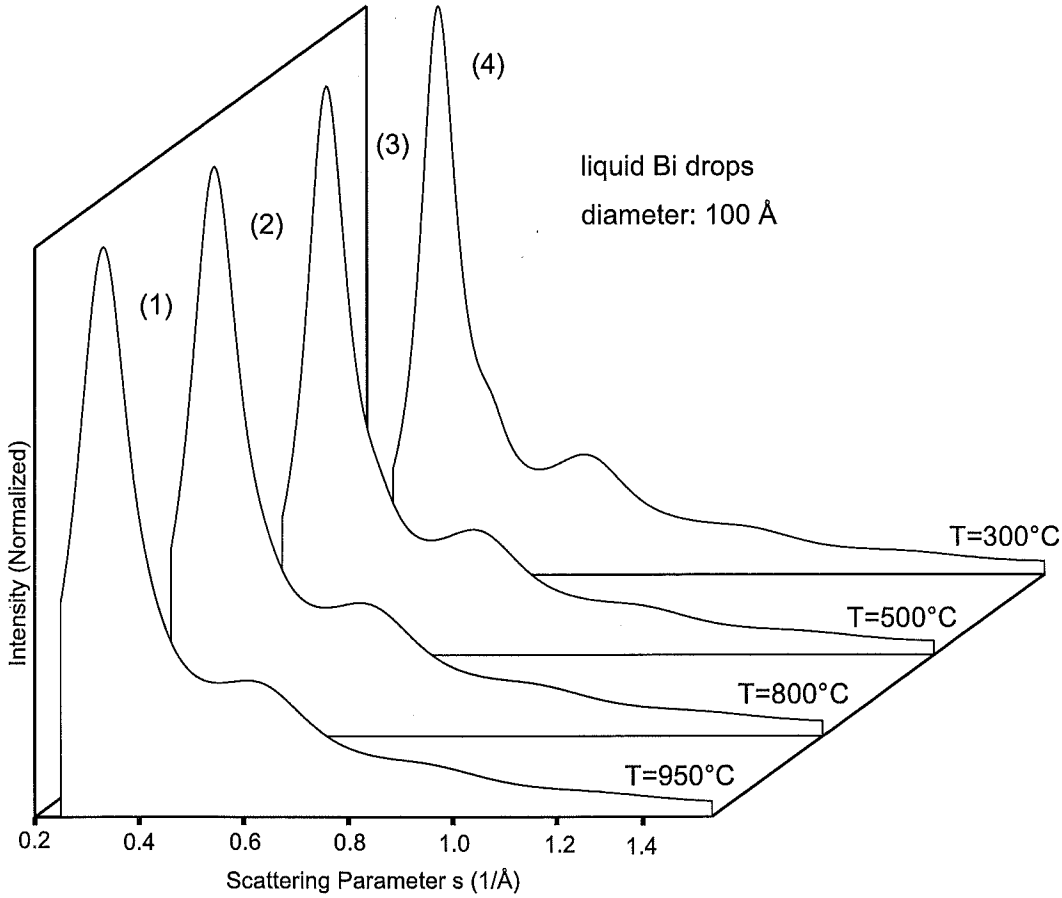

Figure 4.24: Diffraction patterns from liquid drops of Bi with a diameter of 100Å as a function of the temperature of the drop. The patterns are calculated from structure factor data of liquid Bi [30, 31].

References

[1] B. D. Hall, U. Ugarte, D. Reinhard, and R. Monot, J. Chem. Phys. **103**, 2384 (1995).

[2] A. Guinier, *X-Ray Diffraction in Crystals, Imperfect Crystals, and Amorphous Bodies*, W. H. Freeman and Company, 1963.

[3] D. Rez, P. Rez, and I. Grant, Acta Cryst. **A50**, 481 (1994).

[4] B. R. Miller and L. S. Bartell, J. Chem. Phys. **72**, 800 (1980).

[5] L. S. Bartell, B. Raoult, and G. Torchet, J. Chem. Phys. **66**, 5387 (1977).

[6] J. M. Cowley, *Diffraction Physics*, North Holland Physics Publishing, 1984.

[7] B. D. Hall, M. Flüeli, R. Monot, and J.-P. Borel, Phys. Rev. B **43**, 3906 (1991).

[8] B. D. Hall, J. Appl. Phys. **87**, 1666 (2000).

[9] W. H. Press, S. A. Teukolsky, B. P. Flannert, and W. T. Vetterling, editors, *Numerical Recipes in C++: The Art of Scientific Computing*, Cambridge University Press, 1993.

[10] B. E. Warren, *X-ray Diffraction*, Addison Wesley, 1969.

[11] Z. Kaszkur, Appl. Cryst. **33**, 87 (2000).

[12] B. D. Hall, D. Zanchet, and D. Ugarte, J. Appl. Crys. **33**, 1335 (2000).

[13] M. Hyslop, *Electron Diffraction Studies of Unsupported Clusters*, PhD thesis, University of Canterbury, 2002.

[14] R. Kaplow, S. L. Strong, and B. L. Averbach, Phys. Rev. **138**, 1336 (1965).

[15] S. Twomey, *Introduction to the Mathematics of Inversion in Remote Sensing and Indirect Measurements*, Dover Publications, Inc., 1996.

[16] M. Bertero and P. Boccacci, *Introduction to Inverse Problems in Imaging*, Institute of Physics Publishing, 1998.

[17] M. Bertero, P. Boccacci, and M. Robberto, An inversion method for the restoration of chopped and nodded images, in *Infrared Astronomical Instrumentation*, edited by A. M. Fowler, Proc. SPIE, pages 877–886, 1998.

[18] R. L. McGreevy and L. Pusztai, Mol. Sim. **1**, 359 (1988).

[19] V. M. Nield, D. A. Keen, W. Hayes, and R. L. McGreevy, J. Phys. Condens. Matter **4**, 6703 (1992).

[20] T. Proffen and T. R. Welberry, Acta. Cryst. **A53**, 202 (1997).

[21] R. W. G. Wyckoff, *Crystal Structures*, volume 1, John Wiley & Sons, 1963.

[22] G. Wulff, Z. Kristallog. **34**, 449 (1901).

[23] J. Fang, K. L. Stokes, W. L. Zhou, C. B. Murray, and C. J. O. Connor, Mat. Res. Soc. Symp. Proc. **676**, Y8.9.1 (2001).

[24] J. Fang, K. L. Stokes, W. L. Zhou, W. Wang, and J. Lin, Chem. Commun. **18**, 1872 (2001).

[25] Y. Oshima, K. Takayanagi, and H. Hirayama, Z. Phys. D **40**, 534 (1997).

[26] P. C. Sarrah and G. P. Smith, J. Chem. Phys. **21**, 228 (1953).

[27] P. C. Sarrah and R. F. Kruh, J. Chem. Phys. **32**, 241 (1960).

[28] Y. Waseda, *The Structure of Non-crystallic Materials, Liquids and Amorphous Solids*, McGraw-Hill Publ. Co., New York, 1980.

[29] B. D. Hall, *An Installation for the Study of Unsupported Ultrafine Particles by Electron Diffraction with Application to Silver: Observation of Multiply Twinned Particle Structures*, PhD thesis, EPFL, 1991.

[30] X.-W. Zou, Z.-Z. Jin, and Y.-J. Shang, phys. stat. sol. (b) **139**, 365 (1984).

[31] X.-W. Zou, Z.-Z. Jin, and S.-Q. Tang, phys. stat. sol. (b) **142**, 9 (1984).

Chapter 5

A Study of Unsupported Bismuth Clusters

This chapter describes diffraction experiments performed on Bi clusters. The first sections review prior research related to the structure of Bi clusters. Since clusters represent the link between atoms and molecules on one side and the bulk material on the other it is helpful to review first what is known about the bulk material and what can be observed in mass spectra of very small clusters. Important for this study is also the melting of thin Bi films and small clusters. Diffraction techniques offer the best possibilities for the study of the structure of clusters. Previous research includes HRTEM investigations of supported clusters and pioneering diffraction experiments on free Bi clusters by the group of Yokozeki and Stein in 1977 [1]. A very useful tool to theoretically predict the structure of small particles are molecular dynamics (MD) simulations. Because of the lack of well tested potentials for rhombohedral Bi, results from MD simulations are only available for a high pressure phase of Bi.

The measured diffraction patterns are presented in three groups according to the type of carrier gas used. In most cases a sequence of diffraction patterns was obtained by varying only one source parameter. This chapter closes with the discussion of the results.

5.1 Bulk Properties of Bi

The semi-metal bismuth crystallises at room temperature and atmospheric pressure in a rhombohedral lattice with a basis of two atoms. The rhombohedral cell has the dimensions: a_0=4.7459 Å and $\alpha = 57.237°$ (see [2] for a detailed description). The volume of the lattice cell is relatively large leading to the interesting effect that liquid Bi is more dense than the crystalline phase. Bi has a complex phase diagram with as many as 10 different crystallographic phases as can be seen in Fig. 5.1. Compression at room temperature changes the structure from rhombohedral (I) to the phases (II) to (VI) depending on the pressure. The high pressure phase (VI) is BCC [3].

In contrast to most other metals (e.g. Cu, Al, Pb, Tl, Hg, Zn, Sn, etc.), bismuth

THE LIBRARY
UNIVERSITY OF CANTERBURY
CHRISTCHURCH, N.Z.

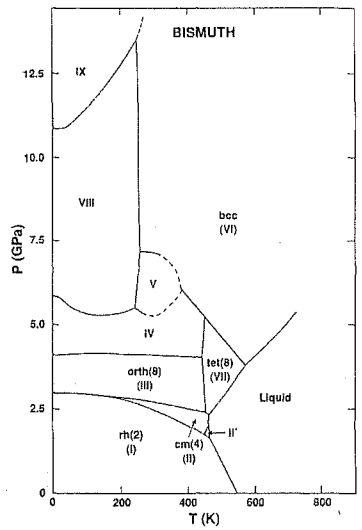

Figure 5.1: The phase diagram of bismuth after [3]. Under standard conditions Bi has a rhombohedral structure. The high pressure phase (VI) is BCC.

forms amorphous films when deposited on cold substrates ($T = 2$ K). These films are stable up to about 15 K and change into the rhombohedral structure at higher temperatures [4]. This behaviour of Bi (and also Ga) can be attributed to the fact that the rhombohedral structure strongly differs from a close-packed structure. Atoms deposited on a cold surface are more or less arranged in a close-packed configuration but are unable to form the Bi bulk lattice because of the large displacements required.

It should also be mentioned that there is only one stable isotope of bismuth: ^{209}Bi.

5.2 Mass Spectra of Bi Clusters

Mass spectra provide valuable insights into the early stages of cluster growth. The composition of Bi vapour created by free evaporation of molecules from the condensed phase (liquid) into vacuum has been measured by Mühlbach *et al.* [5]. In these mass spectra Bi_1 and Bi_2 are prevalent. There are also small abundances of Bi_3 and Bi_4 but they are only detected with about 1% of the monomer intensity. Almost identical results were obtained by laser vaporisation by Geusic *et al.* [6]. The formation of molecules in the vapour is thought to be due to covalent bonding. Within the group V elements[1] the metallic bonding gets stronger from phosphorus to bismuth at the cost of the degree of covalent bonding. This also nicely illustrates why the composition of antimony vapour compared to Bi vapour is centred at larger molecules – it mostly contains Sb_4 molecules

[1]Group V elements: N, P, As, Sb, Bi.

due to the higher degree of coordination in the bonding. When Bi vapour is condensed in cooled inert gas, larger clusters are formed. The size distribution of these clusters is strongly influenced by the temperature and type of inert gas. It has been shown [7, 8] that it is possible to obtain mass spectra for small Bi clusters (Bi_n, $n < 270$) with He as the carrier gas (p $\sim$ 10 Torr) when the gas is cooled down to liquid nitrogen temperature. In this case, the size distribution shows the highest abundance for Bi_5 and Bi_7 with a long flat tail stretching up to approx. Bi_{270}. The fact that Bi_5 and Bi_7 appear with even higher intensities than in the parent distribution (without inert gas) suggests that coalescence of molecules or clusters plays an important role in the growth of clusters [8]. The size distribution, however, is completely different when the temperature of the He gas (p = 5–40 mbar) is much higher (T = 310 K) [9, 10]. Then it more resembles the mass spectra of the free evaporation except that the abundance for Bi_3 and Bi_4 is strongly increased. In this case the largest detectable molecule is Bi_5.

5.3 Bi Cluster Melting

The first detailed experimental results concerning the melting-temperature of Bi clusters were published by Takagi [11, 12]. In these experiments thin Bi films with a mean thickness of 50 Å were prepared on crystal surfaces and then studied at different temperatures by means of the reflection method of electron diffraction. The Bi films were found to aggregate in the form of small islands on the surface of the substrate (see [11] and references therein). During cooling from the liquid state (T = 400°C) a supercooling behaviour with a solidification temperature of 110°C was observed. When the films were re-heated, melting occurred below the bulk melting point (T = 271°C) at T = 248°C.

The size dependence of the melting temperature has been studied for Bi in [13–15]. Bi particles were formed by condensing metal vapour onto an amorphous carbon film and studied with electron diffraction techniques or with a transmission electron microscope (TEM). The melting temperatures obtained in a process of heating for particles with a diameter of 65 Å, 100 Å and 250 Å were found to be 117°C, 177°C, 197°C, respectively [13]. These values, however, rather agree with the solidification temperature than with the melting temperature for the 50 Å films given above [11].

The difference between the melting temperature of small particles and the bulk melting temperature is due to an increased surface to volume ratio. As the relative number of surface atoms increases the contribution of the surface energy becomes significant and leads to a reduction of the melting temperature (see [16] and references

therein). Another possible effect is the surface melting of particles. This has been, for example, observed for small non-spherical lead particles [17, 18]. These particles showed a molten surface layer at temperatures below the melting temperature. The thickness of the molten layer was reported to depend on the curvature of the surface and on the particle temperature. In general, a liquid shell is expected when the energy of the solid surface is higher than the sum of the liquid surface and solid-liquid interface energies [16].

5.4 HRTEM and XRD Studies on Supported Bi Clusters

When comparing results from High Resolution Transmission Electron Microscopy (HRTEM) studies with the diffraction measurements on unsupported clusters the fundamental differences between the two techniques should be kept in mind. The biggest advantage of using an HRTEM is that it is possible to investigate individual particles. Therefore, the particle shape and possibly the crystal structure for single particles can be revealed. However, in most cases it is necessary to employ elaborate image simulations to obtain the complete structure of the clusters. Concerning the study of clusters, the major drawback for HRTEM is the existence of a substrate and the long exposure to a high energy electron beam. Another problem can be contamination of the sample, especially if the sample is exposed to air when transferred to the TEM.

Small Bi clusters on substrates have been studied with HRTEM in [19–22]. The first group of investigations [19–21] were done with samples that were exposed to air between deposition and TEM study. The size of the particles deposited on amorphous carbon ranged from 15 to 200 Å. Only particles larger than 50 Å showed a crystalline contrast and were investigated. These particles had a hemispherical shape and consist of a crystalline core that is surrounded by an amorphous shell (5–20 Å). The shell is assumed to be the result of oxidation of the Bi deposit. It was also observed that during exposure to the electron beam smaller crystalline Bi cores (50–60 Å) decreased in size and subsequently melted. Therefore, it was suggested that a size between 50 and 60 Å was the lower limit of the crystallised Bi phase at room temperature [21]. The Bi cores are free of defects and have the rhombohedral structure of the bulk material. The facets of the core have been identified with the $\{10\bar{1}2\}$ surfaces (corresponding to $\{110\}$ planes in the rhombohedral notation). These findings together with more details are presented in [21]. The experiments by Oshima *et al.* [22] were conducted on clusters deposited in-situ in an UHV–HRTEM on amorphous carbon at room temperature. Particles larger than about 50 Å and smaller than 84 Å were found to have the rhombohedral bulk

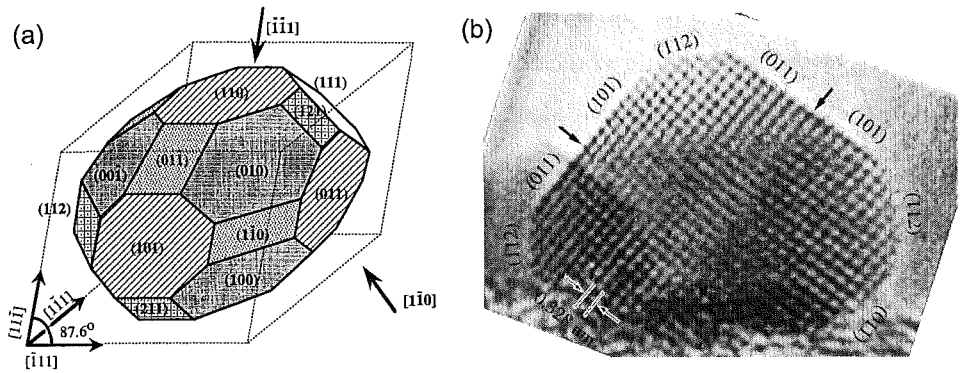

Figure 5.2: (a) Shape of Bi particles with a diameter between 50 and 84 Å as suggested in [22]. (b) HRTEM image of a cluster with a size of 84 Å. It is suggested that this image contrast is attributed to a new particle structure with lattice defects and core with a cubic structure [22].

structure with a shape as shown in Fig. 5.2a. The image contrast of smaller particles changed rapidly so that their structure could not be determined. For clusters with a size of 84 Å and larger (see Fig. 5.2b) a new structure was suggested that includes lattice defects and a core with a cubic structure. Unfortunately, only a two-dimensional model for this structure has been provided. In contrast to the first group of investigations the particles are not surrounded by an amorphous shell. Since these cluster were not exposed to air during deposition and TEM investigation it seems very likely that the amorphous shell observed in [21] is due to oxidised bismuth. The subject of oxidation of Bi particles in air is further discussed below in section 5.7.4.

A study in which supported Bi clusters were investigated with both HRTEM and XRD (X-ray diffraction) has been published in [23, 24]. The particles were produced using a high-temperature organic solution reduction method and were size selected in several steps by selective precipitation of the colloidal mixture. After the 6th size selection a narrow particle size distribution with a mean diameter of 150 Å could be obtained. The mean particle size was estimated from TEM images and from the peak broadening in X-ray diffraction patterns (Scherrer size estimates). Because of the good agreement of the estimates from the two methods it was concluded that the particles were single-crystalline. Furthermore, the peak positions in the X-ray patterns were consistent with those of the rhombohedral structure of bulk bismuth. HRTEM images show that these particles are faceted and have a nearly spherical shape.

XRD measurements have also been used to determine the lattice parameters of single crystalline Bi particles with sizes ranging from 89 Å to 318 Å [25–27]. The

particles were produced with an electrohydrodynamic technique in high vacuum and deposited on a substrate. The particle size was estimated from the broadening of the peaks in the XRD patterns using the Scherrer Equation. The X-ray diffraction patterns show that the particles are crystalline and have a rhombohedral structure. In all XRD patterns, the peak positions were found to deviate from the positions expected for bulk Bi. The lattice parameters calculated from the peak positions reveal a lattice contraction that increases with decreasing particle size. Simple estimates suggest that the lattice contraction is most likely caused by surface stress [26]. The only other available estimate of the lattice parameters for small Bi particles has been obtained by XRD measurements on clusters embedded in a glass matrix [28]. These particles have a mean diameter of 24 Å and show more lattice contraction than the smallest particles (mean diameter: 89 Å) investigated in [25]. A complete list of the measured particle sizes and the corresponding lattice parameters obtained in [25, 28] is presented in section 5.7.5.

5.5 Early Diffraction Studies on Free Bi Clusters

Unsupported Bi clusters were first studied by Yokozeki and Stein [1]. The particles were produced in an inert gas aggregation source similar to the one used in the present study and then probed in flight by an electron beam. Bi clusters were produced with Ar as the inert gas, pressures between 0.55 and 0.83 Torr and crucible temperatures between 903°C and 1093°C. The size of the clusters, estimated with the Scherrer Equation, ranged from 60 to 94 Å. A typical diffraction pattern obtained is shown in Fig. 5.3. The peak positions in the diffraction pattern agree with the indicated positions for rhombohedral Bi. The lattice parameters for the clusters investigated were essentially constant within an estimated error of 0.3% [1].

5.6 Molecular Dynamics Simulations

While MD simulations are a standard tool to theoretically predict the structure of small particles the possibilities for Bi are very limited. Thoroughly tested many-body potentials for 'exotic' materials like bismuth with its rhombohedral structure are simply not available. However, there is a potential for the Bi high pressure phase that has a BCC structure [29]. As suggested in [22] the pressure in small Bi particles might exceed values that favour the high pressure phase, due to the effect of the surface tension. Therefore, two spherical clusters (diameter: 40 and 50 Å) with the high pressure BCC

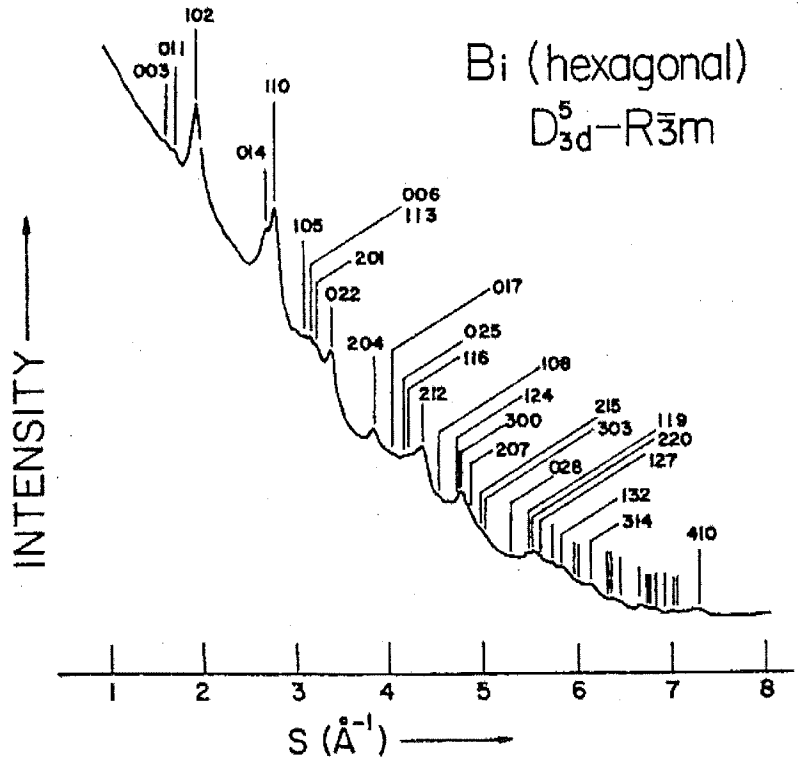

Figure 5.3: Electron diffraction pattern obtained from unsupported Bi clusters by Yokozeki and Stein [1]. The cluster size estimated with the Scherrer Equation is 60 Å. The Miller indices assigned to the peaks are based on the rhombohedral structure of bulk Bi. Note that a different definition for the scattering parameter s is used which results in a scattering parameter that is larger by a factor of 2π than the parameter used in this thesis.

structure were relaxed using a simulated annealing procedure[2]. The relaxed clusters maintain their BCC structure and spherical shape as can be seen in Fig. 5.4. The corresponding diffraction patterns are clearly different from the diffraction patterns of Bi particles with the bulk structure and so these MD simulations are not useful in interpreting the experimental patterns. It would also be interesting to use this potential to simulate clusters above the melting point and compare the results to the measured diffraction patterns.

Another possibility to simulate liquid Bi clusters would be to use the effective pair potential due to Cummings [30] and Bretonnet [31, 32]. The potential is specifically designed for liquid metals and parameters for the potential can be obtained from liquid structure factor data. The parameters for Bi are available in [32].

[2]These simulations were done by S. Hendy, Industrial Research Ltd., Wellington, NZ

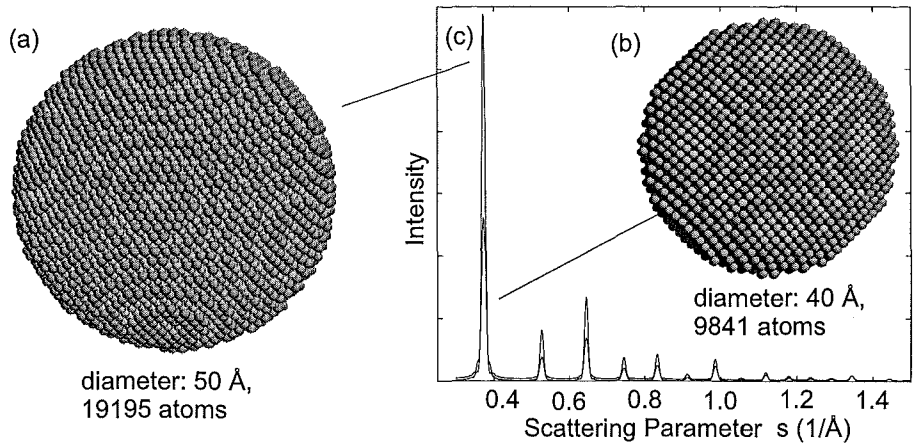

Figure 5.4: MD relaxed Bi clusters with the high pressure BCC structure (a,b) and their diffraction patterns (c). The initial clusters were created by cutting a sphere out of a BCC lattice. The relaxation of the particles was performed by simulated annealing using the potential given in [29].

5.7 Results and Analysis of the Experiments

This section starts with the presentation of the diffraction patterns organised in three groups according to the type of carrier gas used (Ar, He, Ar/He mixture). For experiments using either Ar or He the effects of changing the crucible temperature T_C, the pressure of the inert gas in the source chamber P_G and flow rate are examined. In the third group of experiments several series of diffraction patterns were also obtained by varying the Ar/He ratio. The design of the source used in this study does not allow a change of P_G independent of the gas flow rate. However, it is possible to change the diameter of the first nozzle between experiments to achieve lower or higher pressures for a given flow rate. In general, the results can be divided into diffraction patterns from crystalline clusters and patterns with liquid or amorphous features. Therefore, patterns from crystalline clusters and patterns from non-crystalline particles are analysed in separate sections.

All experimental diffraction patterns presented here have the scattering contribution of the gas in the diffraction chamber removed. A detailed description of the processing of the raw diffraction data is given in section 2.5. For display purposes the intensity of each diffraction pattern in a set of patterns is scaled so that the intensity of the highest peak in each pattern is equal. Every set of patterns is displayed together with a table that provides information about source parameters and size estimates for the clusters. The mean particle sizes were estimated from the diffraction patterns using the Scherrer Equation and the constrained inversion method (see chapter 4), and when

available from TEM images of clusters deposited on amorphous carbon.

The uncertainties in the size estimates from the constrained inversion are approximately ±7 Å while the results from the Scherrer Equation and the TEM measurements have an uncertainty of approx. 10%. Some size estimates are shown in parentheses. In the case of estimates obtained using the Scherrer Equation (section 4.2.2) results in parentheses indicate estimates from possibly non-crystalline particles. Since the Scherrer Equation is limited to crystalline particles these results should be treated carefully. In the case of estimates obtained using the constrained inversion method (section 4.2.4) estimates in parentheses have larger uncertainties (±10 Å) due to the noise in the diffraction patterns.

5.7.1 Experiments with Argon as the Carrier Gas

Figures 5.5 and 5.6 show the evolution of diffraction patterns as T_C is increased while the flow rate (and therefore P_G) is kept constant. For both sets of patterns the diameter of the first nozzle was 2.5 mm. The difference between the sets is a lower constant flow rate for the patterns in Fig. 5.6. It can be seen that, as a general trend, more details appear in the diffraction patterns as the crucible temperature increases. This effect and in particular the splitting of the double peak between $s = 0.40$ Å^{-1} and $s = 0.45$ Å^{-1} suggests an increase in domain or particle size[3] with increasing temperature. Typical for these diffraction patterns is a scattering background, an example of which is indicated in Fig. 5.5 by the broken line (see section 5.7.5 for a discussion). The background starts to become prominent in the low temperature patterns in Fig. 5.5 and Fig. 5.6. Thus, it is not very surprising to see a strong background in the low temperature series in Fig. 5.7 which displays diffraction patterns that were obtained with $T_C = 777$°C and a nozzle diameter of 3.5 mm by varying the flow rate (and therefore also P_G). With this large nozzle relatively high flow rates were required to observe diffraction patterns from clusters. The diffraction pattern with the highest overall intensity in this series was pattern (2). This fact can be clearly seen on the low noise in the diffraction pattern. Above and below the flow rate of 100 sccm the intensity decreases combined with an increase of the background.

Compared to Fig. 5.7 the diffraction patterns in Fig. 5.8 were obtained with a higher crucible temperature $T_C = 834$°C and a smaller first nozzle with a diameter of 1.5 mm. Because of the smaller nozzle diameter diffraction patterns could be observed at lower

[3]Diffraction patterns are only characteristic to the domains in the particles (see section 4.3.2) and therefore this statement only refers to the particle size when clusters are single-crystalline.

flow rates. Typical for this series is the low background. It also indicates that there is no connection between a high background and a low diffraction signal intensity. As it can be seen in Fig. 5.8 and Table 5.4, the cluster size increases with increasing flow (pressure) for the parameter range investigated (13–90 sccm, 3.17–11.1 mbar).

All bismuth diffraction patterns produced with Ar as the carrier gas can be identified as patterns from crystalline clusters. The structure and lattice parameters are discussed further below in section 5.7.5.

The size estimates obtained from the diffraction patterns (Scherrer Equation, inversion) are clearly smaller than the estimates from the corresponding TEM images. In addition, the Scherrer estimates are slightly smaller than the size estimates from the constrained inversion. This discrepancy in the size estimates is discussed later in section 5.7.4.

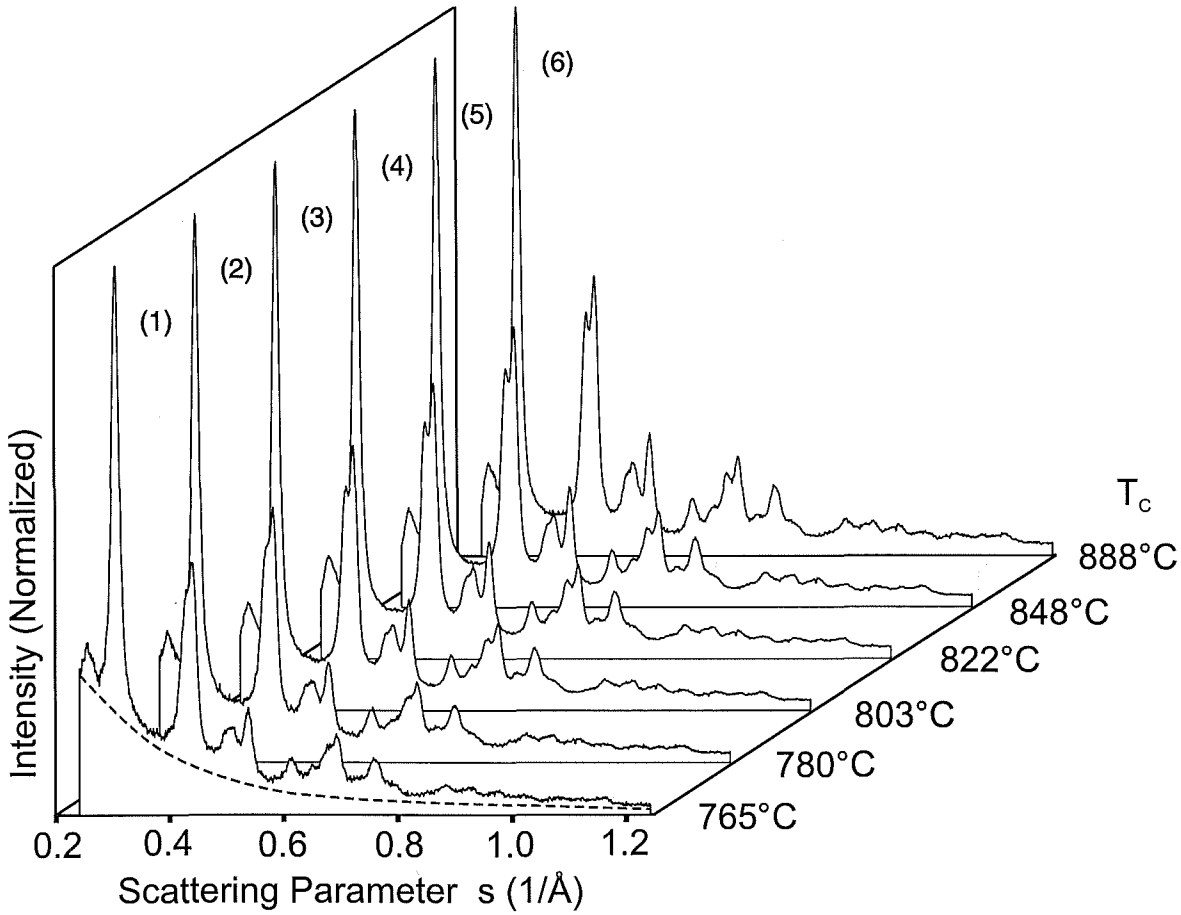

Figure 5.5: Diffraction patterns obtained by varying T_C. The patterns were produced with a constant flow of 80 sccm of Ar ($P_G = 6$ mbar), T_C between 765°C and 888°C and a nozzle diameter of 2.5 mm. The corresponding size estimates are listed in Table 5.1. The broken line represents an approximation of the background in pattern (1). The issue of the background is discussed in detail in section 5.7.5.

Table 5.1: Size estimates obtained for the diffraction patterns displayed in Fig. 5.5.

	T_C	Size (Diameter) Estimates (Å)			
Pattern	(°C)	Scherrer	Inversion	TEM mean	TEM 3rd moment
1	765	61	85	-	-
2	780	64	85	109	124
3	803	76	90	-	-
4	822	77	95	-	-
5	848	80	95	231	252
6	888	76	95	-	-

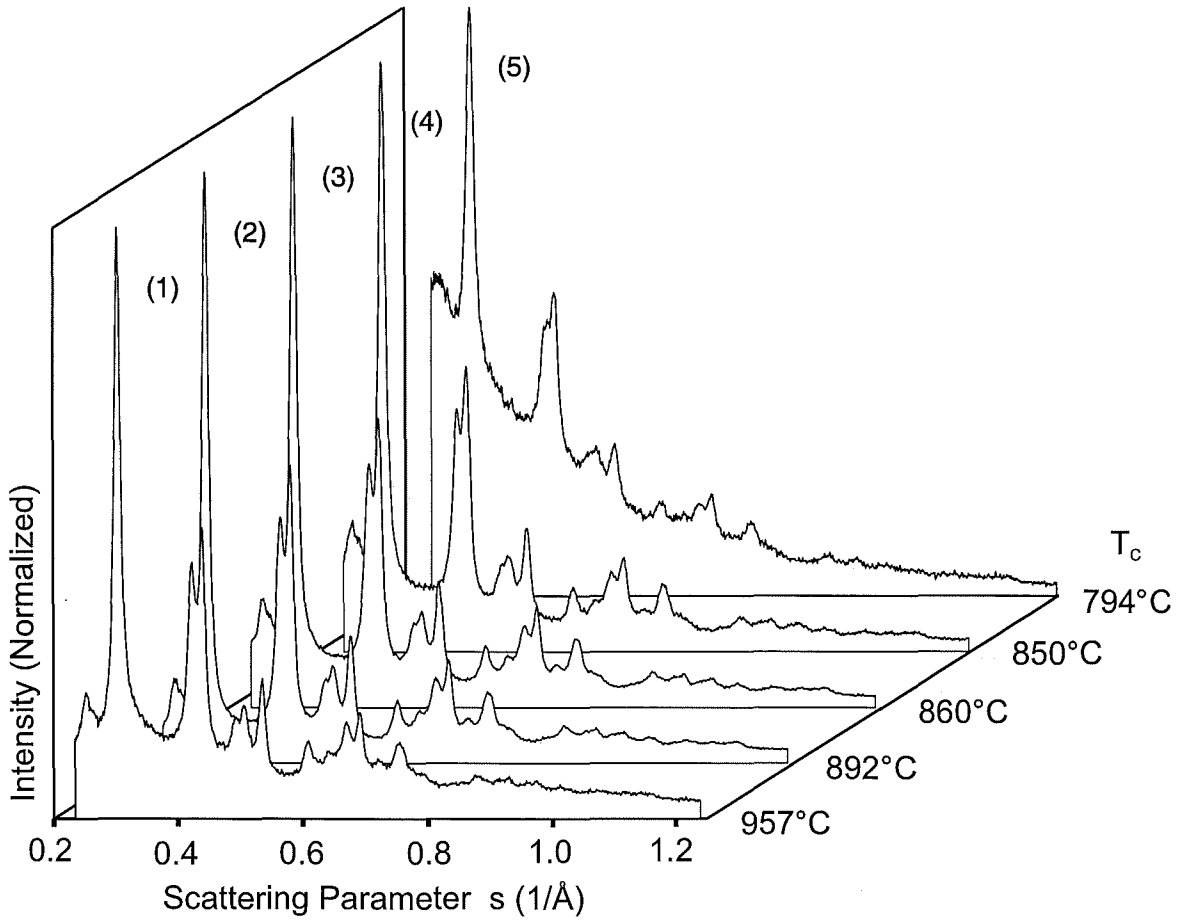

Figure 5.6: Diffraction patterns obtained by varying T_C. The patterns were produced with a constant flow of 50 sccm of Ar (P_G = 3.5 mbar), T_C between 794°C and 957°C and a nozzle diameter of 2.5 mm. Patterns (1,2) and (3–5) belong to different experiments. The corresponding size estimates are listed in Table 5.2.

Table 5.2: Size estimates obtained for the diffraction patterns displayed in Fig. 5.6.

Pattern	T_C (°C)	Size (Diameter) Estimates (Å) Scherrer	Inversion	TEM mean	TEM 3rd moment
1	957	99	110	-	-
2	892	90	110	-	-
3	860	90	100	-	-
4	850	86	100	-	-
5	794	72	85	-	-

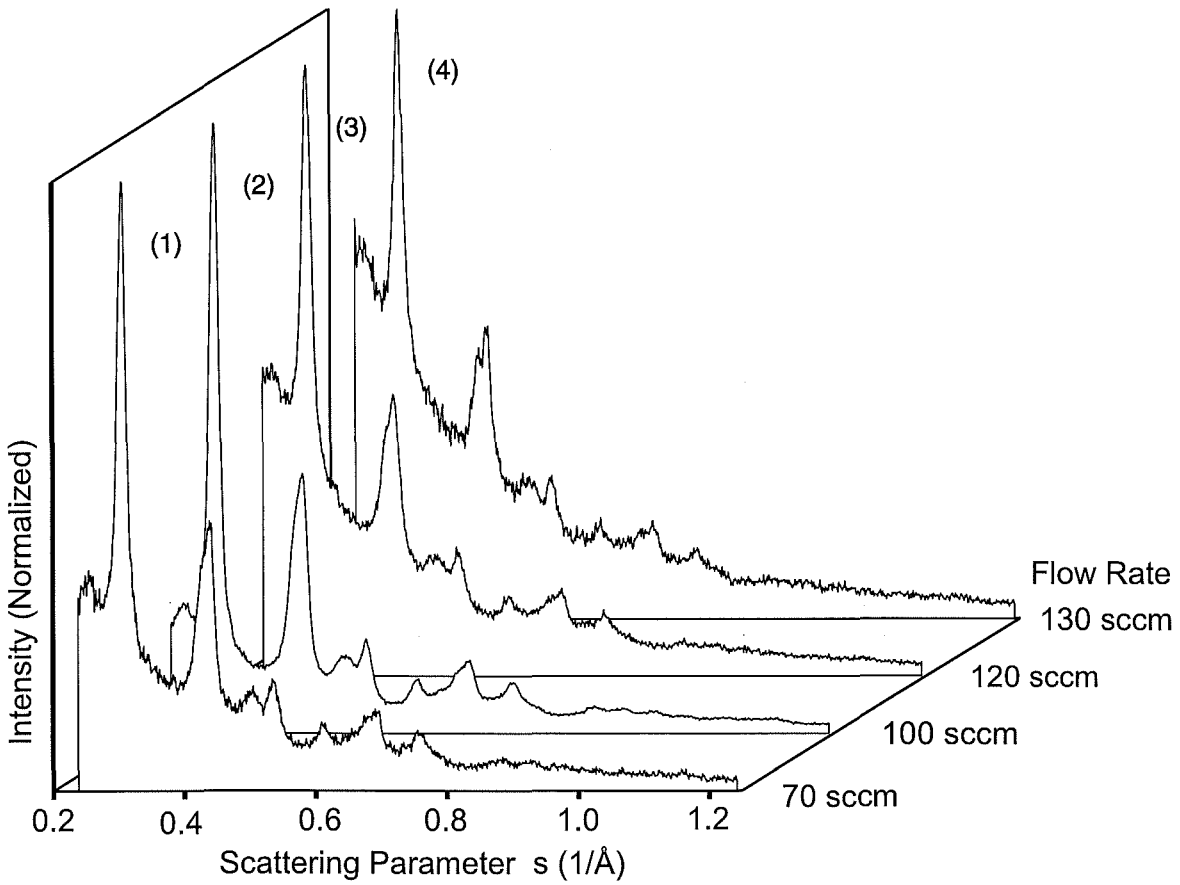

Figure 5.7: Diffraction patterns obtained by varying the Ar gas flow rate. The patterns were produced with a constant T_C of 777°C, gas flow between 70 and 130 sccm and a nozzle diameter of 3.5 mm. The gas flows of 70, 100, 120, 130 sccm correspond to the following pressures of 2.3, 3.3, 3.9 and 4.1 mbar. The size estimates are listed in Table 5.3.

Table 5.3: Size estimates obtained for the diffraction patterns displayed in Fig. 5.7.

Pattern	Flow Rate (sccm)	Size (Diameter) Estimates (Å)			
		Scherrer	Inversion	TEM mean	TEM 3rd moment
1	70	58	82	-	-
2	100	51	75	-	-
3	120	61	82	-	-
4	130	70	85	-	-

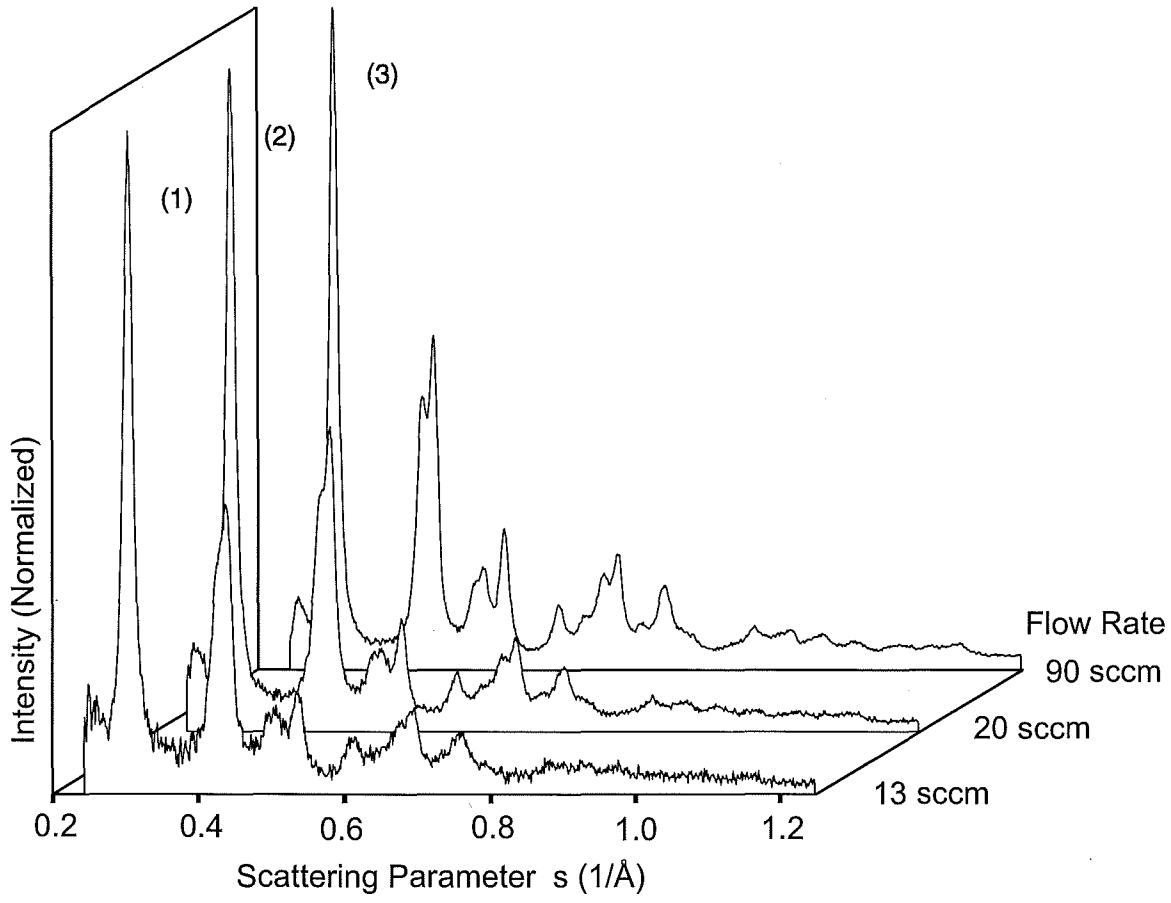

Figure 5.8: Diffraction patterns obtained by varying the Ar gas flow rate. The patterns were produced with a constant T_C of 834°C, gas flow between 13 and 90 sccm and a nozzle diameter of 1.5 mm. The gas flows of 13, 20 and 90 sccm correspond to the following pressures of 3.17, 3.96 and 11.1 mbar. The size estimates are listed in Table 5.4.

Table 5.4: Size estimates obtained for the diffraction patterns displayed in Fig. 5.8.

	Flow Rate	Size (Diameter) Estimates (Å)			
Pattern	(sccm)	Scherrer	Inversion	TEM mean	TEM 3rd moment
1	13	65	78	-	-
2	20	70	82	-	-
3	90	83	95	-	-

5.7.2 Experiments with He as the Carrier Gas

Figure 5.9 represents an overview of the patterns observed with the inert-gas aggregation source using He as the inert gas. It is composed of patterns from three runs with different nozzle diameters (1.0, 1.5 and 2.5 mm). The diffraction patterns (5,6) in Fig. 5.9 were obtained with a 2.5 mm nozzle and are patterns typical for liquid or amorphous particles. Patterns with sufficient intensity could only be observed at high flow rates (pressure). Compared to patterns of crystalline clusters observed in the experiments with Ar as the inert gas, the first peak is shifted to higher s-values ($s \approx 0.33$ Å^{-1}) and is much broader. Characteristic is also the existence of a shoulder at the high s side of the first peak and a broad second and third peak at $s \approx 0.64$ Å^{-1} and $s \approx 0.95$ Å^{-1}. For the 2.5 mm nozzle the pressure range is limited by a flow rate that creates a pressure in the 2nd stage turbo pump close to the operating limit. With this nozzle and within the available parameter space of P_G and T_C only liquid patterns could be measured. Changes of T_C had a negligible effect on the shape of the diffraction pattern and only influenced the overall intensity. However, a transition from liquid to solid clusters could be observed by increasing the source pressure ($P_G > 15$ mbar) which was made possible by using smaller nozzles. Patterns (3,4) were obtained with a 1.5 mm nozzle and show an increase in crystalline features with increasing pressure. The remaining two patterns (1,2) demonstrate that it is possible to make predominantly crystalline clusters with He as the carrier gas. Pattern (1) is comparable to the patterns from crystalline clusters obtained with argon.

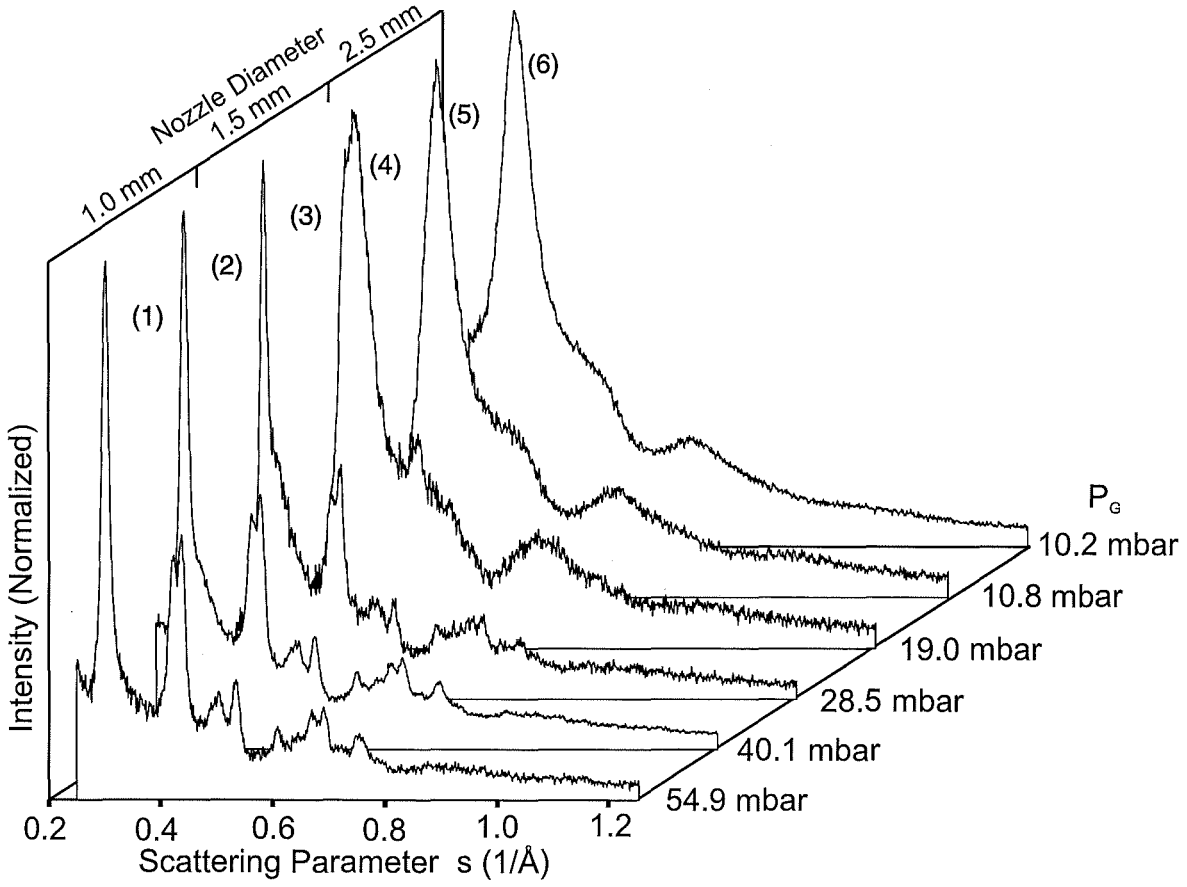

Figure 5.9: Diffraction patterns obtained with He as the inert gas. The results are from three runs with different nozzle sizes. The source parameters and size estimates for the patterns are listed in Table 5.5.

Table 5.5: Source parameters and size estimates obtained for the diffraction patterns displayed in Fig. 5.9.

P.	P_G (mbar)	T_C (°C)	Flow Rate (sccm)	Nozzle (mm)	Size (Diameter) Estimates (Å) Scherrer	Inversion	TEM mean	TEM 3rd moment
1	54.9	822	500	1.0	64	85	-	-
2	40.1	880	300	1.0	63	75	-	-
3	28.5	835	500	1.5	69	75	-	-
4	19.0	839	300	1.5	(20)	50	-	-
5	10.8	950	300	2.5	(20)	40	-	-
6	10.2	880	300	2.5	(20)	40	96	120

5.7.3 Ar–He Mixing Experiments

Figures 5.10 and 5.11 show diffraction patterns obtained by varying the Ar to He ratio from 0% to 35% while maintaining the total gas flow rate and crucible temperature T_C. For all these patterns a nozzle with a diameter of 2.5 mm was used. Note that P_G is not constant and increases with an increasing Ar to He ratio. With pure He as the inert gas the patterns clearly show the features of liquid or amorphous diffraction patterns. When the Ar content is increased, features from crystalline clusters appear and dominate the diffraction patterns at 35% Argon. Higher Ar to He ratios were not used because of experimental restrictions. While for the experiment shown in Fig. 5.10 a constant total gas flow rate of 300 sccm was used, the patterns in Fig. 5.11 were obtained with a higher flow rate of 500 sccm. In the latter case, the patterns from crystalline clusters show a different intensity ratio of the two peaks at $s \approx 0.4$–0.45 Å^{-1} compared to the previous 'crystalline' patterns in which the low s peak appears to be relatively large compared to the high s peak. Patterns (1,2) are the only patterns with this different peak ratio and show crystalline as well as liquid/amorphous features. It has not been possible to obtain patterns with only crystalline features since for a total flow rate of 500 sccm the argon ratio could not be increased to more than 25% (maximum load for the turbo pumps).

Figure 5.12 also shows a series of patterns with different Ar to He ratios. In contrast to the previous two series the total gas flow rate was decreased from 300 sccm (patterns 3–5) to 250 sccm (patterns 1,2). As a result, the values of P_G are similar for patterns (1,3) and (2,4). The comparison of the patterns indicates that with P_G kept constant the crystalline features in the patterns become stronger with increasing Ar to He ratio.

The diffraction patterns in Fig. 5.13 were obtained by varying the gas flow rate while the Ar to He ratio was fixed to 25%, $T_C = 908°\text{C}$ and the nozzle diameter was 2.5 mm. Within the investigated parameter range crystalline features become stronger with increasing gas flow rate (pressure).

Again, there is a clear difference between the size estimates from diffraction patterns (Scherrer Equation, inversion) and from the corresponding TEM images. For a detailed discussion see section 5.7.4. The TEM size estimates indicate a decrease in particle size for sequences from crystalline to amorphous.

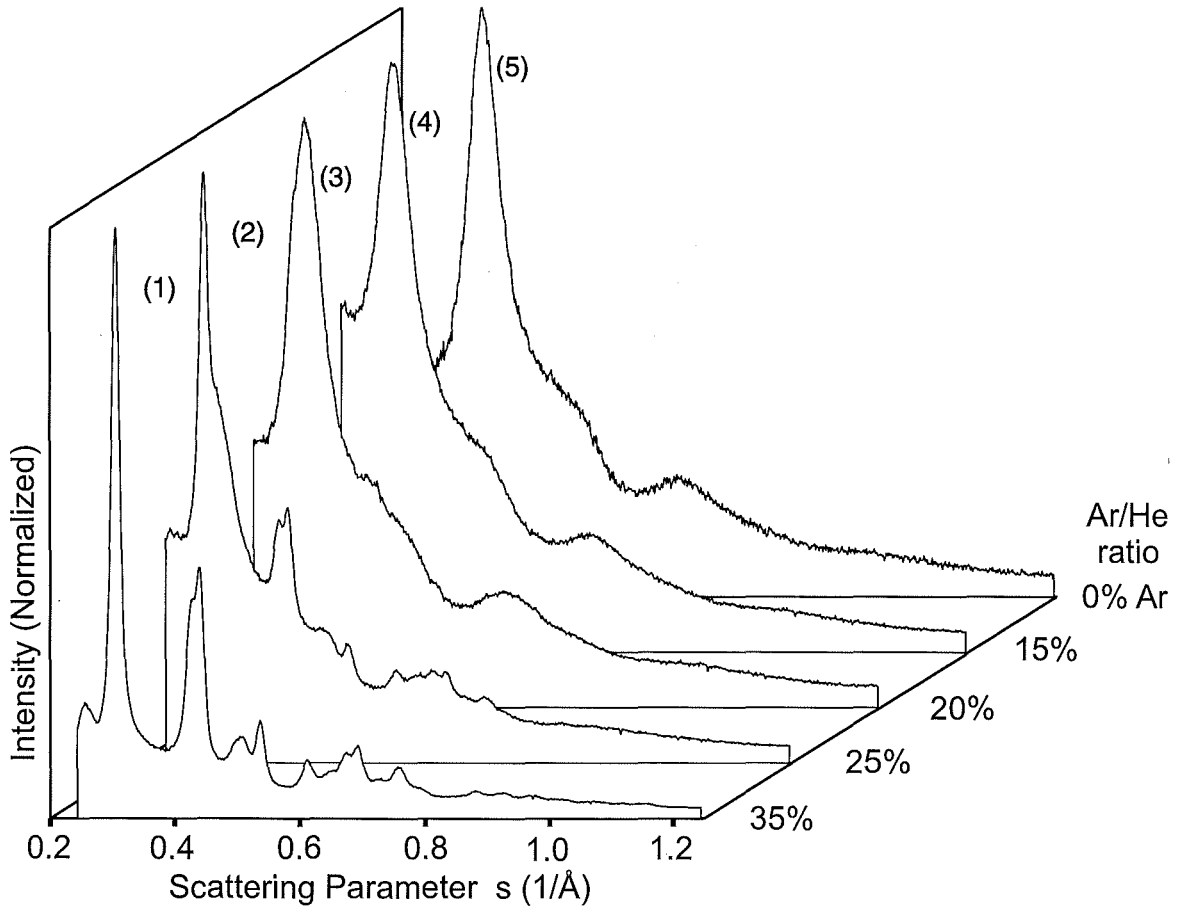

Figure 5.10: Diffraction patterns obtained by changing the ratio of Ar to He from 0% to 35%. The patterns were produced with $T_C = 885°C$, a constant gas flow rate of 300 sccm and a nozzle diameter of 2.5 mm. The source parameters and size estimates are listed in Table 5.6.

Table 5.6: Source parameters and size estimates obtained for the diffraction patterns displayed in Fig. 5.10. Scherrer size estimates could not be determined for patterns with a double peak at $s \sim 0.3$ Å^{-1}.

Pattern	Ar/He ratio (%)	Pressure (mbar)	Size (Diameter) Estimates (Å)			
			Scherrer	Inversion	TEM mean	TEM 3rd moment
1	35	13.8	55	78	131	147
2	25	12.8	-	80	151	169
3	20	12.5	-	50	-	-
4	15	11.5	(20)	40	-	-
5	0	10.2	(20)	40	96	120

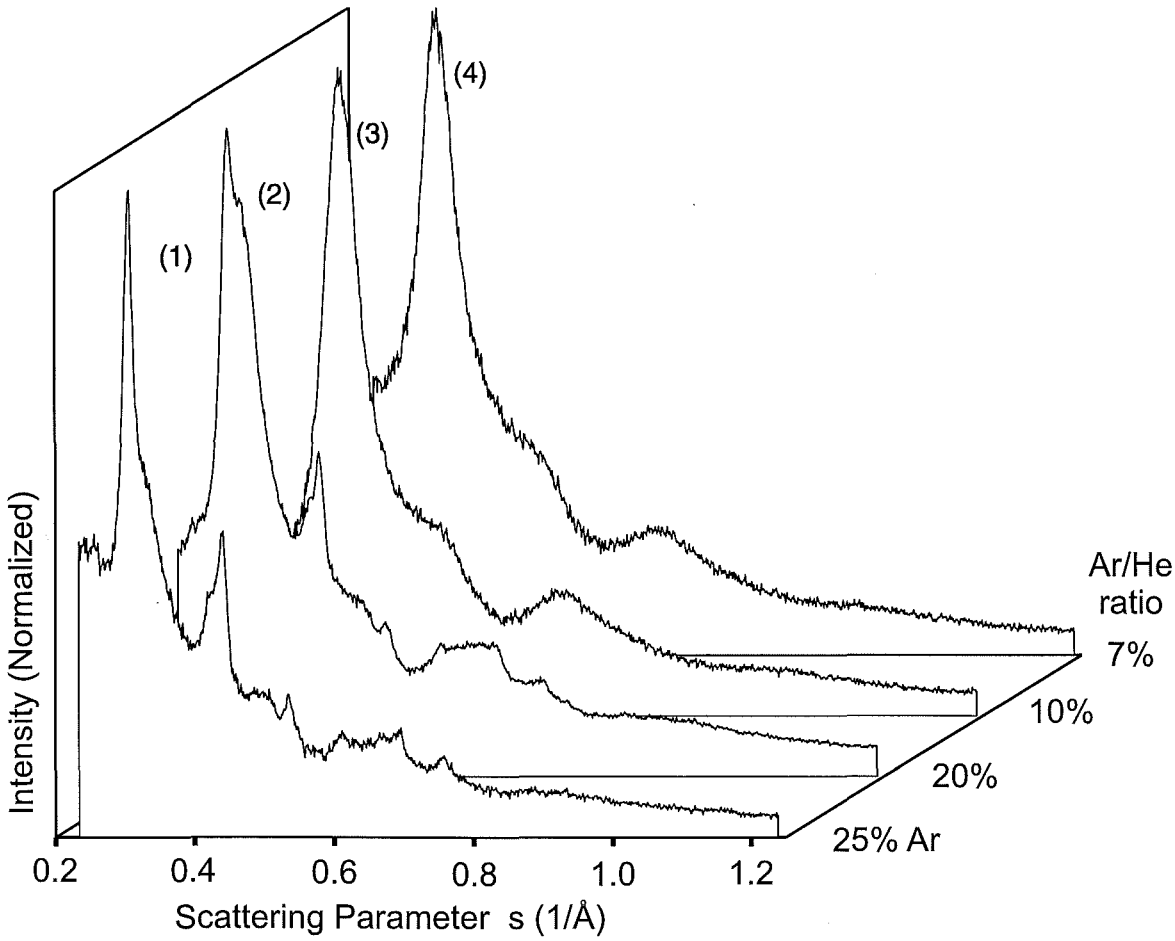

Figure 5.11: Diffraction patterns obtained by changing the ratio of Ar to He from 7% to 25%. The patterns were produced with $T_C = 900°C$, a constant gas flow rate of 500 sccm and a nozzle diameter of 2.5 mm. The corresponding source parameters and size estimates are listed in Table 5.7. Note that the main difference between this series of patterns and the patterns in Figs. 5.10 and 5.12 is the much higher gas flow rate of 500 sccm.

Table 5.7: Source parameters and size estimates obtained for the diffraction patterns displayed in Fig. 5.11. Scherrer size estimates could not be determined for patterns with a double peak at $s \sim 0.3$ Å^{-1}.

	Ar/He ratio	Pressure	Size (Diameter) Estimates (Å)			
Pattern	(%)	(mbar)	Scherrer	Inversion	TEM mean	TEM 3rd moment
1	7	17.5	57	78	-	-
2	10	16.7	-	75	-	-
3	20	15.8	(20)	50	-	-
4	25	15.3	(20)	50	-	-

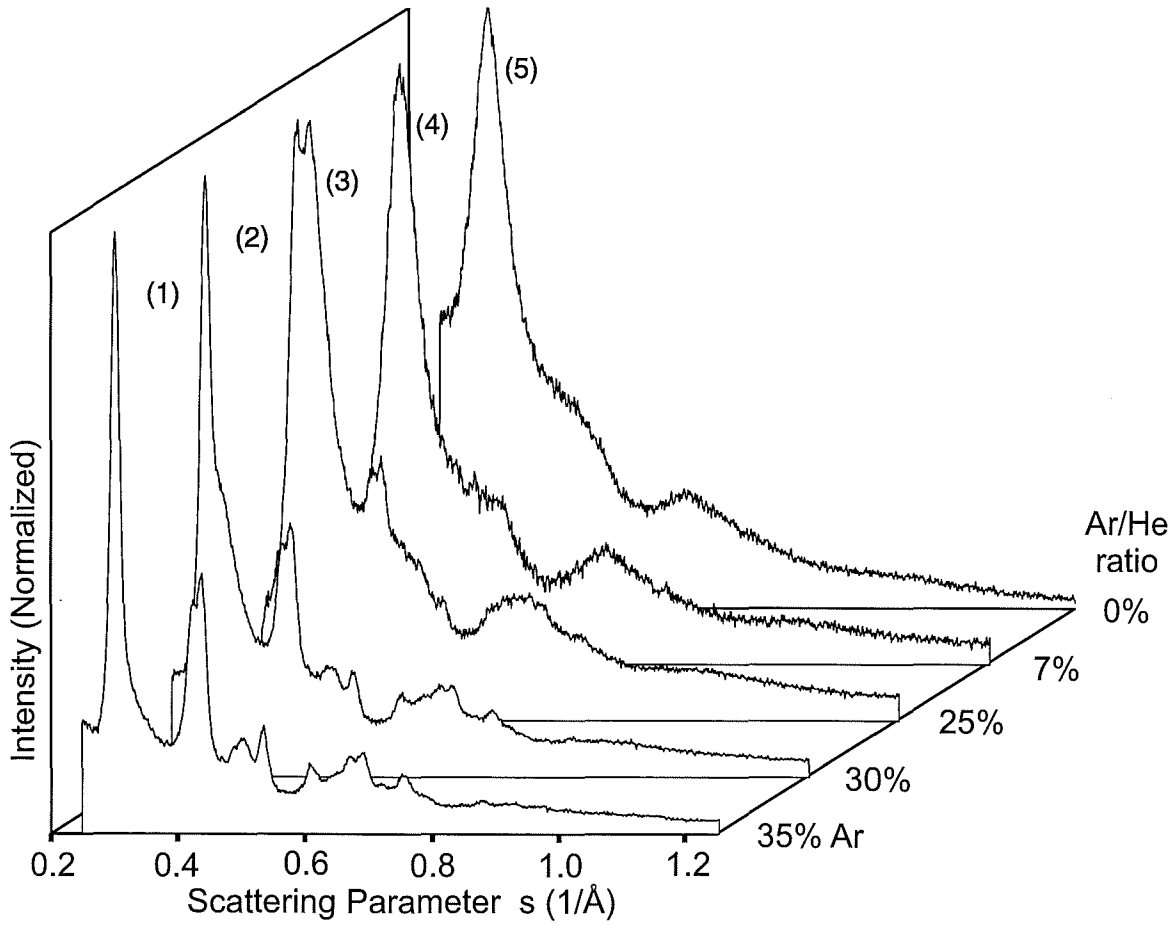

Figure 5.12: Diffraction patterns obtained by changing the ratio of Ar to He from 0% to 35%. The patterns were produced with $T_C = 885°C$, a nozzle diameter of 2.5 mm and a gas flow rate of 250 sccm (patterns 1,2) or 300 sccm (patterns 3-5). The corresponding source parameters and size estimates are listed in Table 5.8.

Table 5.8: Source parameters and size estimates obtained for the diffraction patterns displayed in Fig. 5.12. Scherrer size estimates could not be determined for patterns with a double peak at $s \sim 0.3$ Å^{-1}.

Pattern	Ar/He ratio (%)	Pressure (mbar)	Size (Diameter) Estimates (Å)			
			Scherrer	Inversion	TEM mean	TEM 3rd moment
1	35	11.4	60	75	-	-
2	30	10.8	(50)	70	145	171
3	25	11.7	-	70	133	153
4	7	10.6	(20)	40	92	110
5	0	9.8	(20)	40	69	92

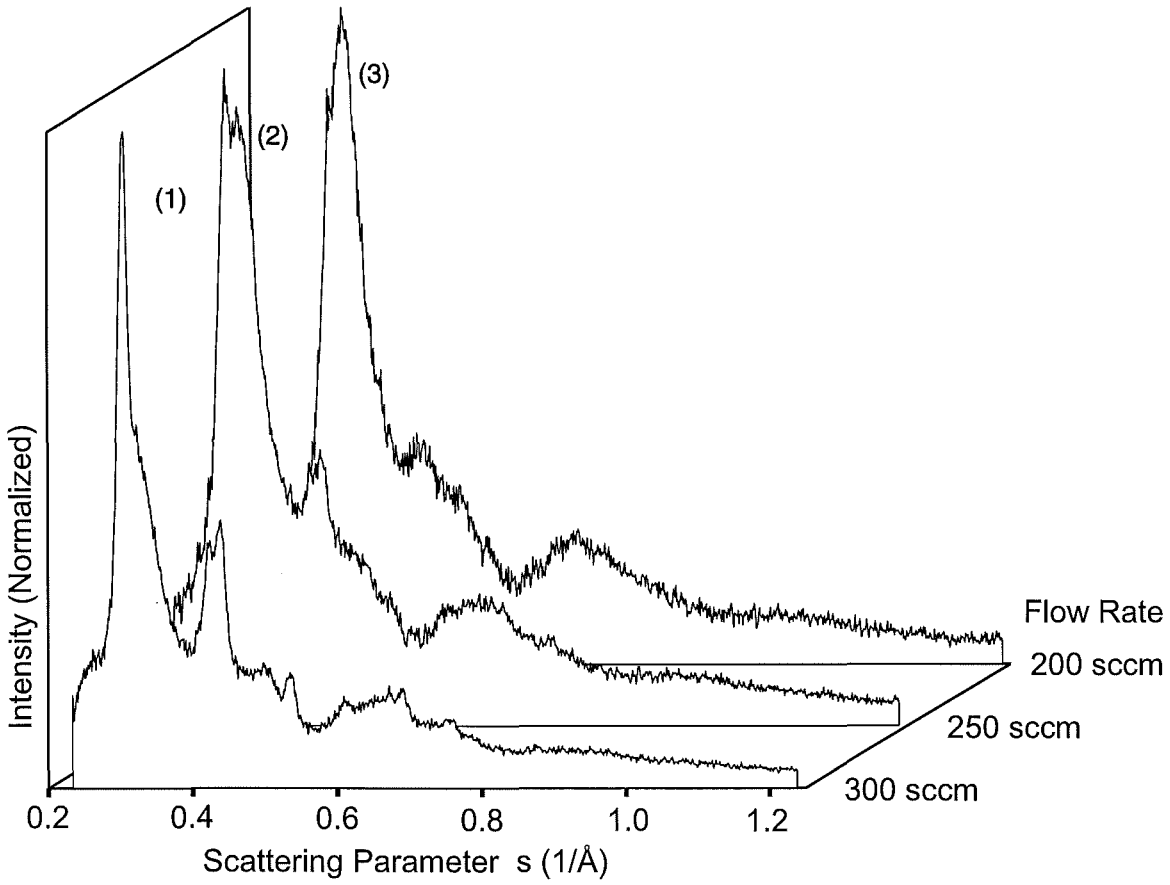

Figure 5.13: Diffraction patterns obtained by varying the total gas flow rate from 200 to 300 sccm while an Ar to He ratio of 25% was maintained. The crucible temperature was $T_C = 908°C$ and a nozzle with a diameter of 2.5 mm was used. The corresponding source parameters and size estimates are listed in Table 5.9.

Table 5.9: Source parameters and size estimates obtained for the diffraction patterns displayed in Fig. 5.13. Scherrer size estimates could not be determined for patterns with a double peak at $s \sim 0.3$ Å^{-1}.

	Flow Rate	Pressure	Size (Diameter) Estimates (Å)			
Pattern	(sccm)	(mbar)	Scherrer	Inversion	TEM mean	TEM 3rd moment
1	300	11.7	(60)	85	-	-
2	250	10.4	-	70	-	-
3	200	9.01	-	(60)	-	-

5.7.4 Discrepancy in the Cluster Size Estimates

Comparing results from the different methods used for the size estimates shows that estimates obtained from TEM images were systematically much larger than the estimates obtained from the diffraction patterns (Scherrer Equation, constrained inver-

sion). There are two possible effects that would lead to a discrepancy in the estimates. Firstly, if there is some degree of disorder in the particles the size estimate is more characteristic to the domain size within the clusters than to the size of the entire particle (see section 4.3.2). Secondly, there are some indications that the cluster size changes during and after deposition on substrates necessary for TEM observations. For the TEM size analysis Bi clusters are deposited on amorphous carbon at room temperature and exposed to air during the transfer to the TEM. It has been observed in [33] that Bi clusters deposited on amorphous carbon at room temperature form larger particles on the support. The mean particle size of 18 Å in the beam changed to mean sizes between 25 and 45 Å depending on the coverage. Judging from the TEM images shown in [33] the coverage is comparable to or lower than the coverage used in this study.

Exposed to air, most metals oxidise and form a thin layer of oxide at their surfaces. The thickness of the film is usually in the order of 50 Å [34]. This has strong consequences for nanoparticles. Within a short amount of time small particles may completely oxidise or be surrounded by an oxide shell. The small Bi particles on amorphous carbon investigated by Treilleux *et al.* [21] show amorphous (Bi oxide) layers with a thickness from 15 to 50 Å. Other studies on Bi nanowires [35] revealed 70 Å thick oxide coatings on crystalline cores with a diameter of 250 Å.

To investigate the possibility that the mean cluster size changes after deposition on the substrate two TEM sample grids have been exposed to the same cluster beam but with different exposure times (factor of 3). Figure 5.14 shows the two size distributions obtained from TEM images of the two grids. The fact that the variation of the coverage does not lead to a noticeable change in the mean particle size suggests that the TEM size measurements are not affected by diffusion of Bi atoms or particles on the amorphous carbon substrate. This finding therefore supports the idea that the size distribution in the cluster beam is the same as on the substrate and that the smaller size estimate from diffraction patterns refer to the size of the domains in the particles (see section 4.3.2) rather than to the size of the whole particle. This in turn implies that the particles are not single crystalline and contain *lattice defects* that separate the domains.

However, some uncertainty remains about the size of the Bi particles in the beam as the TEM size estimates require that the particle shape remains unchanged and that the TEM contrast is not affected by oxidation. If particles, for example, acquire a flattened shape due to the deposition process or interaction with the substrate, the apparent size in the TEM images would be larger than the size of the particles in the cluster beam.

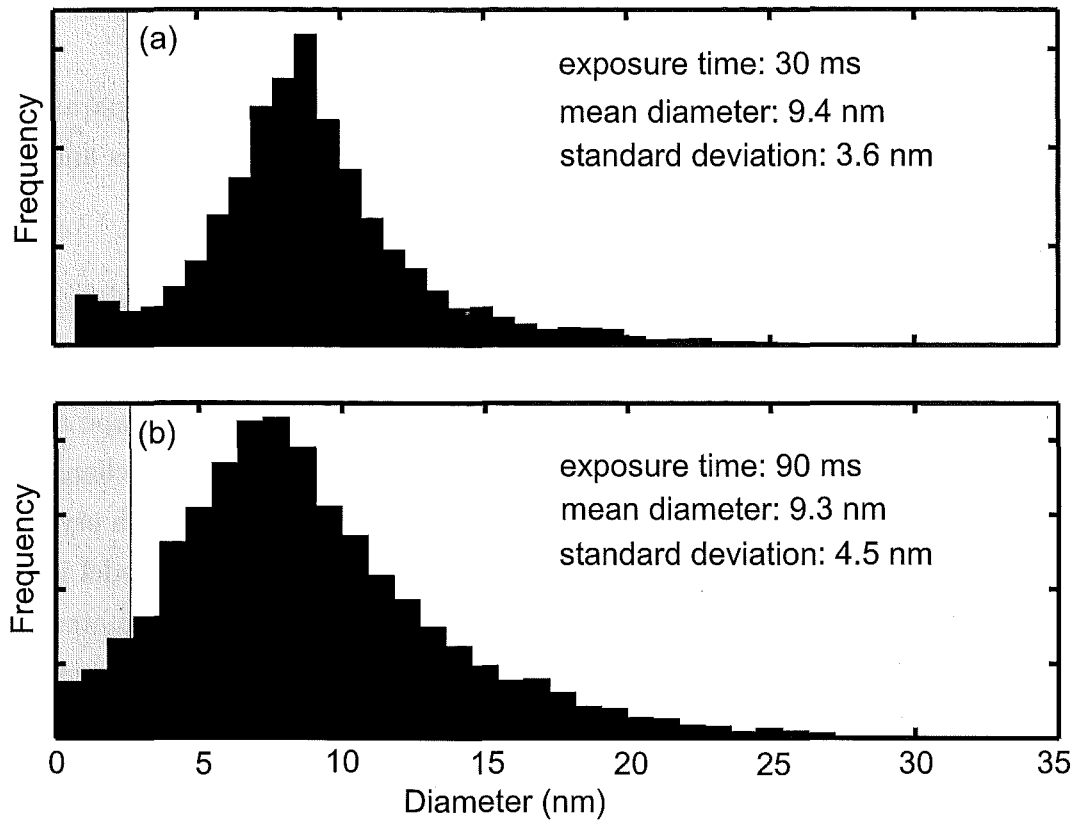

Figure 5.14: Size distributions of particles obtained from TEM images of Bi clusters deposited on amorphous carbon. The TEM sample grids were exposed to the cluster beam for 30 ms (a) and 90 ms (b) with only a short delay between exposures to ensure sampling of the same distribution of clusters in the beam. The fact that the mean particle size on the TEM grids is independent of the coverage (factor of 3) suggests that growth of cluster due to diffusion of Bi atoms or clusters on the substrate is negligible.

It becomes apparent that the size estimates from TEM images of deposited Bi clusters can be problematic and depending on the conditions during deposition could lead to misleading results as shown in [33]. Therefore, it is very desirable to combine the diffraction experiment with a better tool to determine the size distribution in the cluster beam, e.g. a time-of-flight mass spectrometer (TOF-MS).

A TOF-MS is being built and will provide very reliable size estimates for the Bi cluster produced with our inert-gas aggregation source.

5.7.5 Analysis of Patterns from Crystalline Clusters

In this section the patterns from crystalline clusters are investigated in separate parts focusing on the crystal structure, the background and the peak intensities and ratios in the patterns.

Crystal Structure and Lattice Parameters

For a single crystalline cluster with a fixed rhombohedral structure the diffraction pattern depends on the shape of the cluster and on its size. Variations in shape and size only influence the relative intensities and widths of the peaks but do not change their positions. Figure 5.15 shows a typical experimental diffraction pattern with crystalline features together with a pattern calculated from a model cluster. The model is based on a rhombohedral structure with the lattice parameters of the Bi bulk material. Information about the cluster shape (Fig. 4.16, pattern (2)) and the method to calculate the corresponding diffraction pattern can be found in section 4.1. The peak positions in the experimental patterns indicate a rhombohedral structure. However, there are deviations in the peak positions compared to the Bi bulk structure. This is clearly visible in the different separation of the (112) and $(1\bar{1}0)$ peak as shown in the inset of Fig. 5.15. The peak shift has been observed in all diffraction patterns that allow the measurement of the separation of the (112) and $(1\bar{1}0)$ peak and this shift is investigated in more detail further below.

Once the diffraction peaks are indexed with the Miller indices (hkl) of the corresponding Bi bulk crystal, the values of the lattice parameter can be calculated using:

$$\frac{1}{s^2} = a^2 \frac{1 + \cos(\alpha) - 2\cos^2(\alpha)}{(1 + \cos(\alpha))((h^2 + k^2 + l^2) - (1 - \tan^2(\alpha/2))(hk + kl + lh))}, \tag{5.1}$$

where s is the position of the peak and a, α are the parameters for the rhombohedral unit cell [36]. In order to determine the two parameters at least two peak positions are required. The peaks, however, have to be chosen carefully. For small particles the peaks are considerably broadened and overlapping peaks may lead to misleading results. A good way to find out which peaks are suitable for calculating the lattice parameters is to determine a and α from a calculated pattern with known parameters. In our case, the (110), (200) and $(\bar{1}12)$ peaks have been chosen.

The positions of the peaks are determined by fitting a parabola over the data points that contribute to the peak. The peak positions can be measured to about 0.0003 Å^{-1} which is mainly determined by the size of the pixels (one effective pixel: 0.001 Å^{-1}).

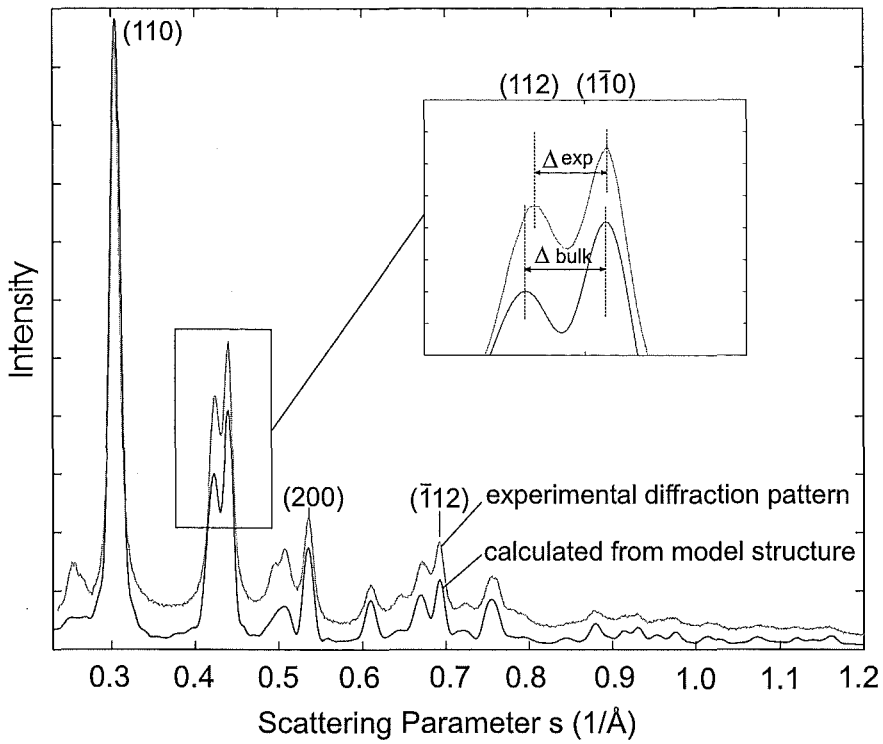

Figure 5.15: Comparison of an experimental diffraction pattern with a pattern calculated from a model cluster (see Fig. 4.16, pattern (2)) with a rhombohedral structure and parameters of the Bi bulk material. The peak positions in the experimental pattern are typical for a rhombohedral structure but do not completely agree with the lattice parameters of the Bi bulk material. The most visible difference is the smaller separation of the (112) and the (1$\bar{1}$0) peak in the experimental pattern.

Using a pair of peaks to calculate the lattice parameters, the corresponding uncertainties are for a: 0.015 Å (approx. 0.32%) and for the angle α: 0.2° (approx. 0.35%). In addition, there is an error from the calibration process (conversion of detector pixel to scattering angle) as described in section 2.5. In first approximation, this causes an offset of the diffraction pattern and results in a error of about 0.0015 Å. This corresponds to a relative error in the position of the first peak of about 0.5%.

The calibration error is large compared to the size and temperature related changes of the lattice parameters expected for small Bi particles. For example, the lattice parameters for particles with a mean diameter of 89 Å have been determined with $a = 4.7292$ Å and $\alpha = 57.384°$ [25]. Compared to the parameters of the bulk material this corresponds to a decrease in a of 0.35% and an increase in α of 0.26%. Changes in lattice parameters due to temperature are even smaller than the size dependent shifts and cannot be detected with our equipment. Using bulk thermal expansion coefficients for Bi [37], the lattice parameters (a, α) have been estimated to be (4.7450 Å, 57.2268°) at 200 K, (4.7459 Å, 57.2367°) at RT and (4.7480 Å, 57.2431°) at 540 K.

Table 5.10: Positions of the (110), (200) and ($\bar{1}$12) peak from the diffraction patterns in Fig. 5.5 and the corresponding lattice parameters. The parameters are determined from two pairs of peak positions: (110/200) and (110/ $\bar{1}$12). The error in the measurement of the peak positions is 0.0003 Å^{-1} (without calibration error) which results in an error for the lattice parameters a, α of 0.015 Å and 0.2°, respectively.

	Positions (Å^{-1})			Lattice Parameters a, α (Å, °)	
Pattern	(110)	(200)	($\bar{1}$12)	(110/200)	(110/$\bar{1}$12)
1	0.3069	0.5379	0.6937	4.71, 57.7	4.74, 57.0
2	0.3066	0.5380	0.6935	4.69, 58.0	4.72, 57.3
3	0.3059	0.5378	0.6939	4.71, 57.6	4.74, 57.0
4	0.3058	0.5378	0.6937	4.69, 58.3	4.74, 56.9
5	0.3061	0.5379	0.6939	4.71, 57.7	4.74, 57.0
6	0.3057	0.5376	0.6938	4.72, 57.5	4.75, 56.9

Table 5.11: Positions of the (110), (200) and ($\bar{1}$12) peak from the diffraction patterns in Fig. 5.6 and the corresponding lattice parameters. The parameters are determined from two pairs of peak positions: (110/200) and (110/$\bar{1}$12).

	Positions (Å^{-1})			Lattice Parameters a, α (Å, °)	
Pattern	(110)	(200)	($\bar{1}$12)	(110/200)	(110/$\bar{1}$12)
1	0.3041	0.5352	0.6912	4.76, 57.2	4.78, 56.7
2	0.3043	0.5355	0.6919	4.76, 57.1	4.78, 56.7
3	0.3044	0.5358	0.6918	4.75, 57.3	4.77, 56.7
4	0.3048	0.5356	0.6918	4.74, 57.5	4.75, 57.1
5	0.3049	0.5357	0.6932	4.75, 57.2	4.75, 57.1

Peak positions and calculated lattice parameters are given for three series of diffraction patterns from crystalline particles and are listed in Tables 5.10 to 5.12. The lattice parameters obtained differ between series, probably due to the calibration error, but are consistent within the experimental error when comparing patterns of the same experimental run. There is a systematic difference in the lattice parameters when determined with the (110/200) or (110/$\bar{1}$12) peak combination. The relatively large calibration error indicates that the *absolute values* of the peak positions cannot be used to determine the lattice parameters with the accuracy necessary to quantitatively measure, for example, size related changes in the parameters.

On the other hand, a deviation from bulk structure is clearly visible for all patterns that allow measuring the separation of the (112) and the (1$\bar{1}$0) peak (see Fig. 5.15). The separation of the peaks in relation to the particle size (Scherrer size estimates) is presented in Table 5.13 and shows that with increasing particle size the two peaks move further apart but are always closer together than the peaks from a bulk sample. Since the calibration error has a negligible effect on the *separation* of two adjacent peaks, the

Table 5.12: Positions of the (110), (200) and ($\bar{1}12$) peak from the diffraction patterns in Fig. 5.8 and the corresponding lattice parameters. The parameters are determined from two pairs of peak positions: (110/200) and (110/$\bar{1}12$).

	Positions (Å^{-1})			Lattice Parameters a, α (Å, °)	
Pattern	(110)	(200)	($\bar{1}12$)	(110/200)	(110/$\bar{1}12$)
1	0.3044	0.5355	0.6913	4.75, 57.3	4.77, 56.8
2	0.3043	0.5359	0.6919	4.76, 57.1	4.78, 56.6
3	0.3043	0.5361	0.6929	4.77, 56.9	4.79, 56.5

Table 5.13: Separation of the (112) and ($1\bar{1}0$) peaks as a function of the estimated mean size of the particles. The maximum error in the measurement of the separation is ±0.0006 Å^{-1}.

Figure	Pattern	Size Estimate (Scherrer) (Å)	Separation (Å^{-1})
5.5	6	76	0.0137
5.5	5	80	0.0139
5.5	4	77	0.0140
5.8	3	83	0.0141
5.6	4	86	0.0145
5.6	3	90	0.0145
5.6	2	90	0.0151
5.6	1	99	0.0160
Bulk	-	-	0.01775

Table 5.14: Separation of the (112) and the ($1\bar{1}0$) peak in patterns calculated from the lattice parameters for Bi particles published in [28] (X) and in [25] (A–F). The lattice parameters given in [25, 28] are specific to the hexagonal unit cell and have been converted to parameters of the rhombohedral cell.

Sample	Lattice Parameters a, α (Å, °)	Size Estimates (Å)	Separation (Å^{-1})
X	4.7139, 57.419	24	0.0165
A	4.7292, 57.385	89	0.0168
B	4.7346, 57.339	132	0.0170
C	4.7396, 57.296	168	0.0173
D	4.7417, 57.274	216	0.0174
E	4.7433, 57.262	269	0.0175
F	4.7444, 57.251	332	0.0176
Bulk	4.7459, 57.237	-	0.01775

distance between the peaks can be used to compared patterns from different series of measurements and to show qualitative changes in the structure of the particles.

The lattice distortion present in the Bi particles allows two interpretations: a lattice contraction due the finite size and therefore larger surface of the particles or that the peak shift is caused by lattice defects in the particles [38]. Both possibilities are

discussed in the following.

The size related contraction of Bi particles has been studied by X-ray diffraction for particles on carbon support with sizes from 89 to 332 Å [25] and for smaller particles embedded in a glass matrix with a mean diameter of 24 Å [28]. Table 5.14 shows the lattice parameters[4] of Bi particles published in [25, 28] together with the separation of the (112) and the $(1\bar{1}0)$ peak in the corresponding calculated diffraction pattern. As can be seen in Table 5.14 the lattice parameters indicate a lattice contraction that increases with decreasing particle size. In addition, the contraction becomes also visible as a reduced separation of the two peaks. However, the separations measured in this thesis work, listed in Table 5.13 (mean size: 76–99 Å), are systematically smaller than the separations in Table 5.14 (mean size: 24–332 Å) which suggests that the lattice distortion observed here is most likely caused by *lattice defects* in the particles and not by a size related lattice contraction.

Lattice defects in particles and especially planar defects (stacking faults, twin defects) can give rise to broadened and also displaced diffraction lines [38]. Thus, the presence of defects can explain the peak shifts and the discrepancy in the size estimates obtained from the diffraction pattern (Scherrer Equation, constrained inversion) and determined from TEM images of deposited clusters.

It should be emphasised that this interpretation of the peak shifts relies on the assumption that the lattice parameters of the clusters (mean diameter: 24 Å, see Table 5.14) embedded in a glass matrix are very close to those of same sized unsupported clusters. If this is not the case and if future TOF-MS size estimates reveal that the clusters are single crystalline (i.e. the TEM size estimates are incorrect), then the peak shifts could be interpreted as due to a size dependent lattice contraction of the particles.

Assuming that the particles are not single crystalline the question arises whether the Scherrer size estimates are correlated to the TEM size estimates or whether they are purely a function of the defect density. For patterns (2,5) in Fig. 5.5 the Scherrer and TEM size estimates are 64, 109 Å (pattern 2) and 80, 231 Å (pattern 5), showing that the domain size increases with increasing particle size.

In summary, the investigation of the peak separation in the experimental diffraction patterns supports the idea that the particles contain (planar) lattice defects and therefore consist of domains. This also means that their size is more accurately described by the TEM size estimates rather than by the size estimates obtained from the diffraction patterns.

[4]The lattice parameters published in [25, 28] are specific to the hexagonal unit cell and have been converted to parameters of the rhombohedral cell.

Background in the Diffraction Patterns

When comparing a measured diffraction pattern to a pattern with similar features calculated from a model cluster with a perfect rhombohedral structure the presence of a diffraction background becomes visible (see e.g. Fig. 5.15). The background varies with the source parameters but is noticeable in all experimental diffraction patterns. A very strong variation of the background as a function of the flow rate of the inert gas is, for example, visible in Fig. 5.7. Note that this background is not due to the inert gas in the beam since the gas contribution has been subtracted in all patterns presented in this chapter (see section 2.4).

In order to identify the cause of the background in the patterns the following possibilities were investigated:

- *Debye–Waller factor:* An increase in the temperature of the cluster and therefore an increase of the DW factor leads to a reduction of the intensity in the peaks. This intensity reappears as a background. However, even a Bi cluster with a temperature close to the melting point (Fig. 5.16a) shows a background considerably smaller than the one found in the experimental patterns.

- *Dynamic diffraction effects:* For larger clusters the kinematic approximation fails to provide the correct diffraction patterns for model clusters. This effect has been studied for gold clusters in [39] and is discussed in section 4.1. The available diffraction patterns for Au particles do not show a strong increase in background intensity and it is therefore unlikely that the background is caused by dynamic diffraction.

- *Atomic Bi, small molecules:* Figures 5.16b–d show experimental diffraction patterns together with the diffraction intensities for Bi_1 and Bi_2 which are scaled to fit the background as well as possible. While the background in Figs. 5.16b,c is quite well approximated by the intensities from Bi_1 and Bi_2, the background of the measured pattern in Fig. 5.16d exceeds the maximum possible contribution from Bi_1 and Bi_2 at low s. In this case, the background might be explained by a distribution of Bi_n molecules, including Bi monomers and dimers. A detailed analysis would require the structure of these molecules which, however, is not known. The experimental patterns in Figs. 5.16c,d were obtained in the same run but with different inert gas flow rates. The peaks in these two diffraction patterns are very similar despite the different background intensities which may

suggest that the background is not caused by structural changes but rather by a different distribution and intensity of Bi molecules in the cluster beam.

Finally, it is worth noting that diffraction patterns show an increased background if the particles contain disorder [38], for example, due to lattice defects or partial melting (e.g. liquid shell surrounding a crystalline core). These possibilities have not been investigated because of the lack of suitable model structures.

In summary, the background in the diffraction patterns is most likely caused by two contributions: the presence of a distribution of Bi_n molecules in the particle beam and lattice defects in the clusters. Lattice defects are expected because of the discrepancy in the size estimates (see section 5.7.4). These findings also show that it is very desirable to combine the diffraction experiment with a TOF mass spectrometer which would directly reveal the distribution of Bi_n molecules in the cluster beam.

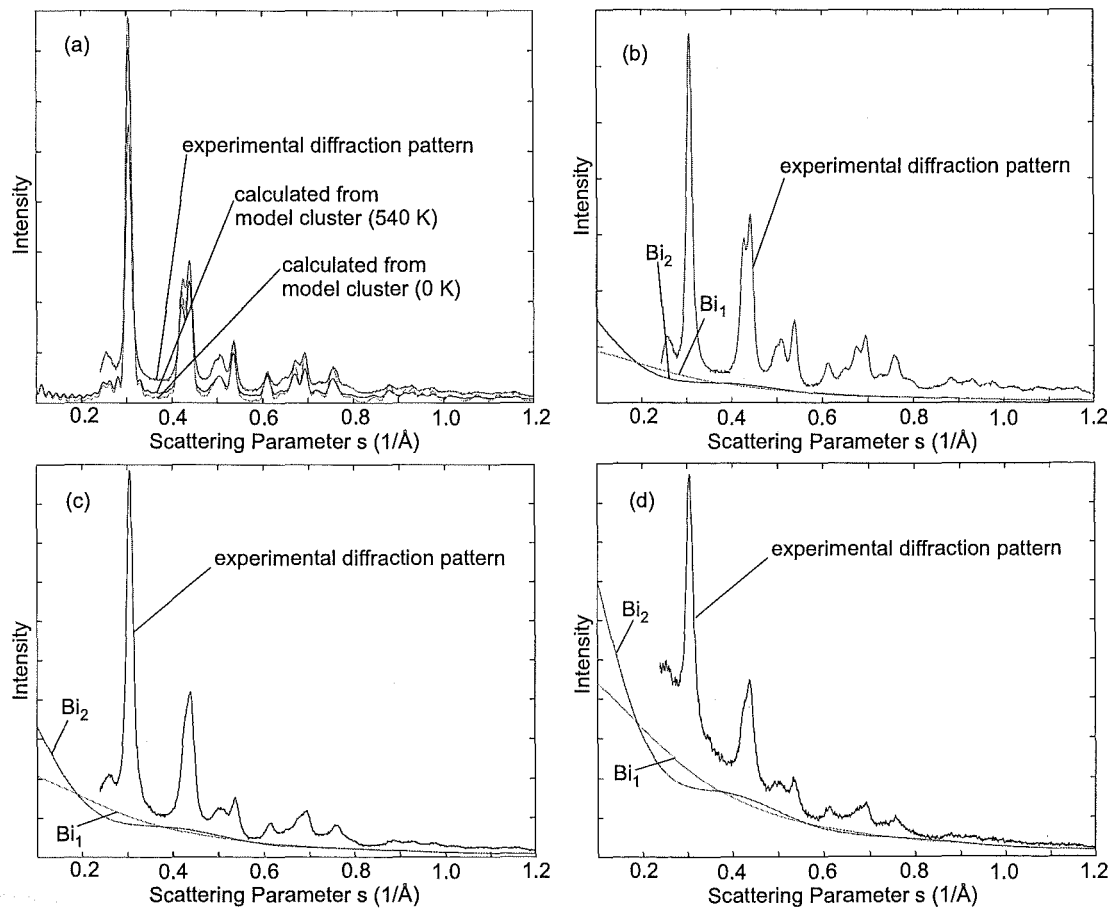

Figure 5.16: Investigation of the background in the experimental diffraction patterns. (a) Influence of the cluster temperature on the background. (b–d) The diffraction patterns from Bi_1 and Bi_2 as a possible explanation of the background in three experimental patterns from (b) Fig. 5.5, pattern (5) and (c,d) Fig. 5.7, patterns (2,3).

Fitting of Diffraction Patterns from Model Structures

In the previous studies on Ag, Cu and Pb clusters [40–42] the diffraction patterns have been mainly analysed by fitting calculated patterns of model structures to the experimental diffraction patterns (see section 4.2.1). For these metals a wealth of structural information from experimental and theoretical work is available. Most importantly, the availability of well tested potentials for MD simulations made it possible to include more realistic imperfect structures in the study and also to explore new structures.

In the case of the Bi clusters investigated in this study, diffraction patterns were not analysed using the fitting procedure because of the following reasons: Firstly, there are no model structures available for large Bi clusters with defects. This is because of the lack of details concerning the type of defects and difficulties to create models of imperfect Bi crystals. In addition, MD simulations could not be employed since a well-tested potential for the 'exotic' material Bi is not available. Secondly, for clusters with sizes ranging from approximately 90 to 231 Å (TEM size estimates) dynamic diffraction effects may become important (see section 4.1) and have to be considered when diffraction patterns are calculated from model structures. So far, we can only calculate diffraction patterns by using the Debye Equation (see section 4.1) which is based on the kinematic approximation for electron diffraction and does not consider dynamic effects.

Peak Intensities and Peak Ratios

A very interesting feature in the patterns from crystalline clusters (see Fig. 5.5) is the splitting of the second peak ($s \approx 0.40$–0.45 Å^{-1}) and the relative intensities of the two sub-peaks. The splitting of the peak is directly related to the size of the domains in the particles. With increasing domain size the width of the peaks decreases allowing the two peaks to be resolved. Figure 5.17a shows three typical measured diffraction patterns in which the peak splitting is visible. The important feature is that, as indicated by the arrows, the peak on the low s side is always smaller than the peak on the high s side.

As shown in section 4.3 the diffraction patterns calculated from single crystalline clusters and in particular the relative intensities of the two peaks between $s = 0.4$ Å^{-1} and $s = 0.45$ Å^{-1} are very sensitive to the cluster shape. Therefore, the series of diffraction patterns for different particle shapes and sizes from section 4.3 have been compared with the experimental data. As a result, four particle shapes have been identified that give rise to diffraction patterns with a double peak ($s \approx 0.40$–0.45 Å^{-1}) for which the low s peak is smaller than or equal to the high s peak. These calculated patterns are

displayed together with typical experimental patterns in Figs. 5.17–5.20.

The diffraction patterns in Fig. 5.17 are calculated from model clusters with a shape as suggested in [22]. According to [22] the model is valid for clusters smaller than 84 Å. Among the patterns from the four particle shapes (Figs. 5.17–5.20) the patterns in Fig. 5.17b show a low s peak that is only slightly smaller than the high s peak and therefore display the least agreement of the peak ratio between calculated and experimental patterns. The shape of the particles is shown in the inset of Fig. 5.17b. Since the experimental patterns do not agree well with these patterns from a relatively spherical clusters (see also Fig. 4.11) it suggests that a particle with a more aspherical shape is preferable.

According to [22] clusters larger than 84 Å have a complicated structure with lattice defects and are faceted by {110} and {111} surfaces. A size series of diffraction patterns for a single crystalline cluster (no defects) faceted by six {110} and two {111} planes is shown in Fig. 5.18. Here, the peak ratio is very close to the ratio found in the experimental patterns.

In order to try out different particle shapes six surface types have been considered ($\{111\}, \{011\}, \{100\}, \{112\}, \{1\bar{1}0\}$). Each set of planes is associated with a parameter specifying the distance of the planes to the origin of the particle. Therefore, there are six free parameters to characterise the shape of a cluster. As a result, two more characteristic particle shapes (Figs. 5.19 and 5.20) have been found that are in good agreement with the experimental data. These are single crystalline particles (Bi bulk structure) faceted by two {112} and six $\{1\bar{1}0\}$ surfaces (relative distances of the planes: 1.0, 1.5) and the particles faceted by two {111} and six $\{1\bar{1}0\}$ surfaces (relative distances of the planes: 0.65, 1.0). Hence, the features in the experimental patterns agree well with the patterns from three particle shapes.

This analysis is limited to investigating the relative intensities of the two peaks between $s = 0.4$ Å^{-1} and $s = 0.45$ Å^{-1} which vary strongly with cluster shape. Finer details in other peaks are not studied since the peak shapes and intensities are also influenced by the size distribution and the temperature of the particles (Debye–Waller factor).

Assuming that the clusters are large and contain defects, the diffraction patterns are indicative only of the domains within the clusters (see section 4.3.2). Therefore, provided that inter-domain scattering (interference) effects can be neglected, these three particle shapes are possible candidates for the shape of the domains. In addition, the fact that the onset of the peak splitting is related to the size of the domains allows

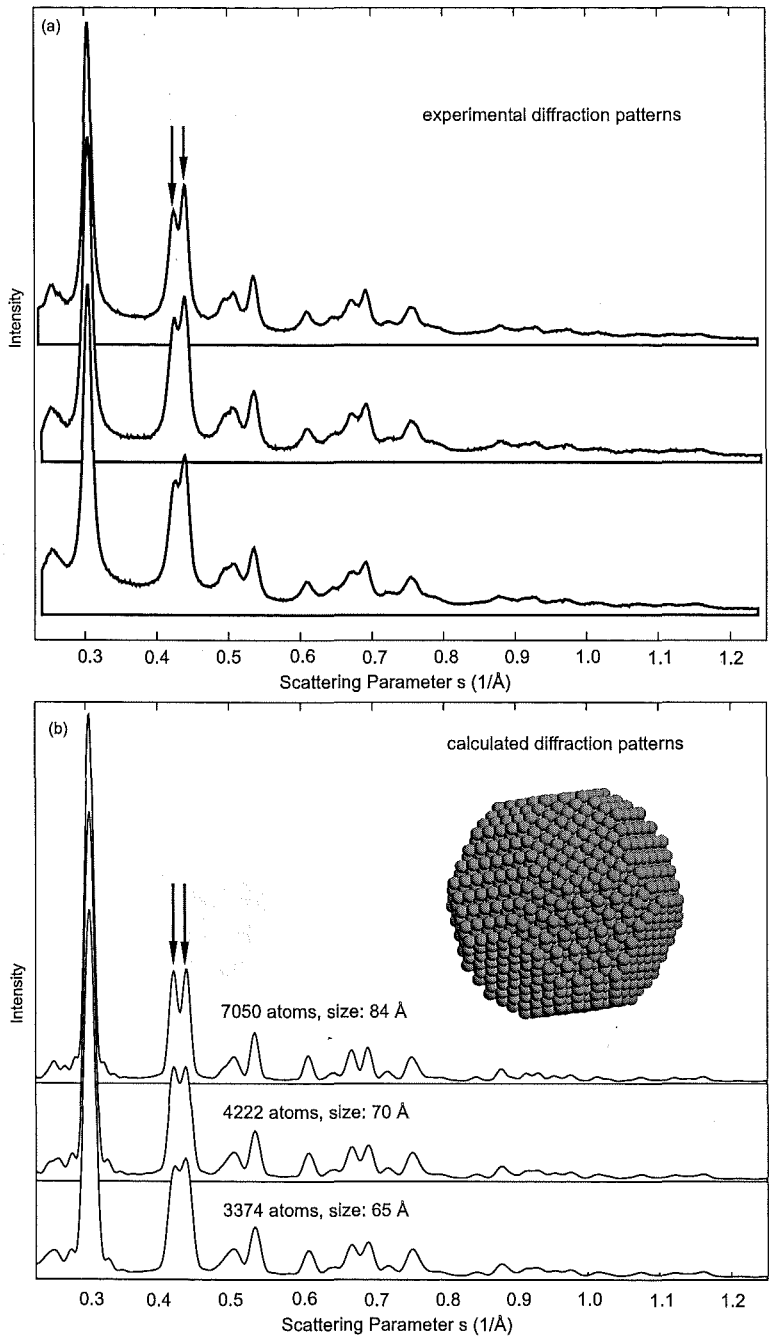

Figure 5.17: Comparison of experimental (a) and calculated diffraction patterns (b) with emphasis on the relative intensities of the two peaks between $s = 0.4$ Å^{-1} and $s = 0.45$ Å^{-1}. (a) Experimental patterns from Fig. 5.7, pattern (3) and Fig. 5.5, patterns (3,5). (b) Calculated patterns from a series of model clusters described in [22]. The clusters are single crystalline (Bi bulk structure) and are faceted by two {111}, six {011}, six {100}, six {112} and six $\{1\bar{1}0\}$ surfaces. The relative distances of the surfaces to the centre of the particle are 0.85, 0.9, 0.95, 1.0, 1.05 in the order of the sets of planes given above. The values of the parameters were chosen according to the Wulff's criterion [43] to agree with the order of surface energies suggested in [22]. Since the actual values of the surface energies are not known variations of these parameters have been investigated while roughly maintaining a cluster shape as shown in [22]. These attempts, however, did not lead to a peak ratio in the second peak ($s \approx 0.4$–0.45 Å^{-1}) that agrees better with the experimental data. The given values for the particle size refer to the largest interatomic distance.

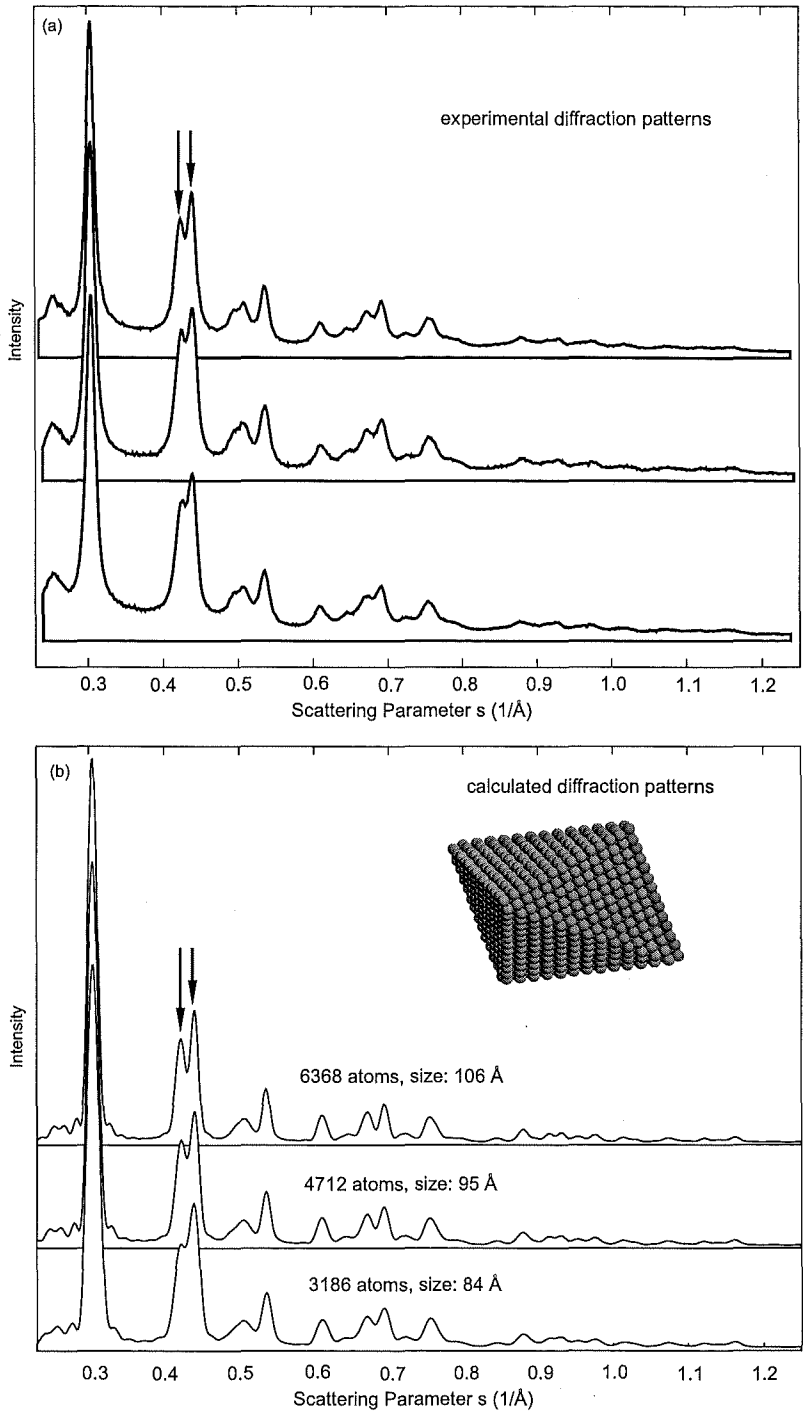

Figure 5.18: Comparison of experimental (a) and calculated diffraction patterns (b) with emphasis on the relative intensities of the two peaks between $s = 0.4$ Å^{-1} and $s = 0.45$ Å^{-1}. (a) Experimental patterns from Fig. 5.7, pattern (3) and Fig. 5.5, patterns (3,5). (b) Calculated patterns from a series of model clusters. The clusters are single crystalline (Bi bulk structure) and are faceted by two {111} and six {011} surfaces. The relative distances of the surfaces to the centre of the particle are 0.75 and 1.0 in the order of the sets of planes given above. The given values for the particle size refer to the largest interatomic distance.

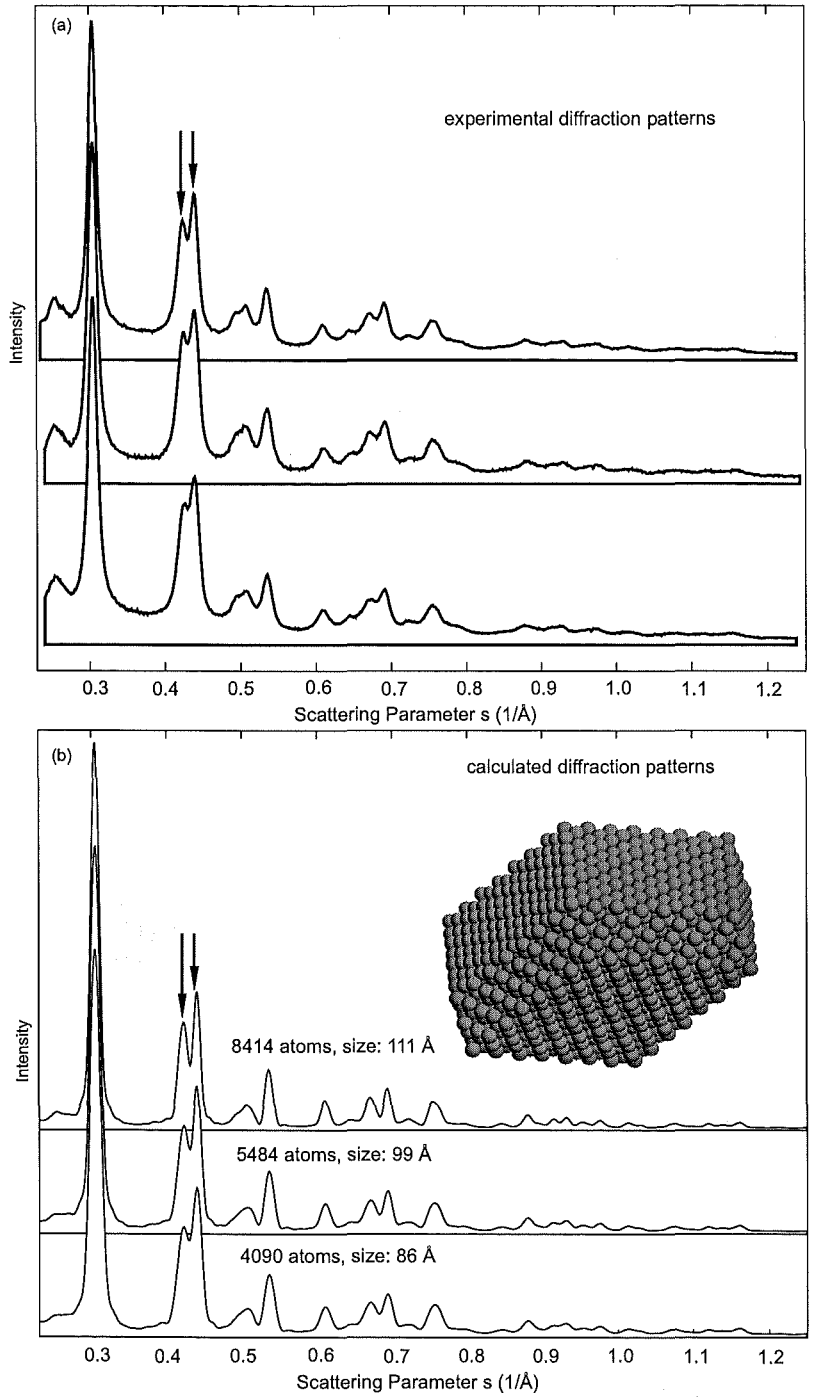

Figure 5.19: Comparison of experimental (a) and calculated diffraction patterns (b) with emphasis on the relative intensities of the two peaks between $s = 0.4$ Å^{-1} and $s = 0.45$ Å^{-1}. (a) Experimental patterns from Fig. 5.7, pattern (3) and Fig. 5.5, patterns (3,5). (b) Calculated patterns from a series of model clusters. The clusters are single crystalline (Bi bulk structure) and are faceted by two {112} and six $\{1\bar{1}0\}$ surfaces. The relative distances of the surfaces to the centre of the particle are 1.0 and 1.5 in the order of the sets of planes given above. The given values for the particle size refer to the largest interatomic distance.

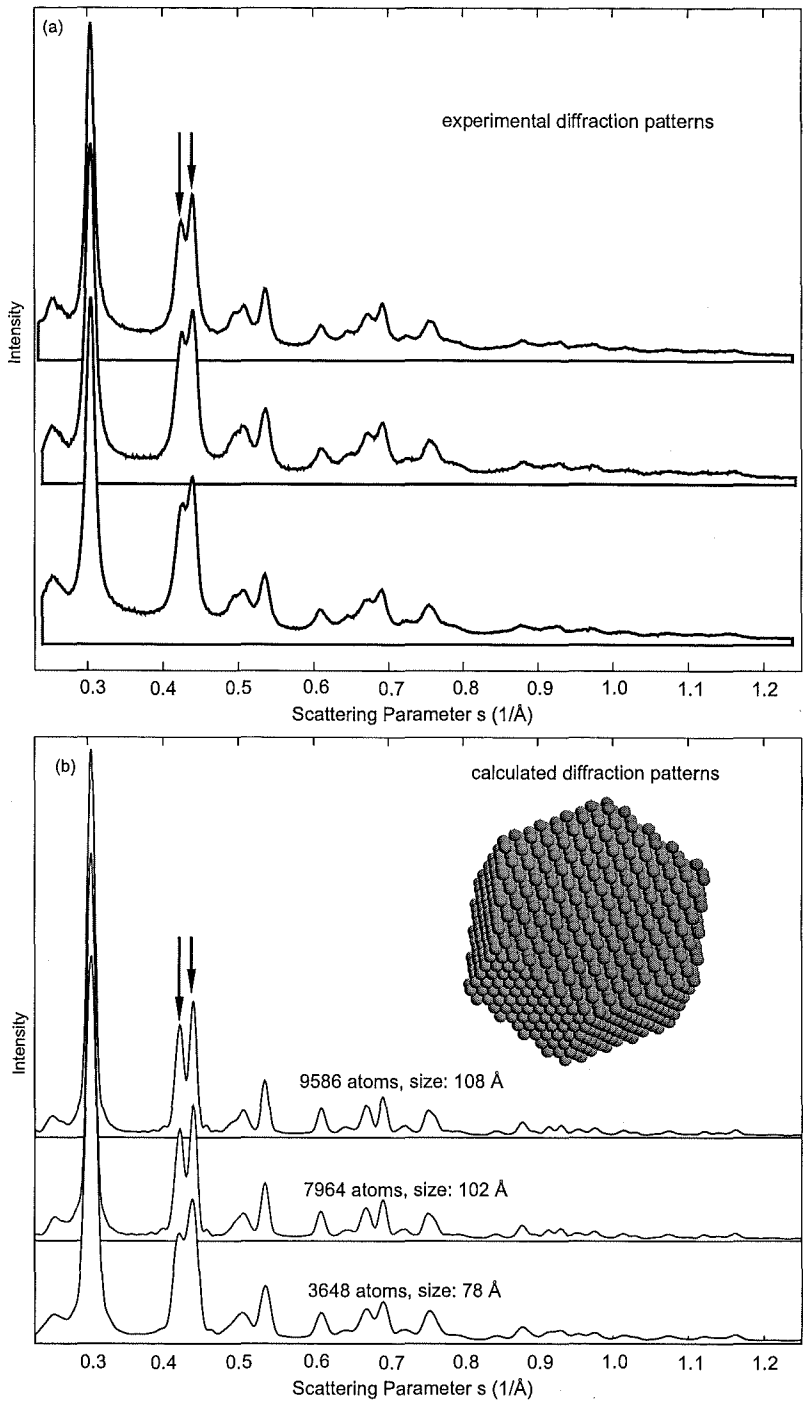

Figure 5.20: Comparison of experimental (a) and calculated diffraction patterns (b) with emphasis on the relative intensities of the two peaks between $s = 0.4$ Å^{-1} and $s = 0.45$ Å^{-1}. (a) Experimental patterns from Fig. 5.7, pattern (3) and Fig. 5.5, patterns (3,5). (b) Calculated patterns from a series of model clusters. The clusters are single crystalline (Bi bulk structure) and are faceted by two {111} and six $\{1\bar{1}0\}$ surfaces. The relative distances of the surfaces to the centre of the particle are 0.65 and 1.0 in the order of the sets of planes given above. In this case, the peak ratio of the second peak is very sensitive to the ratio of the two distance parameters with 0.65 providing the best match of the peak ratio to the experimental data. The given values for the particle size refer to the largest interatomic distance.

the estimation of the domain size. Figures 5.18, 5.19 and 5.20 reveal that the peak splitting becomes visible for clusters with approx. 3300 atoms and a size between 75 and 85 Å.

If, however, future TOF-MS measurements show that cluster sizes agree with the size estimates from the diffraction patterns and therefore the clusters are likely to be single crystalline then the shapes shown in Figs. 5.18, 5.19 and 5.20 represent three possible shapes of the clusters.

Compared to the patterns in Fig. 5.17a, patterns (1,2) in Fig. 5.11 show a slightly different shape of the double peak. In these two patterns the low s peak is also smaller than the high s peak but appears to be not as large as the low s peak (relative to the high s peak) in the patterns in Fig. 5.17a. The difference in peak shape, however, is only small so that the particles shown in Figs. 5.18b to 5.20b are still reasonable models for the domain or cluster shape.

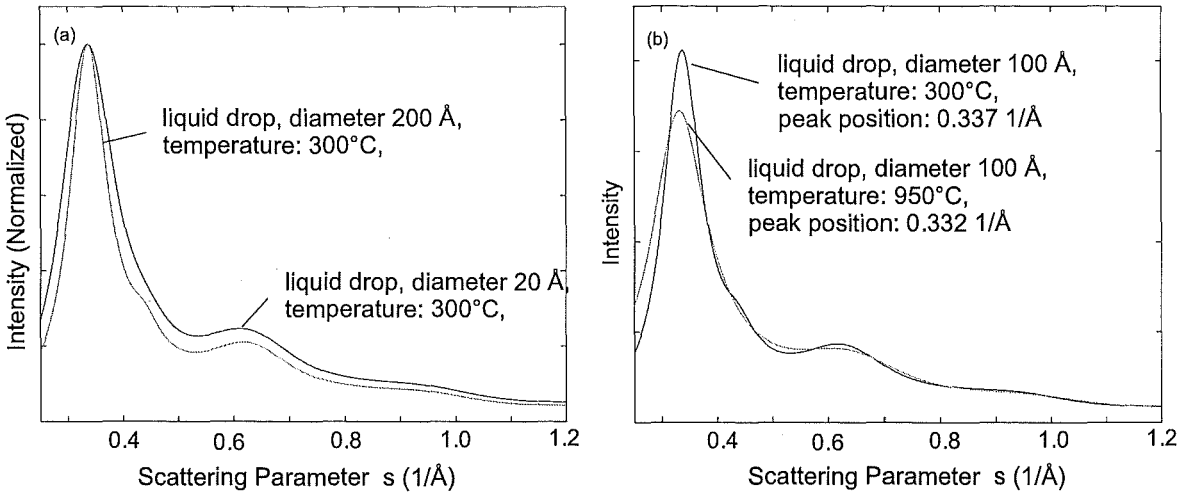

Figure 5.21: Influence of size (a) and temperature (b) of liquid particles on the diffraction patterns. The diffraction patterns are calculated from the analytical expression of the structure factor data for Bi presented in [48].

5.7.6 Analysis of Patterns from Amorphous Clusters

The diffraction patterns with liquid/amorphous features (e.g. Fig. 5.12, pattern (5)) have characteristic broad peaks and a shoulder on the high s side of the first peak. The position of the first peak ranges from 0.3247 $Å^{-1}$ to 0.3296 $Å^{-1}$ (average: 0.326 $Å^{-1}$) for the patterns investigated. Note that the first peak for the crystalline bulk structure is at $s = 0.3046$ $Å^{-1}$. The liquid/amorphous diffraction patterns also show a variation in background.

The structure of liquid bismuth has been investigated by neutron, electron and X-ray diffraction techniques [44–46]. The structure factor data (see section 4.3.3) is available for various temperatures of the liquid metal. Xian-Wou Zou *et al.* [47, 48] have derived a theoretical expression for the structure factor of liquid Bi and calculated the necessary parameters by fitting it to experimental data. In this thesis work, the analytical form of the structure factor is used to calculate diffraction patterns for small liquid drops. Detailed information about the method and the results can be found in section 4.3.3. In the following only the main trends are outlined. Figure 5.21 shows the influence of size and temperature of the liquid Bi drops on the diffraction patterns. As clusters get smaller the width of the first peak increases and the shoulder peak becomes less pronounced. With increasing temperature the first peak shifts to smaller scattering angles s, reflecting a decrease in density of the liquid. In addition, the shoulder peak nearly disappears at high temperatures.

Figure 5.22 shows a comparison of a typical diffraction pattern measured in this

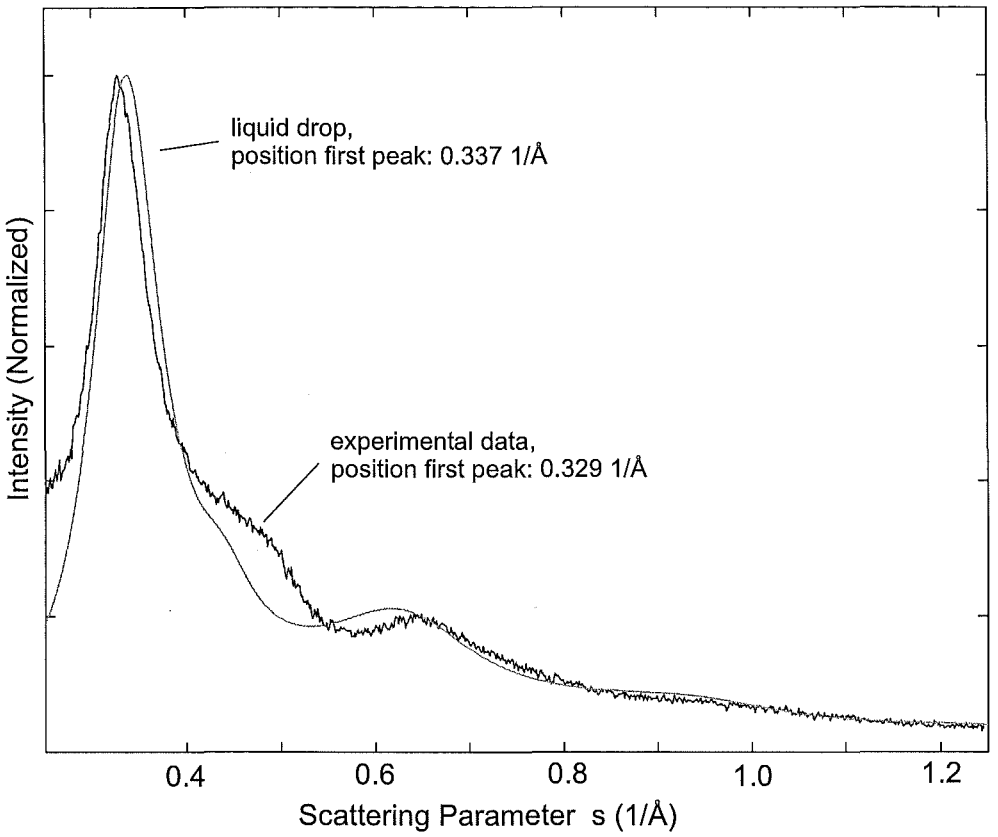

Figure 5.22: Comparison of a typical experimental diffraction pattern with amorphous features and a diffraction pattern of a 100 Å liquid drop with a temperature of 300°C. The measured pattern is pattern (4) in Fig. 5.10.

work with a calculated diffraction pattern for a 100 Å liquid drop of Bi with a temperature of 300°C. The patterns are similar in their features, however, there is no agreement in the positions of the peaks. In the measured pattern the first peak is located at smaller s and the second peak at larger s relative to the pattern of the liquid drop. The position of the first peak ($s = 0.329$ Å^{-1}) is not in the range of peak positions ($s = 0.337$ Å^{-1} (300°C), $s = 0.332$ Å^{-1} (950°C) expected for liquid Bi drops with a temperatures between 300 and 950°C (see Fig. 5.21b). Therefore, the peak position cannot be explained alone by a change in temperature. In addition, the shoulder peak is much more pronounced in the experimental data, and occurs at much larger s.

5.8 Discussion and Conclusions

A finding important for the interpretation of the results is that the particle size estimates obtained from the diffraction patterns are significantly smaller than the sizes calculated from the TEM images of deposited clusters. Assuming that the TEM size estimates are correct the interpretation of the patterns with crystalline features can be summarised as follows:

- The crystalline Bi clusters have a mean particle size ranging from approximately 109 to 231 Å and contain lattice defects. The peak positions in the patterns are very close to the positions expected for the rhombohedral structure of the bulk material. The small deviations in the peak positions are probably caused by the presence of lattice defects. Therefore, the three particle shapes that have been identified from the features in the diffraction patterns represent possible shapes of the domains within the particles.

On the other hand, it cannot completely ruled out that clusters, for example, acquire a flattened shape because of the deposition process which would lead to an over-estimate of the sizes and therefore invalidate the TEM size estimates. If in this case it is assumed that the particles have the sizes as estimated from the diffraction patterns the interpretation of the results would be:

- The pattern with crystalline features are from single crystalline clusters with mean sizes ranging from approximately 50–100 Å. The clusters have a rhombohedral structure and the deviation of peak positions from the positions expected for the bulk structure might be explained by a lattice contraction that increases with decreasing particle size. Note that this interpretation does not agree with the relatively small lattice contraction measured for particles (mean diameter 24 Å) embedded in a glass matrix [28] since a larger contraction is necessary to explain the experimental peak separation (see Tables 5.13, 5.14). Therefore, this interpretation requires that the lattice contraction of clusters embedded in a glass matrix is not comparable to the contraction of a same sized *free* cluster. In this scenario, there are three possible particle shapes (shape of the whole particle) that agree with the features in the measured diffraction patterns.

All patterns with crystalline features show a background that varies depending on the source conditions. The most plausible explanation is the existence of Bi_n molecules or small clusters in the beam. There are three possible ways of dealing with the background

in the patterns. Firstly, the background could be subtracted if the relative abundances of the molecules and their structure were known. Information about mass spectrum of the molecules could be obtained with a TOF-MS. The difficult part, however, is to find structural data (experimental, ab initio calculations) for small Bi_n clusters which is not available to the extent necessary. Secondly, the calculated diffraction patterns from Bi_n clusters could be included in the analysis (fitting of calculated pattern of model structures). This approach, however, is also hampered by the lack of structural data. Furthermore, the large number of additional patterns included in the fitting procedure also increases the number of free fitting parameters which may make it difficult to find a correct solution (multiple solutions). In this case, the mass spectrum from a TOF-MS could be very useful to approve or reject solutions from the fitting procedure. Thirdly, a TOF-MS may allow to tune the source parameters so that the background from small Bi_n clusters is negligible. This all shows how useful a TOF-MS would be for the interpretation of the diffraction measurements. Not only would TOF spectra provide reliable size measurements without the problems associated with substrates but would also offer data about the abundance of small clusters in the beam. Moreover, a TOF-MS delivers data in real time and therefore allows much better tuning of the mean particle size and distribution of sizes by varying the source parameters.

The diffraction patterns with liquid/amorphous features have been compared to patterns of small liquid drops calculated from diffraction data (literature data) of liquid bismuth. The comparison shows that the patterns have similar features but different peak positions. The most striking difference is that the first and second peak in the measured patterns are shifted in opposite direction relative to the liquid patterns. The other typical feature, the shoulder peak at the high s side of the first peak, is much more pronounced in our data.

The calculated diffraction patterns for small drops are based on the structural data of bulk liquid Bi and do not consider size related structural changes. Such a change could be a compression of the liquid clusters due to the large surface tension of small drops. A compression of the drops (higher density, smaller interatomic distance), however, would shift the first peak in the calculated pattern towards larger s and therefore further away from the peak of the experimental pattern. Consequently, this scenario is unlikely.

The diffraction data for liquid Bi available for different temperatures (300°C–950°C) shows an increase of the shoulder peak with decreasing temperature. Following this trend, temperatures below the bulk melting point (271°C) would be necessary to obtain

a strong shoulder peak as measured in this work. Supercooling effects for small Bi particles have been studied by Takagi *et al.* [12] and solidification temperatures as low as 110°C for 50 Å particles have been found. A temperature for liquid clusters below the bulk melting point might account for the prominent shoulder but a low temperature of the particles leads to a higher density and therefore further increases the difference in the peak positions (first peak), suggesting that a supercooling of the particles alone cannot explain the features in the diffraction patterns.

The remaining possibility is a completely amorphous structure of the particles. In inert-gas aggregation sources metal vapour is quenched by an inert buffer gas. During this very short cooling process amorphous structures may be frozen in and are unlikely to change into a crystalline structure in the short time before they are probed by the electron beam. It has been reported that Bi deposited onto cold surfaces ($T = 2$ K) forms amorphous films [4]. These films are stable up to about 15 K and change to the rhombohedral structure for higher temperatures. The stability of the amorphous phase can be understood by the fact that large displacements are necessary to rearrange atoms from a nearly close-packed configuration to the rhombohedral structure with its large lattice cell. Other studies on quench condensed Bi films [49] found a transition from an amorphous to a granular structure ($T = 8$ K) for films with an effective thickness of about 12–14 Å. Raman-scattering measurements on Bi clusters [50] deposited on a substrate at 110 K indicate a transformation with decreasing size from clusters with rhombohedral structure to amorphous particles. The transformation occurs at a cluster size of about 1300 atoms. Using the same technique Merkulov *et al.* [51] investigated Bi clusters on carbon supports below and above the bulk melting point. Larger clusters showed the typical Raman spectra of nanocrystalline particles below the melting point, and spectra of liquid particles above the melting point. In contrast to that, small clusters with a temperature below the bulk melting point show Raman spectra that resemble the spectra in [50] from amorphous clusters measured at 110 K. The critical size for this transition has been estimated to be approx. 1000 atoms (cluster diameter: 45–75 Å).

The liquid/amorphous clusters investigated in this thesis work have a mean particle size of between 69–96 Å (TEM size estimates) and are therefore larger than the critical size for the transition from amorphous to crystalline clusters as reported in [51]. However, since the TEM size estimates also show that crystalline clusters are always larger than amorphous clusters it is possible that there is a (larger) critical size for a structural transition. In this context, it is also interesting to look at the series of

diffraction patterns in Fig. 5.10 which shows the transition from a pattern with pure liquid/amorphous features to patterns with mostly crystalline features as a function of an increasing Ar/He ratio of the carrier gas. On one hand, the production of mostly crystalline clusters at higher Ar/He ratios could be the result of an improved cooling of the metal vapour. On the other hand, a larger Ar content also results in larger particles sizes (TEM size estimates) which could lead to crystalline clusters if there is a size dependent transition from amorphous to crystalline. Since the influence of these two factors (improved cooling, particle size) cannot be investigated independently it is difficult to say what exactly causes the transition from amorphous to crystalline clusters.

In this thesis work, the parameter space of the inert-gas aggregation source has been explored in order to produce beams of Bi clusters with a wide range of (mean) sizes, and with a particular focus on small particles. Crystalline clusters were obtained with mean particle sizes from approx. 109 to 231 Å. The amorphous clusters investigated were found to be smaller with sizes between 69 and 96 Å. Despite all efforts it has not been possible to produce cluster beams with a smaller mean particle size.

References

[1] A. Yokozeki and G. D. Stein, J. Appl. Phys. **49**, 2224 (1978).

[2] R. W. G. Wyckoff, *Crystal Structures*, volume 1, John Wiley & Sons, 1963.

[3] D. A. Young, *Phase Diagrams of the Elements*, The University of California Press, 1991.

[4] W. Buckel, Some remarks on crystal growth in thin films, in *Structure and Properties of Thin Films*, edited by C. A. Neugebauer, J. B. Newkirk, and D. A. Vermilyea, pages 53–57, Wiley, NY, 1959.

[5] J. Mühlbach, P. Pfau, E. Recknagel, and K. Sattler, Surf. Sci. **106**, 18 (1981).

[6] M. E. Geusic and R. R. Freeman, J. Chem. Phys. **89**, 223 (1988).

[7] J. Mühlbach, E. Recknagel, and K. Sattler, Surf. Sci. **106**, 180 (1980).

[8] K. Sattler, J. Mühlbach, and E. Recknagel, Phys. Rev. Lett. **45**, 821 (1980).

[9] P. Pfau, K. Sattler, J. Mühlbach, R. Pflaum, and E. Recknagel, J. Phys. F **12**, 2131 (1982).

[10] E. Recknagel, Ber. Bunsenges. Phys. Chem. **88**, 201 (1984).

[11] M. Takagi, J. Phys. Soc. Jap. **9**, 359 (1954).

[12] M. Takagi, J. Phys. Soc. Jap. **11**, 396 (1956).

[13] V. P. Skripov, V. P. Koverda, and V. N. Skokov, phys. stat. sol. (a) **66**, 109 (1981).

[14] G. L. Allan, R. A. Bayles, W. W. Gile, and W. A. Jesser, Thin Solid Films **144**, 297 (1986).

[15] M. Treilleux et al., Z. Phys. D **20**, 263 (1991).

[16] T. B. David, Y. Lereah, G. Deutscher, R. Kofman, and P. Cheyssac, Phil. Mag. A **71**, 1135 (1995).

[17] Y. Lereah, G. Deutscher, P. Cheyssac, and R. Kofman, Europhys. Lett. **8**, 53 (1989).

[18] Y. Lereah, G. Deutscher, P. Cheyssac, and R. Kofman, Europhys. Lett. **12**, 709 (1990).

[19] M. Treilleux et al., Z. Phys. D **12**, 131 (1989).

[20] G. Fuchs et al., Phil. Mag. A **61**, 45 (1990).

[21] M. Treilleux et al., Phil. Mag. A **67**, 1071 (1992).

[22] Y. Oshima, K. Takayanagi, and H. Hirayama, Z. Phys. D **40**, 534 (1997).

[23] J. Fang, K. L. Stokes, W. L. Zhou, C. B. Murray, and C. J. O. Connor, Mat. Res. Soc. Symp. Proc. **676**, Y8.9.1 (2001).

[24] J. Fang, K. L. Stokes, W. L. Zhou, W. Wang, and J. Lin, Chem. Commun. **18**, 1872 (2001).

[25] X. F. Yu, X. Liu, K. Zhang, and Z. Q. Hu, J. Phys. Condens. Matter **11**, 937 (1999).

[26] A. M. Stoneham, J. Phys. Condens. Matter **11**, 8351 (1999).

[27] X. F. Yu, J. Phys. Condens. Matter **11**, 8353 (1999).

[28] G. Kellerman and A. F. Craievich, Phys. Rev. B **65**, 134204 (2002).

[29] M. Yan et al., Phys. Rev. B **47**, 5571 (1993).

[30] P. T. Cummings, Metal Phys. **9**, 1477 (1979).

[31] J. L. Bretonnet, G. G. Gasser, A. Bath, and R. Kleim, phys. stat. sol. (b) **114**, 243 (1982).

[32] J. L. Bretonnet, Solid State Comm. **47**, 395 (1983).

[33] F. S. Aires et al., Z. Phys. D **12**, 149 (1989).

[34] L. E. Russel, Powder Metallurgy **10**, 239 (1967).

[35] S. B. Cronin et al., Nanotechnology **13**, 653 (2002).

[36] K. W. Andrews, D. J. Dyson, and S. R. Keown, *Interpretation of electron diffraction patterns*, Adam Hilger Ltd., 1971.

[37] E. F. Cave and L. V. Holroyd, J. Appl. Phys. **31**, 1357 (1960).

[38] A. Guinier, *X-Ray Diffraction in Crystals, Imperfect Crystals, and Amorphous Bodies*, W. H. Freeman and Company, 1963.

[39] B. D. Hall, U. Ugarte, D. Reinhard, and R. Monot, J. Chem. Phys. **103**, 2384 (1995).

[40] B. D. Hall, *An Installation for the Study of Unsupported Ultrafine Particles by Electron Diffraction with Application to Silver: Observation of Multiply Twinned Particle Structures*, PhD thesis, EPFL, 1991.

[41] D. Reinhard, *Croissance et Stabilité d'Agrégats d'Argent et de Cuivre, Etudiés en Jets Moléculaires par Diffraction d'Electrons à Haute Energie*, PhD thesis, EPFL, 1996.

[42] M. Hyslop, *Electron Diffraction Studies of Unsupported Clusters*, PhD thesis, University of Canterbury, 2002.

[43] G. Wulff, Z. Kristallog. **34**, 449 (1901).

[44] P. C. Sarrah and G. P. Smith, J. Chem. Phys. **21**, 228 (1953).

[45] P. C. Sarrah and R. F. Kruh, J. Chem. Phys. **32**, 241 (1960).

[46] Y. Waseda, *The Structure of Non-crystallic Materials, Liquids and Amorphous Solids*, McGraw-Hill Publ. Co., New York, 1980.

[47] X.-W. Zou, Z.-Z. Jin, and Y.-J. Shang, phys. stat. sol. (b) **139**, 365 (1984).

[48] X.-W. Zou, Z.-Z. Jin, and S.-Q. Tang, phys. stat. sol. (b) **142**, 9 (1984).

[49] M. M. Rosario and Y. Liu, Phys. Rev. B **65**, 094506 (2002).

[50] M. G. Mitch, S. J. Chase, J. Fortner, R. Q. Yu, and J. S. Lanin, Phys. Rev. Lett. **67**, 875 (1991).

[51] V. I. Merkulov and J. S. Lannin, Phys. Rev. B **58**, 7373 (1998).

Chapter 6

Conclusions and Outlook

Electron Diffraction on a molecular beam containing small particles is a very powerful technique to study the structure of unsupported clusters. The major advantage is that the particles are probed in a high vacuum environment and are therefore free of contamination and any perturbing effects due to a substrate. In addition, the clusters are only exposed to the electron beam for a short time, minimising the interaction of the electron beam with the sample. However, these advantages come at the price of a complicated analysis of the diffraction patterns as the beam consists of randomly oriented particles with possibly different sizes and structures.

The two main parts of this thesis work are the development of a new detector system to record the electron diffraction patterns, and the study of the structure of unsupported Bi clusters. In addition, two new analysis tools based on the Reverse Monte Carlo method and a constrained inversion technique have been developed and implemented.

The new detector system uses a pair of linear diode arrays to measure the radial intensity profile of the ring diffraction pattern. It is operated in integration mode and thereby avoids the systematic errors of its predecessor that were caused by using the counting mode. Compared to the old detector the quality of the diffraction patterns has been improved considerably. The typical time for a measurement of a high quality diffraction pattern is about 50 seconds.

Several series of diffraction patterns from crystalline as well as liquid or amorphous Bi clusters have been presented in chapter 5. Using Ar as the inert gas the patterns are from crystalline clusters. When using He the features in the patterns changed from purely liquid/amorphous to crystalline with increasing pressure (flow rate) of the inert gas. A similar transition could be achieved by increasing the Ar content in a He/Ar gas mixture from 0% to about 35%. There are diffraction patterns that show liquid/amorphous as well as crystalline features.

The structure of the crystalline clusters has been identified as being rhombohedral. It has been found that particle sizes estimated from the diffraction patterns are signif-

icantly smaller than size estimates obtained from TEM images of deposited clusters. Since there is no direct evidence that the TEM size estimates are influenced by the substrate or the deposition process (flattened shape of the clusters), the most plausible interpretation is that the crystalline particles have a mean size ranging from 109 to 231 Å and contain lattice defects. In this case, the diffraction patterns are characteristic of the domains within the particles. By comparing the peak ratios in the measured diffraction pattern to the peak ratios in calculated patterns from model structures, three particles shapes have been identified that are possible approximations of the shape of the domains.

The patterns with crystalline features also show a diffraction background that varies depending on the source conditions. The most plausible explanation is the existence of Bi_n molecules or small clusters in the cluster beam.

The diffraction patterns with liquid/amorphous features have been compared to patterns of small drops calculated from structure factor data of liquid Bi. Although the patterns are similar in their features, the peak positions do not agree and the experimental patterns show a much more pronounced shoulder peak, therefore, suggesting a new amorphous structure that is different to the structure of bulk liquid Bi. The mean size of the amorphous particles, estimated from TEM images, ranges from 69–96 Å.

In the present setup of the diffraction experiment, the analysis of the diffraction patterns is limited by several factors:

Firstly, the inert gas aggregation source produces a distribution of particles sizes with variable and unknown temperature. As a consequence, the analysis has to cope with a large number of unknown parameters which in turn reduce the level of details that can be extracted from a diffraction pattern. Another difficulty related to a broad size distribution of the particles arises from the fact that the diffraction signal is proportional to the particle volume. If small particles are produced together with larger particles the diffraction pattern is dominated by the signal of the larger particles which makes it very difficult to investigate the smaller particles. Secondly, diffraction patterns from model structures are calculated with the Debye Equation which is part of the kinematic diffraction theory. For larger particles and heavy elements, the Debye Equation becomes inaccurate and dynamic diffraction effects have to be considered to retrieve as much information as possible from the patterns. It has been shown in [1] that it is possible, although computationally expensive, to include dynamic effects by using the multi-slice method. At present, this technique is not available as a general tool.

In general, the experiment would greatly benefit from modifications that reduce the number of unknown parameters. This could be achieved by

- the use of a mass spectrometer or a mass filter. A time-of-flight mass spectrometer (TOF-MS) is currently being designed and will replace the existing TEM sampling. It will allow real-time measurement of the size distribution and should avoid the problems of the TEM sampling (contact with a substrate, contamination) completely. A further increased level of quality could be achieved with a mass filter since the size distribution would be narrower and also tuneable. Disadvantages of mass spectrometer and filters are the need to ionise the clusters and in the case of the mass filter a much lower cluster intensity.

- the installation of a drift chamber between the source and the diffraction chamber to thermalise the particles [2, 3]. This modification would allow the study of the temperature dependence of physical properties of the clusters. Such a device would also lead to a reduced cluster intensity.

The above modifications would lead to a reduced particle intensity in the cluster beam and therefore to a much weaker diffraction signal. While a weaker signal could be compensated by a longer exposure time, the limiting factor here is the diffraction background from the residual inert gas in the diffraction chamber. Since the gas background is measured separately and is subtracted from the pattern, small errors in the measurement of the background result in large errors in the cluster diffraction pattern if the background is large relative to the cluster signal. In addition, the noise of the background is imprinted on the weak cluster signal. Therefore, a weak signal requires a reduction of the pressure in the diffraction chamber from presently $2 \cdot 10^{-6}$ Torr to preferably $1 \cdot 10^{-7}$ Torr or lower. This could be achieved by improving the existing pumping capacities and possibly by an additional pumping stage. Another important factor is the distance from the electron beam aperture to the detector plane as it influences the intensity of the gas background. Consequently, a shorter distance is preferable because it reduces the gas background.

A technique that addresses the difficulties outlined above is the Trapped Ion Electron Diffraction (TIED) [4, 5]. This method relies on a RF Paul trap to accumulate and store size selected ionised clusters for electron diffraction measurements. The temperature of the trapped particles can also be controlled by brief exposure to low pressure He gas. The mass selection and the temperature control are distinct advantages of the TIED technique. However, the RF Paul trap imposes an upper limit on the mass of the

cluster that can be investigated and therefore restricts the technique to small clusters (e.g. Bi_n, $n < 200$).

Electron diffraction on a beam of clusters is a very useful tool for studying the structure of larger unsupported clusters that are not accessible by TIED. These large clusters are very interesting objects: deviations from the bulk structure already become visible for clusters with several thousand atoms and the shape of the clusters can provide valuable information about the surface tension of crystal surfaces. Although a technological challenge, the development of these instruments will focus on mass selected and temperature controlled cluster beams. With a large number of materials waiting to be investigated, research and development efforts will definitely be rewarded.

References

[1] B. D. Hall, U. Ugarte, D. Reinhard, and R. Monot, J. Chem. Phys. **103**, 2384 (1995).

[2] H. Abe, W. Schulze, and B. Tesche, Chem. Phys. **47**, 95 (1980).

[3] W. Schulze, F. Frank, K. P. Charle, and B. Tesche, Ber. Bunsenges. Phys. Chem. **88**, 263 (1984).

[4] M. Maier-Borst, D. B. Cameron, M. Rokni, and J. H. Parks, Phys. Rev. A **59**, 3162 (1999).

[5] S. Krückeberg, D. Schooss, M. Maier-Borst, and J. H. Parks, Phys. Rev. Lett. **85**, 4494 (2000).

Appendix A

Electron Diffraction From Atomic Cluster Beams (book chapter)

B. D. Hall, M. Hyslop, A. Wurl and S. A. Brown,
in *Fundamentals of Gas–Phase Nanotechnology*,
Editors: L. Kish, C. G. Granqvist, W. Marlow and R. W. Siegel,
Kluwers Academic Publishing, 2003.

Chapter 6

ELECTRON DIFFRACTION FROM ATOMIC CLUSTER BEAMS

B. D. Hall
Measurement Standards Laboratory of New Zealand,
Industrial Research Ltd.,
Lower Hutt, New Zealand.

M. Hyslop, A. Wurl, and S. A. Brown*
Nanostructure Engineering Science and Technology Group
and Department of Physics and Astronomy,
University of Canterbury,
Private Bag 4800, Christchurch, New Zealand.
**Corresponding author*

Abstract Electron diffraction is a direct method which can be used to probe *in-situ* the structure of unsupported nanoparticles in molecular beams. The technique is important because it permits a determination of structure, free of the perturbing effects of a substrate, matrix or chemical contamination.

This chapter reviews diffraction experiments with particular emphasis on metal clusters and including some of the work done on rare-gases. These experiments are linked by the observation of multiply twinned (five-fold symmetric) structures for small clusters of materials that have face-centered-cubic bulk structure. As well as describing the historical development of the measurements and the apparatus used, the chapter discusses some of the most recent experimental data for bismuth and lead clusters. Some emphasis is given to the interpretation of diffraction measurements, which is complicated by the fact that nanoparticles cannot usually be described in terms of an underlying crystal lattice.

Keywords: Electron diffraction, Unsupported clusters, Nanoparticles, Metal clusters, Rare gas clusters

1. INTRODUCTION

Nanoparticles with sizes ranging from a few atoms through to tens of thousands of atoms can be seen as spanning the critical size range where the properties of single atoms evolve into the very different properties of macroscopic materials. Virtually all physical and chemical properties of nanoparticles are strongly size dependent, and it is believed that the often novel characteristics that are observed and predicted make nanoparticles good candidates for applications ranging from catalysis to single electron transistors to quantum dot lasers.

In the same way that crystal structure determines electronic band structure and, hence, the other properties of bulk materials, the structure of a nanoparticle can be seen as underpinning all its other properties. The development of a detailed understanding of the factors determining nanoparticle structure is, therefore, an important goal.

Experiments have revealed a remarkable variety of structural properties, but perhaps the most striking is the occurrence of stable and symmetric non-crystalline structures characterised by five-fold axes of symmetry (which are forbidden in bulk crystals). These 'Multiply-Twinned Particles' (MTPs) occur in many face-centered-cubic (FCC) materials, both metals and rare-gases, and are actually preferred energetically to the bulk FCC structure at sufficiently small sizes. Curiously, MTPs much bigger than their thermodynamic critical-size are regularly observed. This underlines an important feature of nanoparticle growth: that the observed structure can be influenced by *both* thermodynamic *and* kinetic factors. It also suggests that control can be exerted over nanoparticle structure: an exciting prospect for future nano-scale engineering.

One of the key factors determining the structure of a nanoparticle is the high proportion of surface atoms. In a 40 Å lead particle, for instance, roughly 40% of atoms are at the surface. These atoms experience a quite different environment from those inside, and competition between surface and volume energies determines the intrinsic structure. However, the balance between these energies is delicate and any interaction between a nanoparticle and its surroundings may significantly influence its behaviour.

Isolated in high vacuum, nanoparticles flowing in a molecular beam are in an almost ideal environment for studying their intrinsic physical properties. However, they are not in an environment which allows application of some of the standard structure determination techniques: particles flowing in a beam cannot be viewed individually (for example, by high-resolution transmission electron microscopy (HRTEM)); further-

more, the volume density of the particle beam is low, precluding the use of x-ray diffraction techniques. Electrons have a much higher scattering crossection than x-rays, and so the best technique available is high-energy electron diffraction.

This chapter presents an overview of electron diffraction from atomic cluster beams, with particular emphasis on metal clusters and including some of the work done on rare-gases, which exhibit structural properties that closely resemble those of FCC metal clusters. It traces developments in both types of cluster studies, from the earliest experiments in the 1970's to the present day. Throughout the chapter we use the word 'cluster' to indicate a nanoparticle in a molecular beam.

The chapter begins with an introduction to electron diffraction and the calculation of diffraction patterns. Following this, the chapter traces the development of the electron diffraction technique. The first measurements, on rare gases, are discussed, followed by the development of techniques suitable for metal clusters. After reviewing the results of experiments on metals as diverse as bismuth and copper, the chapter concludes with a section on recent experimental developments. Throughout the discussion, emphasis is given to the difficulties inherent in the interpretation of experimental diffraction patterns.

2. ELECTRON DIFFRACTION FROM ATOMIC CLUSTERS

The diffraction experiments of interest have a simple crossed-beam geometry: a high-energy electron beam impinges on the molecular beam of clusters at right-angles, and a diffraction pattern is observed below the beam crossing (see Section 5. for more details). Clusters have no preferred orientation in the beam so the diffraction pattern produced is a radially symmetric Debye-Scherrer 'powder' pattern.

2.1 KINEMATIC DIFFRACTION

The Debye-Scherrer pattern of a cluster can be calculated using the Debye equation [1]. This describes the radial distribution of intensity and assumes that kinematic scattering conditions apply. For clusters containing only one type of atom, the intensity scattered per unit solid angle is given by

$$I_N(s) = I_0 N f^2(s) \left[1 + \frac{D(s)}{N} \sum_{n \neq m} \frac{\sin(2\pi s r_{mn})}{2\pi s r_{mn}} \right] , \qquad (6.1)$$

where $s = 2\sin(\theta)/\lambda$, with θ equal to half the scattering angle and λ the radiation wavelength. I_0 is the incident intensity, N is the number of atoms in the cluster and r_{mn} is the distance between atom m and atom n. The atomic scattering factor, $f(s)$, represents the single-atom contribution to scattering, and is available in tabulated form [2]. The factor $D(s)$ expresses attenuation of the interference term in the Debye equation, due to thermal vibrations and static imperfections. It commonly takes the form: $D(s) = \exp\left[-Ms^2\right]$, with M constant.

Equation (6.1) represents the elastic scattering only. Inelastic scattering can be included by adding the term $4NS(s)/a^2s^4$, where $S(s)$ is the x-ray incoherent scattering factor (also tabulated in [2]), and a is the Bohr radius.

Kinematic scattering assumes that incident beam intensity is unchanged in propagating through the particle [3]. However, this may not be true over even a short path through a metal, due to the relatively large value for the atomic scattering crossections. For heavy atoms, such as gold, departures from the Debye equation can occur in nanoparticles containing only a few hundred atoms [4, 5]. Fortunately, the kinematical calculations tend to overestimate the differential crossection by a roughly constant factor, and so the effects of dynamical scattering may not seriously affect identification of structures [5].

2.2 TYPICAL PROFILES

Fig. 1 shows examples of the most commonly observed structures for elements that are FCC in the bulk form. Much of the the recent research into cluster structure, and much of this chapter, is centred on these structures. Calculated diffraction patterns for these structures are shown in Fig. 2.

Particles with FCC structures are conveniently modelled with the cuboctahedral form shown in the first column of Fig. 1. The models used contain between 147 and 1415 atoms, representing diameters from 16 Å to 39 Å. In this case, the models are actually small pieces of a FCC gold lattice, so diffraction peaks could be expected at the positions of bulk diffraction features. Diffraction patterns for the three small FCC particles (Fig. 2 (a)) show that, in fact, some small peak shifts can be discerned and there are clearly 'ripples' in the diffraction pattern that are not related to atomic structure. These are indications of the size-dependent nature of diffraction patterns for nanoparticles. For example, the ripples to the left of the (111) peak change quite noticeably with the cluster size. Also, the 'overlap' of distinct bulk peaks is severe for small

particle sizes. In fact, as equation (6.1) shows, it is more appropriate to think of a cluster's diffraction pattern as a continuous intensity profile.

The icosahedral structure (second column, Fig. 1) is non-crystalline and consists of twenty tetrahedral units joined at a common apex. Although individual tetrahedra may be thought of as distorted FCC tetrahedra, they are in fact exact sub-units of a rhombohedral lattice [6]. The translational symmetry is broken, however, because each tetrahedron is twinned with its three immediate neighbors. The basic hard-sphere packing structure for an icosahedron was first described in [7], however Ino introduced physical model structures for some metals that incorporated uniform elastic strain and these have been used here [8].

Fig. 2(b) shows three diffraction patterns for model icosahedral particles. The positions of bulk FCC peaks are shown again to emphasize the similarity in the appearance of the MTP and FCC diffraction patterns, although icosahedra are not FCC-based structures. The size effects visible in this panel are stronger than those in the FCC patterns. Apart from the strong peak at $s \sim 0.43$ Å^{-1}, the detail in the patterns changes appreciably at each size. Note, in particular, the small peak on the right flank of the main peak which moves to higher s as the size decreases.

Fig. 2(c) shows three diffraction patterns for model decahedral particles. The decahedra are also non-crystalline and can be assembled from five tetrahedra sharing a common edge (which becomes the five-fold axis of symmetry for the particle). However, the distortion of the base FCC structure in these tetrahedral units is less severe than in the icosahedral case, and there are fewer tetrahedral units. The diffraction pattern is similar to that for very small FCC particles, as can be seen in Fig. 2(a). This of course makes identification of decahedra by diffraction very difficult. The distorted tetrahedra of a perfect decahedron actually belong to an orthorhombic lattice [6]. In Ino's more physical model, the thin external wedges of the geometric decahedron are truncated by (100) planes, resulting in a more compact structure [8].

2.3 RELATING MEASUREMENTS TO STRUCTURE

The lack of translational symmetry in nanoparticles makes it often inappropriate to apply traditional crystallographic methods of analysis (e.g.: indexing 'peaks'; estimating particle size from peak broadening; estimating strain and disorder; etc) in nanoparticle studies, especially in studies of FCC materials [9, 10, 11, 12, 13, 14]. This has a profound

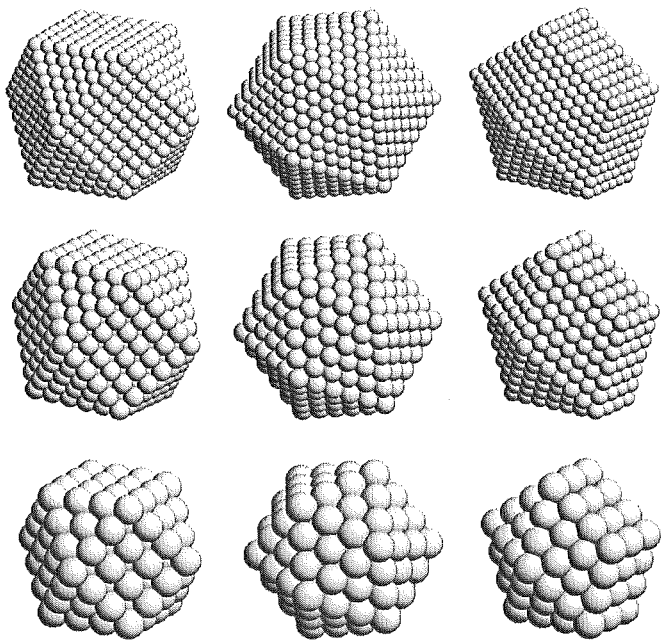

Figure 1 Examples of three types of cluster structures: FCC cuboctahedra, icosahedra and decahedra. The cuboctahedra (first column, N=1415; 561, 147 atoms, from top to bottom) have the same FCC arrangement of atoms as the bulk structure, and are typically observed for large particle sizes. The icosahedral (second column; N=1415, 561, 147 atoms also) and decahedral (third column; N=1514, 605, 116 atoms) structures are believed to be energetically favoured only for very small clusters. These models correspond to the structures used to calculate the diffraction patterns of Fig. 2.

effect on data analysis[1]. It turns out to be necessary to identify all types of structure that could arise in the experiment *before* beginning quantitative analysis. Hence, theoretical tools, such as molecular dynamics (MD) simulations can be very valuable in identifying low-energy structures. Also, observations using HRTEM have been important in

[1]Our comments about the ineffectiveness of traditional methods apply to clusters in which the size of crystalline domains is of the order of a few tens of Å, or where non-crystalline structures exist. If a sample is known to consist of larger, nearly perfect, crystalline particles, as in Section 6.1 then there is no problem.

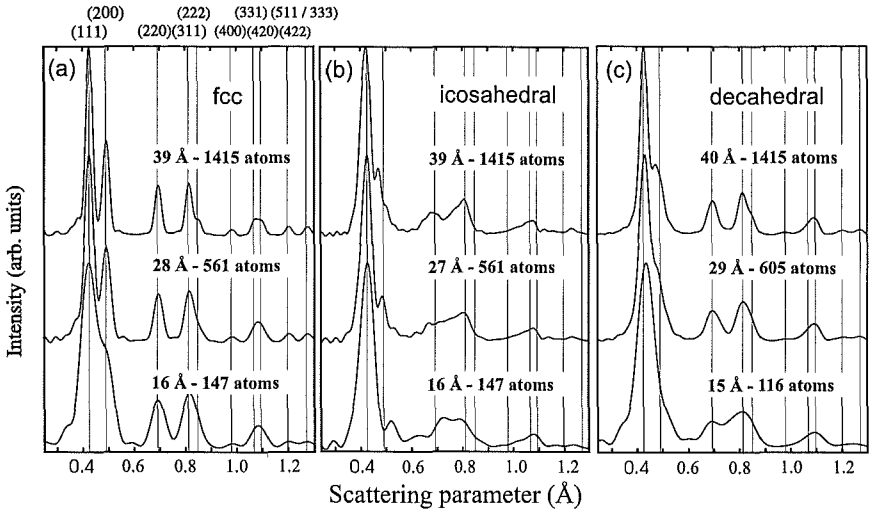

Figure 2 Calculated diffraction patterns for three characteristic forms of nanoparticle structure: FCC (a); icosahedral (b); and decahedral (c). Each panel shows diffraction patterns for particles of different sizes. The calculations used equation (6.1) and parameters for gold ($D(s)$ was set to unity, no inelastic scattering, energy 100 kV). The patterns have been offset vertically, and the intensity at the first maximum normalized, for clarity. The position of bulk Bragg diffraction peaks are labeled at the top of panel (a) and are also marked in panels (b) and (c). Note: positions of FCC Bragg peaks are given in (b) and (c) only to ease comparison; the MTP structures are non-crystalline so there is no associated reciprocal lattice.

identifying structures that must be considered in the analysis of experimental diffraction data.

Often, structure determination is best carried out by comparing calculated diffraction patterns, based on realistic models of structure, with a diffraction measurement. A measurement can be interpreted by selecting the calculated pattern, or a combination of patterns, that best matches the observations. This approach is widely accepted and has been particularly successful in studies of rare-gas clusters, discussed in Section 3.. However, it must be borne in mind that similarity of diffraction patterns does not guarantee agreement between underlying structures. More correctly, when diffraction patterns are similar it suggests that the respective sets of inter-atomic distances (rather than atomic coordi-

nates) are also similar[2]. The decahedral particles in Fig. 2 are a good example of this: it is difficult to distinguish between FCC particles and decahedra, especially when the molecular beam contains a significant distribution of particle sizes.

In an experiment, where the clusters may not have perfect geometric structures, it is difficult to distinguish between whole-particle structure and the structure of coherent domains. Diffraction measurements on particles in which there is some degree of disorder are dominated by the larger domains of coherent structure: in general, therefore, measurement results should be considered as characteristic of the domain structure rather than of the entire particle. It turns out that inter-domain interference effects can be neglected to a first approximation. These important points have been illustrated in many studies, for example: in experimental studies of argon nanoparticles [15]; in simulations of materials with randomly oriented crystalline domains [16, 17]; and in a simulation of fifty five Au_{55} icosahedra, arranged in a slightly perturbed 'super' icosahedral structure [18].

3. RARE-GAS CLUSTERS - THE ORSAY GROUP

The first electron diffraction measurements of unsupported cluster structure were performed by Philippe Audit in 1969, at the *Laboratoire de Diffraction Eléctronique, Université Paris-Sud*, France [19]. These experiments produced clusters of rare-gases, and CO_2, in supersonic beam expansions. The results were compelling: they showed that a variety of clusters could be produced, ranging from larger particles resembling the bulk crystal structure to smaller unidentified structures and liquid drops. The work demonstrated that electron diffraction could provide unique and valuable information about the structure of unsupported clusters.

The success of this first study prompted the construction of an improved apparatus, by Raoult and Farges [20]. It is this set-up that provided the results discussed in this section; it continues to be used today.

[2]McGreevy gives a more detailed discussion of the relationship between structure models and diffraction measurements [72], in the context of the so-called Reverse Monte Carlo method for structure determination of liquids and amorphous bodies [73].

3.1 EARLY RESULTS AND ANALYSIS

Early results were interpreted by comparing measured diffraction patterns with calculated patterns for geometrical structures. For Ar, the results suggested that clusters had the FCC structure and contained ~500 atoms [21] (later revised upwards to ~ 3000 atoms [22]). However, the experimental pattern (see Fig. 2 in Ref. [21]) could not be explained in detail: the (111) peak is abnormally high and the (200) peak was not distinctly separated from it, as expected. At the time, it was thought that these anomalies were due to atoms in close-packed, but non-FCC, sites – a remnant of non-crystalline precursor structures at smaller sizes. It is interesting that, despite the seemingly obvious FCC component in the diffraction patterns, these early measurements have been difficult to interpret in detail and their interpretation remains an area of active research [12, 15, 23] (see further discussion in Section 3.2).

In an attempt to observe the early stages of the growth sequence, the source was adjusted to produce smaller clusters. The minimum observable size was ~20 atoms. Measurements over the size range 20–50 atoms clearly showed that cluster structure could not be explained by either FCC, icosahedral or liquid structures [22]. In fact, the diffraction patterns appeared very similar to those from amorphous metals [22].

Molecular dynamics simulations (using the Lennard-Jones potential) were used to provide more accurate models for comparison with the data. The MD routine could search for the lowest energy structure by simulating the cooling of a liquid drop, allowing time for rearrangement of the atoms to occur, even after solidification [22, 24]. The routine could also be used to compare the stability of different structures, as well as to observe the dynamics of a system at finite temperature.

MD simulations were performed for Ar cluster sizes up to ~150 atoms, identifying a structural change at approximately 50 atoms. Below 50 atoms, Ar clusters adopted a poly-icosahedral structure containing deformed 13-atom icosahedral cages [22]; this changed to a multi-layer icosahedral structure for the larger clusters [24]. The MD simulations also predicted that multi-layer icosahedra with less than ~82 atoms could have a twinned outer layer. Experiments were in excellent agreement with the MD-model diffraction patterns, and showed both the predicted structural transition, as the cluster size was increased, and evidence of a twin layer on the smaller multi-layer icosahedra.

For cluster sizes greater than ~150 atoms MD was too computationally intensive so unrelaxed geometrical icosahedra were used as the model structures. Nevertheless, excellent agreement was reported between these diffraction patterns and experiments, up to a size of ~750

atoms [24]. Beyond this, the appearance of peaks in FCC positions heralded a further structural transition, which is discussed in the next section.

3.2 ICOSAHEDRAL-TO-FCC TRANSITION

It has generally been assumed that for large enough unsupported Ar clusters the bulk FCC crystal structure will predominate, however, this has not been observed[3]. There are many estimates of the critical size at which the FCC structure will become energetically preferred to the icosahedral structure [25, 26, 27, 28]. These estimates vary widely, with the lowest [27] being N$\sim$2000-3000, close to the transition observed in Refs. [11, 24]. Interesting too is the prediction that decahedra are preferred in an intermediate size range falling between the icosahedron, at smaller sizes, and FCC, at larger sizes [25]. However, decahedra have never been identified in experimental results from Ar, or other rare-gas clusters.

Critical size predictions assume that growing clusters achieve thermodynamic equilibrium. Farges *et al.* [22] argue that the smaller Ar clusters have sufficient time (10^{-4} s time-of-flight after nucleation) and energy (temperature $\sim$27 K, c.f. melting point $\sim$35 K) to adopt the equilibrium structure. However, for larger clusters this may not be the case. The energy required to change structure increases with N, and both growth history [28] and growth rate [29, 30] also influence the structure. These factors may result in the production of meta-stable cluster structures [12].

It would be of considerable interest to resolve the question of how, and when, the five-fold symmetric structures that predominate at small cluster sizes can transform into an FCC structure and continue growing. To allow this transition to take place in a natural way, van de Waal [23] has proposed a complex model structure containing intersecting pairs of twin planes which give rise to local regions of five-fold symmetry. This model provides a plausible growth sequence: in a relatively small cluster, the regions of five-fold symmetry dominate (and hence will be observed in experiments), however, the particular arrangement of twin planes promotes FCC growth at the surface. Hence, although containing several small defects, a large cluster essentially has the FCC structure. Diffraction patterns calculated using this model structure match the experiments very well for clusters with $\sim$3000 atoms.

[3]The preference for FCC structure in the bulk is actually not well understood, see [12, 23] and references therein.

Unfortunately, the van de Waal structure does not describe the features of the experimental diffraction pattern for still larger clusters [11, 15]. Indeed, recently de Feraudy *et al.* [11] reported that Ar clusters with $\sim 10^4$ atoms begin to show features characteristic of stacking faults in the diffraction pattern, creating a shoulder on the (111) peak. De Feraudy proposed that these features are created by parallel stacking faults in a FCC cluster, however, diffraction patterns of model structures do not reproduce the peak broadening observed. The most recent study of large Ar clusters ($10^3 < N < 10^5$) now suggests that, in fact, large clusters never adopt a coherent FCC structure [12]! Instead, growth conditions probably lead to formation of inhomogeneous particles with mixed regions of close-packed structure, including FCC, hexagonal close-packed and random stacking of close-packed layers.

4. EARLY METAL PARTICLE STUDIES

The first diffraction measurements on free metal clusters were performed by Gilbert Stein's group at Northwestern University, USA. [31].

4.1 THE NORTHWESTERN SOURCE

Supersonic expansion cluster sources can be used for gases (Ar, CO_2, etc) [19, 21, 32], and seeded supersonic expansions can produce very small metal particles [33]. However, sources for diffraction studies of metals need to provide cooling rates (supersaturation) much higher than those in supersonic expansions, in order to generate intense particle beams. The inert-gas-aggregation (IGA) technique provides suitable conditions and so IGA was readily adapted to provide a particle beam source for diffraction studies [34].

In an IGA source (see Fig. 3), clusters are formed in the gas phase by isobaric cooling. Hot metallic vapour, from an evaporation source, is cooled by an inert buffer gas at room temperature. As it cools, the metallic vapour supersaturates in the vicinity of the evaporation source and clusters nucleate and grow as they are carried away by the buffer gas [34]. This is entirely different to the clustering process in supersonic expansion sources, where cooling and growth occur during the expansion of the gas. In an IGA source, the mixture of gas and formed clusters also passes through nozzle apertures, however this is done to provide a well-collimated particle beam and, more importantly, it allows a large proportion of the unwanted buffer gas to be pumped away.

The original Northwestern source was designed to produce clusters of between 500 and 5000 atoms. In operation, it achieved a background gas pressure of about 10^{-5} mbar in the diffraction chamber. Two tech-

niques for evaporating metal were used: a tungsten filament, in which pieces of metal were inserted; and a boron nitride crucible with a coiled filament heater. The capacity of the these was small and was one of the factors limiting beam life-time and stability: diffraction patterns were commonly visible for about 10 s and never for more than 90 s.

4.2 SOURCE CHARACTERISTICS

The technique of IGA has been used extensively for cluster production under static conditions (see, e.g. [35, 36, 37, 38, 39]), as well as with a flowing buffer gas as in Stein's design [34, 40, 41]. The formation of clusters by IGA is understood qualitatively, however the precise conditions prevailing during experiments are not well known. Cluster formation depends on a variety of parameters: the inert gas pressure p_g; the temperature at the surface of the evaporating material T_m; the buffer gas weight and heat capacity, etc. Stein used p_g and T_m to exert control over the mean cluster size [34]. It was found empirically that as the product $p_g \cdot T_m$ was increased clusters of larger diameter were formed, but in smaller numbers.

Stein and co-workers explored the effect of different buffer gases (Ar, He, CO_2 and SF_6) [42] on the production of Ag cluster beams. These experiments were consistent with the $p_g \cdot T_m$ relation, however the heavier gases produced a given cluster size at a lower value of the pressure-temperature product. This implied that heavier gases, especially molecular gases with larger heat capacity, can enhance the production of clusters and lead to significant cluster production at substantially lower evaporation temperatures. Experiments with the two different evaporation methods described above indicated that these details of the source configuration can have a significant effect on the size distribution (i.e., the nucleation and growth processes) [34].

4.3 EXPERIMENTS ON METAL CLUSTERS

Bismuth, lead, indium and silver clusters with sizes from 2500 to 3×10^4 atoms (diameters between 40–110 Å) were investigated by Stein and co-workers [31, 34, 42]. Stein's group analysed their measurements in terms of an underlying crystal structure: peaks were indexed and their positions and widths measured; changes in lattice parameter were used to estimate cluster temperature, using bulk expansion coefficients. They also recognized the limitations of the kinematic scattering approximation and took steps to investigate its validity [42].

Measurements on indium clusters of between 42 Å and 81 Å, revealed a structural change, from the bulk tetragonal structure to FCC, for clus-

ters with sizes smaller than $\sim$ 50 Å ($\sim$ 3000 atoms) [34]. The diffraction patterns clearly show this transition – the indexing of an FCC structure is unambiguous – however, the possibility of deviations from FCC structure at still smaller sizes was not investigated.

On the other hand, diffraction patterns of bismuth clusters, of between 60-95 Å, showed no departure from the rhombohedral structure, nor any significant size-dependent change in lattice parameter [34].

Investigations of lead (30-100 Å [31, 34]) and silver (40-110 Å [42]) were published in more detail. In the case of lead, careful analysis of peak positions and intensity data revealed anomalies. However, simple dynamical scattering corrections could account for some of the discrepancies and a liquid component was postulated to make an oscillatory contribution to the otherwise monotonic gas background signal. In the case of silver, anomalous observations for smaller clusters could not be reconciled with dynamic scattering corrections and various possible explanations were apparently explored, including the liquid background, MTPs, and stacking faults, without success.

5. FURTHER STUDIES OF METALS

Stein's early work on metal particles was important because it showed the potential of the electron diffraction technique to work under the conditions required to produce metal clusters. An improved apparatus was built, in collaboration with Stein, in the laboratory of Jean-Pierre Borel and René Monot at the *Ecole Polytechnique Fédérale de Lausanne* (EPFL), Switzerland [43]. The design improved on the Northwestern source in several ways: it had much greater evaporation source capacity, allowing longer experiments; an extra pumping stage was added to the source, making the background pressure in the diffraction chamber lower and thereby enhancing the sensitivity to weak diffraction signals; it provided on-line, as opposed to photographic plate, diffraction pattern measurements.

5.1 UNSUPPORTED METAL MTPS

Silver was the first material to be studied at EPFL since it was known to form MTPs and could be readily produced using the IGA technique. The experiments were intended to investigate whether or not the occurrence of MTP structures was in some way an artifact of the particle-substrate interaction in conventional TEM studies [44].

The results showed convincingly that MTPs do occur in small isolated clusters [43]. The careful analysis of series of diffraction patterns for different source conditions showed that, although the cluster samples had

roughly comparable size distributions, there were varying proportions of FCC, icosahedral, and decahedral domains present. The icosahedral signature clearly dominated in one pattern, and the FCC structure was identified in another. Intermediate diffraction pattern shapes were found to have a mixture of decahedral and varying amounts of either icosahedral or FCC domains, suggesting that the decahedral domains were most likely to form under conditions in between those favoring FCC or icosahedra, in accord with predictions of the phase diagram for metal nanoparticles [45].

Two factors were important in the success of these experiments [43]. Firstly, the IGA source was tuned to produce much smaller clusters than those observed by Stein. Secondly, the size distribution of clusters in the beam was explicitly considered in the analysis for the first time. If a range of sizes is present, and there are features in the diffraction pattern that are size-related, then a combination of individual cluster diffraction patterns must be used to interpret the data.

5.2 LARGE METASTABLE ICOSAHEDRA

Following this study, further improvements were made to the apparatus [46]. In particular, a 100 kV electron beam illumination system and a new diffraction pattern recording unit were installed (see Fig. 3). Measurements were faster and much less sensitive to the inevitable drift of the particle beam intensity.

In this new configuration, an investigation of anomalous structure in large silver clusters was undertaken. While still being tested, the modified apparatus had produced observations of unusually large icosahedra under certain source conditions [46]. The unexpected phenomenon was carefully studied by tracing the changing structures in the particle beam as a function of nucleation conditions [30]. Icosahedral clusters as large as 110 Å in diameter were found and it was observed that their structure could apparently be 'tuned' between icosahedral and FCC, while the overall size of the clusters remained roughly constant. This was achieved by either changing the evaporation source temperature or the molecular weight of the carrier gas. Smooth variation of the latter was achieved by introducing a mixture of argon and helium into the source chamber. MD simulations of the growth of Ag clusters have recently shed more light on the processes which may lead to the formation of larger icosahedra [29].

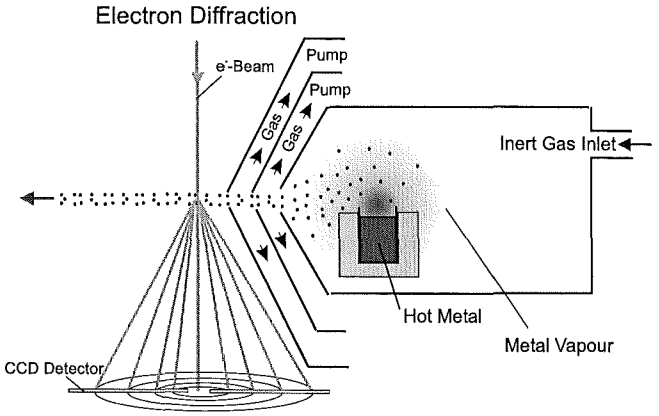

Figure 3 A schematic diagram of the EPFL apparatus. On the right, clusters form in an inert-gas-aggregation source. The mixture of clusters and gas is then drawn through two differential pumping stages before entering the diffraction chamber. The electron and cluster beams cross at right-angles, forming a radially symmetric Debye-Scherrer diffraction pattern. The intensity along a diameter of the pattern is recorded by a pair of charge-coupled device (CCD) detectors. This apparatus has since been relocated to the University of Canterbury, New Zealand (see Section 6.).

5.3 STRUCTURAL TRANSITIONS IN COPPER

MD simulations, performed by Valkealahti and Manninen, have investigated the relative stability of different cluster geometries in copper for sizes up to about 10^4 atoms [47]. The study predicted a critical size of about 2500 atoms (about 38 Å diameter): below this limit, icosahedral clusters were the preferred structure; above it, cuboctahedral (FCC) clusters.

The EPFL apparatus was used to investigate this size dependence. A series of diffraction patterns were obtained for a range of source conditions, intended to span the MD-predicted critical cluster size [48, 49]. These patterns showed clear evidence of structural change taking place (Fig. 4). Detailed analysis revealed a net preference for icosahedral structure in smaller particles and a dominance of FCC domains at larger sizes. Although the experimental uncertainty was rather large, the results of this study supported the theoretical predictions and the critical size estimated from experiment was very close to the MD predicted value.

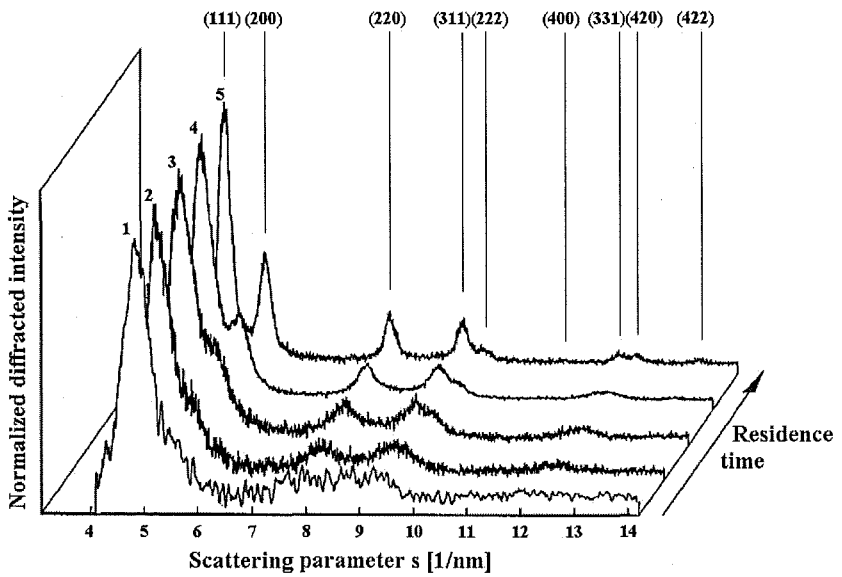

Figure 4 A succession of diffraction patterns from copper clusters presented in increasing order of mean cluster size (patterns 1 to 5), from [48].

6. RECENT STUDIES

In 1998 the EPFL apparatus (see Section 5.) was re-established at the University of Canterbury, New Zealand, where again the focus is on the structure of metallic clusters. Work on bismuth and lead clusters performed at Canterbury since then is discussed in separate subsections below.

6.1 BISMUTH CLUSTERS

The structure of unsupported bismuth particles was first studied by Yokozeki and Stein [34], who reported rhombohedral structures for particles with sizes between 60 and 95 Å (Section 4.).

Besides Stein's work, previous studies of the structure of bismuth clusters have mainly used HRTEM, in which case the clusters are supported on a substrate [50, 51, 52, 53]. These studies have produced a number of conflicting results. Bi particles on an amorphous carbon substrate were found to have a single-crystalline core (50-100 Å diameter, rhombohedral structure) surrounded by an amorphous shell (probably consisting of oxidised Bi), but smaller particles had an amorphous contrast [52, 53]. Other investigations [50] have found a structural transition at a particle size of 84 Å. Particles larger than $\sim$ 50 Å and smaller than 84 Å had the rhombohedral structure of the bulk material, with the shape of a truncated rhombohedron, while larger particles had a complex structure containing lattice defects.

Due to the variety of observations regarding the structure of Bi particles, a further series of experiments have been performed on unsupported clusters. These experiments have explored a large range of cluster sizes as well as investigating the effects of a range of source parameters (gas type, evaporation temperatures, gas pressures) on cluster structure.

6.1.1 Experiments using argon as the carrier gas. Using argon as a carrier gas, bismuth diffraction patterns were obtained for $770°C < T_m < 950°C$. The crucial parameter for the formation of a high cluster flux was p_g. The optimum pressure for cluster beam intensity shifted from 12 mbar at 770°C to 22 mbar at 893°C.

The diffraction patterns shown in Fig. 5 (a)-(d) are characteristic of relatively large clusters and display the rhombohedral structure of the bulk material. Average diameters, determined by the Scherrer formula [1], were 65 Å, 75 Å, 85 Å and 45 Å for patterns (a), (b), (c) and (d), respectively. The uncertainties in these estimates are $\pm$ 10 Å. Relatively small clusters are produced with the original source chamber configuration (Fig. 5(d)), whereas larger clusters were produced when the source

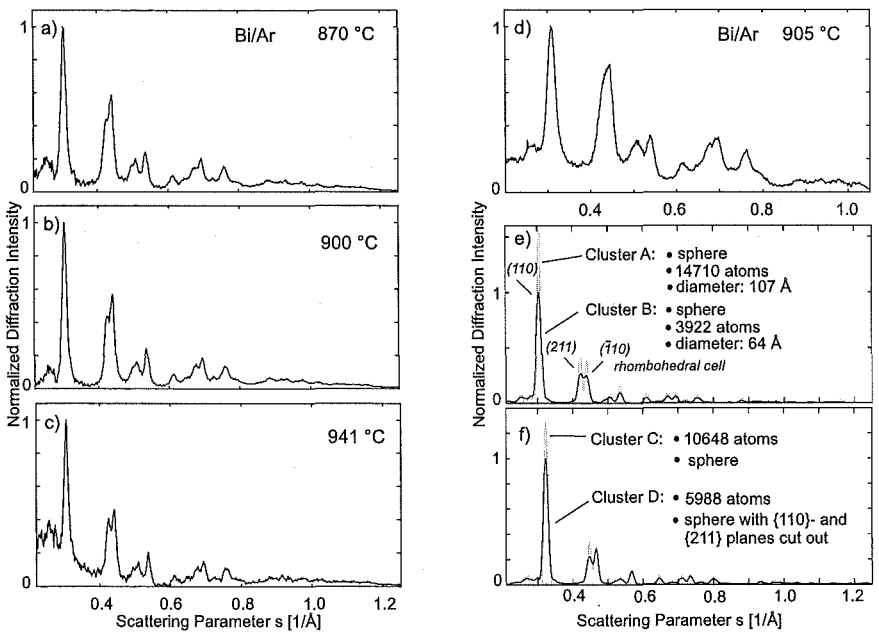

Figure 5 (a)-(c): Experimental diffraction patterns of bismuth clusters produced in Ar. Increasing the evaporation temperature leads to an increase in cluster size, shown by the narrowing of the main diffraction peak and by the clearer splitting of the peaks at $s \sim 0.43$ Å^{-1}. Experiments (a)-(c) were performed in a modified source chamber with improved heat-shielding of the evaporation source, while (d) was performed in the original source chamber and shows smaller clusters. (e) Calculated diffraction patterns for two spherical model structures showing that the (211)/($\bar{1}$10) peak splitting becomes visible for clusters larger than $\sim$ 60 Å. (f) Model structure diffraction patterns showing that the intensity ratio of the (211) and ($\bar{1}$10) peaks can be adjusted by removing some {211} planes from the spherical cluster.

chamber was modified to improve heat shielding of the carrier gas from the evaporation source (Fig. 5 (a)-(c)).

Additional estimates of cluster size can be obtained by comparing the experimental diffraction patterns with calculated patterns of model structures. The splitting of the peak at $s \sim 0.43$ Å^{-1} is clearly visible in calculated patterns for spherical clusters that have a diameter greater than 60 Å (Fig 5(e)). The intensity ratio of the (211) and ($\bar{1}10$) peak in the pattern of the spherical model structures (Fig. 5 (e) and (f)) does not agree with the experimental patterns. However, this intensity ratio can be adjusted to match the experimental patterns by changing the shape of the model clusters i.e. by removing some of the {211} planes from the spherical clusters (Fig. 5 (e)). The low intensity of the (211) peak, therefore indicates a non-spherical shape for the clusters, suggesting that the clusters have the same, truncated rhombohedron, form reported in Ref. [50]. Fig. 5(c) exhibits a residual diffraction background, which may be caused by a high density of atomic bismuth in the cluster beam at higher temperatures.

6.1.2 Experiments using helium as the carrier gas. The production of bismuth clusters using helium required very high gas pressures – beyond the range of our pressure gauge – hence we know only that the pressure was higher than 12 mbar in these experiments. Diffraction patterns of crystalline bismuth clusters were obtained for $T_m > 846$°C (Fig. 6(a)). Additional features begin to appear in the diffraction pattern at $T_m \sim 925$°C (Fig. 6(b)), indicating the formation of a significantly different structure, which becomes dominant for $T_m > 940$°C (Fig. 6(c)). The broad features in these diffraction patterns suggest the presence of amorphous or liquid clusters and are very similar to electron, and x-ray, diffraction patterns from liquid bismuth [54, 55].

During these experiments, a modification was made to the IGA source chamber to improve the heat shielding of the crucible and thereby reduce the transfer of heat from the evaporation source to the inert buffer gas. This effectively enhanced the cooling of the metal vapour by the buffer gas. After this modification, only crystalline diffraction patterns were observed (Fig. 6 (d) and (e)).

The diffraction patterns shown in Figs. 6 (a), (d) and (e) are compatible with the rhombohedral structure, with the lattice parameters of the bulk material. The average diameter of the clusters, determined with the Scherrer formula, is 65 Å, 85 Å and 95 Å for Fig. 6 (a), (d) and (e), respectively. There is no evidence in these observations to support the claim in Ref. [50] that larger clusters undergo a transition to a new cubic-like structure.

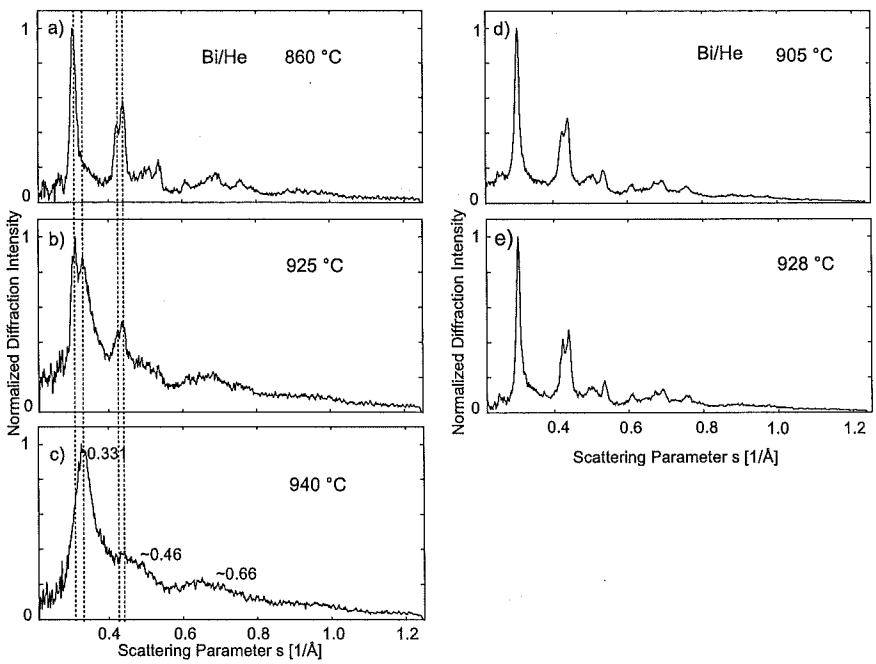

Figure 6 (a)-(c): Experimental diffraction patterns from clusters produced in helium at various evaporation temperatures. The diffraction pattern at 860° C is clearly from crystalline clusters. At 925° C additional features can be observed in the diffraction pattern which dominate the diffraction pattern at 940° C. When modified to provide better heat shielding of the crucible, the source chamber produced only crystalline clusters over the whole accessible temperature range, panels (d) and (e).

6.2 LEAD CLUSTERS

The earliest experimental studies of unsupported 80-100 Å Pb clusters identified clusters with the bulk FCC structure, although they were thought possibly to include amorphous regions [34, 56]. The predominance of FCC structure is consistent with early MD simulations [57] which found that cuboctahedra (FCC structure) were energetically favoured in lead at all cluster sizes. However, this behaviour is in contrast to that of many other FCC metals, for which transitions from FCC to icosahedral structures have been predicted [8, 58, 59] and observed [30, 49, 60, 61], and suggests that Pb clusters are in some way different to other more extensively studied FCC metals: Cu [49], Ag [62] and Au [63, 64].

In a subsequent MD study [65], however, a simulated quench was performed on a large, liquid, 8217-atom lead droplet and the resulting structure was characterised as 'icosahedral-like'. It was not the lowest energy structure, but was thought to occur due to initial formation of (111) planes at the droplet's surface allowing crystallisation to proceed inwards.

6.2.1 Results. Diffraction patterns from lead clusters have been observed across a wide range of T_m and p_g. The diffraction patterns are not observed to change considerably with variations in T_m and p_g, and the previously reported increase in size with $p_g \cdot T_m$ (Section 4.) is not observed clearly in this work. However, by varying the molecular weight of the inert gas (changing the He:Ar ratio) very significant changes in particle size and structure can be achieved. Fig. 7 shows typical diffraction patterns obtained using only Ar, or He, at similar T_m and p_g.

Fig. 8 shows a series of diffraction patterns obtained by varying the He:Ar proportions in the source chamber, while keeping the total inert gas pressure at approximately 4 mbar. A smooth evolution of diffraction patterns was observed between the two extremes shown in Fig. 7. The sharpening of features from pattern 1 to pattern 6 suggests an increase in cluster size, and the evolution of the shoulder feature at ~ 0.4 Å^{-1} indicates a change in the structure of the clusters.

6.2.2 Analysis. Lead cluster diffraction patterns have been analysed by comparison with diffraction patterns from geometric model clusters. A fitting routine [66] combines model diffraction patterns from preselected structures to produce a best match to the experimental data. The model structures used are closed-shell geometrical cuboctahedra (FCC), truncated decahedra, and icosahedra ranging in size from 55 to 6525 atoms (diameters ~15 to ~80 Å).

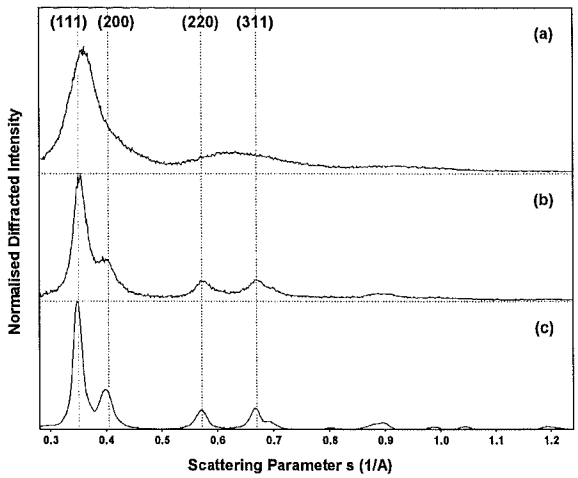

Figure 7 Diffraction patterns obtained from Pb clusters with different inert gases: (a) pure He and (b) pure Ar. For both patterns $T_m = 810°C$ with $p_g = 5$ mbar and $p_g = 2$ mbar, for (a) and (b) respectively. Panel (c) shows the diffraction pattern of a large model decahedron cluster, shown for comparison with experimental patterns from large particles. The positions of the bulk (FCC) peaks for Pb are indicated by the dashed lines.

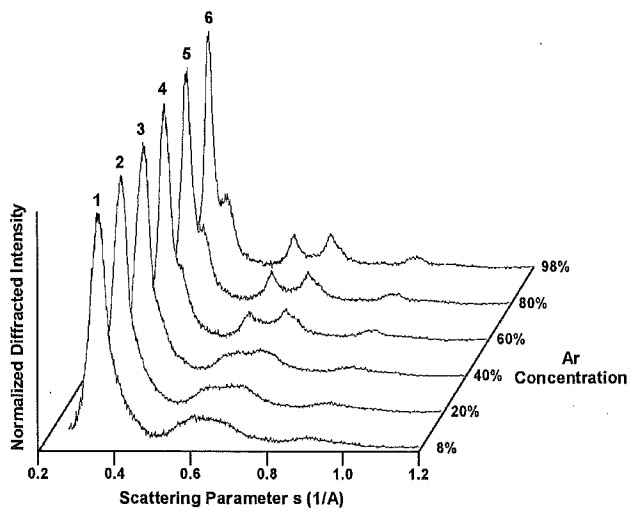

Figure 8 Diffraction patterns obtained from Pb clusters by increasing the mixing ratio of Ar to He from profile 1 to 6. $T_m = 840°C$ and the total inert gas pressure is ~4 mbar.

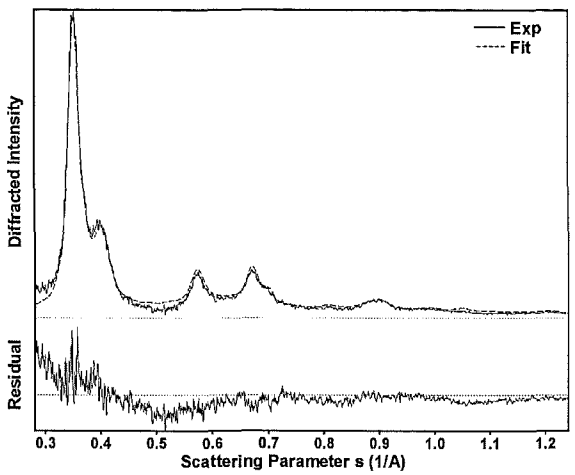

Figure 9 Fit for pattern 6 in Fig. 8. The experimental curve is well matched by the inclusion of large decahedral domains. The lower panel is the difference between experiment and fit (on an expanded scale).

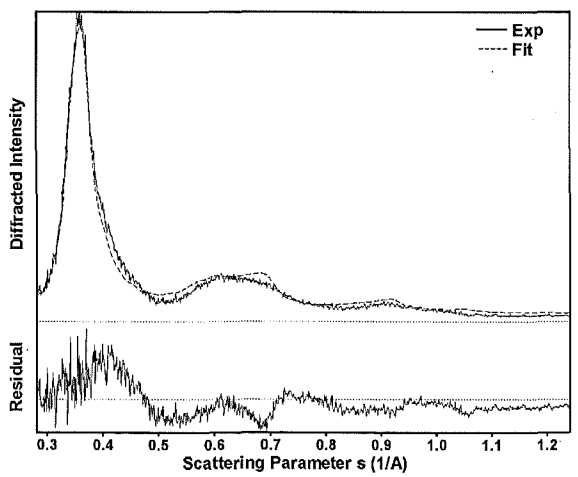

Figure 10 Fit for pattern 1 in Fig. 8. The fit does not accurately reproduce the shapes of the shoulder at 0.4 Å^{-1} and the broad peak centred on 0.62 Å^{-1}, indicating that alternative structures must also be considered. The lower panel is the difference between the experiment and fit (on an expanded scale).

Estimates of the mean experimental cluster size are made using several methods: the Scherrer formula [1], Fourier inversion of the diffraction pattern [14], and from results of the fitting analysis (note that, as discussed in Section 2., a size estimate obtained from fitting will be indicative of the domain size, which may be smaller than the particle size).

Table 6.1 summarises the results of the fitting procedure for patterns 1, 3, 4 and 6 from Fig. 8, as well as the various size estimates. The rather good agreement between the different size estimates suggests that the fits may be identifying domain structures that fill most of the clusters' volume.

6.2.3 Discussion. The fit for pattern 6 is shown in Fig. 9. The results (Table 6.1) suggest that pattern 6 is dominated by large decahedral domains. The resemblance between diffraction patterns, from large decahedral clusters, and the experimental pattern is striking (see Fig. 7(c)). However, the decahedron is not the preferred structure at these sizes so its observation is unexpected. The experimental diffraction pattern has also been compared (by fitting) to other candidate structures, such as twinned FCC clusters, however decahedral patterns provide the best fit to the experimental data.

The fit for pattern 1 is shown in Fig. 10. Here, the results indicate that domains are predominantly icosahedral. However, in this case, fitting does not satisfactorily reproduce the shapes of the shoulder at 0.4 Å^{-1} and the broad peak centered on 0.62 Å^{-1}. This indicates that the basis patterns used for fitting can not completely reproduce the cluster structures in the beam: alternative structural models need to be considered as well.

The results of the fitting procedure (Table 6.1) for patterns 1, 3, 4, and 6 in Fig. 8 show that the composition of the cluster beam changes as the proportion of He:Ar is altered. Compared to pattern 1, there is an increase in average domain size for patterns 3 and 4 (note the appearance of a clear splitting between the peaks at 0.57 Å^{-1} and 0.67 Å^{-1}) and the continued dominance of icosahedral domains. The fitting analysis of pattern 4 also reports a population of large decahedral domains, which increases for pattern 6. Interestingly none of the patterns in Fig. 8 include the bulk FCC structure, in sharp contrast to initial studies [34] which found that slightly larger Pb clusters had exclusively the bulk structure. This may indicate that a transition to bulk structure occurs at a size larger than 70 Å, however structural analysis in the earlier study did not fully consider the possibility of MTP structures.

Table 6.1 Results of fitting procedure for experimental patterns 1, 3, 4, and 6 from Fig. 8. The parameter d is the average (volume weighted) domain size for each structure, δ_d is the standard deviation of d, and v is the proportion of each structure (by volume). The size estimates from three independent methods are also shown.

Structure		Experimental Profile 1	3	4	6
Cuboctahedral	d(Å)	-	-	-	-
	δ_d(Å)	-	-	-	-
	v(%)	0.0	0.0	0.0	0.0
Decahedral	d(Å)	19	42	77	75
	δ_d(Å)	3	6	7	11
	v(%)	3.5	0.2	14.4	58.5
Icosahedral	d(Å)	29	34	43	37
	δ_d(Å)	12	10	14	16
	v(%)	96.5	99.8	85.6	41.4
Size estimates	Fitting ±1	28	34	48	59
(Å)	Inversion ±5	30	35	40	60
	Scherrer ±10	20	25	30	40

Research on lead clusters is ongoing. Other model structures (especially relaxed MD generated structures) need to be compared with our experimental results. Further experiments will also be performed, examining the effects of growth time and enhanced cooling of the metal vapour.

7. ALTERNATIVE ELECTRON DIFFRACTION TECHNIQUES

Inevitably, suitable particle sources generate clusters with a distribution of sizes, so a measured diffraction pattern reflects the ensemble as a whole and is not characteristic of a single particle size. In a continuous beam system, mass filtering has the potential to select particles of a single size but will significantly reduce the diffracted intensity, thus worsening the signal-to-noise in the measurement. In this section we highlight a recently developed alternative technique and discuss some of its advantages and disadvantages.

7.1 DIFFRACTION FROM TRAPPED CLUSTERS

The Trapped Ion Electron Diffraction (TIED) technique [67, 68], developed at the Rowland Institute, Boston, relies on a RF Paul trap to size-select and accumulate clusters. Neutral clusters are produced by either a Knudsen oven [67] or an IGA source [68] and then ionised, so that they can be loaded into the trap. Both the neutral cluster beam and the trapped ions can be probed by a 40 kV electron beam. A carefully designed Faraday cup captures unscattered electrons and a microchannel plate and phosphor screen system, inside the vacuum chamber, is used to image the diffraction pattern in conjunction with an external CCD camera.

The TIED technique works by selecting ions with a certain mass-to-charge ratio. The excellent mass resolution of the system has been demonstrated for $(CsI)_nCs^+$ ions, where the dominant structure (bulk CsI) for $n = 32$ is observed to be different to that for other members of the sequence $n = 30 - 39$ (NaCl structure).

One significant difference between TIED and the molecular beam techniques discussed elsewhere in this chapter is that the clusters are ionised. Electron scattering from a charged body is different from a neutral one. However, the extent of s over which significant differences in the scattering factor occur is roughly from $s = 0$ up to the reciprocal of the particle size [3]. Hence, for metal clusters larger than ~ 10 Å the effect of charging the particle can safely be ignored.

An excellent feature of the TIED technique is that it permits the temperature of the trapped ions to be controlled by brief exposure to low pressure He gas. In contrast, particle temperature in the molecular beam produced by an IGA source is difficult to control. (It can be achieved by allowing the particles to thermalize in drift region separated from the nucleation chamber [40, 41], but it is unlikely that this can still provide an intense particle beam for diffraction).

TIED offers several significant advantages over molecular beam techniques, but it also has some unique difficulties of its own, and in particular the combination of an RF trap with a sensitive electron-beam apparatus is not technically trivial. The Rowland group has carefully characterised their experiment and has shown that many possible problematic effects can be ignored. For example, the perturbing effects of RF fields on the electron probe have been calculated and observed, and are shown to be small.

The TIED technique has yet to be applied to metal clusters, and so the effect of a relatively long exposure period to the electron beam

($\sim$ 45 s per data sequence [67]) have yet to be clarified. It is well-known from HRTEM studies that supported nanoparticles of the order of 30 Å or less undergo rapid structural rearrangements when irradiated with a high-energy electron flux [45, 69, 70]. In contrast to TIED, fast moving clusters from a continuous molecular beam source are individually exposed to a very weak electron flux; so weak in fact that the probability of more than one electron scattering from a single cluster is very low [71].

8. CONCLUSION

Electron diffraction measurements on molecular beams of clusters have been reviewed. Emphasis has been given to studies of beams of metal clusters and the closely related work on inert gas clusters. Improvements in both source design and diffraction techniques over the last 20 years have been discussed alongside the experimental data.

Unsupported silver and copper clusters have been investigated in some detail in the past and deviations from the bulk FCC structure have been clearly observed. For small enough particles icosahedral structures are preferred energetically but much larger meta-stable icosahedral particles have also been observed under rapid growth conditions. The detailed examination of silver and copper clusters contrasts with the scarcity of data for the majority of metal clusters and further investigations are very much needed.

Preliminary new results on bismuth clusters, which exhibit the bulk structure as well as a clear phase transition, and lead clusters, for which the bulk FCC structure is not observed, have been presented. Finally, a new development in the technology of electron diffraction from clusters, the trapped ion electron diffraction technique has been reviewed.

References

[1] A. Guinier, *X-ray diffraction in crystals, imperfect crystals and amorphous bodies*, Dover, New York, 1994.

[2] A. J. C. Wilson, editor, *International tables for crystallography*, volume C, Kluwer, Dordrecht, 1992.

[3] B. K. Vainshtein, *Structure analysis by electron diffraction*, Pergamon Press, Oxford, 1964.

[4] L. S. Bartell, B. Raoult, and G. Torchet, J. Chem. Phys. **66**, 5387 (1977).

[5] B. D. Hall, D. Ugarte, D. Reinhard, and R. Monot, J. Chem. Phys. **103**, 2384 (1995).

[6] C. Y. Yang, J. Cryst. Growth **47**, 274 (1979).

[7] A. L. Mackay, Acta Cryst. **15**, 916 (1962).

[8] S. Ino, J. Phys. Soc. Jpn. **27**, 941 (1969).

[9] L. H. Germer and A. H. White, Phys. Rev. **60**, 447 (1941).

[10] C. W. B. Grigson and E. Barton, Brit. J. Appl. Phys. **18**, 175 (1967).

[11] M. de Feraudy and G. Torchet, J. Cryst. Growth **217**, 449 (2000).

[12] B. W. van de Waal, G. Torchet, and M. F. de Feraudy, Chem. Phys. Lett. **331**, 57 (2000).

[13] C. B. Walker, Acta Cryst. A **33**, 342 (1977).

[14] B. D. Hall, D. Zanchet, and D. Ugarte, J. Appl. Cryst. **33**, 1335 (2000).

[15] B. W. van de Waal, J. Mol. Struct. **485-486**, 269 (1999).

[16] F. Betts and A. Bienenstock, J. Appl. Phys. **43**, 4591 (1972).

[17] F. L. Galeener and M. M. Rodoni, Calculation of interparticle contributions to x-ray scattering by a microcrystalline medium, in *Amorphous and liquid semiconductors*, edited by J. Stuke and W. Brenig, pages 101–108, Taylor and Francis, London, 1974.

[18] W. Vogel, B. Rosner, and B. Tesche, J. Phys. Chem. **97**, 11611 (1993).

[19] P. Audit, J. Phys. **30**, 192 (1969).

[20] B. Raoult and J. Farges, Rev. Sci. Instr. **44**, 430 (1973).

[21] J. Farges, B. Raoult, and G. Torchet, J. Chem. Phys. **59**, 3454 (1973).

[22] J. Farges, M. F. de Feraudy, B. Raoult, and G. Torchet, J. Chem. Phys. **78**, 5067 (1983).

[23] B. W. van de Waal, Phys. Rev. Lett. **76**, 1083 (1996).

[24] J. Farges, M. F. de Feraudy, B. Raoult, and G. Torchet, J. Chem. Phys. **84**, 3491 (1986).

[25] B. Raoult, J. Farges, M. F. De Feraudy, and G. Torchet, Phil. Mag. B **60**, 881 (1989).

[26] J. Xie, J. A. Northby, D. L. Freeman, and J. D. Doll, J. Chem. Phys. **91**, 612 (1989).

[27] B. W. van de Waal, J. Chem. Phys. **90**, 3407 (1989).

[28] B. W. van de Waal, J. Chem. Phys. **98**, 4909 (1993).

[29] F. Baletto, C. Mottet, and R. Ferrando, Phys. Rev. Lett. **84**, 5544 (2000).

[30] D. Reinhard, B. D. Hall, D. Ugarte, and R. Monot, Phys. Rev. B **55**, 7868 (1997).

[31] A. Yokozeki, J. Chem. Phys. **68**, 3766 (1978).

[32] G. D. Stein and J. A. Armstrong, J. Appl. Phys **58**, 1999 (1973).

[33] G. D. Stein, Surf. Sci. **156**, 44 (1985).

[34] A. Yokozeki and G. D. Stein, J. Appl. Phys. **49**, 2224 (1978).

[35] R. Uyeda, J. Cryst. Growth **24/25**, 69 (1974).

[36] Y. Saito, S. Yatsuya, K. Mihama, and R. Uyeda, J. Cryst. Growth **45**, 501 (1978).

[37] T. Hayashi, T. Ohno, S. Yatsuya, and R. Uyeda, Jpn. J. Appl. Phys. **16**, 705 (1977).

[38] S. Kasukabe, S. Yatsuya, and R. Uyeda, Jpn. J. Appl. Phys. **13**, 705 (1974).

[39] C. G. Granqvist and R. A. Buhrman, J. Appl. Phys. **47**, 2200 (1976).

[40] H. Abe, W. Schulze, and B. Tesche, Chem. Phys. **47**, 95 (1980).

[41] W. Schulze, F. Frank, K. P. Charlé, and B. Tesche, Ber. Bunsenges. Phys. Chem. **88**, 263 (1984).

[42] B. G. D. Boer and G. D. Stein, Surf. Sci. **106**, 84 (1981).

[43] B. D. Hall, M. Flüeli, R. Monot, and J.-P. Borel, Phys. Rev. B **43**, 3906 (1991).

[44] J.-P. Borel, Surf. Sci. **106**, 1 (1981).

[45] P. M. Ajayan and L. D. Marks, Phys. Rev. Lett. **60**, 585 (1988).

[46] B. D. Hall, M. Flüeli, D. Reinhard, R. Monot, and J.-P. Borel, Rev. Sci. Instrum. **62**, 1481 (1991).

[47] S. Valkealahti and M. Manninen, Phys. Rev. B **45**, 9459 (1992).

[48] D. Reinhard, B. D. Hall, P. Bertould, S. Valkealahti, and R. Monot, Phys. Rev. Lett. **79**, 1459 (1997).

[49] D. Reinhard, B. D. Hall, P. Bertould, S. Valkealahti, and R. Monot, Phys. Rev. B **58**, 4917 (1998).

[50] Y. Oshima, K. Takayanagi, and H. Hirayama, Z. Phys. D **40**, 534 (1997).

[51] M. Treilleux, G. Fuchs, F. S. Aires, P. Melinon, and A. Hoareau, Z. Phys. D **20**, 263 (1991).

[52] M. Treilleux, G. Fuchs, C. Montandon, F. Santos Aires, P. Melinon, B. Cabaud and A. Hoareau, Phil. Mag. A **67**, 1071 (1993).

[53] G. Fuchs, M. Treilleux, F. S. Aires, A. H. B. Cabaud, and P. Melinon, Phil. Mag. A **61**, 45 (1990).

[54] M. Takagi, J. Phys. Soc. Jpn. **11**, 396 (1956).

[55] P. C. Scharrah, J. I. Petz, and R. F. Kruh, J. Chem. Phys. **32**, 241 (1960).

[56] A. Yokozeki and G. D. Stein, J. Appl. Phys. **49**, 2224 (1978).

[57] H. S. Lim, C. K. Ong, and F. Ercolessi, Surf. Sci. **269/270**, 1109 (1992).

[58] J. E. Hearn and R. L. Johnston, J. Chem. Phys. **107**, 4674 (1997).

[59] S. Valkealahti and M. Manninen, Z. Phys. D **26**, 255 (1993).

[60] L. D. Marks, Rep. Prog. Phys. **57**, 603 (1994).

[61] S. Ino, J. Phys. Soc. Jpn **21**, 346 (1966).

[62] S. Giorgio, J. Urban, and W. Kunath, Phil. Mag. A **60**, 553 (1989).

[63] C. L. Cleveland, U. Landman, T. G. Schaaff, M. N. Shafigullin, P. W. Stephens and R. L. Whetten Phys. Rev. Lett. **79**, 1873 (1997).

[64] K. Heinemann, M. J. Yacaman, C. Y. Yang, and H. Poppa, J. Cryst. Growth **47**, 177 (1979).

[65] H. S. Lim, C. K. Ong, and F. Ercolessi, Comp. Mat. Sci. **2**, 495 (1994).

[66] B. D. Hall, J. Appl. Phys. **87**, 1666 (2000).

[67] M. Maier-Borst, D. B. Cameron, M. Rokni, and J. H. Parks, Phys. Rev. A. **59**, 3162 (1999).

[68] S. Kruckeberg, D. Schooss, M. Maier-Borst, and J. H. Parks, Phys. Rev. Lett. **85**, 4494 (2000).

[69] S. Iijima and T. Ichihashi, Phys. Rev. Lett. **56**, 616 (1986).

[70] D. Ugarte, Elec. Microsc. **2**, 677 (1992).

[71] B. D. Hall, *An installation for the study of unsupported ultrafine particles by electron diffraction with application to silver*, PhD thesis, EPFL, Lausanne, Switzerland, 1991, No. 954.

[72] R. L. McGreevy, J. Non-Cryst. Solids **156-158**, 949 (1993).

[73] R. L. McGreevy and L. Pusztai, Mol. Simul. **1**, 359 (1988).

List of Figures

List of Tables

List of used Acronyms

BCC	-	Body-centred cubic
CCD	-	Charge-coupled device
DFT	-	Density functional theory
FCC	-	Face-centred cubic
FFT	-	Fast Fourier transform
FWHM	-	Full width at half maximum
HCP	-	Hexagonal close-packed
HRTEM	-	High resolution transmission electron microscopy
MC	-	Monte Carlo (calculation)
MD	-	Molecular dynamics (calculation)
LDA	-	Linear diode array
RMC	-	Reverse Monte Carlo (method)
TEM	-	Transmission electron microscopy
TIED	-	Trapped ion electron diffraction
TOF-MS	-	Time-of-flight mass spectrometer
UHV	-	Ultra high vacuum
XRD	-	X-ray diffraction

Acknowledgements

First of all, I would like to thank my supervisor, Dr. Simon Brown, for his support, encouragement and the many fruitful and inspiring discussions during my thesis work.

This thesis has also benefited greatly from the experience and expertise of Dr. Blair Hall at Industrial Research Limited in Lower Hutt. During his thesis work at EPF, Lausanne, he performed diffraction experiments on Ag clusters and worked on major improvements to the experimental equipment which was later relocated to the UOC. Dr. Hall provided valuable assistance when it came to problems with the equipment, question concerning the data analysis or detector issues.

I would like to thank Dr. Michael Hyslop who spend the first year of his PhD on the reconstruction of the equipment and with whom I shared the challenge to produce clusters and measure diffraction patterns. I also heavily used his TEM image processing software.

This thesis includes results from MD simulations of bismuth clusters which were performed by Dr. Shaun Hendy from Industrial Research Limited in Lower Hutt, NZ. This contribution is greatly appreciated.

All modifications to the experimental equipment and in particular the development of the new detector system were only made possible due to the very high level of skill and competence of the technical staff at the Physics and Astronomy Department. Nearly all of them have contributed to this study. In particular, I would like to mention Ross Ritchie, Geoff Graham and Graeme Kershaw for their work on the new detector system and the flow controller, and Graeme McDonald, Wayne Smith and Ron Cully who worked hard to tackle any electrical and mechanical problems.

I also would like to thank Jan MacKenzie for making her TEM lab available to us and for her time spent helping.

Furthermore, I am most grateful for the companionship and assistance from the fellow research students in the cluster group: Dr. Michael Hyslop, Monica Schulze, Martin Kaufmann, Dr. Juern Schmelzer and Rene Reichel.

Finally, I would like to acknowledge the funding received from the German Academic Exchange Service (DAAD) as part of the HSP III of the Federal Government and States, Germany.